

Fundamental Investigation for 3D Reactive Inkjet Printing of Bisphenol A-Polycarbonate

By

Qifeng Qian, B.Eng.

A Doctoral Thesis Submitted in Partial Fulfilment of the Requirements for the Award of Doctor of Philosophy of the University of Nottingham

Department of Mechanical, Materials and Manufacturing Engineering

October 2018



Abstract

Additive Manufacturing (AM) techniques have gained extensive attention recently because they are in general able to produce 3D parts in a layer-by-layer manner directly. When compared to the traditional manufacturing techniques such as tooling and milling, AM generally has a higher design freedom of the geometry and reduces material waste. Many AM techniques have the potential to revolutionize manufacturing industry and inkjet printing is one such technique. Inkjet printing is able to dispense liquid material in a form of tiny droplets (i.e. picolitre scale) through a printhead. The solidification of the deposited material is usually completed by UV photoinitiation or solvent evaporation. The viscosity of the liquid material is the key factor to consider when implementing inkjet printing, as it requires a low range (usually less than 30 cP) which makes it difficult to direct inkjet printing some high molecular weight polymers in solution. There is an emerging inkjet printing approach, known as “reactive inkjet printing”, which could solidify the material on the substrate by means of a chemical reaction rather than photoinitiation. Low viscosity monomer or oligomeric materials are used instead of using the polymer directly to form reactive inks which are dispensed and mixed on the substrate. The materials then cure to form the 3D solid parts, layer by layer.

Bisphenol A-polycarbonate (BPA-PC) is one of the important engineering thermoplastic materials, which has excellent mechanical strength, optical transparency and thermal resistance. The only commercial AM techniques to produce BPA-PC is Fused Deposition Modelling (FDM) which relies on the direct hot-melt extrusion of the polymer. Such FDM made parts, however, have low feature resolution and poor surface textures due to the extremely high melt viscosity of BPA-PC. This research focuses on the development of a novel reactive ink and the establishment of the reactive inkjet printing approach to fabricating BPA-PC. Two different routes (hot-melt and solvent-based printing) were explored to fundamentally study the feasibility.

For the hot-melt route, the monomers, Bisphenol A (BPA) and Bis-Methyl Salicyl Carbonate (BMSC) were directly melted to form inks which could be printed using a high temperature printhead. The waveforms for actuating the droplets of the two monomers were optimized to achieve stable droplet formation, respectively. The droplet deposition of the hot-melt inks was investigated to ascertain the suitable droplet spacing to form well-defined continuous patterns. However, due to the restriction of the temperature specification of the printhead, to take this approach further, an investigation is recommended to proceed with the development of the printhead assembly, though, in general, it has great potential to study the reactive hot-melt approach to fabricating 3D BPA-PC parts.

For the solvent-based route, novel reactive inks were developed by dissolving BPA and BMSC in organic solvents with a catalyst to form a precursor reactive mixture ink. Different solvents were investigated to maximize the loading of reactive mixture and to meet the rheology requirement of the inkjet printing. Dimethylformamide (DMF) and 1,4-dioxane were chosen to form two reactive inks with different compositions. Subsequently, a range of substrate temperatures and droplet spacings were explored to find suitable printing process parameters. The reactive mixture deposited also required post processing where a vacuum oven was used to further polymerise the printed samples to a desired molecular weight in an elevated temperature and low-pressure environment. The sample morphology was evaluated by a white light interferometer. A range of characterisation techniques, including DSC, TGA, GPC and NMR were applied to examine the thermal and chemical properties and the results confirmed the formation of high molecular BPA-PC by this novel approach. Finally, a ‘polymerisation layer by layer’ strategy was explored to build a 3D ziggurat structure of BPA-PC, which successfully demonstrated the AM capability of BPA-PC by reactive inkjet printing.

Acknowledgement

I came across many people who have been always helping and supporting me to progress towards a PhD degree during the past four years. It has been a great honor to have these people with me throughout my PhD and I would like to say more than a ‘THANKS’ to all of them.

Firstly, I would like to express my sincere gratitude to my supervisor Professor Christopher Tuck, Professor Ricky Wildman and Professor Richard Hague for offering the great opportunity to me for completing my postgraduate research in the world-leading Centre for Additive Manufacturing (CfAM) research group at the University of Nottingham. They always give invaluable support, guidance and encouragement throughout my PhD. I feel so fortunate to conduct my research under their dedicated supervision.

A special thanks to Dr Belen Begines as my additional supervisor who gave countless help and support throughout my research. I always received her patient guidance on the chemistry work and useful comments on the paperwork.

I extend my deep appreciation to the industrial sponsor SABIC Innovative Plastics Bergen op Zoom for their financial support to my PhD. My sincerely thanks are dedicated to Dr Hao Gu, Dr Brian Price and Dr Jan Henk Kamps for their technical suggestions and encouragement during the project.

I would like to express my immense thanks to Mr Mark East and Mr Mark Hardy for their technical support in CfAM. Without them my experimentation work would not go smoothly towards completion.

I am very grateful to all my colleagues and ex-colleagues in CfAM for their support and help throughout my research, especially Dr Yinfeng He, Mrs Hagit

Gilon, Dr Asish Malas, Dr Elisabeth Clark, Dr Craig Sturgess and Dr Fan Zhang for their patient and kindly lab equipment training for me, as well as their suggestions for my research.

It would not be possible to complete my research without many other support staff in the university. Here I would like to sincerely thank Dr Guping He and Miss Xue Wu in the Department of Chemistry, for their kindly help for the use of the GPC equipment. I am also thankful to Dr Aslam Shazad in the Department of Chemistry for the training of NMR.

I express my sincere thankfulness to all my friends in Nottingham for bringing happiness to me in the most difficult time. I give my deepest gratitude to my father and mother for their constant support and understanding for my study abroad. Finally, I wish to express my gratitude to my beloved, Yaoyao, for her patience, understanding and encouragement in the past a few years. It is a long journey towards a PhD, but her unconditional and warm companion made my journey pleasant, motivated and comfortable.

Table of Contents

Abstract ..... **I**

Acknowledgement ..... **III**

Table of Contents ..... **V**

List of Figures ..... **XI**

List of Tables ..... **XIX**

List of Schemes ..... **XXI**

Acronyms ..... **XXII**

1. Introduction **1**

1.1. Background 1

1.2. Research Scope 2

1.3. Research Concept 3

2. Literature Review **5**

2.1. Additive Manufacturing 5

2.1.1. Basic Concept of Additive Manufacturing 5

2.1.2. Development of Additive Manufacturing 6

2.1.3. Process Chain of Additive Manufacturing 7

2.1.4. Classification of Additive Manufacturing 8

2.1.5. Applications of Additive Manufacturing 10

2.2. Inkjet Printing Technology 11

2.2.1. Basic Concept of Inkjet Printing 11

2.2.2. 2D Inkjet Printing to 3D Inkjet Additive Manufacturing 12

2.2.3. Classification of Inkjet Printing Technology 13
2.2.4. Continuous Inkjet 13
2.2.5. Drop-on-demand (DoD) Inkjet 15
2.2.6. Inkjet Printing of Polymers 18
2.3. Reactive Inkjet Printing (RIP) 19
2.3.1. Basic Concept of RIP 19
2.3.2. Ink Requirement for RIP 20
2.3.3. Actuation and Droplet Formation 23
2.3.4. Droplet Deposition 28
2.3.5. Drying Mechanisms of Inks 32
2.3.6. Applications of RIP in Polymeric Material Deposition 36
2.4. Polycarbonate 40
2.4.1. Evolution of Polycarbonate Chemistry 40
2.4.2. Synthesis of Polycarbonate 41
2.4.3. Comparison of Synthesis Routes for Polycarbonate 44
2.4.4. Transfer to Non-Phosgene Melt Polymerisation 44
2.4.5. Polycarbonate in Additive Manufacturing 45
2.4.6. *In-situ* Polymerisation for Synthesis of Polycarbonate 47
2.5. Conclusions from the Literature 48
2.5.1. Research Novelty 48
2.5.2. Research Challenge 49
3. Methodology and Experiment 50
3.1. Research Approach 50

3.2. Reactive Inkjet Printing of Hot-melt Inks 52

3.2.1. Development and Assessment of Hot-melt Inks 52

3.2.2. Printing of Hot-melt Inks 56

3.2.3. Printhead Modification 63

3.2.4. Sample Characterisations 64

3.3. Reactive Inkjet Printing of Solvent-based Inks 65

3.3.1. Development of Reactive Solvent-based Inks 65

3.3.2. Printability Assessment of the Solvent-based Reactive Inks 67

3.3.3. Printing of Reactive Solvent-based Inks 68

3.3.4. Polymerisation Conditions for Post Processing 72

3.3.5. Sample Characterisations 73

4. Results: Reactive Inkjet Printing of Hot-melt Inks 76

4.1. Introduction and Research Rationale 76

4.1.1. Reactive Inks Formulation 77

4.1.2. Composition and Stability of Reactive Inks 78

4.2. Printability Assessment of Hot-melt Inks 80

4.2.1. Melt Behaviour of BPA and BMSC 80

4.2.2. Viscosity of BPA and BMSC 82

4.2.3. Surface Tension of BPA and BMSC 83

4.2.4. Printability Assessment for Molten BPA and BMSC 84

4.3. Characterisation of Jetting Mixture 85

4.3.1. Rheological Behaviour of Mixture 86

4.3.2. Bulk Polymerisation of BPA and BMSC 87

4.3.3. Interpretation of FT-IR Spectrum for Bulk Polymerisation 88
4.4. Thermal Stability of Hot-melt Inks 90
4.4.1. Thermal Stability Study of Monomers 91
4.5. Droplet Formation of Hot-melt BMSC 94
4.5.1. Droplet Formation Stability Observation 94
4.5.2. Waveform Optimisation for Jetting Hot-melt BMSC 95
4.5.3. Droplet Volume and Velocity Modulation 98
4.6. Ink Deposition of Hot-melt BMSC 101
4.6.1. Single Droplet Deposition of Hot-melt BMSC 102
4.6.2. Film Printing of Hot-melt BMSC 103
4.7. Droplet Formation of Hot-melt BPA 106
4.7.1. Droplet Formation Optimisation with Waveform 106
4.7.2. Droplet Volume and Velocity Modulation 108
4.8. Ink Deposition of Hot-melt BPA 111
4.8.1. Single Droplet Deposition of Hot-melt BPA 111
4.8.2. Film Printing of Hot-melt BPA 112
4.9. Summary 114
5. Results: Reactive Inkjet Printing of Solvent-based Inks 116
5.1. Introduction and Research Rationale 116
5.2. Printability Assessment for Reactive Inks 117
5.2.1. Viscosity of Reactive Inks 117
5.2.2. Surface Tension of Reactive Inks 119

5.2.3. Overall Consideration for the Printability of Reactive Inks.....119
5.3. Droplet Formation of Reactive Inks.....120
5.3.1. Effect of Temperature on Droplet Formation 121
5.4. Droplet Deposition Study for Reactive Inks 126
5.4.1. Single Droplet Deposition 127
5.4.2. Thin Film Printing 132
5.4.3. Thick Film Printing 137
5.5. Summary.....140
6. Results: Post Processing and Characterisations for BPA-PC.....142
6.1. Introduction and Research Rationale.....142
6.2. Post Processing for As-Printed Reactive Mixture 143
6.2.1. Post Processing for the Thin Films 143
6.2.2. TGA Study for Melt Polymerisation.....148
6.3. Chemical Characterisations 150
6.3.1. Study of BPA-PC Molecular Weight Growth.....150
6.3.2. NMR Spectroscopic Analysis for BPA-PC 152
6.4. Thermal Characterisations.....155
6.4.1. DSC Study for BPA-PC.....155
6.4.2. Thermal Stability Analysis of BPA-PC by TGA 157
6.5. 3D Reactive Inkjet Printing of BPA-PC 160
6.5.1. The Design of the 3D Printing Pattern 161
6.5.2. The Surface Profile Analysis of the 3D Printed Structure 162

6.6. Summary 164

7. Conclusion and Future Work 165

7.1. Conclusion 165

7.2. Future Work 168

8. Reference 171

9. Appendix A: 13C-NMR Spectra for the RIP samples 188

10. Appendix B: TG and DTA for Reference BPA-PC 190

List of Figures

Figure 2-1: A generic process chain of additive manufacturing systems, modified from (8) 7
Figure 2-2: Different end-use for additive manufacturing techniques (25) 10
Figure 2-3: Classification of Inkjet Printing Technologies (45) 13
Figure 2-4: A typical schematic diagram of binary deflection continuous inkjet printing (42) 14
Figure 2-5: A typical schematic diagram of multiple deflection continuous inkjet printing (42) 15
Figure 2-6: two typical thermal inkjet printhead configurations: a roof and a side shooter (from left to right) (42) 16
Figure 2-7: The four common modes of piezoelectric inkjet (45) 17
Figure 2-8: Structures produced by depositing 25 microdrops on top of each other at various jetting frequencies. The material used is Candelilla wax at 100 ºC. (54) 18
Figure 2-9: Cross-sectional view of an ink channel (64) 24
Figure 2-10: Single trapezoidal drive waveform in piezoelectric DoD inkjet printhead (66) 25
Figure 2-11: The variation of droplet volume and velocity with (a) pulse width; (b) pulse amplitude (Butyl Carbitol at 2kHz with a piezoelectric DoD inkjet device with a simple ‘On-Off’ pulse waveform) (66) 25
Figure 2-12: The effect of driving voltage and liquid properties on the satellite effect during liquid breakup: 1) Water (μ=1 cP, γ=73 mN/m); 2) Glycerin/water mixture 48/52 (μ=5 cP, γ=68 mN/m); 3) Glycerin/water/isopropanol 34/53/13 (μ=5 cP, γ=35 mN/m) 27
Figure 2-13: The schematic diagram for illustrating the droplets forming the large area by overlapping with each other, with a droplet spacing (D) smaller than the dimeter (2*R) 30

Figure 2-14: The printed track morphologies after drying of an organometallic ink on a silicone substrate with the droplet spacing of: (a) 55 μm; (b) 60 μm; (c) 85 μm 31
Figure 2-15: The mechanism explained by Deegan: a, the droplet shrinks due to evaporation without internal flow; b, the internal compensating flow to keep the contact line (81). 31
Figure 2-16: (a) a CAD design of a twisted pyramid; (b) a photo of the pyramid showing the twisted design; (c) profile view of the pyramid (99).....34
Figure 2-17: Reactive inkjet printing of hydrogel: two routes for jetting hydrogel microarray *in-situ* pico-nano litre polymerisation (113) 37
Figure 2-18: The RIP of PEDOT layers on textile fabrics to fabricate conductive layers.....37
Figure 2-19: Inkjet dots of diol and diisocyanate reactive inks (1 to 5 layers) observed by confocal laser scanning microscopy: (a) reflectance images; (b) fluorescence images 38
Figure 2-20: The stepped ziggurat structure of PDMS printed by the RIP method and the profile analysis for the ziggurat structure (119).....39
Figure 2-21: Choi's experimental set-up for batch and semi-batch melt polymerisation 45
Figure 2-22: Process of FDM and printed model: (a) 1-Nozzle; 2-Building material; 3-Movable table in x-y-z direction (136); (b) FDM pyramid model by pure PC at 265 ºC (137).....46
Figure 2-23: A schematic of reaction injection moulding (RIM) for thermosets/thermoplastics (left) and linear BPA-PC production with macro cyclic oligomers (bisphenol A bis-chloroformate) by RIM (right).....48
Figure 3-1: Sample appearance of (a) BPA and (b) BMSC 53
Figure 3-2: The active hood cartridge for the rheology measurement on the Malvern Kinexus Pro Rotational Rheometer 54
Figure 3-3: Experimental configuration for pendant droplet formation of BPA and BMSC for surface tension measurement 55
Figure 3-4: The PiXDRO LP50 inkjet printer and its main modules (141) 57

Figure 3-5: The PHA modulus and the Océ Crystalpoint™ printhead 58
Figure 3-6: The PAINT function in the HMI software, where the number represents the times of diagnosis and the colour in each block indicates the status of each nozzle. Green represents good status of the nozzle, yellow represents medium quality of the jetting and red means a maintenance function is needed to improve the nozzle function. 59
Figure 3-7: Waveform pattern used in Océ Crystalpoint™ printhead.....60
Figure 3-8: An example of merged images of droplet formation by ADA. The horizontal axis is the time delay. 62
Figure 3-9: Correlation between the set point and sensing temperature with an external resistor of 22 kΩ on the heating element of channel block and melting unit.....63
Figure 3-10: Leakage (highlighted in red) of BPA from the bottom of MU 64
Figure 3-11: The DMP2800 series printer and its main components, modified from (149).....68
Figure 3-12: The main components of a Dimatix cartridge (149).....69
Figure 3-13: The waveform pattern for jetting low viscosity fluid (<5 cP) on DMP 70
Figure 3-14: The external heater for the substrate heating up to 200 ºC.....72
Figure 4-1: Solubility test for 3 different solvents (Toluene, Dioxane and DMF) used for reactive ink formulation 77
Figure 4-2: The stability of reactive inks over 90 days period: (a) fresh DMF35 as formulated; (b) fresh DOX25 as formulated; (c) DMF35 after storage for 90 days; (d) DOX25 after storage for 90 days 79
Figure 4-3: Thermal analysis results of BPA (a) and BMSC (b) by DSC 81
Figure 4-4: Viscosity for pure BPA monomer between 160 and 170 ºC (average ± standard deviation, n=5) 82
Figure 4-5: Viscosity for pure BMSC monomer between 120 and 135 ºC (average ± standard deviation, n=5) 83
Figure 4-6: Pendant drops of (a) BPA and (b) BMSC captured by high speed camera (3000 fps, 1/50000 second, 1024×1024 pixels) 84

Figure 4-7: Comparison of shear viscosity for BPA, BMSC and their mixture upon melting (average ± standard deviation, n=5) 86
Figure 4-8: Bulk polymerisation for BPA (~0.8423g) and BMSC (~0.5708g) in a 170 ºC oil bath: 3 samples on the left are mixed without aqueous NaOH; 3 samples on the right are mixed with 62.5 µL 0.1 mol/L aqueous NaOH. (a) (d): reacted as melt for comparison; (b) (e): reacted for 1 hour; (c) (f): reacted for 2 hours 88
Figure 4-9: FT-IR spectrum for bulk polymerisation of BPA and BMSC without catalyst 89
Figure 4-10: FT-IR spectra for bulk polymerisation of BPA and BMSC with catalyst 90
Figure 4-11: Results of thermal stability of BPA: (a) pure BPA; (b) pure BPA with nitrogen purge; (c) BPA with NaOH; (d) BPA with NaOH and nitrogen purge. From left to right in each set of experiment, the residence time is 0 hour (as melt), 2 hours and 4 hours, respectively. Temperature is kept at 170 ºC .92
Figure 4-12: Results of thermal stability of BMSC: (a) pure BMSC; (b) pure BMSC with nitrogen purge; (c) BMSC with NaOH; (d) BMSC with NaOH and nitrogen purge. From left to right in each set of experiment, the residence time is 0 hour (as melt), 2 hours and 4 hours, respectively. Temperature is kept at 120 ºC..... 93
Figure 4-13: Jet experiment with BMSC at 1 kHz droplet ejection rate using single nozzle..... 95
Figure 4-14: The effect of pulse width on the velocity of the droplets (unit of pulse width: µs) 96
Figure 4-15: Effect of the rising and falling slope (a and b, respectively) on the droplet formation of hot-melt BMSC (unit of ISource and ISink: µs) 98
Figure 4-16: Trajectory error of droplet in flight at low voltage amplitude below 40 dac units 98
Figure 4-17: The BMSC drop volume and velocity variation with the reference jetting voltage amplitude (average ± standard deviation, n=5) 100

Figure 4-18: Droplet evolution of hot-melt BMSC at different voltage amplitude with a strobe delay at (a) 110 µs; (b) 120 µs; (c) 130 µs; (d) 140 µs 101
Figure 4-19: Droplet size on glass slide varied with voltage amplitude: (a) 120; (b) 150 dac units.....102
Figure 4-20: Optical images of hot-melt BMSC films (1 × 1 mm) printed on glass slide at 25 ºC showing receding of the film within 5 mins (0 to 5 min from left to right) 104
Figure 4-21: Optical images of hot-melt BMSC films (1 × 1 mm) printed on polyimide (Kapton) substrate at 25 ºC (a) camera view; (b) microscopic view 105
Figure 4-22: Results of white light surface of printed hot-melt BMSC film (1 × 1 mm) on polyimide (Kapton) substrate (X and Y axis profiles) 105
Figure 4-23: Satellite effect of hot-melt BPA and its wetting area development on the nozzle plate 106
Figure 4-24: The effect of pulse width on droplet velocity of hot-melt BPA (unit of pulse width: µs), the strobe LED delay is 70 (a) and 80 µs (b) from left to right, respectively 107
Figure 4-25: Effect of the rising and falling slope (a and b, respectively) on the droplet formation of hot-melt BPA (unit of ISource and ISink: µs) 108
Figure 4-26: The droplet evolution of hot-melt BPA at different voltage amplitude with a strobe delay at (a) 60 µs; (b) 70 µs; 109
Figure 4-27: The BPA drop volume and velocity variation with the reference jetting voltage amplitude (average ± standard deviation, n=5) 110
Figure 4-28: Printed droplets with a printing distance of 500 (left) and 300 µm (right) 112
Figure 4-29: Hot-melt BPA printed on glass slide with droplet spacing: (a) 50.8 µm (500 dpi); (b) 42.3 µm (600 dpi); (c) 36.3 µm (700 dpi).....113
Figure 5-1: The viscosity of the 2 reactive inks from 25 to 45 ºC with a shear rate range between 10 and 1000s^{-1}: (a) DOX25; (b) DMF35 (average ± standard deviation, n=5).....118

Figure 5-2: Surface tension measurement by pendent drop method for DMF35 and the DOX25 from 25 to 45 ºC (average ± standard deviation, n=10) 119
Figure 5-3: The droplet formation evolutions of DOX25 at different temperatures: (a) 25 ºC; (b) 35 ºC and (c) 45 ºC, viewed by the stroboscopic camera on the Dimatix printer 123
Figure 5-4: The droplet formation evolutions of DMF35 at different temperatures: (a) 25 ºC; (b) 35 ºC and (c) 45 ºC, viewed by the stroboscopic camera on the Dimatix printer 125
Figure 5-5: The optical microscope images of the single droplet deposition of DOX25 on the microscope glass slide at different substrate temperatures ..127
Figure 5-6: The optical microscope images of the single droplet deposition of DMF35 on the microscope glass slide at different substrate temperatures ..128
Figure 5-7: The effect of different substrate temperatures on the droplet diameter of DOX25 and DMF35 (average ± standard deviation, n=6).....129
Figure 5-8: The effect of the substrate temperatures on the cartridge temperatures at different stand-off distances.....130
Figure 5-9: The surface profiling results of (a) DOX25 droplet at a substrate temperature of 60 ºC and (b) DMF35 droplet at a surface temperature of 80 ºC 131
Figure 5-10: The optical images for the thin films of DOX25 with different droplet spacing at different substrate temperatures.....133
Figure 5-11: The optical images for the thin films of DMF35 with different droplet spacing at different substrate temperatures.....134
Figure 5-12: The surface profiles of the thin films as printed by white light inteferometer: (a) 1 layer film of DOX25 with a droplet spacing of 30 μm at 60 ºC substrate temperature; (b) 1 layer film of DMF35 with a droplet spacing of 15 μm at 80 ºC substrate temperature. (The X and Y profiles in the right-hand side figure pertain to the lines of crosshair in the left side figures) 136
Figure 5-13: The optical images of multi overprints of reactive mixtures (5 × 5 mm) in side view: (a) a film of 80 successive layers of DOX25 with a droplet

spacing of 30 μm on the glass surface of 60 ºC; (b) The surface profile of the 80 layer thick film of DOX25, taken by Alicona G5 Infinite.....137
Figure 5-14: The DSC thermogram of the as-printed reactive mixture in DOX25.....139
Figure 5-15: The DSC thermogram of the as-printed reactive mixture in DMF35.....139
Figure 6-1: The comparison of 1 to 5 layers thin film surface profiles between the as-printed and post-processed samples produced by DOX25 144
Figure 6-2: The comparison of the thickness of the thin films from 1 to 5 layers between the as-printed and the post-processed samples produced by the dioxane inks (average ± standard deviation, n=3) 145
Figure 6-3: The comparison of 1 to 5 layers thin film surface profiles between the as-printed and post-processed samples produced by DMF35 147
Figure 6-4: Surface profile analysis of 5 layers films produced by DMF35 as the comparison between the as-printed and the post-processed films.....148
Figure 6-5: A multi-stage isothermal TGA curve for the melt polymerisation process of the as-printed thin film samples.....149
Figure 6-6: The ^{1}H-NMR spectra for the samples from DOX25, $CDCl_3$, 40 ºC 154
Figure 6-7: The ^{1}H-NMR spectra for the samples from the DMF35, $CDCl_3$, 40 ºC, 300 MHz 154
Figure 6-8: The DSC thermogram of the polymerised PC samples as a comparison among the DOX25-PC, DMF35-PC, reference high M_w PC and low M_w PC 156
Figure 6-9: The TG and DTG curves of DOX25 at different heating rates in a nitrogen environment.....158
Figure 6-10: The TG and DTG curves of DMF35-PC at different heating rates in a nitrogen environment.....159
Figure 6-11: An example of the 40 layers thick PC film printed DOX25 and post-processed by the ‘polymerisation as a whole’ approach.....161

Figure 6-12: The designed ziggurat structure to demonstrate the 3D printing capability: (a) the ziggurat bitmap design for the Dimatix printing pattern; (b) the printed ziggurat structure (5 layers per step, 25 layers in total) 162
Figure 6-13: The surface profile analysis for the 3D ziggurat structure using Bruker Contour GT by the 'polymerisation layer by layer' approach: (a) 1 layer per step; (b) 5 layers per step 163
Figure 9-1: The ^{13}C-NMR spectra for the samples from DOX25 and DMF35, $CDCl_3$, 40 ºC.....188
Figure 10-1: The TG and DTG curves of the reference high M_w PC samples 190
Figure 10-2: The TG and DTG curves of the reference low M_w PC samples191

List of Tables

Table 2-1: seven categories and definitions of AM processes according to ASTM-F2792: Standard Terminology for Additive Manufacturing Technologies (4) 9
Table 2-2: The drying mechanism of different inks for inkjet printing, reproduced from Le (42) 33
Table 2-3: Comparison of interfacial and melt processes for BPA-PC (121) .. 44
Table 3-1: Physical and chemical properties of BPA and BMSC as stated in MSDS 53
Table 3-2: The main specifications for the Océ Crystalpoint^{TM} printhead 58
Table 3-3: Default jetting parameters used in Océ Crystalpoint^{TM} electronic drive 61
Table 3-4: Jetting parameter of the waveform for jetting DOX25 and DMF35 70
Table 3-5: The stepped polymerisation profile for post processing the as-printed reactive mixture using the vacuum oven 73
Table 4-1: The two compositions of the reactive inks containing dioxane and DMF as solvents 79
Table 4-2: Summary of physical properties of BPA and BMSC at various processing temperature beyond the melting point and theoretical printability assessment 85
Table 4-3: BMSC droplet size variation on the glass with the voltage amplitude of waveform (average ± standard deviation, n=5) 103
Table 4-4: BPA droplet size variation on the glass slide with the voltage amplitude of waveform (average ± standard deviation, n=5) 112
Table 5-1: Summary of physical properties of DOX25 and DMF35 at various processing temperature for reactive inkjet printing and theoretical printability assessment 120
Table 5-2: Summarisation of droplet formation behaviour at varied cartridge temperatures and the corresponding droplet velocity 126

Table 5-3: The droplet diameters of two reactive inks deposited onto the microscope glass slide with different substrate temperatures.....129
Table 5-4: The average central height of the solidified droplet on microscope glass slides at different substrate temperatures.....132
Table 6-1: Molecular weight and polydispersity index (PDI) of different reactive inks compared to the reference PC materials produced from the bulk polymerisation 151
Table 6-2: Degree of polymerisation for the reactive samples and reference PC materials.....152
Table 6-3: ^{1}H-NMR data for the cast, as-printed and post-process BPA-PC, $CDCl_3$, 300 MHz 153
Table 6-4: The T_g values of the PC samples from the DSC thermogram 156
Table 6-5: The thermal data obtained from the TG and DTA curves.....160
Table 9-1: ^{13}C-NMR data for the cast, as-printed and post-process BPA-PC, $CDCl_3$, 300 MHz 189

List of Schemes

Scheme 2-1: The reaction mechanism for free radical photopolymerisation ..35
Scheme 2-2: The process of interfacial polymerisation of BPA-PC (125) 41
Scheme 2-3: The process of melt polymerisation of BPA-PC (125) 43
Scheme 3-1: The melt polymerisation from BPA and BMSC to yield BPA-PC and the by-product methyl salicylate 51
Scheme 4-1: Alkaline cleavage of BPA at elevated temperature at 170-230 ºC 91

Acronyms

3DP	Three Dimensional Printing
ADA	Advanced Droplet Analysis
AM	Additive Manufacturing
APS	Ammonium Persulphate
ASTM	American Society of Testing Materials
ATR	Attenuated Total Reflection
BHT	Butylated Hydroxytoluene
BPA	Bisphenol A
BPA-PC	Bisphenol A-Polycarbonate
BPM	Ballistic Particle Manufacturing
CAD	Computer Aided Design
CB	Channel Block
DAC	Digital to Analog Converter
DDM	Dimatix Drop Manager
DIY	Do-It-Yourself
DMF	Dimethylformamide
DMLS	Direct Metal Laser Sintering
DMP	Dimatix Materials Printer
DoD	Drop on Demand
DP	Degree of Polymerisation
DPC	Diphenyl Carbonate
DSA	Drop Shape Analyser
DSC	Differential Scanning Calorimetry
EDOT	3,4-ethylenedioxythiophene
FDM	Fused Deposition Modelling
FEM	Finite Element Method
FT-IR	Fourier-Transform Infrared Spectroscopy
GE	General Electric
GPC	Gel Permeation Chromatography

HMI	Human Interface
HP	Hewlett-Packard
HPLC	High-performance Liquid Chromatography
IBM	International Business Machines Corporation
LAN	Local Area Network
LBMD	Laser-based Metal Deposition
LENS	Laser Engineered Net Shaping
LOM	Laminated Objet Manufacturing
LS	Light Scattering
MIT	Massachusetts Institute of Technology
MSDS	Material Safety Data Sheet
MU	Melting Unit
NMR	Nuclear Magnetic Resonance
OLED	Organic Light-emitting Device
PAINT	Piezo-Acoustic sensing of INk channels in the Time domain
PC	Polycarbonate
PDI	Polydispersity Index
PDMS	Polydimethylsiloxane
PEDOT	Poly (3,4-ethylenedioxythiophene)
PHA	Printhead Assembly
PPV	Poly (*p*-phenylene vinylene)
PZT	Lead Zirconate Titanate
RIM	Reaction Injection Moulding
RIP	Reactive Inkjet Printing
RP	Rapid Prototyping
SABIC	Saudi Basic Industries Corporation
SEC	Size Exclusion Chromatography
SGC	Solid Ground Curing
SLA	Stereolithography
SLS	Selective Laser Sintering

SSP	Solid State Polymerisation
STL	Stereolithography
TEMED	Tetramethylethylenediamine
TGA	Thermal Gravimetric Analysis
THF	Tetrahydrofuran
$TMAH \cdot 5H_2O$	Tetramethyl Ammonium Hydroxide Pentahydrate
UAM	Ultrasonic Additive Manufacturing
UV	Ultraviolet

1. Introduction

1.1. Background

Additive Manufacturing (AM) is a collective term of describing several manufacturing approaches which allow a solid component to be fabricated directly from a digital model using specific materials in a layer-by-layer approach. Since 30 years ago when the first commercial stereolithography printer emerged on the market, AM technologies have rapidly grown to become a multi-billion dollar industrial segment (1). Compared to traditional subtractive manufacturing, AM has many distinct advantages such as higher freedoms in part design, potential for lower environmental impact and higher economic efficiency at lower volumes. Today, AM has a wide range of applications in a diversity of sectors such as aerospace, automotive, construction, medicine, tissue engineering, functional prototyping, etc.

Polycarbonate (PC) is a group of polymers which contain the carbonate group in the backbone structure. Commercial PCs that are available are predominantly linear aromatic thermoplastic PC which are derived from bisphenol A (BPA) as the monomer. Bisphenol-A polycarbonate (BPA-PC) is an important engineering thermoplastic which has excellent properties in optical transparency, impact and thermal resistance. Therefore, it finds a variety of industrial applications such as civil construction, automotive and optical devices. In the context of AM, BPA-PC also has attracted interest both in academia and industry. For example, selective laser sintering (SLS) using BPA-PC powders was studied (2) to investigate the parts morphology and mechanical properties. However, the parts suffer shrinkage and cracking due to extensive residual stress, and degradation occurs even at a low energy density of the laser. This severely compromises the physical and mechanical properties of the PC parts. Fused Deposition Modelling (FDM) is currently the only commercial AM technology to directly fabricate the BPA-PC parts by extruding within the melt phase of a BPA-PC polymer filament. Some major

suppliers for extrusion-grade filament BPA-PC include Stratasys, SABIC, and 3DXTech (3). Nevertheless, FDM made BPA-PC parts have several inherent drawbacks that limit its applications, such as poor surface finish without post processing and low printing resolution owing to the extremely high viscosity of the polymer at melt. Transparent parts are not easily achieved either, due to the fissures between the bonded layers. Therefore, an alternative AM technology is needed to address those issues in SLS and FDM processes.

Reactive inkjet printing (RIP) is an emerging AM technology to potentially solve those problems by depositing low viscosity BPA-PC precursors in the liquid form instead of directly melting BPA-PC polymer. With certain post-process environmental conditions such as conductive heating, the precursors on the substrate are then able to polymerise *in-situ* to form BPA-PC parts. Owing to the pico-litre volume of the droplets generated by an inkjet printing assembly, the feature size and resolution that can be achieved by RIP method is in the range of several microns rather than several 100 microns achieved in FDM. Additionally, this liquid-based process may enhance the adhesion between layers of a part and thus achieve a higher level of optical transparency. As a result, this work focuses on the fundamental investigation and understanding of the RIP process to fabricate the BPA-PC parts which would potentially open the new AM route for BPA-PC.

1.2. Research Scope

The aim of the research is to gain a fundamental understanding of the fabrication of BPA-PC by the RIP approach. Several objectives are identified to achieve the aim of the research as following:

- To assess the printability of the BPA-PC precursors which are used for the hot-melt inkjet printing

- To carry out a proof-of-concept study in inkjet printing of hot-melt BPA-PC precursors and to optimize the inkjet parameters
- To develop suitable ink formulations of BPA-PC precursor for solvent-based reactive inkjet printing
- To establish and optimize the process parameters of printing and post-processing to obtain the BPA-PC components
- To characterise the chemical composition, the thermal properties of the printed BPA-PC to evaluate the performance with the commercial reference BPA-PC produced by bulk synthesis method
- To investigate the surface morphology of the printed layer of BPA-PC and propose the printing strategy to fabricate the 3D structure of BPA-PC components.

1.3. Research Concept

The direct melting of the BPA-PC results in an extremely viscous polymer matrix due to the polymer chain entanglement, which is impossible to be printed by the inkjet method. Therefore, it is necessary to investigate the possibility of jetting the monomers – that have viscosities that are within the range of being jettable – which are then able to react within the necessary environmental conditions to form the BPA-PC product.

The first method investigated to fabricate the micro-scale BPA-PC parts was to print the monomers in a hot-melt configuration which meet the general inkjet requirement of low viscosity (usually below 30 cP) and a proof-of-concept study was carried out to demonstrate their printability. Conceptually, the monomers are deposited sequentially on the substrate and they are able to mix and polymerise upon the heating from the substrate in the hot-melt state. This method requires a feasibility study of the printing assembly as most of the piezoelectric inkjet printheads do not favour the jetting at elevated

temperatures due to the design limitations of the piezo-ceramics. In addition, stable droplet formation was aimed to be achieved by optimizing the actuation waveform and other inkjet parameters.

The second method refers to solvent-based reactive inkjet printing. The monomers for the BPA-PC were dissolved in an organic solvent to form oligomers as the reactive mixture. The reactive mixture is precipitated onto the substrate upon solvent evaporation. Elevated temperatures and a vacuum environment are required in the post-processing stage to further polymerise the printed samples until a desired molecular weight was obtained. Although the introduction of the solvent might limit its use due to environmental concerns, the solvent-based reactive inks of BPA-PC do not require droplet mixing during the printing stage and the stoichiometry of the monomers can be controlled in the formulation. The chemical and thermal properties of the BPA-PC produced from the inkjet method were compared with commercial BPA-PC samples produced from bulk polymerisation to evaluate the material properties. Ultimately the post-processing strategy for direct fabricating 3D structure of BPA-PC was be investigated to potentially disclose a novel AM approach to print high-resolution 3D micro-scale BPA-PC parts.

The two methods disclose a novel reactive inkjet printing approach to produce 2D patterns and 3D structures of BPA-PC, which have not been investigated in the existing literature. This research could potentially broaden the AM techniques for making BPA-PC which is a critically important material in the engineering industry.

2. Literature Review

2.1. Additive Manufacturing

This section will give the basic concepts and details of additive manufacturing technologies and will include a review of up-to-date scientific literature.

2.1.1. Basic Concept of Additive Manufacturing

Additive Manufacturing (AM) is a term, more commonly known as 3D Printing (3DP), referring to a wide spectrum of fabrication technologies which directly construct three-dimensional geometries or components layer by layer, under the automatic control of computer aided design (CAD). An official industrial definition of AM could be found in ASTM Standard F2792-12a (4), quoted:

‘A process of joining materials to make objects from 3D model data, usually layer upon layer, as opposed to subtractive manufacturing methodologies.’

AM is opposite to conventional ‘Subtractive Manufacturing’ which is based on cutting materials from blocks, and compared to be more efficient and effective (5). Traditional subtractive manufacturing, such as milling and turning, generates inevitable wastage intrinsically. However, AM significantly simplifies the process of building complex 3D parts from digital data and thus makes it possible to have zero waste material during the process. In addition, it provides high levels of freedom for customisation as shapes and geometries are completely created by computer software. With the development of AM in recent years, direct fabrication of end-use products has gradually become revolutionary in the field of manufacturing (6).

AM was originally called ‘Rapid Prototyping (RP)’ that emphasized the high speed in creating objects which were dominated by models and prototypes. Other terms standing for different viewpoints to describe the same or similar processes to AM include ‘Solid Freeform Fabrication’ focused on solid state

final product, ‘Digital Fabrication’ emphasized on automatic computer-aided process and ‘Layer Manufacturing’ orientated to the layer-wise manufacture fashion (6)(7). The most commonly used terminology among those could be ‘3D printing’, however, this refers also to a binder jetting technology patented by Massachusetts Institute of Technology (MIT) and can therefore be confusing. In general, ‘3D Printing’ seems to be more popular in public and is often used interchangeably with AM.

2.1.2. Development of Additive Manufacturing

The origin of AM may be difficult to trace but development of AM associated techniques such as computers and controllers boosted in the early 1980s to be aligned with AM (6). The first commercial RP system named SLA-1 (short for Stereolithography or Stereolithography Appratus), emerged in 1987 developed by 3D Systems, which was a U.S company that was credited with the invention of AM technology (8). The working principle is Stereolithography that relies on solidification of UV-sensitive liquid polymer by laser. This 3D printer was a milestone as it was the first time when clients would be able to generate a conceptual physical model directly from digital data. Since then, some companies started to adopt AM into tooling and prototyping commercially by using the model from 3D Systems. A demonstrative example is provided by the company General Motors who acquired SLA-250 systems (enhanced model from SLA-1) to prototype parts such as connector feeder tracks and cranking motor nose housings (9).

Latterly other AM technologies were subsequently developed and commercialized. A group from MIT patented a 3D Printing (3DP) process (10) which was licensed to Z-Corporation exclusively for commercialisation in 1995. It deposits binder material onto a powder bed selectively to build the expected geometry. Following, Fused Deposition Modelling (FDM) from Stratasys (11), Laminated Object Manufacturing (LOM) from Helisys (12–14) and Solid

Ground Curing (SGC) from Cubital (15) were patented and commercialized, expanding the family of AM technologies in 1991.

The activities and development of AM have been tremendous in recent years around the world. It is challenging to name all of them due to their high number, though some of the key innovations and breakthroughs have been stated as aforementioned. A comprehensive historical perspective associated with AM technologies can be found in the open literature (16)(17). There is also detailed list on various AM processes schematics, principles and their developers (18). It is noted that people are aware of expirations of some foundational patents for AM technologies such as FDM (which expired in 2010). Consequently, the numbers and types of FDM extrusion-based machines have increased significantly over these years (19). A significant number of early patents in key AM processes such as SL and SLS expired between 2013 and 2014 – this may lead to a new exponential growth in AM technologies, companies and innovations in the near future.

2.1.3. Process Chain of Additive Manufacturing

All the AM techniques share the generic procedure despite the different principles they adopt. It is important for designers and developers of AM to plan, commission and implement techniques. A schematic diagram of the general process chain of AM is illustrated in Figure 2-1.

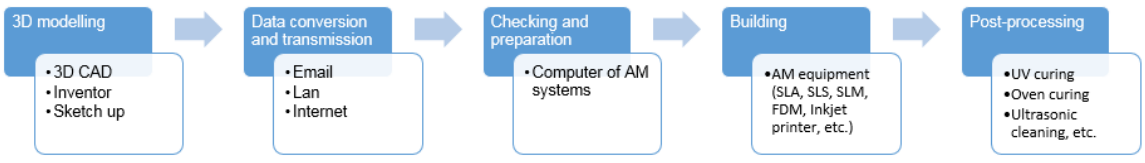


Figure 2-1: A generic process chain of additive manufacturing systems, modified from (8)

As described in Figure 2-1, a sequence of five steps includes 3D modelling, data conversion and transmission, checking and preparation, building and

post-processing. Firstly, a desired geometric model is created by CAD which will in turn examine and verify the process parameters, for example, by finite element method (FEM) and stress analysis. Then the model will not be valid until it is converted to STL (an abbreviation for Stereolithography) file format which originated from 3D Systems for SLA but now it has become a universal format for almost all AM systems, where the model is made up of small triangles. Transmission of this STL file to AM systems is readily achieved by a hard drive or a local area network (LAN). Then the specialized software will spot any errors in the files and human operators would correct those errors before models are verified to determine the process parameters such as building orientation, support structure and spatial assortments. Once the STL is well prepared, the building process could be initiated by the AM systems, most of which are fully automatic. In the final stage, the built part must be realized by post-processing. For instance, the excess powders have to be removed from a SLS part and surface polish may be required for a FDM part. It is note that post-processing is not a necessity for all AM techniques and that some post-processing tasks are integrated into the building procedure (8).

It is valuable to point out that the generic process chain is often iterated dependent on the quality and complexity of the product, where in such a case the process is comparatively time-consuming to a larger extent, or even leads to a failure. In other literature, there are alternative process chains introduced although they virtually follow the same rules and principles (6).

2.1.4. Classification of Additive Manufacturing

There are a considerable number of AM process classifications. It was popular to sort AM technologies into various categories in accordance with the underpinning principle (20) such as extrusion-based, laser-based etc. Kruth (21) proposed two possible classifications of AM relating to the raw material used and the shape built, respectively. Pham and Gault (22) illustrated a comprehensive tree view involving more features such as mechanical

properties of parts, building accuracy and usage of end-use components. Most of them are intricate, however, and grouping AM technologies into them often causes overlapping or deficiency. There was no universally acknowledged classification until an industry standard, ASTM-F2792, was established by ASTM F42 committee and it is now widely recognized (4). There are seven standardized categories presented in F2792:

Table 2-1: seven categories and definitions of AM processes according to ASTM-F2792: Standard Terminology for Additive Manufacturing Technologies (4)

Category	**ASTM Definition**	**Examples**
Vat photopolymerisation	an additive manufacturing process in which liquid photopolymer in a vat is selectively cured by light-activated polymerisation	Stereolithography (SLA)
Powder bed fusion	an additive manufacturing process in which thermal energy selectively fuses regions of a powder bed	Direct metal laser sintering (DMLS), Selective Laser Sintering (SLS)
Material extrusion	an additive manufacturing process in which material is selectively dispensed through a nozzle or orifice	Fused deposition modelling (FDM)
Material jetting	an additive manufacturing process in which droplets of build material are selectively deposited	Polyjet, Inkjet printing
Binder jetting	an additive manufacturing process in which a liquid bonding agent is selectively deposited to join powder materials	Three-dimensional printing (3DP)
Sheet lamination	an additive manufacturing process in which sheets of material are bonded to form an object	Ultrasonic additive manufacturing (UAM), Laminated objet manufacturing (LOM)
Directed energy deposition	an additive manufacturing process in which focused thermal energy is used to fuse materials by melting as they are being deposited	Laser-based metal deposition (LBMD), Laser engineered net shaping (LENS)

From Table 2-1 there are only a few examples given corresponding to each category. As AM technologies has been proliferating over recent years, more AM machines and processes have emerged, and it turns out that they can be well aligned to the ASTM standard. For this PhD, inkjet (which belongs to material jetting) will be focused upon and details will be elaborated. More information about other six categories can be found in the literature (4)(6)(8).

2.1.5. Applications of Additive Manufacturing

At the onset of AM technology, it mainly served to create models and prototypes (23). However, applications have been expanding over recent years and finished products are able to be made by AM techniques with papers, metals, plastics, ceramics and composites (24). Wohler's (25) conducted a survey to visualize the statistics on different usage for AM processes and the result is presented in Figure 2-2:

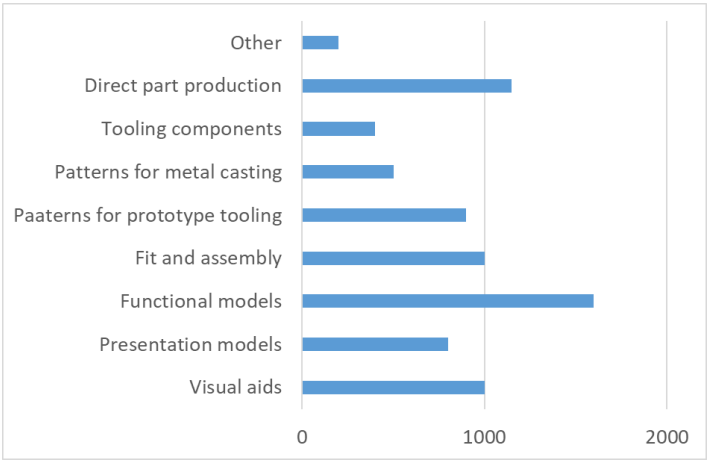


Figure 2-2: Different end-use for additive manufacturing techniques (25)

The overall capacity of the survey was around 5000 customers and users from 24 manufactures and it showed that functional models and direct part production were predominant AM applications. It is in accord with the fact that the recent focus on AM applications is moving to the increase of functionality and complexity of the components (26). There is also a statement that cost minimisation could be facilitated by AM energy consumption, thus motivating

the AM sustainability and broadening the AM applications, although for some AM processes the energy consumption can be excessive compared to traditional manufacturing (27). Currently, industries closely related to AM development include automotive, aerospace, architecture, medical, biological, electronics amongst others (28–30). There is also a significant number of communities developing fashion, furniture and lighting applications using AM techniques such as SLA (31, 32). For non-industrial users, numerous desk-use 3D printers in markets are available for them to perform do-it-yourself (DIY) projects and some easily navigable software enable users to design the models themselves without high level of technical ability (33–35).

2.2. Inkjet Printing Technology

This section will review the literature which is fundamental to understand the principles and applications of inkjet printing.

2.2.1. Basic Concept of Inkjet Printing

Inkjet printing is a technology that can produce a droplet of a specific liquid which is jetted through a small aperture onto substrates selectively to form 2D images or 3D parts. The basic mechanism presented stems back to 1878 when Lord Rayleigh mathematically summarized the study that had been conducted by Plateau on the breakup of liquid jets (36). Based on Rayleigh's theory, Rune from Siemens-Elema in Sweden devised and patented the first practical inkjet apparatus about 70 years later (37). In 1965, Sweet claimed (38) that a certain pressure waveform would render that the liquid ink streams break into tiny droplets after they leave the print nozzle and he patented a fluid droplet recorder along the principle of a continuous inkjet by using an electric field to control the trajectory of droplets in flight (39). Sweet's achievement was to pioneer to the first commercial 2D inkjet printer in the 1970s when International Business Machines Corporation (IBM) licensed the continuous

inkjet technology to develop their first computer-interface printer, IBM 4640 (40).

While continuous inkjet printing was developing, the Drop-On-Demand (DoD) inkjet started to be popularized where ink will only be dropped when needed. This is a progress on reducing the complexity of inkjet devices (e.g. elimination of the previous electric charge devices) and minimizing the wastage it generates (no recycling and contamination). The first DoD piezoelectric inkjet printer was designed by Zoltan from Clevite Inc. in 1972, which utilized a piezo-ceramics to control the drop formation (41). Other types of 2D DoD printer applying different mechanisms emerged later. Notable commercial examples include ‘Bubble Jet’ from Cannon and ‘ThinkJet’ from Hewlett-Packard (HP) company (42).

There are more comprehensive reviews on 2D inkjet printing technology in the open literature while the course of inkjet printing development is rapid with each passing day (42).

2.2.2. 2D Inkjet Printing to 3D Inkjet Additive Manufacturing

Early commercial inkjet printers are only for the use in graphic arts, office printing and large formatting. People started to realize, however, that inkjet has the great potential to fabricate parts directly. The first occurrence of extending 2D printing to 3D fabrication by inkjet appeared with the patent related to Ballistic Particle Manufacturing (BPM) in 1987 by which particles are deposited using a piezoelectric jetting system onto an article under control of a computer system (43). In 1994, Solidscape Inc. (called Sanders Prototype later) developed the first commercially successful 3D inkjet system, ModelMaker^{TM}, to deposit wax material through a printhead to form the part directly rather than binding it (33). Several other companies developed inkjet machines afterwards but all of them relied on deposition of molten waxy thermoplastics. For example, 3D Systems launched their first jetting printer

called Actua 2100 which deposited wax material for metal casting. The second wave of inkjet technology was led by Objet Geometries of Israel in 2000. They announced the launch of the Quadra 3D inkjet printer that used UV light to cure liquid-state photopolymer. A competing 3D printer, modelled as InVision, was then developed by 3D Systems (16). Up to now much effort has been involved in transferring inkjet printing into manufacturing of end-use parts with functionalities, especially in the field of polymer deposition (44).

2.2.3. Classification of Inkjet Printing Technology

A common classification of modern inkjet printing technologies is presented by Wijshoff (45) in Figure 2-3. Inkjet printing is primarily categorized into Continuous and Drop-On-Demand (DoD). Under each of the major categories, minor categories are present and some of them will be elaborated in the following section.

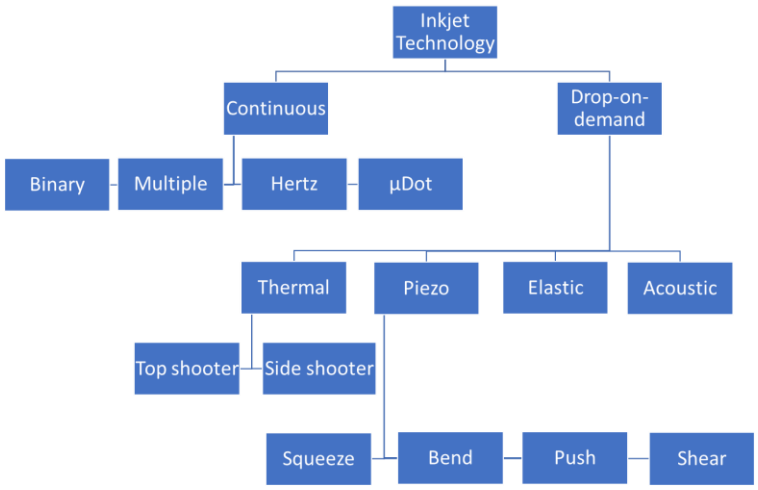


Figure 2-3: Classification of Inkjet Printing Technologies (45)

2.2.4. Continuous Inkjet

According to the classification of continuous inkjet technology, there are four minor categories among which most vendors are opting to use the binary and multiple continuous inkjet printers of which will be the main focus in this

section. There is open literature describing the Hertz (42) and MicroDot process (46) in details.

Figure 2-4 illustrates a schematic of binary deflection continuous inkjet printing process. Firstly a steady pressure is applied to the ink reservoir (a printhead) resulting in a continuous liquid stream generated from the nozzle on the reservoir. After departing from the nozzle, the liquid will break up into uniform droplets consistently by modulating a certain frequency of pressure wave due to Rayleigh instability (36). A pair of charging electrodes is then introduced for the droplets to attain electrostatic charges selectively. This is achieved by varying the field strength between the charging electrodes. The subsequent trajectory could be controlled by rendering charged droplets as they pass through a high voltage deflection plate to be directed to a single location on the substrate, while uncharged droplets will be trapped to a collection gutter for disposal and recycling.

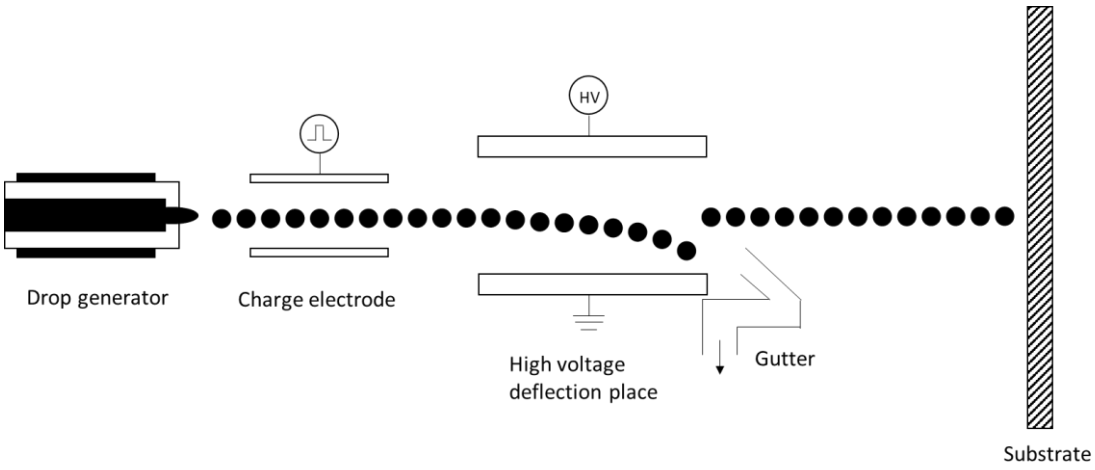


Figure 2-4: A typical schematic diagram of binary deflection continuous inkjet printing (42)

There is a highly similar process, multiple deflection system of inkjet printing, which can deflect the droplets to different locations on the substrate as shown in Figure 2-5. By applying a ladder-shaped pulse in the charge electrodes, the droplet jets are able to form a small image swath by a single printhead.

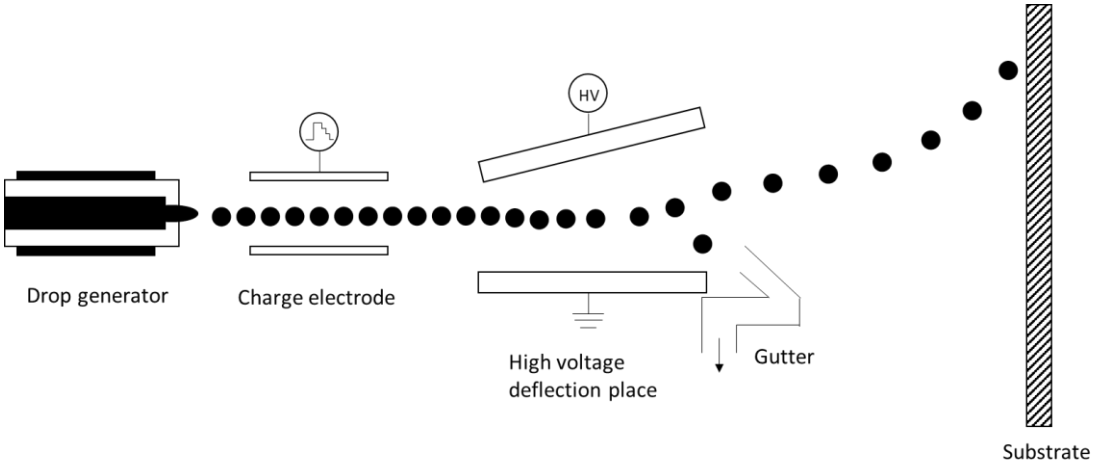


Figure 2-5: A typical schematic diagram of multiple deflection continuous inkjet printing (42)

Although the continuous inkjet printing enjoys a wide spread of applications in food, pharmaceutical labelling and coding market owing to high throughput rate, it has an intrinsic drawback that reuse or recycling of the ink risks contamination which is wasteful and undesired in many processes (47). It is also noted that the ink must be conductive otherwise the droplets will not be charged, which confines the inks to a narrow range (6).

2.2.5. Drop-on-demand (DoD) Inkjet

DoD inkjet printing is dominant today in the industry and market. It employs a mechanism that droplets of the ink are formed from nozzles by creating pressure pulses using a certain type of actuator such as thermal, piezoelectric, electrostatic and acoustic etc. Among those technologies, most manufacturers adopt thermal and piezoelectric mechanisms. The remaining two types, electrostatic and acoustic inkjet, are still in the stage of development and limited commercial products can be seen (48)(49). In this section, thermal and piezoelectric print modes will be focused.

Thermal Inkjet

Thermal inkjet (also refer to Bubble Jet) is one of the most successful DoD printing methods nowadays. Figure 2-6 presents two typical types of thermal inkjet. Dependent on the location of the orifice to the heater, it could be classified to a roof shooter or a side shooter. In both configurations, a rapid transient heat is applied to the ink in the cavity and then a short-duration bubble is created right on the interface between the ink and the heating element. When the bubble reaches a certain volume a jet of ink will be squeezed out of the nozzle, following that the ink will be redrawn from the filling port after the bubble collapses. The repetition of the same process can achieve a thermal DoD inkjet printing process and it is extensively adopted in home and office-use printers. However, it places a significant restriction on jetting materials because the vapour pressure of the ink must be relatively low in order to create vaporized bubbles (50).

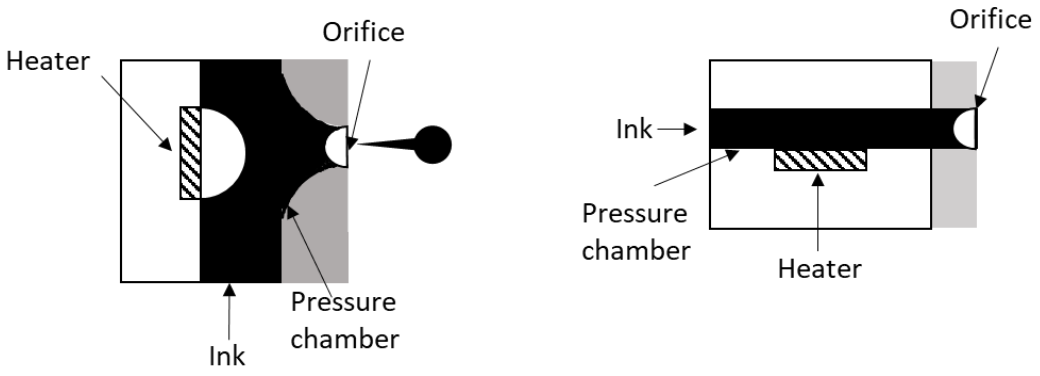


Figure 2-6: two typical thermal inkjet printhead configurations: a roof and a side shooter (from left to right) (42)

Piezoelectric Inkjet

Many industries are more affiliate to piezoelectric inkjet techniques when compared to thermal jetting systems, since there is no such requirement of volatility to the jetting material for the piezoelectric DoD inkjet. It simply relies on the deformation of a piezo-ceramics to cause the volume reduction in the ink reservoir from which the droplet will be ejected. There are four common modes of piezoelectric inkjet depending on the deformation matrix of the

piezo-ceramics: squeeze, bend, push and shear mode (45), as shown in Figure 2-7.

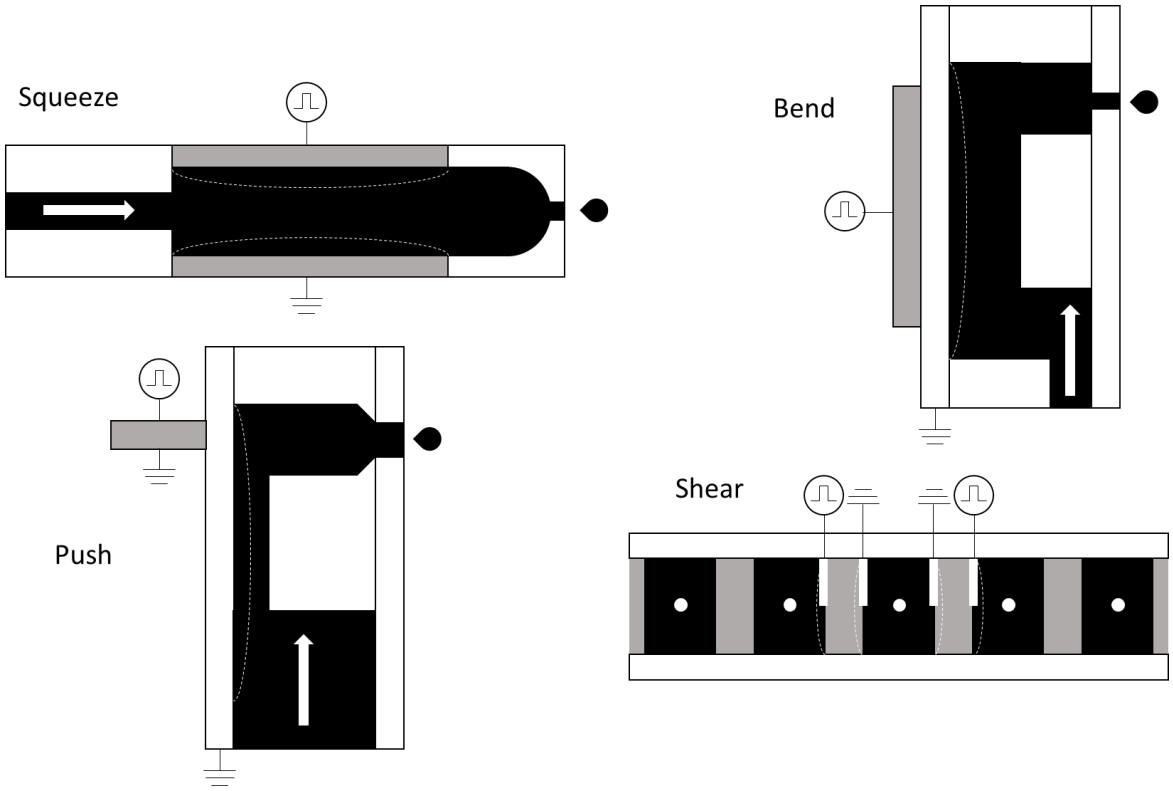


Figure 2-7: The four common modes of piezoelectric inkjet (45)

The first squeeze mode piezoelectric actuator was proposed in the U.S. Patent 3,683,212 from the Clevite Inc (51). In this mode, the piezo-ceramics is radially polarized to expel the ink droplets. In the market, Siemens PT-80 implements this squeeze mode actuator. Two patents were filed almost at the same time that relate to the bend mode of piezoelectric operation in 1973 (45). In this mode, the electric field is imposed in the polarisation direction of the piezo-ceramics. A practical example could be found in Epson's Colour Stylus inkjet printers. The push mode inkjet actuator was firstly described in the U.S Patent 4,459,601 by Howkins from the Exxon company back in 1984. It shares the high similarity to the bend mode as aforementioned, that a piezo-ceramics rod expands upon the electrical poling to force the ink out of the orifice. The successful applications could be found in the printheads from Dataproducts, Trident and Epson. Fischbeck proposed the shear mode actuator in the U.S.

Patent 4,584,590 with a more sophisticated configuration than other three types. The electrical filed applied is set perpendicular to the piezoelectric element, which makes it fundamentally different from other types of printheads. Xaar is one of main printhead manufacturers for the shear mode printhead(52). Spectra is also among the pioneers in the shear mode implementation.

2.2.6. Inkjet Printing of Polymers

Inkjet printing is considered as one of the key technologies in polymeric AM. Materials can be deposited by the jetting nozzles in the form of a dilute solution or a colloidal dispersion (44). One of the representative applications in the printing of polymers is the development of polymer organic light-emitting diodes (OLED) where polychromic 50 μm subpixel polymers can be jetted (53). The main ingredient of the ink they use is 0.5-2% by weight poly (*p*-phenylene vinylene) (PPV) derivatives dissolved in organic solvents such as tetraline, anisole and o-xylene. The polymers that remain on the substrate after solvent evaporation exhibit homogeneous thickness with good colour uniformity.

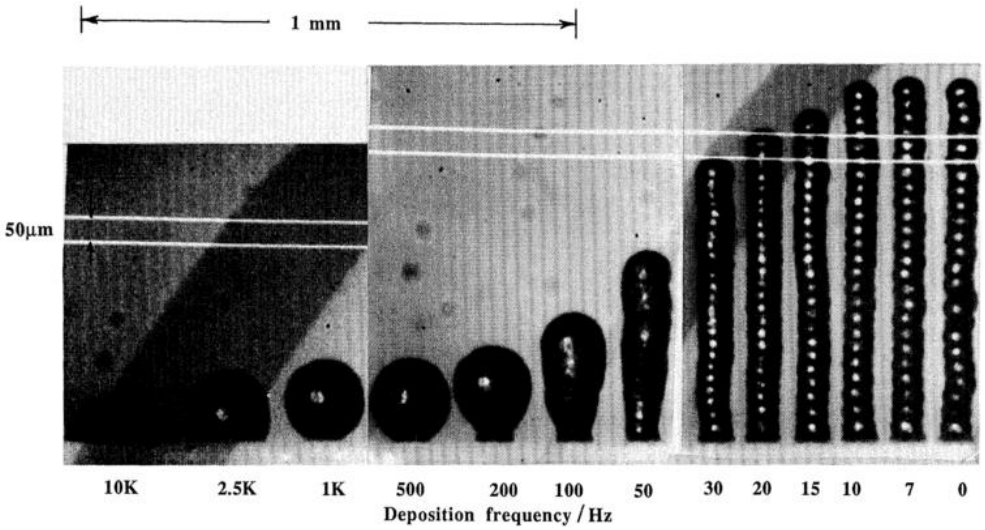


Figure 2-8: Structures produced by depositing 25 microdrops on top of each other at various jetting frequencies. The material used is Candelilla wax at 100 ºC. (54)

Waxes are also a typical family of relatively low molecular weight printable polymers. Printing wax is rapid, inexpensive and it is particularly feasible in

creating prototypes. It has also played an important role in the graphics industry because of the fast solidification upon natural cooling. In addition, their low viscosity typically below 15 cP at low melting point (50-90 ºC) is suitable to make phase-change hot melt inks for piezoelectric inkjet printing (55). The first fundamental research on printing wax material was published by Gao and Sonin (54) where they investigated the interaction between wax droplets and substrates. They also studied the effect of jetting frequency on the solidification phenomenon in the vertical pillar formation as presented in Figure 2-8. At lower frequency (below 10 Hz) the distinct dropwise solidification occurs to form identical vertical pillars independent of frequency. Though a transition in the moderate frequency (10-50 Hz), the insufficient solidification time between successive droplets coalesce into a hemispherical liquid tip which keep moving upwards until the deposition is terminated. A more recent application of printing wax is the fabrication of paper-based microfluidics devices by penetrating the wax into the whole thickness of the paper to create ~300 µm wide hydrophilic channels (56).

2.3. Reactive Inkjet Printing (RIP)

2.3.1. Basic Concept of RIP

The definition of reactive inkjet printing (RIP) is not universal. It usually refers to a collection of inkjet printing processes where the *in-situ* (post-deposition) chemical reaction occurs to form a desired pattern or product directly (57). The mechanisms of the chemical reaction can be varied which include photo-polymerisation and thermal curing. A recent article (57) has arranged RIP into two categories where the first type is called ‘single RIP’ where one reactant is deposited by an inkjet printer onto another reactant already printed on the substrate; whereas the second type, ‘full RIP’, is capable of dispensing more than two reactive inks simultaneously or sequentially by a inkjet printer with multiple printheads.

Recently RIP has appealed to a number of researchers for its several inherent advantages. As a consequence of the pico-liter volume droplets (~20 to 80 μm in diameter) when compared to extrusion nozzles (300 to 3000 μm), mixing behaviour and heat transfer are significantly improved in favour of a higher extent of reaction and resolution. The high deposition precision at small scale also allows for minimal material consumption and hazardous material generation.

2.3.2. Ink Requirement for RIP

Developing a new formulation of an ink for RIP normally requires fluid characterisation. It is attributed to the strong influence of physical properties on the droplet formation mechanism. Among those properties of the inks, viscosity, surface tension and density are of great significance and they are usually assessed individually or collectively.

Viscosity

The rheological property of a fluid is important in controlling the droplet formation and impingement on a droplet/substrate. The viscosity of a fluid plays a critical rule in damping the acoustic pressure pulse in the channel block and resisting the break-up of jets on the nozzle. If the viscosity is too high, the actuating pressure pulse will not be sufficient to overcome the resistance of the fluid to be deformed upon shear forces or called viscous dissipation. At the opposite extreme, low viscosity leads to a long tail behind the head of the droplet. Therefore viscosity must be suitably low. Most commercial inks for piezoelectric RIP have viscosity no more than 20 cP which is acceptable for the majority of applications (44).

Surface Tension

Surface tension is vital in disrupting a liquid column into small droplets by means of Rayleigh instability, as well as sustaining a liquid meniscus at the end of the orifice (58). It also roughly indicates the pressure needed to create

a new surface area of the jets. A good approximation of the pressure required in the reservoir of a jetting system is the energy conservation low as follows:

$$E_{imparted} = E_{loss} + E_{surface} + E_{kinetic} \tag{2-1}$$

Where the first term on the right accounts for the viscous dissipation of the fluid due to viscosity; the second term corresponds to the energy required to create a new surface for droplet formation and the last term is the remaining kinetic energy to impel the liquid towards substrates. A piezoelectric actuated pressure is able to propagate against surface tension and the internal friction is in most of the cases dominant (38). Therefore, the effect of the surface can be tuned by adjusting the pressure induced by the actuator to provide sufficient energy creating a new liquid surface. Practically, inks with surface tensions between 28 and 73 mN/m are common (59) but a few activities also report the successful printing case at 350 mN/m for a molten solder (60).

Density

The influence of the density on the droplet formation is minor when compared to viscosity and surface tension. It has direct impacts on the propagation and reflection of the acoustic pressure waves speed. Hook's Law correlates the acoustic velocity and physical properties of the fluid:

$$c = (\frac{K}{\rho})^{1/2} \tag{2-2}$$

Where c is the acoustic velocity (m/s) in the fluid; K is the bulk modulus elasticity (Pa); ρ is the density of the fluid (kg/m^3). If the acoustic velocity is changed, the acoustic impedance towards the meniscus is changed. Therefore, waveforms must be tuned to facilitate the drop formation on the nozzle accordingly.

Printability Assessment

As inkjet printing is inherently a complex process, there are continuing research activities surrounding this subject (61). However, there is a dearth of precise methods to determine whether a fluid is printable or not. Nevertheless, a common approach has been adapted widely in evaluating the material for printing. Among those parameters, most useful dimensionless groupings of physical properties are the Reynolds (*Re*), Weber (*We*) and Ohnesorge (*Oh*) numbers:

$$Re = \frac{v\rho\alpha}{\eta} \tag{2-3}$$

$$We = \frac{v^2\rho a}{\gamma} \tag{2-4}$$

$$Oh = \frac{\sqrt{We}}{Re} = \frac{\eta}{(\gamma\rho\alpha)^{1/2}} \tag{2-5}$$

$$Z = \frac{1}{Oh} = \frac{(\gamma\rho\alpha)^{1/2}}{\eta} \tag{2-6}$$

Where v is droplet velocity after departing from the nozzle, ρ is the density of the fluid, η is viscosity of the fluid, γ is surface tension of fluid and α is a characteristic length which is normally nozzle diameter. Z is considered the printing indicator which defines the range of printable fluid. Generally, at low values of Z, the viscous behaviour is dominant and therefore the majority of acoustic energy is dissipated preventing the droplet ejection from the nozzle. While at relatively higher values of Z, the liquid column will be deposited in the form of satellite rather than single droplet break-up. Reis and Derby (62) proposed the range of Z between 1 and 10 for stable drop formation by performing computational fluid dynamics modelling in conjunction with a parallel experimental study on free surface flow characteristics. It has been extensively studied over a wide range of fluids even with particle-loaded systems that the $1<Z<10$ usually gives a good validity. In addition, Jang *et al.*

(63) refines the printable range as $4<Z<14$ by further considering the additional parameters such as single droplet formability, positional accuracy and maximum jetting frequency. It is worth remembering that the printing indicator Z is merely a guide rather than a law. It is useful, however, to benchmark and evaluate a new material to be printed.

2.3.3. Actuation and Droplet Formation

With the proper drive electronics, the piezoelectric printhead can be actuated to eject droplets from the nozzles. Depending on the pulses, the droplet volume and velocity can be tuned accordingly. There are several physical phenomena in the droplet formation profiles, of which satellite effect is a common one in poor control during the droplet breakup.

DoD Actuation Device

A typical piezoelectric DoD inkjet printhead from Océ Technologies is referenced to illustrate the operation principle. It has two horizontal arrays of 128 ink channels each on the nozzle plate. A cross-sectional view of the ink channel is presented in Figure 2-9 to demonstrate the principle. The ink channel (typical length 5-20 mm) between the body of channel plate and flexible foil connects the open end (reservoir) and the closed end (nozzle). A nozzle plate which is made from metallic material with polyimide coating to protect from the heating effect, has arrays of drilled holes as nozzles to form liquid jets. At the open end, a filter is placed to block impurities from entering the ink channel. A piezo unit is attached to the flexible foil to actuate the jetting with the stimulus of the pressure pulse, by deforming the wall of the ink channel. The most common material of the piezo unit is a ceramic perovskite one, Lead zirconate titanate with a chemical formula of $Pb(Zr_xTi_{1-x})O_3$ ($0 \leqslant x \leqslant 1$), or PZT. The material is remarkable for its piezoelectric effect and it is insoluble in almost all known solvents.

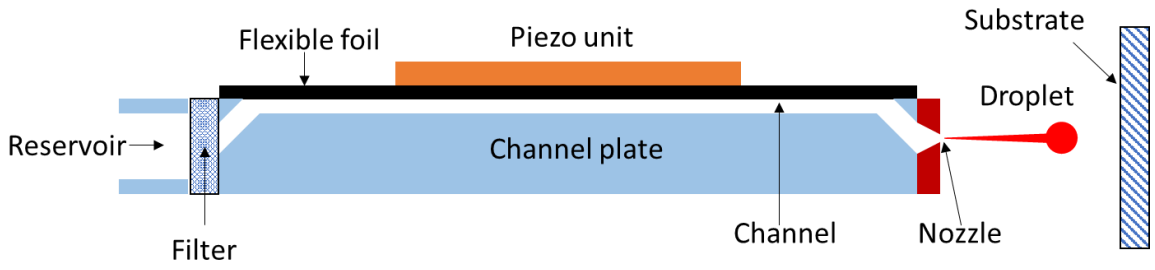


Figure 2-9: Cross-sectional view of an ink channel (64)

DoD Actuation and Waveform

The drive electronics will generate a waveform consisting of either a single trapezoidal voltage pulse, or a bipolar pulse depending on the electronics. In some cases, more complex waveforms with several pulses are customized to control the stability of the droplet formation. The simplest waveform is a single 'On-Off' pulse which is shown in Figure 2-10. Initially, the positive pulse leads to a radial expansion of the ink channel with a corresponding rise time. It allows the generated pressure waves to propagate for a certain time (known as pulse width) in the channel towards both directions. After the two acoustic pulses reflect back from both ends, the voltage falls down to zero, which results in the contraction of the channel. This adds a negative pulse to the channel with the same pressure distribution as initially. Consequently, the wave propagating to the nozzle end is amplified and the wave propagating to the open end is minimized. This implies an optimum pulse width to trigger the acoustic resonances at which the wave propagating to the nozzle end is doubled and the wave propagating to the open end is annihilated completely. This effect was experimentally and theoretically studied by Bogy *et al.* (65). There is good agreement between the experimental and theoretical results that the optimum time delay for the wave propagation is at the instant of $t_0 + l/c$, where t_0 is the starting point of positive pulse, l is the length of the channel and c is the acoustic speed in the fluid. In this case, the droplet will be ejected at $t_0 + 3l/2c$ with the maximum volume and velocity given the fixed amplitude. In Figure 2-11 (a), the curve shows the maximum drop velocity and volume are achieved at the optimal pulse width of 38 µs.

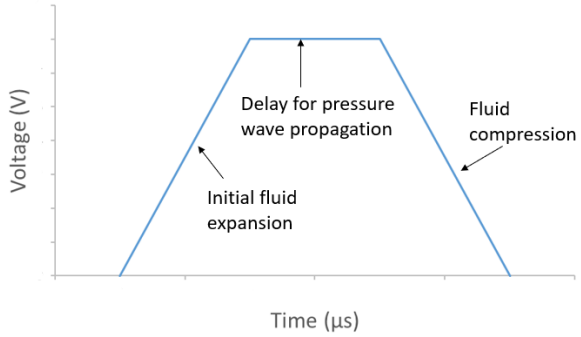


Figure 2-10: Single trapezoidal drive waveform in piezoelectric DoD inkjet printhead (66)

At a fixed jetting frequency and pulse width, the pulse amplitude also has impact on the drop velocity and volume. The work done by Microfab Technologies, Inc. in Figure 2-11 (b) illustrates the effects. The drop volume is almost linear in relation to the pulse amplitude which can be proportionally determined by the drive voltage. In the relatively low amplitude range, the viscous dissipation is dominant because of the low energy input. Thus, the restraining force due to the viscosity is significant enough to cause non-linearity. By increasing the pressure wave energy, the radial displacement of the ink channel is enlarged. This results in the more dramatic meniscus oscillation of the ink and a greater volume is achieved in droplet formation. Visually it can be seen from a longer tail or even a secondary droplet (satellite effects). The drop velocity variation with the amplitude has the similar trend, because of the increasing kinetic energy with the drive voltage.

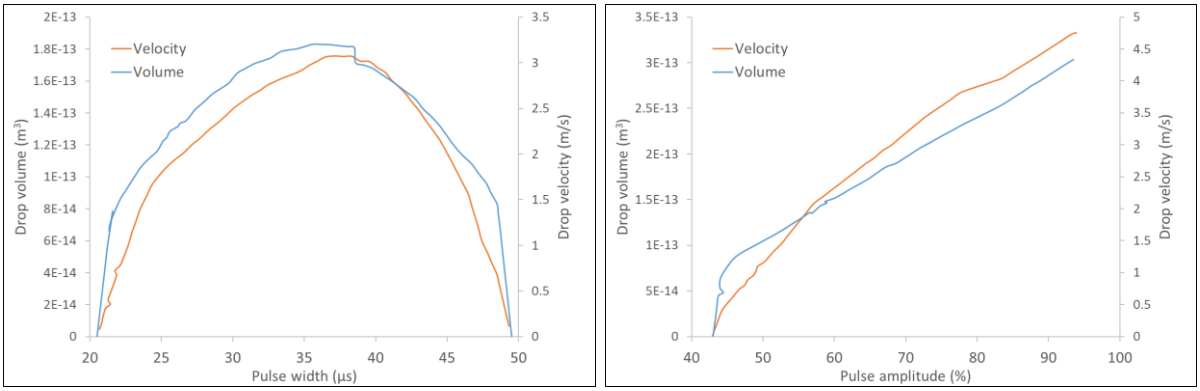


Figure 2-11: The variation of droplet volume and velocity with (a) pulse width; (b) pulse amplitude (Butyl Carbitol at 2kHz with a piezoelectric DoD inkjet device with a simple 'On-Off' pulse waveform) (66)

For high productivity jetting, each single droplet should be ejected without interfering with one another. There is a wave residual pressure, however, that limits the minimum time delay between two consequent pulses which can be achieved. To increase the jetting speed and stability, a more complex waveform is needed to suppress the residual oscillation sufficiently. One of the proposed methods is to design a two-pulse bipolar waveform of which the second pulse is used to speed up the decay of the residual wave (67). By introducing a negative pulse with the same amplitude as the first one, the jetting frequency can increase up to three times, given the optimal starting dwell time. However, this also increases the design complexity of the drive electronics that implement high-speed jetting. Its use also highly depends on the physical phenomenon such as the ink/nozzle plate interaction (68)(69).

Satellite Effect

The liquid jets may break up into several droplets with one primary drop ahead of one or more satellite drops. This is detrimental to the droplet placement accuracy so it is undesirable in many engineering applications (70). It was initially observed by Savart (71) when he conducted the first modern experimental work on droplet formation in 1833. While he confirmed the breakup of the liquid jets in flight, he also noticed the appearance of smaller ‘satellite’ between the adjacent primary droplets. Afterwards, extensive effort has been made to understand the satellite formation and researchers started to understand that satellite formation is related to non-linear breakup near pinch-off point on the jets due to surface tension.

Recently, it was found that a low viscosity liquid is more likely to be ejected from the ink nozzle to form multiple satellites (59). Dong *et al*. have observed two modes of liquid thread breakup. The first is the multiple breakups due to capillary wave instability particularly observed in the low viscosity liquid (Figure 2-12 (1)) and the length of the liquid thread becomes longer with the increase of the driving voltage. It also forms more satellites of varying sizes

with a longer liquid thread. The several instances of satellites increase the difficulty in controlling precise deposition and it is not easily predicted. It was found, however, that the increase of liquid viscosity can eliminate the multiple breakups from Figure 2-12 (2). In this case, a long thread with end-pinching is observed instead of multiple breakups. The secondary liquid thread will experience necking, contraction, breakup and finally recombination into a single satellite, provided that sufficient drive voltage is inputted (25.6 V in Figure 2-12 (3)). This pinch-off mode was proposed by Henderson *et al.* (72) using linear instability analysis to estimate the breakup times of liquid thread, which turns out to be a good approximation. The criteria for avoiding satellites are not generic, however, for the reason that a successful droplet generation relies on various factors including pressure wave propagation, interactions between ink and nozzle plate, and compatibility of the ink with the printhead. For many applications, modulating viscosity and surface tension is an easier way to avoid liquid breakup, rather than changing electronic signals.

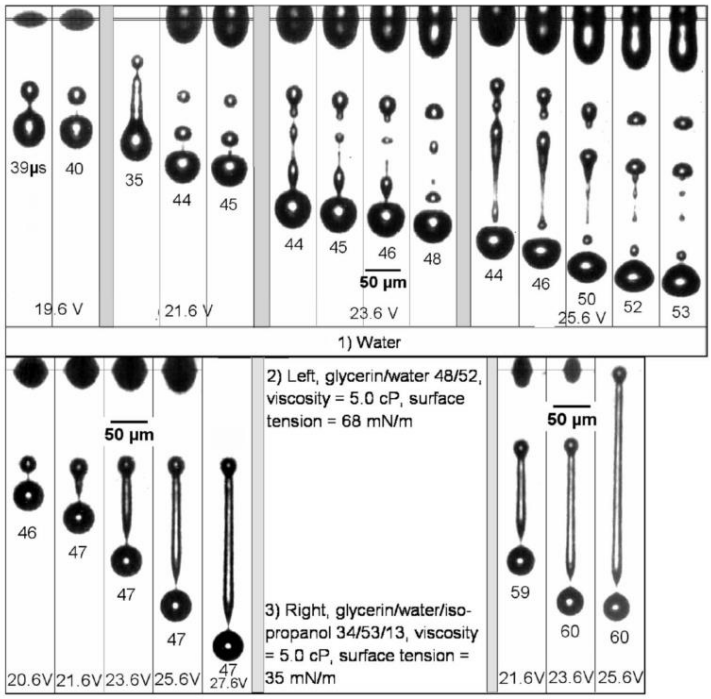


Figure 2-12: The effect of driving voltage and liquid properties on the satellite effect during liquid breakup: 1) Water (µ=1 cP, γ=73 mN/m); 2) Glycerin/water mixture 48/52 (µ=5 cP, γ=68 mN/m); 3) Glycerin/water/isopropanol 34/53/13 (µ=5 cP, γ=35 mN/m)

2.3.4. Droplet Deposition

It is important to understand the interaction between the droplets and the substrate in order to design the appropriate printing strategies and to achieve the desired printing quality. There are several physical phenomena associated with the droplet deposition which are essential to be considered during printing patterns, and they are discussed in this section.

Droplet Impact on a Dry Solid Surface

The droplet impact on a dry solid surface is a combined result of a number of factors including the impact velocity, the impact angle, the surface condition of the substrate (temperature, roughness and wettability), the physical properties of the droplets (viscosity, surface tension, density, solidification and evaporation etc). Yarin (73) extensively reviewed droplet impact dynamics from the literature and the impact phenomenon was generally categorized into splashing, spreading, receding and bouncing depending on the physical properties of the droplets and the surface textures. Mathematically the impact behaviour can be expressed by the dimensionless number of Reynolds (*Re*), Weber (*We*) and Ohnesorge (*Oh*). Sikalo (74) experimentally studied the droplet impact on dry surfaces for liquids with different viscosities, attempting to predict the droplet dynamics outcome after impact. Their subsequent numerical research on this validated the model they developed to anticipate the droplet spread factor and height with less than 1% uncertainty.

Chandra and Avedisian (75) studied the surface temperature effect on the liquid droplet collision on a solid metallic surface, for a fixed impact energy (i.e. the fixed *We* number). They found that the final droplet spreading area was dependent on the surface temperature. As the droplet approaches the surface, the liquid starts to evaporate because of heat transfer. With increase in the surface temperature, a fast evaporation rate would exert a gas pressure between the droplet and surface and act as a brake to suppress the

droplet/surface contact. The spreading area was then limited due to this effect, although they also found that the shape of the droplet was unaffected.

The capillary effect was studied using both experimental and numerical simulation approaches by Pasadideh *et al.* (76). The droplet recoiled after impact and this behaviour was controlled by both the inertial and capillary force, although the capillary effect could be neglected during the drop impact if *We* was far larger than $Re^{1/2}$. Another finding from the study was that the addition of a surfactant to the liquid droplet could result in the reduction of the recoil height, due to the change in the surface tension.

Droplet Impact onto and Mixing with a Thin Liquid Layer

When the first several droplets form a liquid layer on the substrate, the following droplets will impact on a liquid layer. Rein (77) summarized four regimes of the droplet collision with the pre-existing liquid layer, where floating, bouncing, coalescence and splashing would occur in different conditions. The droplet would float on the liquid layer for a few seconds before submerging but this phenomenon is rarely seen as it requires high cleanliness of the liquid layer surface. The bouncing is also hardly to be seen unless *We* is extremely small (78). Coalescence and splashing are two more commonly seen phenomena. The transition from bouncing to coalescence begins with a partial coalescence where the normal component of the impact velocity reaches a critical value to cause the coalescence without disturbing the surface. When the impact energy is further increased, i.e. at higher *We*, splashing is likely to occur to generate secondary droplets and it forms a corona-like flow pattern.

Droplet Spacing

Droplet spacing is the distance between the centres of the two adjacent droplets and it is a critical factor to be considered for printing a stable and continuous pattern on the substrate. The two adjacent droplets need to overlap with each other by an appropriate droplet spacing to form a

continuous feature. Figure 2-13 shows a schematic diagram to illustrate the relationship between the design of a printed pattern and the droplet spacing. For example, a square shaped pattern can be printed with a drop array with minimum 2 × 2 drops. If the droplet spacing (D) is smaller than the diameter of the droplet (2*R), i.e. D<2*R, the adjacent droplets can collide and cover the area by surface tension.

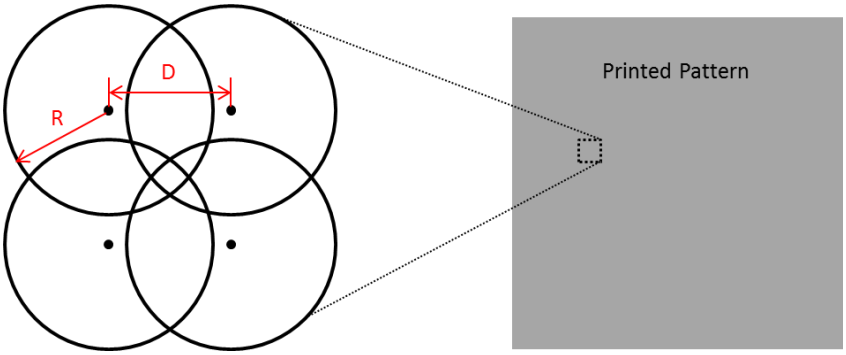


Figure 2-13: The schematic diagram for illustrating the droplets forming the large area by overlapping with each other, with a droplet spacing (D) smaller than the dimeter (2*R)

Droplet spacing effects on the morphology of the inkjet printing pattern was studied by Chen and Hung (79). A major finding was that the excessive accumulation of the droplets in a unit area (i.e. smaller droplet spacing) would result in the local bulging of the printed line, although that an increased line width would mitigate the bulging effect due to higher aspect ratio of the droplet volume to the area. A similar research on the inkjet bead stability by Derby and Stringer (80) found a periodic curvature for a droplet spacing larger than a critical value, as shown in Figure 2-14. This was due to insufficient fluid to form a stable bead on a high contact angle substrate.

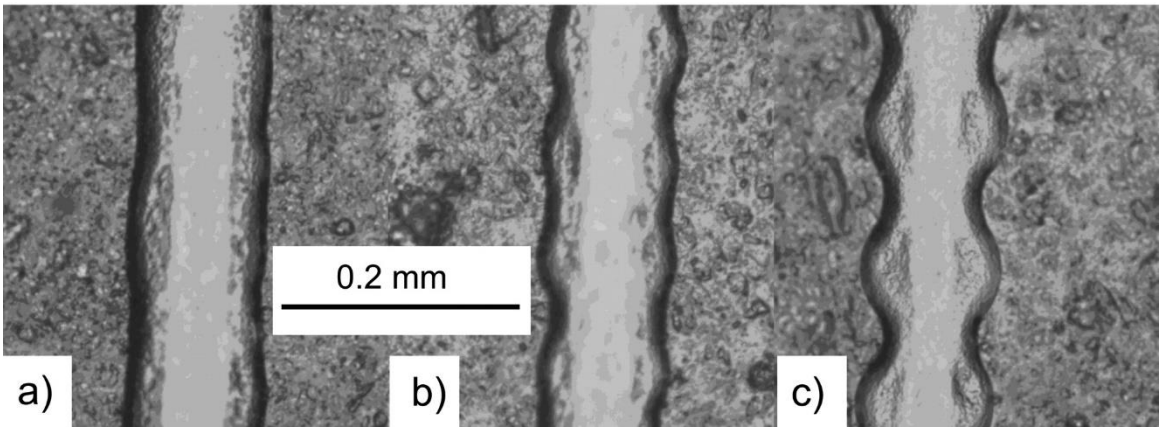


Figure 2-14: The printed track morphologies after drying of an organometallic ink on a silicone substrate with the droplet spacing of: (a) 55 µm; (b) 60 µm; (c) 85 µm

Coffee Ring Effect

The coffee ring effect, or coffee stain effect, is a phenomenon when a spilt coffee drop leaves a ring-like stain after drying on a solid surface. It is analogically used in the inkjet printing, where a suspension-based or a solvent-based droplet is deposited on the solid substrate to form a similar annular pattern.

The mechanism of this effect was first explained by Deegan *et al.* (81) (82). The key physical principle behind this phenomenon is that a pinned contact line of the droplet must be maintained by an internal outward flow to compensate the liquid evaporation at the edge. As shown in Figure 2-15 (a), the droplet will shrink due to the liquid evaporation at the edge. To keep the contact line pinned, the internal fluid must flow outwards to make up for the volume as shown in Figure 2-15 (b).



Figure 2-15: The mechanism explained by Deegan: a, the droplet shrinks due to evaporation without internal flow; b, the internal compensating flow to keep the contact line (81)**.**

Furthermore, Hu *et al.* (83) proposed an additional explanation for the coffee ring effect, except for the pinned contact line. It was shown that the coffee-ring effect also required a suppression of Marangoni effect which is a convective liquid flow in the droplet induced by the surface tension gradient. With the non-uniform evaporation of the droplet due to different thermal conduction paths, the temperature at the centre of the droplet is lower which results in a higher surface tension. The thermal-induced surface tension gradient strongly pulls the liquid inwards, which counters the compensating flow outwards. If the Marangoni effect is suppressed by the surface tension change in the droplet surface due to surfactant contamination, the outward compensating flow dominates leading to the coffee ring effect.

On the other hand, the coffee ring effect could be minimized by manipulating the Marangoni flow. Some research has reported that the addition of a small amount of surfactant can produce a uniform deposited pattern rather than concentrating the solutes at the edge (84–86). By the presence of the surfactant, local surface tension is increased at the edge of the droplets, which facilitates the Marangoni flow towards the centre of the droplets to form a more uniform distribution of the solutes. It was also reported that an additional introduction of a higher boiling point and lower surface tension solvent into a solution will reduce the coffee ring effect (87). By using the mixed solvent, the concentration of the higher boiling point solvent at the edge of the droplet is dramatically greater than that in the centre. This concentration variation in turn leads to a surface tension gradient to promote the Marangoni flow from the outer rim to the centre.

2.3.5. Drying Mechanisms of Inks

After the droplets were deposited on the substrate, they dry in different ways to form the pattern or the structure. Depending on the ink types, the drying mechanisms of the most common inks are listed in Table 2-2.

Table 2-2: The drying mechanism of different inks for inkjet printing, reproduced from Le (42)

Ink	Drying Mechanism
Aqueous/water based	Absorption, Penetration, Evaporation
Oil based	Absorption, Penetration
Solvent based	Evaporation
Hot-melt	Solidification
UV curable	Polymerisation (Free radical, Cationic, etc)
Reactive (two-part)	Polymerisation, Oxidation

Aqueous or oil-based inks generally have water or oil as a base carrier to form a solution or suspension with other functional chemical additives such as dyes, pigments, surfactants and viscosity modifier. As the water is drying slowly and oil is non-evaporative, the main drying mechanisms for the aqueous or oil-based inks are the penetration and absorption on a porous absorptive substrate such as papers. Originally they were designed for office 2D printing applications but recently there are a number of research activities focusing on the water based conductive polymer ink development (88) (89) in microelectronic fabrication.

A solvent based ink relies on the solvent evaporation to precipitate the solutes on a substrate which is not necessarily a porous media. Therefore, it has high compatibility with the non-porous substrate such as metal, glass or plastic. In the polymer inkjet printing, the polymers are dissolved in a solvent or a mixture of solvents. However, due to the narrow viscosity range for the piezoelectric DoD inkjet printing assemblies, the polymer loading is usually low and the printability is strongly dependent on the viscosity of the polymer which is a function of polymer weight (90). A majority of the solvent-based inks related research focus on the fabrication of conductive lines and films (91–93), light-emitting devices (94) and solar cells (95). There are only a few published studies reporting the 3D polymer microstructure fabrication by solvent-based inks due to low drying rates thus limiting the capability of layer stack-up (96–

98). An example of a 3D microstructure produced by direct solvent-based inkjet printing is shown in Figure 2-16.

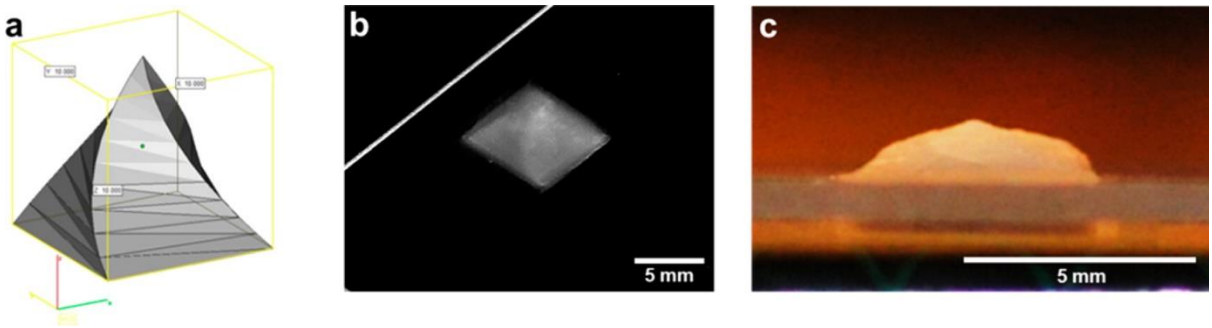
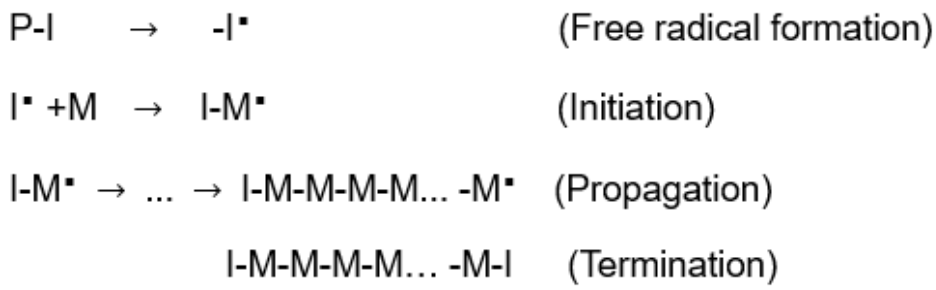


Figure 2-16: (a) a CAD design of a twisted pyramid; (b) a photo of the pyramid showing the twisted design; (c) profile view of the pyramid (99)

The hot-melt ink, or phase-change ink, is a solid ink which is jetted as molten liquid to the substrate. It solidifies immediately upon impinging on the surface and this prevents spreading on the surface. Its solvent-free nature also makes it a good alternative for the solvent based ink (100). The hot-melt ink normally contains a thermoplastic polymer and it is made molten directly in the printhead. However, as the hot-melt viscosity is a function of the polymer molecular weight, a limited range of the polymeric materials can be compatible with the inkjet printing which has a narrow process window for the ink viscosity. Another limiting factor for hot-melt inkjet printing thermoplastic polymer is the design of high temperature printhead.

A UV curable ink is a particular type of AM material where the ink cures through UV light illumination to form solid parts on a substrate. The process can be controlled by the UV source by tuning the UV light wavelength, UV power and exposure time. Another advantage of UV curable inks is the high durability in the printhead as it will not readily clog the nozzles unless exposed to the UV light (101). Their solvent-free nature also eliminates the use of volatile organic solvents and many applications can be found in the coating, printing and adhesive industries (102).

There are two main photoinitiation mechanisms for the UV curing process: free radical photopolymerisation and cationic photopolymerisation. A free radical photopolymerisation process takes a few steps to form a crosslinked polymer network, as shown in Scheme 2-1. Firstly, a photoinitiator (P-I) absorbs a radiation energy and is activated to generate a reactive portion (I·). The reactive portion then reacts with a monomer (M) to form a free radical (M·). The free radicals then tend to propagate and crosslink with other monomer molecules. Finally the termination step takes place to complete the polymerisation (103). The most common material used in the free radical UV curing process is the acrylate monomer which has intrinsic low viscosity for the inkjet printing. A range of acrylate materials have been studied in the inkjet printing (104–106). However, the primary issue associated with the free radical UV curing process is oxygen inhibition in that the atmospheric oxygen reacts with the free radical component to form peroxy radicals which are chemically inert to terminate the photoinitiation. An oxygen-free environment or appropriate photoinitiator is usually required to reduce the oxygen inhibition effect (107).



Scheme 2-1: The reaction mechanism for free radical photopolymerisation

Similarly, a cationic photopolymerisation takes place when a cationic photoinitiator transfer charges to form reactive species. A significant advantage of cationic curing process over free radical is the absence of oxygen inhibition which eliminates the need for an oxygen-free environment during curing. Epoxies are the most common cationic photopolymer, such that the ring-structure epoxy monomers undergo ring-opening process to build the

polymer network (108). The cured epoxies usually have much less tendency to shrink compared to acrylate materials for free radical polymerisation. However, the viscosity of typical epoxies is too high for inkjet printing and volatile solvents must be used as a diluent to modify the viscosity. It also requires post-cure treatment to enhance conversion (109).

Reactive inkjet printing is a relatively new approach to jetting that has emerged from the literature recent years (110). The reactive components are commonly dissolved or suspended in a solvent with the catalyst or other additives (viscosity modifier, surfactant, etc), and they are chemically stable until the reaction is triggered upon mixing. After the two (or more) reactive components are deposited onto the substrate simultaneously or sequentially from independent printheads, the two reactants will undergo a chemical reaction, i.e. usually a polymerisation, to form the pre-designed 2D or 3D pattern *in-situ*. A few examples of the applications for the reactive inks will be introduced in the next section.

2.3.6. Applications of RIP in Polymeric Material Deposition

RIP is an emerging approach to defined polymer deposition and it shares numerous applications since the first reported inkjet chemical dispenser, ChemJet, was invented for combinatorial library synthesis (111). One of the polymeric RIP applications was demonstrated by Limen *et al.* (112) that they used a dual head IIS printing unit in conjunction with modified HP bubble jet cartridges and a customized printer incorporating Xaar® printheads to deposit alternative layers of anionic and cationic polyelectrolytes. The system is fully automated to form a multi-layer stack of self-assembling hydrogels within several millimetres thickness. A similar approach to patterning hydrogel microarrays is reported in the literature (113) as shown in the Figure 2-17. The monomer, tetramethylethylenediamine (TEMED) and the initiator, ammonium persulphate (APS) are printed sequentially on a pre-treated glass slide to

initiate the polymerisation and gelation. The method potentially discloses a reasonable approach to exploring the small-scale polymer synthesis.

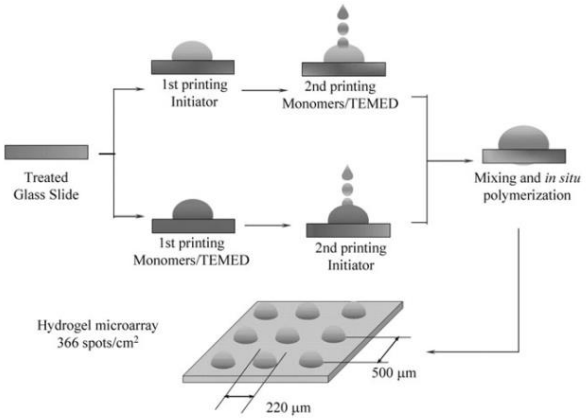


Figure 2-17: Reactive inkjet printing of hydrogel: two routes for jetting hydrogel microarray *in-situ* pico-nano litre polymerisation (113)

A RIP method to fabricate conductive layers by the deposition of poly (3,4-ethylenedioxythiophene) (PEDOT) on synthetic textile fabrics was reported by Stempien *et al.* (114) . As shown in Figure 2-18, printhead 1 was filled with an alcohol solution of 3,4-ethylenedioxythiophene (EDOT) and printhead 2 was filled with an aqueous solution of ferric nitrate·$9H_2O$. The EDOT ink was deposited line by line firstly followed by the deposition of the ferric nitrate·$9H_2O$ ink by the same line by line strategy on the EDOT layer. A hot plate was used to heat the textile fabrics up to 85 °C to facilitate the solvent evaporation and the oxidative polymerisation of PEDOT. The formed conductive polymer exhibited a low surface resistance and a good adhesion on the fabric substrates.

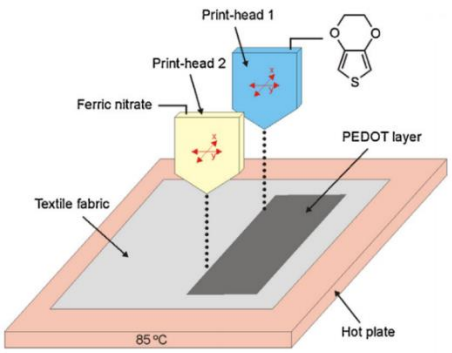


Figure 2-18: The RIP of PEDOT layers on textile fabrics to fabricate conductive layers

Recently there are some activities focused on RIP for engineering polymers synthesis. A typical illustrative example is the *in-situ* reaction of a diol and a diisocyanate to form a cross-linked network of thermoset polyurethane (115). The cross-linking agent and solvent are added to both monomers yielding two reactive inks which are jetted sequentially at elevated temperature in order to decrease the viscosity to a manageable range. The reactants are quickly cured upon heating on the substrate (90 ºC) within 3 minutes, converting to cross-linked polyurethane and the conversion is up to 70%. Another distinction in the case is that they demonstrated the homogeneous mixing of two ink droplets by tracing the fluorescence microscopy images as shown in Figure 2-19.

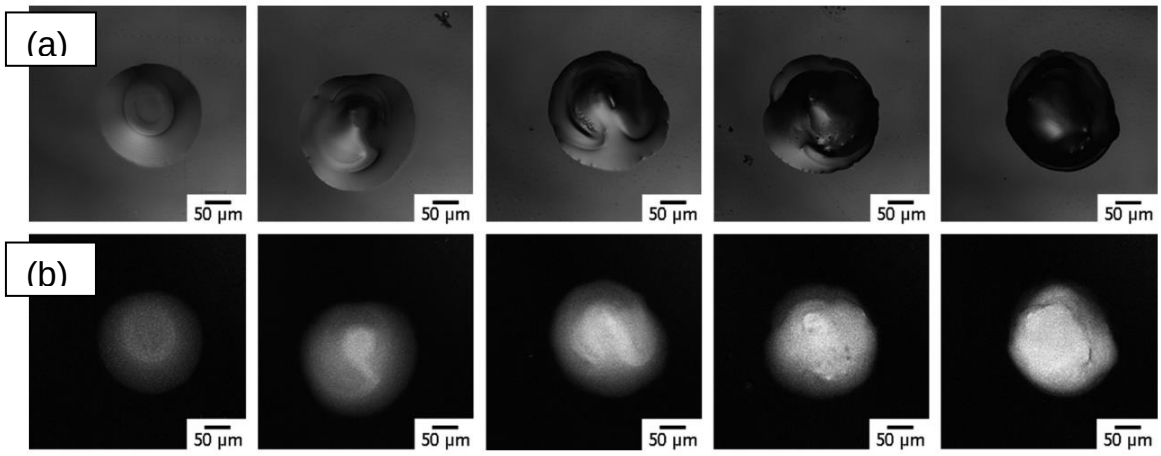


Figure 2-19: Inkjet dots of diol and diisocyanate reactive inks (1 to 5 layers) observed by confocal laser scanning microscopy: (a) reflectance images; (b) fluorescence images

Apart from thermosets, novel research on reactive ink jetting thermoplastic polymers is also emerging. Work by Fathi *et al.* investigated the bulk polymerisation of caprolactam (116) to find the optimal conditions for reactive ink jetting caprolactam. The results are later referenced to explore the RIP of nylon materials (52) by preparing sets of activator and catalyst compounds in the caprolactam in different ratios to *in-situ* synthesize functional nylon-6 parts. Although the monomer conversion achieved was lower than half of the bulk polymerisation approach even with the optimized conditions, many process

parameters were investigated such as droplet formation, nozzle wetting behaviour and microcrystal particles effects on jetting (68,117,118).

Despite the RIP developments in the material and process as above, none of them illustrated the direct RIP method to build 3D structure of a polymeric material until recently Sturgess *et al.* developed a RIP method to fabricate complex 3D geometry using a two-component ink of polydimethylsiloxane (PDMS) (119). The two parts of the PDMS inks contained silicone hydride and silicone oligomer with the Pt catalyst in octyl acetate as the solvent, and they were deposited onto the modified glass slide by a bespoke dual-head printing station and the inks were mixed and cured *in-situ* solely by heating on the substrate. Figure 2-20 showed the stepped ziggurat structure printed by this two-component reactive inks using a line-by-line printing scheme and the profile analysis, which fully demonstrated the capability of 3D RIP method to fabricate the part. A very similar study by PPG Industries and The University of Nottingham also reported a RIP method to build 3D objects of polyurea by the crosslinking of two reactive components which widen the jetting material category for the 3D printing (120).

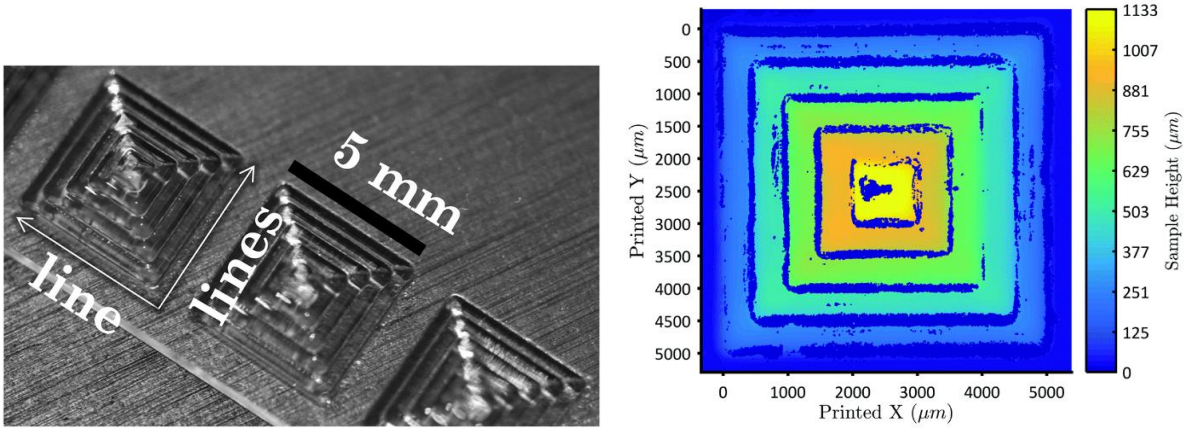


Figure 2-20: The stepped ziggurat structure of PDMS printed by the RIP method and the profile analysis for the ziggurat structure (119)

2.4. Polycarbonate

This section has a focus on the polymerisation for polycarbonate, including the fundamental knowledge of polycarbonate, synthesis of polycarbonate and its relevance to the applications in AM will also be discussed.

2.4.1. Evolution of Polycarbonate Chemistry

Polycarbonates are an important engineering thermoplastic polymer with carbonate group in the repeating structure. Its significance in engineering is attributed to its high temperature tolerance, excellent optical clarity and incredible toughness (121). Therefore, the polymer type has sustained academic interest over many years and new avenues of applications are being exploited.

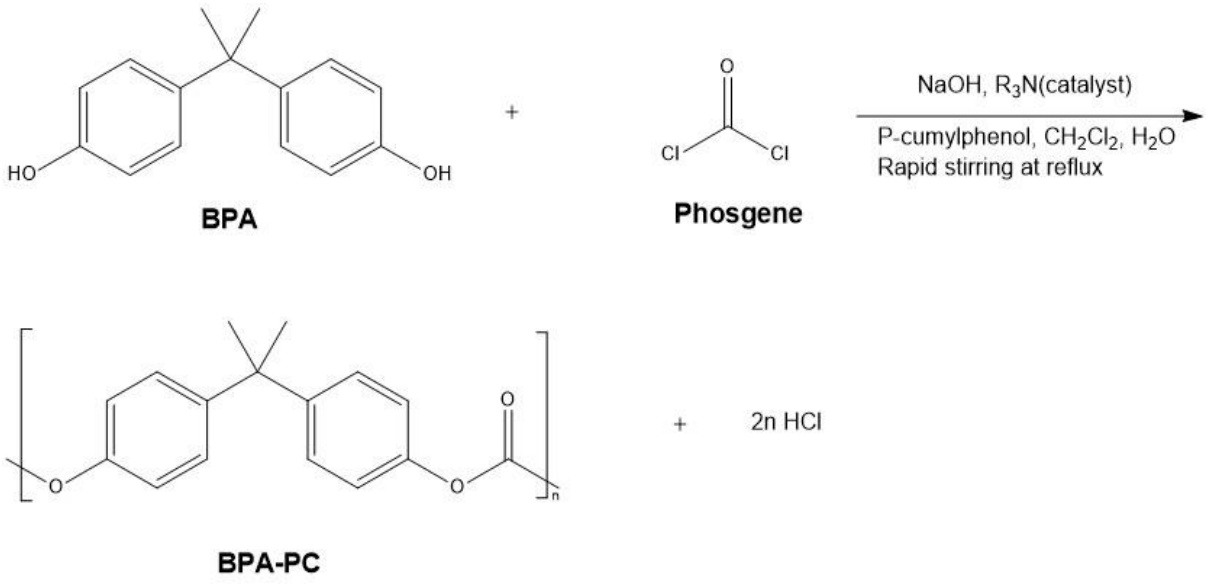
The most industrially valuable polycarbonate is aromatic but there are also aliphatic PCs. Early reports from the 1930's suggest that aliphatic polycarbonates are a corollary from aliphatic polyesters that Carothers and his colleagues were extensively working on (122). Nevertheless, none of these polyesters or 'deductive polycarbonates' had become a commercially independent class of engineering thermoplastic due to low hardness and low melting point below 100 ºC.

The first linear aromatic polycarbonate emerged when Einhorn, a Germany chemist, performed reactions with hydroquinone and resorcinol in pyridine by introducing phosgene to yield an insoluble polycarbonate that melted beyond 280 ºC in 1898 (122). This phosgene procedure was followed several years later by Bischoff and Hedenstroem who developed the synthesis of the same polycarbonate by melt transesterification of hydroquinone with diphenyl carbonate. This could have been a significant opportunity to develop aromatic polycarbonate further. The limited analytical characterisation methods and poor processing conditions, however, lead to the suspension of aromatic

polycarbonates for the following 50 years or so. In 1953, Daniel Fox at General Electric (GE) and Herman Schnell at Bayer prepared polycarbonate from bisphenol A (BPA) simultaneously (121)(123). It is considered as a breakthrough in the evolutionary history of aromatic polycarbonate because it was found that BPA-derived polycarbonates exhibit excellent thermal, optical and mechanical properties and they are not offset by any other commercially available polymers. Within the following decade, both companies commercialized BPA polycarbonate (BPA-PC) with establishment of their own production facilities.

2.4.2. Synthesis of Polycarbonate

Schnell disclosed two routes for making BPA-PC commercially (124) and until now they are still the only economically viable options. The first one refers to an interfacial polymerisation which typically involves a solution of BPA with a portion of chain stoppers such as p-cumylphenol in methylene chloride and water, while sodium hydroxide solution is continuously added to maintain the appropriate pH (between 10-12) and phosgene is introduced to the mixture concurrently in presence of a trace amount of tertiary amine catalyst (125). An illustration of this process is present in Scheme 2-2.

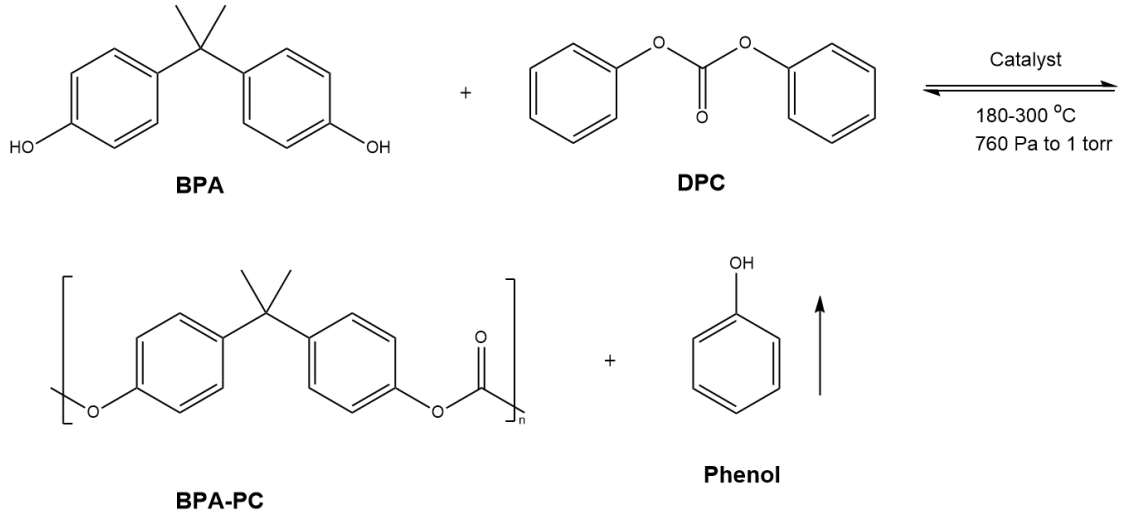


Scheme 2-2: The process of interfacial polymerisation of BPA-PC (125)

The reaction effectively occurs on the interface of the four phases in the mixture (Solid BPA, methylene chloride, gaseous phosgene and aqueous phase). Therefore, efficient stirring of the mixture is essential to ensure the complete reaction, along with over-phosgenation. The by-product, sodium chloride will be concentrated in the aqueous phase and it is separated first; following that the methylene chloride is washed by acid and water to remove the amine and base residue. After drying at 120 to 130 ºC, granular BPA-PC is ready to be further processed. This method is conducted at room temperature or slightly elevated temperature occasionally and BPA-PC with a molecular weight over 200,000 could be produced.

The final quality of the product, e.g. molecular weight, is kinetically controlled because high temperatures are not involved in the interfacial process. The sufficient contact between each phase makes it possible to have high molecular weight enhancement. End-capping agents are often introduced to control molecular weight. However, the disadvantages of interfacial polymerisation are trivial in that the polymer achieved in a non-equilibrium state is easily altered (intrinsic viscosity, molecular weight etc.) upon further thermal processing. In addition, complex multi-stage isolation and purification is engaged and phosgene's toxicity characteristics do not meet modern stringent environmental standards (122). For the lab use, phosgene is highly dangerous and thus not preferred in AM.

The second commercial production of BPA-PC is based on a poly-condensation type reaction, commonly called melt polymerisation. GE was the originator to commercialise this solvent-less process. The principle of this method is the base-catalysed transesterification between aromatic dihydroxy compounds, i.e. BPA in this case and diaryl carbonates, primarily diphenyl carbonate (DPC) with equal-stoichiometric amounts (125). Phenol is liberated during this process and removed to forward the reaction. The process is demonstrated by Scheme 2-3.



Scheme 2-3: The process of melt polymerisation of BPA-PC (125)

Practically, melt polymerisation involves two stages. In the first stage of the reaction, both BPA and DPC monomers are fed into the melt reactor with a base catalyst at ppm or even ppb level, such as NaOH, LiOH and tetra-alkyl ammonium salt. Elevated temperature is applied and kept increasing to control the extent of the reaction (normally 180 to 300 ºC or higher). Vacuum is necessary to remove the phenol for the purpose of driving the reaction forward, during which a portion of DPC also devolatilizes from the reactor. A stoichiometric excess of DPC is considered to compensate the loss in principle. As the molecular weight grows, the viscosity of the melt becomes significantly high. In order to facilitate the mobility of the components and the ease of phenol removal, good surface renewal must be implemented. Increasing temperature and vacuum is useful in the stage. Alternatively, wipe film evaporators and vacuum-vented extruders are also effective equipment commonly to expedite the mass transfer in the melt. When the desired viscosity is achieved, BPA-PC with a molecular weight of 20,000 to 80,000 is obtained.

2.4.3. Comparison of Synthesis Routes for Polycarbonate

Recently, extensive efforts have been invested on the melt polymerisation rather than the interfacial method, in order to achieve the transition to the non-phosgene technology (126). The solvent-free process could be applied to prepare low or medium BPA-PC resins. On the other hand, the thermodynamic nature of melt polymerisation is that there is no tendency towards molecular weight redistribution (122). From both points of view, the melt polymerisation is apparently more desirable. Although the BPA-PC obtained through the melt process is of relatively low molecular weight, the solid state polymerisation (SSP) technique has recently demonstrated its potential to increase the degree of polymerisation for BPA-PC with easy processing and use of inexpensive equipment (127)(128). A comparative scheme of interfacial and melt processes is listed in Table 2-3.

Table 2-3: Comparison of interfacial and melt processes for BPA-PC (121)

Interfacial Process	**Melt Process**
Kinetically controlled reaction	Thermodynamic control
Mw control via chainstopper	Mw control via extent of reaction
Amine catalysis in solvent	Base catalysis of condensation
Low temperature (~40 ºC)	High temperature (~360 ºC)
Washing and isolation necessary	Direct isolation via extrusion
High Mw can be easily achieved	Low Mw easy to achieve (optical)
Good colour, near 100% endcapping	Good colour, 60-90% endcapping
Few by-products or side reactions	Side reactions may occur at high T
Requires phosgene and solvent	Requires DPC and basic catalyst
Brine recycle controls Cl usage	May or may not require phosgene

2.4.4. Transfer to Non-Phosgene Melt Polymerisation

Choi's group has conducted a series of detailed mechanistic research on the melt polymerisation of BPA and DPC to polycarbonate in both batch and semi-batch reactors (129)(130)(131). They use a bench scale reaction system to carry out the batch and semi-batch reaction sequentially as presented in Figure 2-21. BPA and DPC are supplied separately since the reaction start immediately upon melting and mixing. The LiOH aqueous solution is injected thereafter. The reaction temperature is maintained at 180 ºC initially for 2

hours and then goes up to 250 ºC in 30 minutes. Afterwards the semi-batch mode is activated by reducing the pressure to 150 mmHg for 1 hour and 50 mmHg for 1 hour without the change of temperature. Meanwhile, the distillation column distils off phenol and refluxes DPC into the reaction system to maintain the initial molar ratio of phenyl carbonate group to hydroxyl group. Finally, the temperature is elevated to 280 ºC and pressure is lowered to 10 mmHg for 1 more hour to finish the polymerisation. During the process the viscosity increases gradually as the molecular weight of polycarbonate grows therefore mechanical stirring is needed to facilitate the liberation of by-product. The experimental outcome is in reasonable agreement with molecular species model that the ratio between different end-grouped oligomers is particularly important to the molecular weight enhancement of polycarbonate resins.

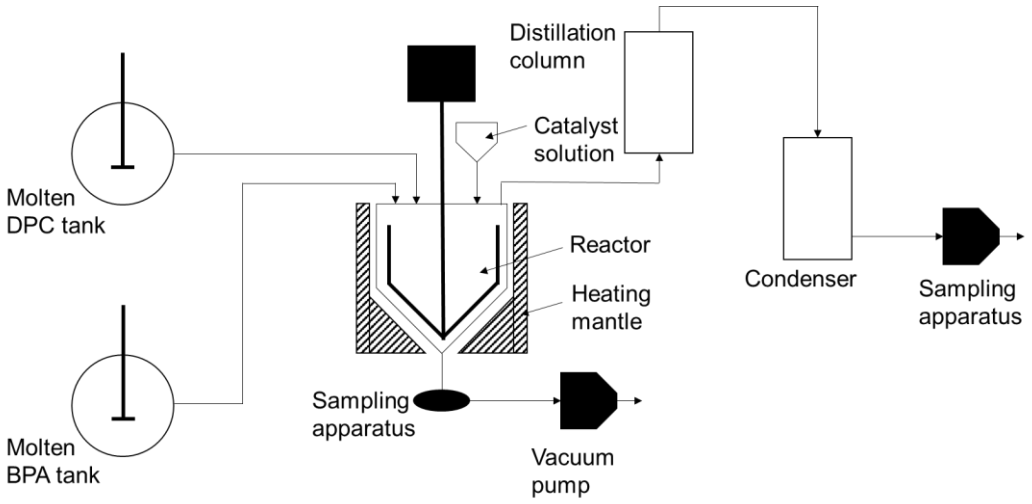


Figure 2-21: Choi's experimental set-up for batch and semi-batch melt polymerisation

2.4.5. Polycarbonate in Additive Manufacturing

The first attempt to produce BPA-PC parts in an AM method was probably the SLS process fusing 30 μm BPA-PC powders to solid parts (132). The product was found to be porous and mechanical toughness was compromised. After post-processing by elevated temperature of up to 190 ºC and reduced pressure, the SLS parts of BPA-PC still exhibited weak properties because of

the non-fully dense structure, although the pore shrinkage became more uniform (133).

Apart from the SLS process, there is a commercial AM technology to fabricate BPA-PC by FDM. As one of the most common engineering thermoplastic materials used in FDM, BPA-PC in a filament form is extruded through a nozzle to build a part's cross-sectional geometry layer by layer. A schematic is presented in Figure 2-22 to illustrate the process more intuitively. The nozzle is combined with a melting unit to extrude molten BPA-PC which hardens upon impinging the substrate or the previous layer. The BPA-PC parts by FDM are generally tough and durable and also the cost is relatively low therefore it is much more suitable for rapid prototyping, functional testing, and installation (134). However, the defects are also significant in that the FDM BPA-PC parts suffer poor surface texture and finish due to extremely high viscosity of the melt filament. In addition, 30 to 60% tensile strength of FDM parts is decreased compared to bulk PC properties because of the anisotropic effect (135). These drawbacks make it difficult to fabricate BPA-PC parts with reasonable mechanical strength by FDM.

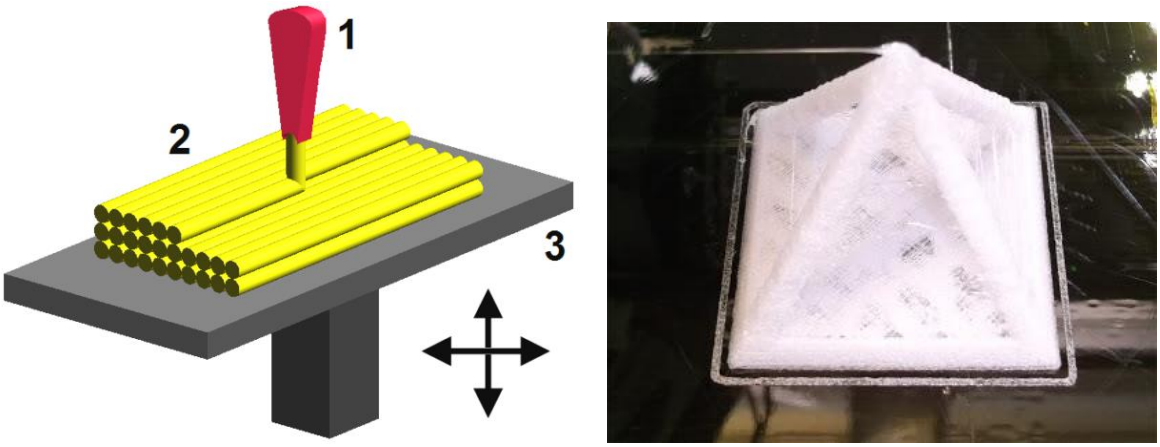


Figure 2-22: Process of FDM and printed model: (a) 1-Nozzle; 2-Building material; 3-Movable table in x-y-z direction (136)**; (b) FDM pyramid model by pure PC at 265 ºC** (137)

2.4.6. *In-situ* Polymerisation for Synthesis of Polycarbonate

For extrusion-based technologies of producing BPA-PC parts, such as FDM, the most significant problem is the extremely high melt viscosity which results in poor surface finish and low resolution of the product. The problem also needs to be particularly considered in processes such as reaction injection moulding (RIM), which is usually implemented to produce reinforced thermoplastics with or without glass fibres, including polycarbonates. A typical schematic of RIM process is illustrated in Figure 2-23. To increase the impregnation of the injection matrix, low viscosity thermoplastic precursors (monomers or oligomers) are introduced which can be polymerised *in-situ*, rather than extruding high molecular weight thermoplastics directly. The reaction is expected to cure the matrix during a relatively short time frame and any by-product is undesirable. If the conversion is incomplete or there is by-product remaining, the mechanical and physical properties of the thermoplastic composites will be affected. The most relevant RIM development is the production of linear BPA-PC using cyclic oligomers by ring-opening polymerisation (138) as presented in Figure 2-23. The reaction is triggered by mixing the molten macrocyclic oligomers and anionic activators. The initial viscosity of macrocyclic oligomers is 1 Pa.s and the conversion is over 99% within 2-5 minutes to obtain linear BPA-PC (M_w>300,000) (139).

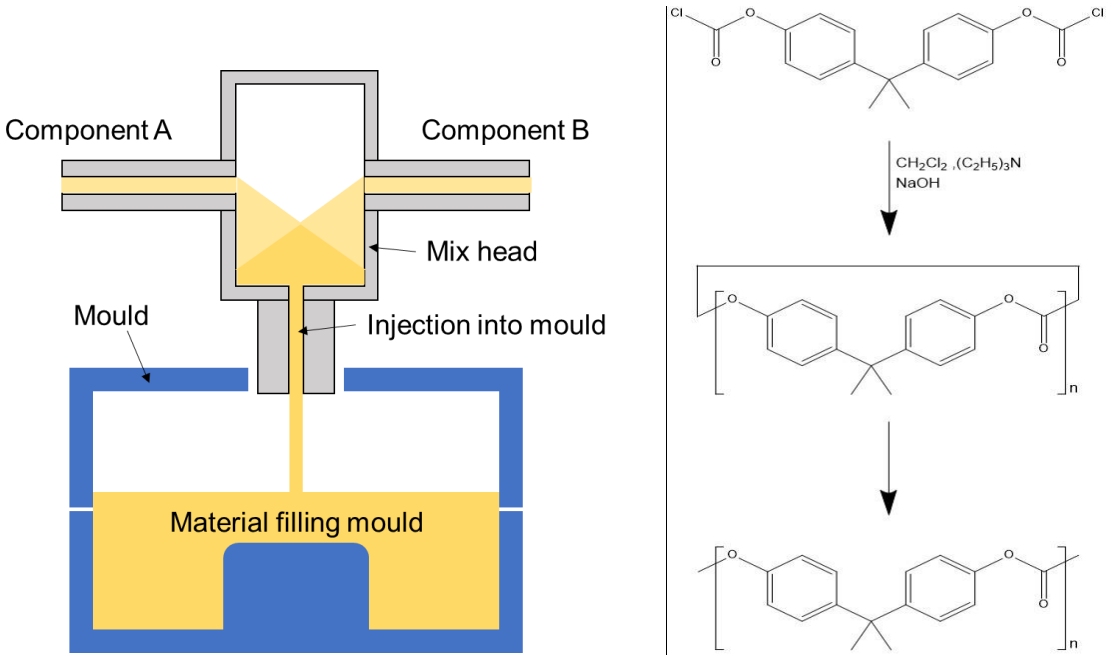


Figure 2-23: A schematic of reaction injection moulding (RIM) for thermosets/thermoplastics (left) and linear BPA-PC production with macro cyclic oligomers (bisphenol A bis-chloroformate) by RIM (right)

2.5. Conclusions from the Literature

2.5.1. Research Novelty

From the literature review, it can be concluded that the concept 'reactive inkjet printing of BPA-PC by melt polymerisation' is novel. There are no reported research activities focused on inkjet-based AM technology of polycarbonates. The most relevant research as reference is the *in-situ* ring opening polymerisation of caprolactam to synthesise nylon 6 (52), *in-situ* cross linking of polyurethane materials (115) and *in-situ* curing of PDMS to directly fabricate parts by the means of two-part reactive inkjet printing. Although commercial FDM has demonstrated the feasibility of building BPA-PC structures, the extrusion-based technology has inherent limitations in part density and surface finish, limiting the industrial application of the material in an AM context. It is worth exploiting alternative routes to overcome the weakness of the resolution, among which the reactive inkjet printing of low viscosity

monomers is promising. It aims to directly fabricate micron-scale BPA-PC structures via reactive inkjet printing.

2.5.2. Research Challenge

The concept of reactive inkjet printing of BPA-PC is to be investigated by two methods; hot-melt inkjet printing and solution-based inkjet printing. The starting materials are BPA and diaryl carbonate in their solid form. Their nature of low viscosity in the molten state or in the solution form is likely to meet the general requirement for piezoelectric inkjet printing. Firstly, the jetting monomers were characterised to identify the feasible jetting method and assembly. After achieving reliable droplet formation and optimizing process windows for monomers, a method to directly fabricate 3D structure will be explored.

As has been discussed, the melt polymerisation for synthesis of BPA-PC is, however, a poly-condensation process which brings more constraints to the research. One of the features for the poly-condensation is the generation of low molecular weight by-products, methyl salicylate, which is detrimental to the desired polymerisation. For bulk polymerisation, the by-product is removed by elevating the temperature beyond its boiling point. Meanwhile the efficient stirring for highly viscous reaction mixtures is essential. For drop scale *in-situ* polymerisation, finding an effective approach to remove the by-product without disturbing the droplet formation and deposition is identified as a significant challenge. The relatively slow polymerisation rate when compared to instant curing mechanisms (i.e. UV curable inks) also poses a challenge for 3D fabrication.

3. Methodology and Experiment

In this chapter, detailed research methodologies for the holt-melt inkjet printing and solvent-based reactive inkjet printing will be introduced and the use of experimental apparatuses (both for printing and characterisation) will be presented. Also, the post-processing method for the solvent-based inkjet printing will be introduced.

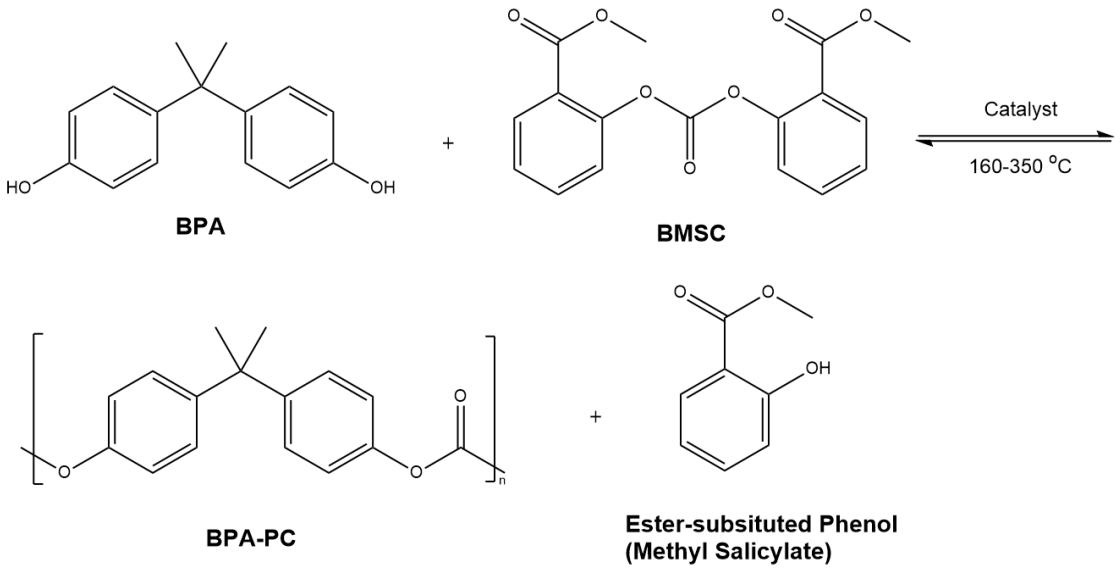
3.1. Research Approach

There were two different routes explored to investigate the reactive inkjet printing of BPA-PC depending on the types of ink formulation.

Route 1: Reactive Inkjet Printing of Hot-melt Inks Summary

BPA and Bis-Methyl Salicyl Carbonate (BMSC) are both solid monomers at room temperature, and they are molten to polymerise into the BPA-PC as a bulk synthesis method shown in Scheme 3-1. Therefore, the hot-melt, or phase change, inks were considered a suitable route to be developed for the reactive inkjet printing. A commercial high temperature printhead (Océ, Canon Group, Netherland) was investigated to melt and dispense the monomers. Before the printing trials, the printability of these two monomers were assessed including the melt behaviour, rheology and surface tension to ensure they were in the required printability range for the printhead. The melt behaviour was assessed using differential scanning calorimetry (DSC8000, PerkinElmer); the rheology was characterised with a rotational rheometer (Malvern Kinexus Pro, UK); the surface tension was measured by a drop shape analyser (DSA100s, KRÜSS GmbH Germany). The printing of hot-melt BMSC was firstly conducted using a PiXDRO LP50 inkjet printer (Meyer Burger, The Netherlands) and then the waveform for actuating droplets was optimized using the Advanced Drop Analysis (ADA) function in the software to obtain the stable droplet formation. Thin films of hot-melt BMSC were printed onto glass slide and polyimide substrate to investigate the ink deposition

performance and the surface morphology of the thin films were analysed with a microscope (Eclipse LV100ND, Nikon UK Ltd) and white light interferometry (ContourGT, Bruker). In order to provide sufficient temperature for BPA to melt up to 170 ºC, it was necessary to create a workaround by modifying the heating sensor in the printhead to outreach the standard temperature upper limit. Then similar approaches were applied to the printing of hot-melt BPA to optimize the droplet formation by tuning the waveform and to evaluate the ink deposition by printing thin films on a glass slide substrate. The BMSC and BPA together as reactive mixture was also characterised by a FT-IR spectroscopy (Frontier, PerkinElmer, USA) to demonstrate the reaction kinetics and evaluate the feasibility of jetting hot-melt reactive mixture.



Scheme 3-1: The melt polymerisation from BPA and BMSC to yield BPA-PC and the by-product methyl salicylate

Route 2: Reactive Inkjet Printing of Solvent-based Inks Summary

The printability of hot-melt BMSC and BPA was demonstrated with successful drop formation, but further investigation could not proceed due to the design limitations of the printhead. A solvent-based ink was then considered to be developed as the BMSC and BPA could be precipitated onto a substrate upon the solvent evaporation. An ink formulation consisting the reactive mixture

(BMSC, BPA, a catalyst) and an organic solvent was then explored by using commonly used solvents (1,4-dioxane, DMF and toluene). Solubility of the reactive mixtures were determined in these three solvents, and 1, 4-dioxane and DMF were selected to formulate the reactive inks which were studied further. The printability of these two formulations using different solvents was then assessed in terms of the rheology and surface tension. A Dimatix Materials Printer (DMP2800 series, Fujifilm) was used to print the thin films and multi-layer thick films of the reactive mixture. To polymerise the reactive mixture to BPA-PC polymer, the as-printed samples were post-processed using a vacuum oven which provided both high temperature and low-pressure environment to facilitate the melt polymerisation. The surface morphology of the as-printed and post-processed samples were assessed and compared by a white light interferometry. The molecular weight characterisation of the BPA-PC was carried out with a gel permeation chromatographic system (GPC, Agilent 1260 Infinity, USA). The polymer structures were studied by a Bruker DPX300 nuclear magnetic resonance spectrometer (NMR) operating at 300 MHz. The glass transition temperatures of the BPA-PC samples were investigated by using a differential scanning calorimetry (DSC8000, PerkinElmer). The thermalgravimetric analysis (TGA) of the BPA-PC samples was investigated using a TGA4000 (PerkinElmer) to study the thermal stability. Finally, the two printing strategies were investigated to establish the methodology of reactive inkjet printing 3D structure of BPA-PC.

3.2. Reactive Inkjet Printing of Hot-melt Inks

3.2.1. Development and Assessment of Hot-melt Inks

Bisphenol A (BPA) and Bis-Methyl Salicyl Carbonate (BMSC) were both supplied by SABIC Bergen op Zoom in sealed bottles. Both are white solids in atmosphere. BPA is flaky material whereas BMSC is foam-like solid.

For hot-melt inkjet printing, BMSC and BPA granules as received were used for the jetting experiments on two separate Océ printheads. Considering the maximum capacity of the ink reservoir, 1-2 g of BMSC or BPA granules were added, and the nozzles were purged for 2 seconds before printing. No alkaline catalyst was added for the jetting experiment to avoid any potential undesired oxidation of the monomers. Figure 3-1 is the sample appearance of monomers as received and Table 3-1 is a summary for properties of both monomers.

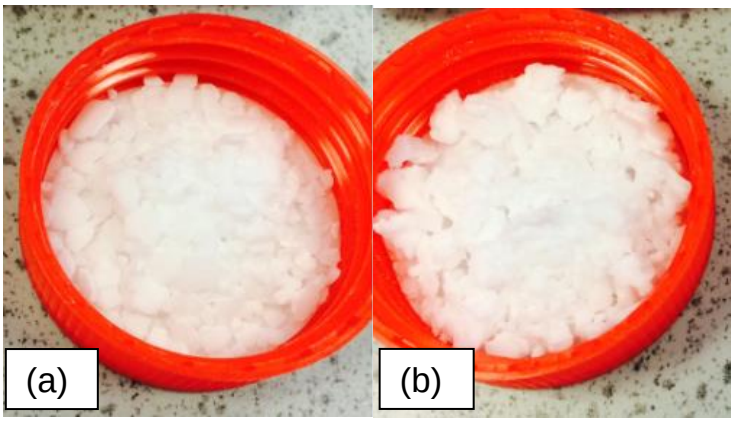
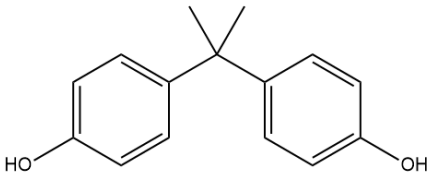
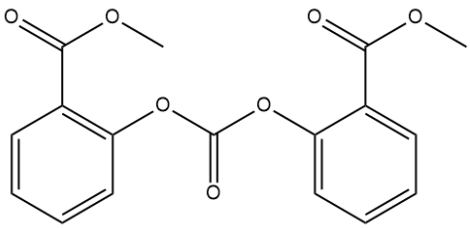


Figure 3-1: Sample appearance of (a) BPA and (b) BMSC

Table 3-1: Physical and chemical properties of BPA and BMSC as stated in MSDS

	Molecular structure	Molecular weight (g/mol)	Density (g/cm^3)	Melting point (ºC)
BPA		228.3	1.15	159
BMSC		330.3	1.17	109-114

The melt behaviour of the monomers was investigated by using differential scanning calorimetry (DSC8000, PerkinElmer). The program was set to heat the BPA and BMSC from 25 to 170 ºC at the rate of 10 ºC/min and then to cool down at the same rate. Nitrogen was used as the purge gas in a rate of 20 mL/min and the data was analysed by the Pyris software. Approximately 5 mg of the solid monomer sample was added for the each run to a DSC pan which was crimped with an aluminium lid.

The rheology of the molten monomer was investigated by a rotational rheometer (Malvern Kinexus Pro, UK). The solid monomers were placed on the plate in an active hood cartridge (as shown in Figure 3-2) to be molten at elevated temperatures. Then the plate gap was set to 150 μm and the cartridge was closed for the temperature control to start the measurement. The shear rate was set between 10 and 1000 s^{-1} at each temperature specified (120 to 135 ºC for BMSC and 160 to 170 ºC for BPA at a 5 ºC increment).

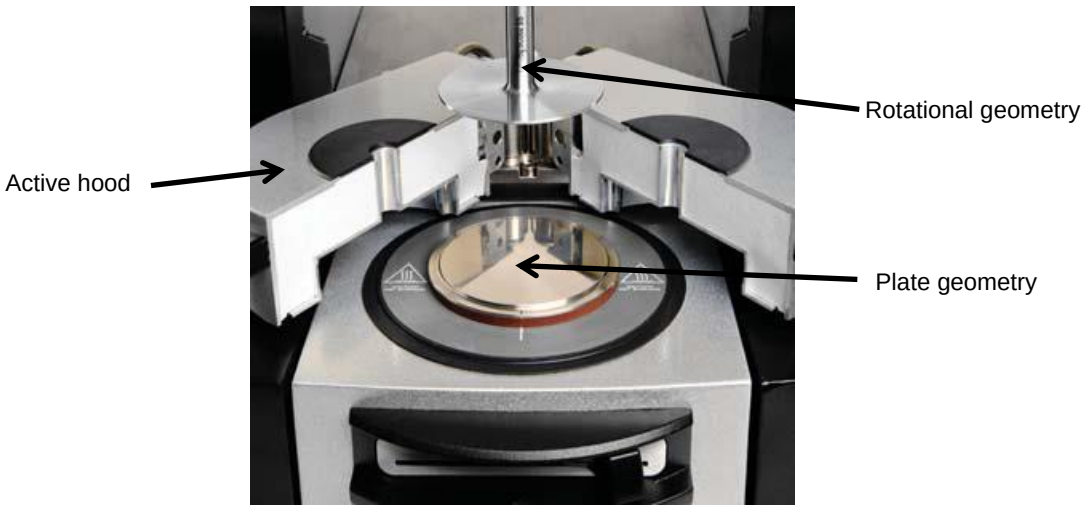


Figure 3-2: The active hood cartridge for the rheology measurement on the Malvern Kinexus Pro Rotational Rheometer

The surface tensions of both molten monomers were measured by a drop shape analyser (DSA100s, KRÜSS GmbH Germany). There is no available environmental controller box sustaining the sufficient temperature to melt

monomers into liquid droplets for pendant drop analysis. An auxiliary configuration as shown in Figure 3-3 was set up to form pendant droplets. A 5 mL glass syringe (SAMCO Silicone Products, UK) fitted with a stainless-steel needle was fixed on an iron stand and BPA or BMSC was filled into the syringe. Melting of the monomer was achieved by a heat gun (rated temperature at 300 ºC) applying heat directly around the syringe. The short-duration droplet formation process on the needle was captured by a high-speed camera (3000 fps, 1/50000 second, 1024 ×1024 pixels) and the frames extracted from the video were profiled by the software of DSA100s. The surface tension was calculated by Young-Laplace fitted to a pendant drop using the DSA software. At least 4 pendant drops during the continuous droplet formation sequence were extracted for the surface tension measurement.

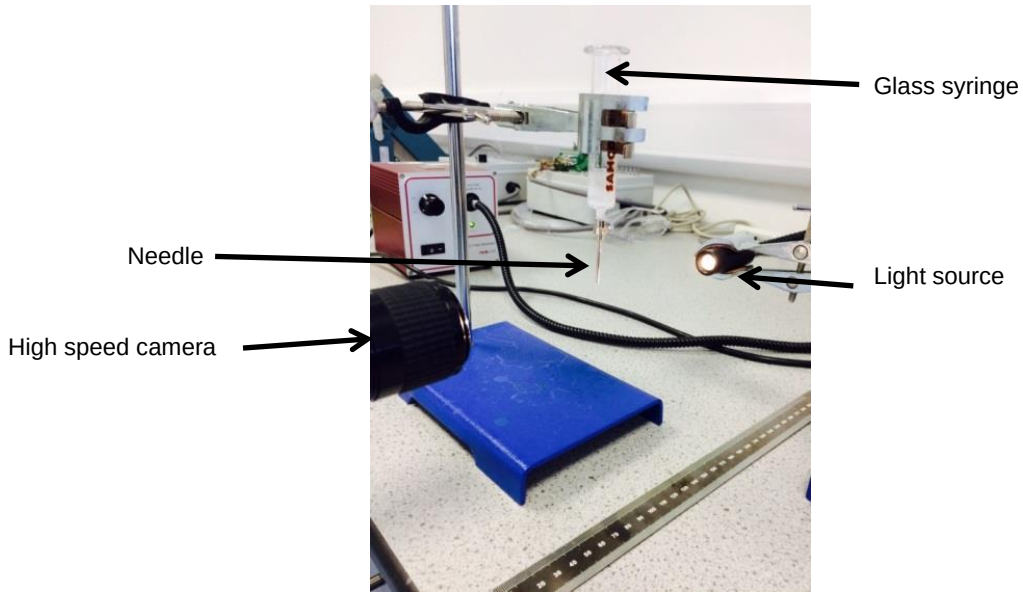


Figure 3-3: Experimental configuration for pendant droplet formation of BPA and BMSC for surface tension measurement

Palit (140) has described the thermodynamic interpretation of surface tension for a wide range of liquid with the following equation

$$\gamma(Mv_{sp})^{2/3} = K_E(T_c - T) \qquad (3\text{-}1)$$

where γ is the surface tension, M is the molecular weight of the liquid, v_{sp} is specific volume, T_c is critical temperature and K_E is a constant value. This empirical equation reveals the linear relationship between surface tension and the liquid temperature for a specific material. In this experiment, however, there is no direct measurement of exact temperature at which the free droplets form. It is assumed that the onset of droplet formation occurs immediately when it reaches the melting point of the monomer. Therefore, the temperature effect on the surface tension is neglected. The surface tension is estimated around the melting points of both monomers.

For the thermal stability study of monomers, the powdered BPA and BMSC were directly used without further purification. Sodium hydroxide pellets (NaOH, melting point is 323 ºC, data provided by VWR International Ltd.) was chosen as the alkali catalyst for the melt transesterification. NaOH was prepared as a dilute solution in deionized water with a concentration of 0.1 mol/L. A 20 mL capped vial stirred magnetically and heated with an oil bath was charged with either 2.5×10^{-3} mol of BPA (0.5708 g) or 2.5×10^{-3} mol of BMSC (0.8423 g) powder. 62.5 µL aqueous NaOH was added as the transesterification catalyst (2.5×10^{-4} mol of NaOH per mol of BPA or BMSC). The oil bath temperature was set at 170 ºC for BPA and 130 ºC for BMSC to ensure that the monomers remained in the molten state. For comparison, nitrogen was charged to the vial by a needle to remove the oxygen inside.

3.2.2. Printing of Hot-melt Inks

A PiXDRO LP50 inkjet printer (Meyer Burger, The Netherlands) was used as the printing platform for the hot-melt inkjet printing. Figure 3-4 shows the main modules of a PiXDRO LP50 inkjet printer (141).

It is an advanced inkjet printer ideal for the hot-melt inkjet printing reseach and development. It mainly consists of a motion system, a printhead assembly (PHA), a substrate table and a computer with a human interface (HMI)

software. The digital-controlled motion system has a 5 axes for the movement, with X axis controlling the movement of the PHA, Y axis driving the substrate moving continuously while printing, Z axis adjusting the height of PHA to the substrate, P axis rotating the PHA for different droplet spacing requirements, and S axis enabling the angle alignment of the substrate. The substrate table has dimensions of 327 × 227 mm which allows an A4 sized area to be fully covered by the droplet deposition. It is able to clamp different substrates by vacuum and the substrate temperature can be raised up to 90 ºC.

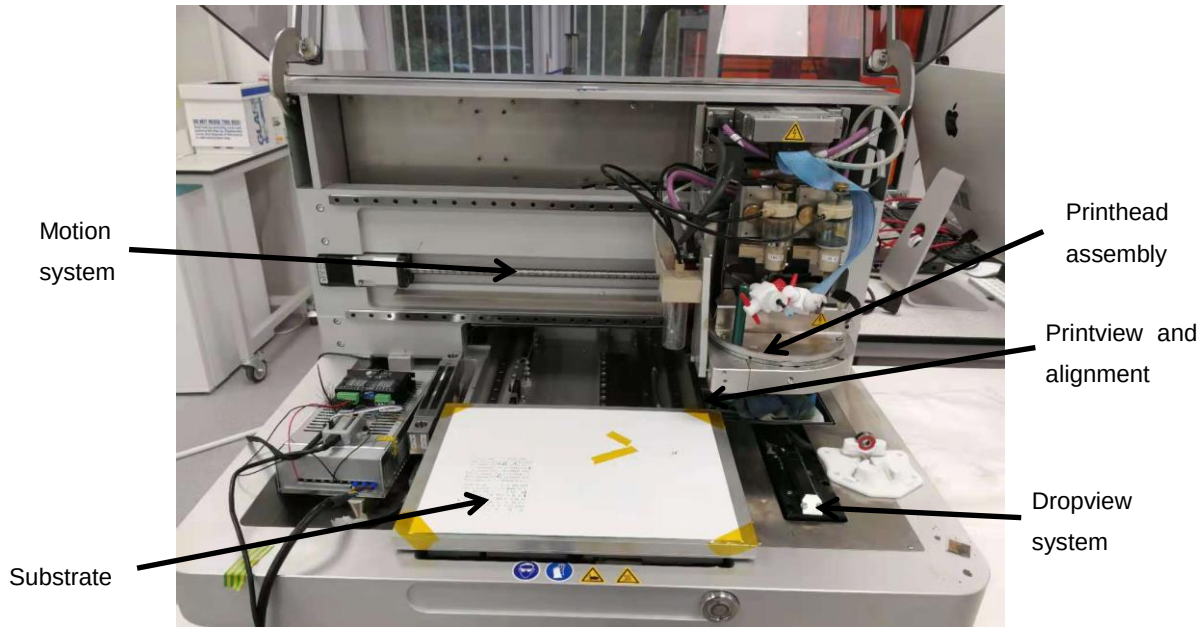


Figure 3-4: The PiXDRO LP50 inkjet printer and its main modules (141)

The PHA module is a mechanical and electrical interface to mount a specific printhead on it. There are a range of printheads which can be integrated with the PHA module on the PiXDRO LP50 printer depending on the different requirements for the inks. For hot-melt inkjet printing, an Océ Crystalpoint printhead (Océ, Canon Group, The Netherlands) was chosen for the research. This piezoelectric printhead is originally used in commercial available office large-format printers such as Océ ColorWave 600, and it can be also extended to a range of polymer-based inks because the printhead's operating temperature reaches up to 140 ºC (142). It mainly consists of an ASIC

electronic board to drive the printhead, a melting unit (MU) to liquefy the solid polymer, a graphite channel block (CB) to contain inks and a nozzle plate to eject droplets by piezoelectric actuation. The solid inks can be fed directly into the MU to rapidly form a liquid and ejected from the nozzles with high deposition accuracy. Both MU and CB are equipped with a heater and sensor to ensure the inks remain liquid at a constant temperature. Table 3-2 shows the general specifications of the Océ Crystalpoint™ printhead.

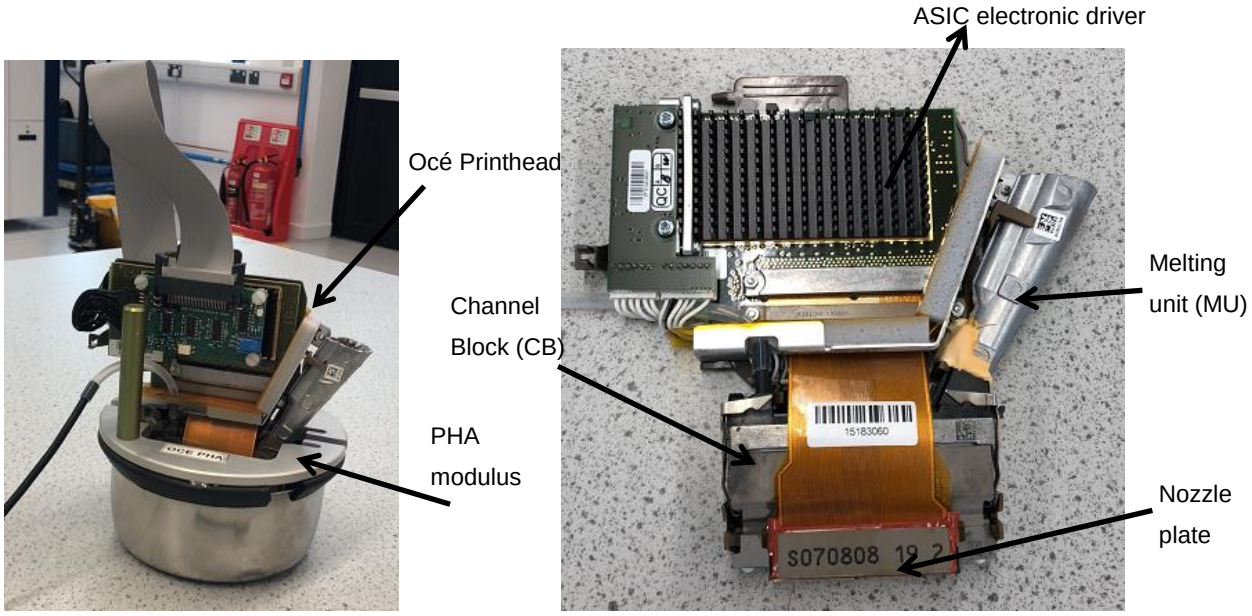


Figure 3-5: The PHA modulus and the Océ Crystalpoint™ printhead

Table 3-2: The main specifications for the Océ Crystalpoint™ printhead

Parameter	**Value**
Total number of nozzles	256 (2 rows × 128 nozzles)
Nozzle pitch per row	75 npi (nozzles per inch)
Distance between nozzle rows	8.5 mm
Nominal drop volume	10 to 30 picoliter
Maximum jetting frequency	Up to 20 kHz (ink dependent)
Temperature	Up to 140 ºC

The Océ head also allows the printhead to self-diagnose the status of each nozzle without actually ejecting a droplet by the PAINT (Piezo-Acoustic

sensing of INk channels in the Time domain) technology. By measuring the current from the piezo element when a driving waveform is applied, the status of the nozzle can be predicted. Within a few hundred milliseconds, the PAINT measurement can be completed, and the diagnosis results can be displayed in the 256 coloured blocks in the HMI software. The colours indicate the function of each nozzle, where a green colour represents a good jetting stability of the nozzle and a yellow or red block suggests the purge of nozzles. This function allows for the highest possible quality assurance of the printing result. An example of the PAINT function displayed in the HMI software is shown in Figure 3-6.

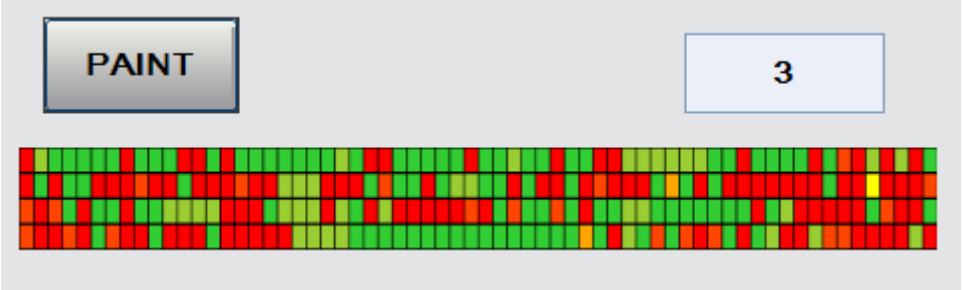


Figure 3-6: The PAINT function in the HMI software, where the number represents the times of diagnosis and the colour in each block indicates the status of each nozzle. Green represents good status of the nozzle, yellow represents medium quality of the jetting and red means a maintenance function is needed to improve the nozzle function.

There are also a few auxiliary moduli on the PiXDRO LP50. For example, the printview and alignment system allows the visualisation and alignment of the substrate with the camera which is mounted on the left side of the PHA. The camera is equipped with coaxial and diffuse illumination to view or screenshot the printed pattern on the substrate. Similarly, the dropview system enables users to view the drop in-flight from each nozzle. The short optical light pulse allows the stroboscopic view of the drops as if they are frozen in flight. By changing the pulse delay, they can form a pseudo-sequence of the droplet evolution from the nozzle. In addition, a wiping and capping system is inside the printing chamber for the nozzle maintenance such as purging and wiping to remove the excess inks from nozzles. A waste station is designed to

remove the excess inks from maintenance and to creative the necessary vacuum for performing the maintenance.

It was found that BMSC and BPA has similar physical properties to the commercial ink, Océ TonerPearls, which is a toner-based hot-melt ink dedicated to the Océ printhead (see Chapter 4 for the monomer viscosity details). The shear viscosity test for Océ TonerPearls revealed its viscosity of 11.0 cP at 130 ºC, which was close to 13.3 cP for BMSC at the same temperature. Therefore, jetting with TonerPearls was firstly undertaken as a functionality test with the Océ printhead. The experiments with TonerPearls showed stable droplet formation with the suggested single waveform by the manufacturer as shown in Figure 3-7.

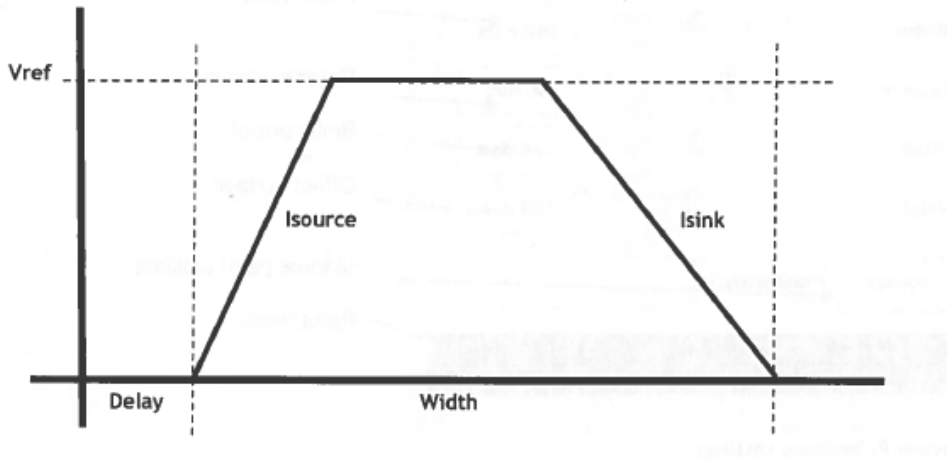


Figure 3-7: Waveform pattern used in Océ Crystalpoint™ printhead

The single trapezoidal waveform can be created as Figure 3-7 shows and was also used for the initial jetting experiments of BMSC. It was noted that the total pulse width is the sum of rising time (Isource), dwell time (plateau) and fall time (Isink). The default jetting parameters of the waveform are listed in Table 3-3. Due to the limitation of the drive electronics, complex waveforms could not be achieved so only a single pressure pulse was used.

Table 3-3: Default jetting parameters used in Océ Crystalpoint™ electronic drive

Waveform segment	Typical value[a]	Unit	Remarks
Delay	9	µs	Delay
Width	11.6	µs	Pressure pulse width
Isource	135	DAC unit[b]	Source current
Isink	84	DAC unit	Sink current
Vref	157	DAC unit[c]	Reference voltage

a. The typical value is suggested optimal for Océ TonerPearls only and it is subject to be varied among different types of ink

b. DAC values correspond to the slope for the current source and sink, which is between 0 and 255.

c. DAC values for reference voltage are ranging from 0 to 255, resulting in a trapezium pulse with a height of (48*X/255) volts. The maximum jetting voltage that can be achieved is 48V.

The optimisation of the waveform was achieved by using the add-on function of the HMI, Advanced Droplet Analysis (ADA), for the automated multi-dimensional research of droplet formation. It enables the dropview camera to automatically and sequentially record the droplet formation while the jetting parameters are varied. Each segment of the waveform can be individually assessed and optimized with the ADA and an example of the merged droplet images by ADA is presented in Figure 3-8. The droplet volume and velocity were also calculated by the ADA. The droplet volume was estimated by slicing the droplet on the image into a series of cylinders. The overall volume of the droplet was the sum of the volumes of cylinders. The droplet speed was calculated by comparing the vertical position change of the droplet on two droplet images at a sequential time delay. Though the droplet volume and speed calculation were subject to the image resolution, it provided a reasonable estimation of the speed and volume change for different jetting parameters.

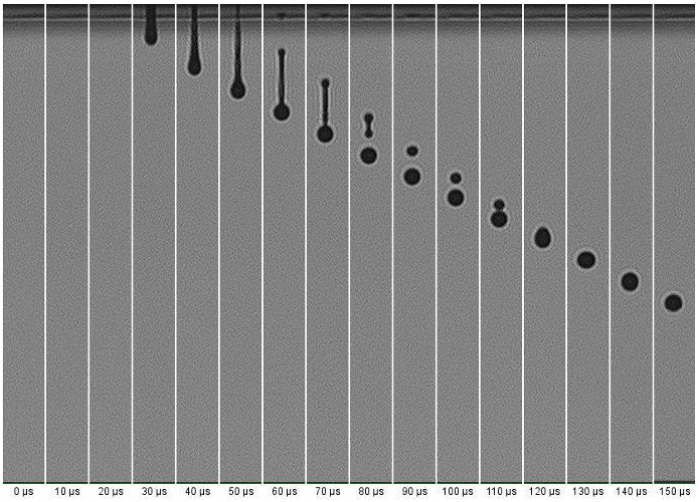


Figure 3-8: An example of merged images of droplet formation by ADA. The horizontal axis is the time delay.

Other controllable variables for jetting include the melt temperature, meniscus pressure at the nozzle plate and jetting frequency. The temperature for both the melting unit (MU) the channel block (CB) was set to 130 ºC to ensure BMSC or BPA was sufficiently molten in the reservoir and near the nozzle plate, which improved the stability of the drop ejection. The meniscus pressure is usually between -10 to -25 mar to prevent the ink dripping out of nozzles and it is not usually sensitive to a variation of a few mbar. As a guideline from the manufacturer, the meniscus pressure was set to -15 mbar. The jetting frequency could be adjusted from 1 to 20 kHz under the droplet formation observation mode (Dropview). Before observing the droplet formation process, a purge pressure of 250 mbar was applied for twice to remove bubbles in the ink channel and the meniscus on the nozzle plate was cleaned with a clean fiber-free polyester wiper (AlphaWipe, from Texwipe, Beacon Technologies, Inc.) until the PAINT function in the software displayed that acoustic pressure consistently propagated across all the nozzles.

The hotmelt inks were either printed on a glass slide or a polyimide sheet (Kapton HN thermal insulating film, Dupont).

3.2.3. Printhead Modification

During the heating process in the MU and CB on the Océ printhead, it was found that a safety feature had been built inside the electronic drive. It protected the printhead from overheating over 140 ºC. In order to provide sufficient temperature for BPA to melt up to 170 ºC, it was necessary to create a workaround by modifying the heating sensor on both MU and CB to bypass the safety feature. Increasing the impedance by adding an external resistor to the voltage divider, the output voltage of the heating sensor could be modified to increase the actual heating temperature. A resistor of 22 kΩ was welded to the wire on the heating element and the actual temperature was measured by a digital thermometer (Tenma 72-7712). The non-linear correlation between the set point and the sensing temperature was shown in Figure 3-9. To melt BPA, a minimum set point of 102 ºC was required to heat over 160 ºC. The CB and MU were both heated to 170 ºC where the set point was located at 103 ºC.

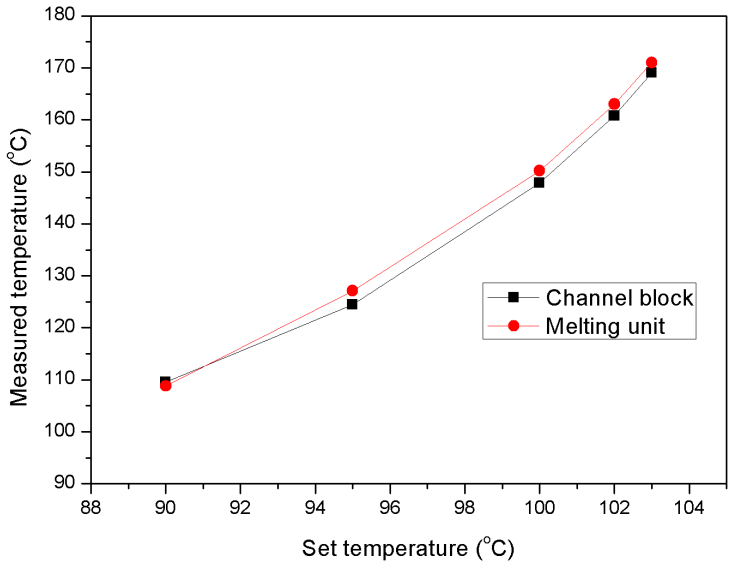


Figure 3-9: Correlation between the set point and sensing temperature with an external resistor of 22 kΩ on the heating element of channel block and melting unit

It was found from the initial jetting experiments that the MU suffered from leaking of molten BPA at the bottom as highlighted in Figure 3-10. It was possibly due to the incompatibility of BPA with the inner rubbery sealing

material inside the ink reservoir at high temperature. The leakage was sealed by encapsulating the silicone adhesive sealant paste (Silcoset 152, Acc Silicones).



Figure 3-10: Leakage (highlighted in red) of BPA from the bottom of MU

3.2.4. Sample Characterisations

The molten mixture of the BPA and BMSC was characterised by a FT-IR spectrometer (Frontier, PerkinElmer, USA) in the attenuated total reflection (ATR) mode. The mixture was scanned from 4000 to 600 cm^{-1} in steps of 1 cm^{-1} and three measurements were repeated for each sample. The spectrum was analysed to confirm the formation of the BPA-PC backbone structure and to illustrate the necessity for jetting the monomers by two separate printheads.

The surface morphology of the printed BMSC and BPA monomers was observed by the PHA camera on the PiXDRO LP50 printer. Images with higher magnification were obtained using a microscope (Eclipse LV100ND, Nikon UK Ltd) with reflected illumination. For the surface roughness and profile analysis, a white light interferometer (ContourGT, Brüker) was used to provide the numerical characterisation of the surface structures. The numerical results of the sample surface were analysed by the Vision software.

3.3. Reactive Inkjet Printing of Solvent-based Inks

3.3.1. Development of Reactive Solvent-based Inks

The solvent-based ink normally consists of the target material in a solvent which will evaporate quickly on impact to precipitate the material on the substrate. It was found by the reported data by Silvi *et al*. (143) that the reactive mixture (i.e. BPA, BMSC and a transesterification catalyst, e.g. Tetramethyl ammonium hydroxide pentahydrate) was equilibrated at temperatures ranging between 100 and 400 ºC in an organic solvent (e.g. methyl salicylate) to form a solution of PC oligomer. However, there is a dearth of information in the existing literature about whether the solid BMSC and BPA can convert to printable ink by this method. It was decided to prepare such solvent-based inks to carry out the reactive inkjet printing to build 3D structures of BPA-PC. One advantage of this method compared to the direct hot-melt inkjet printing is the formulation of the reactive mixture in the solvent to avoid undesirable thermal interaction of catalyst with the monomer at elevated temperature. In addition, BPA and BMSC can be mixed in the desired stoichiometry before they are transferred onto the substrate. Due to the nature of melt polymerisation, however, the molecular weight enhancement of BPA-PC requires post-processing stage providing the sufficient temperature and vacuum level. A vacuum oven was considered to accommodate the environmental conditions for the melt transesterification.

For common applications of inkjet printing with a solvent-based polymer ink, the concentration of the polymer is low ranging from 1 to 10% by weight due to the high molecular weight of the polymer (144) and this then also produces a low thickness of the deposited layer (53). The high loading of polymer in a solvent will result in an ink viscosity higher than printable range (>20 cP) and non-Newtonian behaviour of the ink which may cause instability of jetting (58). However, the high fraction of evaporative solvent will cause a great loss of the deposited layer volume which will lower the printing efficiency. Therefore, to

select a proper solvent and minimize the number of passes during printing, the maximum solubility of the reactant that retains the printability of the ink is expected (97). Another important factor when selecting the solvent is the stability of the solvent. In the meniscus ink layer on the nozzle plate, the liquid is exposed to the open environment which will cause a local precipitate due to solvent evaporation to potentially block the nozzle. This phenomenon is more significant when the printhead is in stand-by mode. The physical properties of the solvent associated with the phenomenon are the boiling point and vapor pressure of the solvent at the printing temperature. Although a solvent with low boiling point and high vapor pressure evaporates quickly on contact with the substrate, it will increase the instability of the meniscus. As suggested by similar work by He (145), a solvent with relatively high boiling point (>100 ºC) and moderate vapor pressure should be considered to increase the ink stability without compromising the precipitation rate on the substrate. With those principles, 3 solvent candidates were considered which were:

- DMF (N, N-dimethylformamide, Fisher Scientific UK, bp = 150 ºC) (146);
- Dioxane (1, 4-dioxane, extra pure and stabilized with BHT, Fisher Scientific UK, bp = 101 ºC) (147); and
- Toluene (Sigma Aldrich UK, bp=110 ºC) (90).

The BMSC and BPA flakes were ground with a mortar and pestle and stored separately in two capped glass vials. With a stoichiometric ratio of 1.02 to compensate for the potential evaporative loss of BMSC in reaction, the two powders were weighed and mixed evenly in another capped vial as the reactive solid mixture. The mixtures contained BMSC and BPA in the stoichiometric ratio of 1.02 and is regarded as one single component when is referred to as the ‘weight concentration’ in reactive inks. Tetramethyl ammonium hydroxide pentahydrate ($TMAH{\cdot}5H_2O$, 181.23 g/mol, Sigma-Aldrich) was to initiate the oligomer formation as the catalyst (148).

To formulate reactive inks, the solubility of reactive mixtures in the solvent should be investigated to find out the appropriate composition. For each solvent, about 4.7 to 4.9 mL was pipetted and weighed in 4 empty vials to have 5 g of solvent in each vial. Reactive inks with 10 to 40 wt% of reactive mixture were prepared by adding the reactive solid mixture in to each vial. $TMAH{\cdot}5H_2O$ was added to each solution (1×10^{-4} mol per mol of BPA) with care to minimize the exposure of $TMAH{\cdot}5H_2O$ to moisture in the air. The solutions were then magnetically stirred at 1000 rpm and kept at 35 ºC on a hot plate (IKA RCT Basic IKAMAG Magnetic Stirrer) for 10 hours. Then each solution was settled for 18 hours at room temperature (~20 ºC) to release bubbles and to allow any undissolved solid precipitated.

3.3.2. Printability Assessment of the Solvent-based Reactive Inks

The rheology of the solvent-based reactive inks was investigated by a rotational rheometer (Malvern Kinexus Pro, UK). Approximately 2 mL of ink was pipetted onto the plate in an active hood cartridge (as shown in Figure 3-2) to be measured. Then the plate gap was set to 150 μm and the cartridge was closed for the temperature control to start the measurement. The shear rate was set between 10 and 1000 s^{-1} for 25 to 45 ºC at a 10 ºC increment.

The surface tension of the solvent-based reactive inks was studied by a drop shape analyser (DSA100s, KRÜSS GmbH Germany) using the pendant drop method. An environmental controller box was equipped to maintain the temperature around the needle tip by circulating water. The temperature range for the surface tension measurement was the same as those for the rheology measurement (25 to 45 ºC at a 10 ºC increment). The pendant drop profile was extracted and analysed by the DSA software to calculate the surface tension.

3.3.3. Printing of Reactive Solvent-based Inks

A Dimatix Materials Printer (DMP2800 series, Fujifilm) was used to perform the printing of reactive solvent-based inks for synthesis of BPA-PC. The DMP printer consists of a motion system, a jetting device, a substrate platen, a drop watcher, a maintenance station and a printing chamber as shown in Figure 3-11 (149). The printer can be controlled by the Dimatix Drop Manager (DDM) software. This printer is ideal for the solvent-based ink evaluation and development with piezoelectric technology.

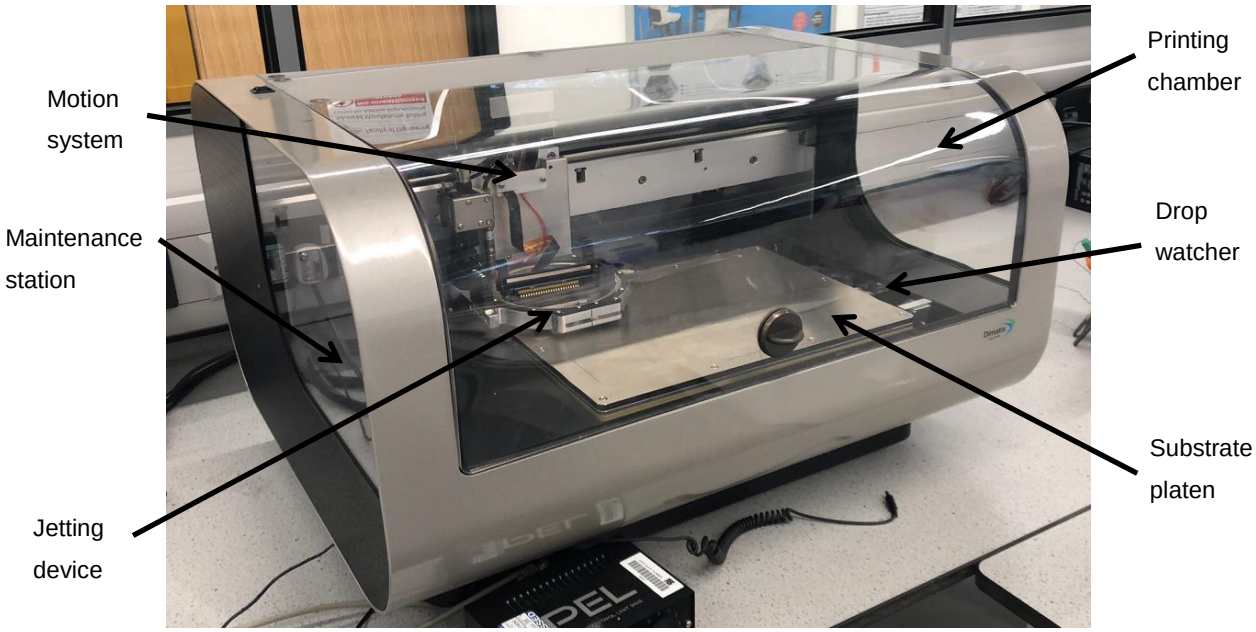


Figure 3-11: The DMP2800 series printer and its main components, modified from (149)

The jetting device is a major component in the DMP, and it can be fitted with a disposable Dimatix Cartridge. As shown in Figure 3-12, the cartridge consists of a fluid module and a jetting module which are both disposable and replaceable. About 3 to 4 mL of liquid ink can be filled into the fluid module by a syringe and a tip. The jetting module is clamped to the jetting module. There are 16 nozzles with 254 μm spacing between each other, and the nozzle has two different nominal drop volumes available (1 and 10 picolitre). For the research, the 10 picolitre cartridge was used to increase the ink throughput for the 3D structure fabrication.

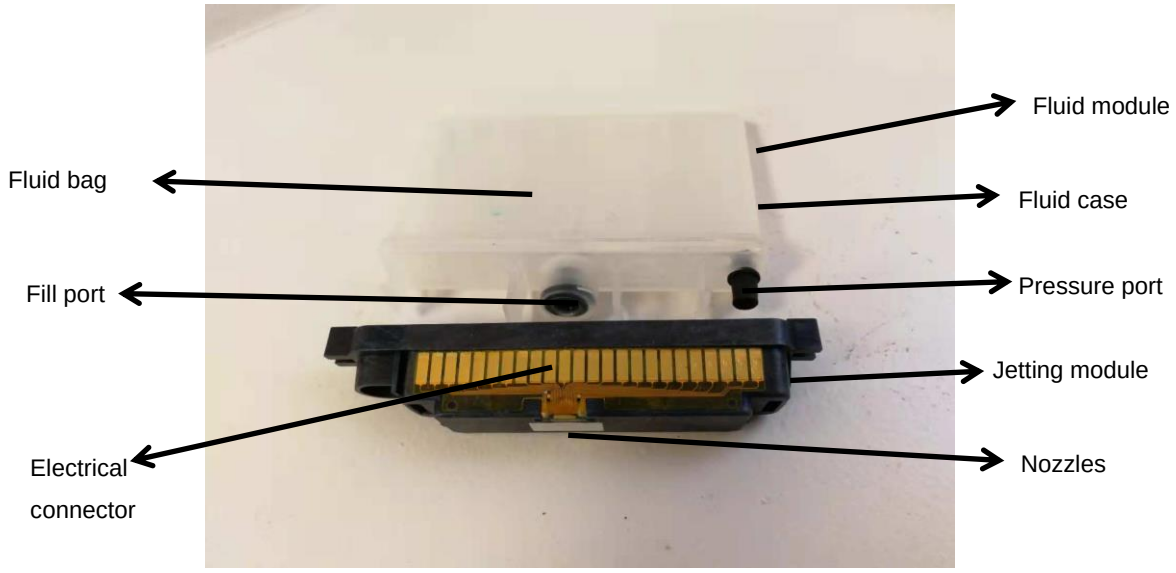


Figure 3-12: The main components of a Dimatix cartridge (149)

A DMP cartridge was filled with approximately 4 mL of DOX25 or DMF35 by a 5 mL syringe (B. Braun Injekt® Luer Solo 5 mL). The syringe was fitted with a filter (Millex-HA syringe filter unit 0.45 µm, mixed cellulose esters) and a Dimatix Materials Cartridge fill tip to exclude any particles with a diameter larger than 0.45 µm. The cartridge was tapped manually to remove air bubbles and then assembled with the nozzle plate. A single waveform specifically designed for jetting low viscosity fluids on the Dimatix printer was used. Figure 3-13 showed the waveform pattern applied in the experiment. It was found that each nozzle had different velocity profiles of jetting liquid at the same jetting voltage input. This inconsistency was also observed in other studies (150). Therefore, the jetting voltage for each nozzle was individually adjusted to keep the velocity of droplets at the same level. Table 3-4 elaborated all the parameters of jetting waveform described in Figure 3-13.

Table 3-4: Jetting parameter of the waveform for jetting DOX25 and DMF35

Waveform description			
Segment	Level (%)	Slew rate	Duration (μs)
1	80	0.36	6.528
2	0	0.22	13.888
Overall	-	-	20.416
Other jetting parameters			
		DOX25	DMF35
Maximum jetting frequency (kHz)		5	3
Jetting voltage for each nozzle(V)		23-24	25-26

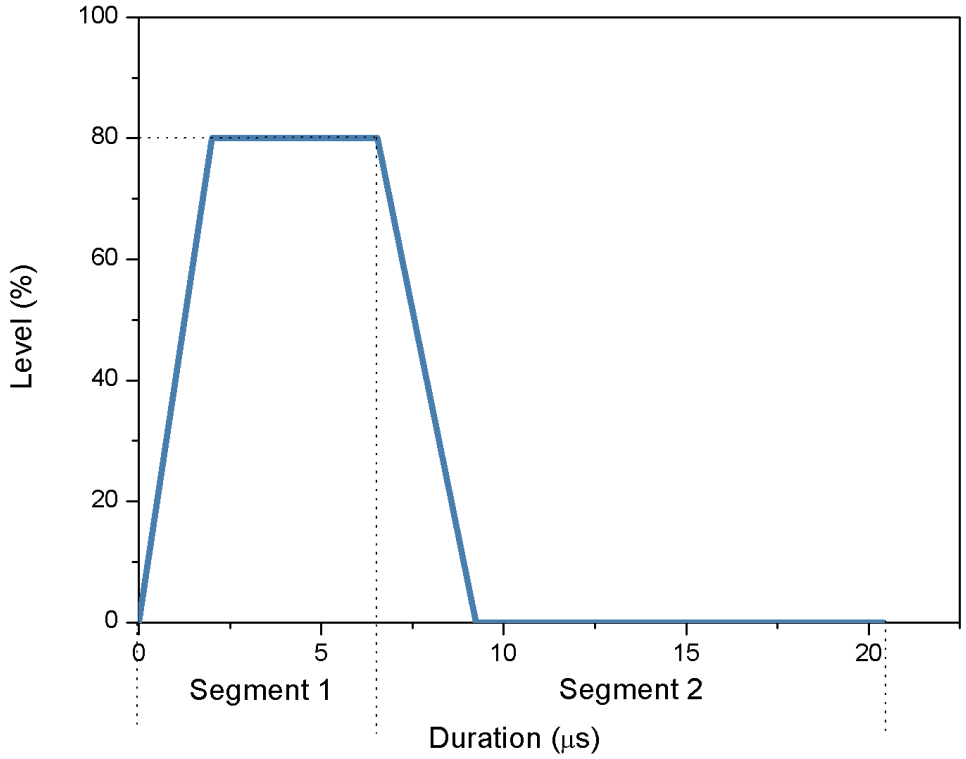


Figure 3-13: The waveform pattern for jetting low viscosity fluid (<5 cP) on DMP

The inks were filled into the Dimatix cartridge with the same procedure as that for droplet formation study (See Section 5.3). A microscope glass slide (Thermo Scientific, 1 mm thick) was used as the deposition surface which was fixed on the heater described in Chapter 3. The surface temperature of the

microscope glass slide was altered by the heat conduction from the heater which was controlled by the Arduino software. The stand-off distance was kept at 1 mm and all the nozzles were purged for 0.2 s before printing to remove any particles or bubbles around nozzles.

The substrate platen is equipped with vacuum clamp to affix a range of substrates. It is also temperature adjustable up to 60 ºC. However, for the higher substrate temperature requirement, an external heater as shown in Figure 3-14 is placed on the substrate platen. The heater consists of a thin Kapton insulated flexible foil heater (KHLV-103/10, Omega Engineering Ltd UK) embedded on a fire brick whose bottom and top are covered by stainless steel plates. The rated temperature is up to 200 ºC which is controlled by the open-source Arduino Software. This heater is placed on the DMP substrate platen and the substrate for the printing (such as a microscope glass slide) is directly placed on the heater to meet the substrate temperature requirement.

The pattern can be either created by the pattern editor in the DDM software or converted from the external bitmap files. The pattern resolution can be altered from 100 dpi up to 5080 dpi (the corresponding droplet spacing from 254 μm to 5 μm). There is a fiducial camera on the side of the jetting device which is able to move along with the cartridge to help visualize the printed pattern on the substrate as well as to adjust the printing position. The drop watcher in the printing chamber allows droplet formation videos or images to be directly evaluated on the main screen of DDM. A disposable cleaning pad is in the maintenance station to blot the nozzle surface of the cartridge and to contain the fluid produced from the purging and blotting process.

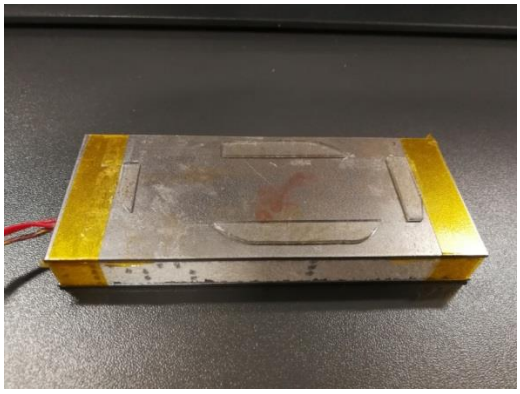


Figure 3-14: The external heater for the substrate heating up to 200 ºC

3.3.4. Polymerisation Conditions for Post Processing

The samples printed by the solvent-based inkjet printing method required post processing to undergo further polymerisation and to achieve the desired molecular weight. Recently a patent on reactive inkjet printing BPA-PC was released which illustrated the possibility of *in-situ* polymerizing the printed PC monomers by a high temperature and vacuum system in the printing area (151). However, positioning a high temperature and vacuum system in the printing area might result in instability and failure of the jetting. In addition, the reaction temperature up to 300 ºC would be detrimental to the printing system if no proper cooling systems could be implemented. In this research a separate shelf-heated vacuum oven (VT6060P, Thermo Scientific) was used to polymerise the as-printed reactive mixture in order to maintain the initial geometry and also to obtain the BPA-PC.

The melt polymerisation for BPA-PC followed a stepped profile where the temperature was gradually elevated to 280 ºC and the pressure was reduced to a near vacuum level. It was reported by Kamps *et al.* (152) that using BMSC instead of DPC would significantly increase the reaction rate by following the polymerisation profile as shown in Table 3-5. Aiming to achieve a comparable molecular weight, the as-printed reactive mixture was placed in the vacuum oven chamber which was set to the same polymerisation profile.

Table 3-5: The stepped polymerisation profile for post processing the as-printed reactive mixture using the vacuum oven

Polymerisation Steps	Temperature (ºC)	Pressure (mbar)	Time (min)
1	180[a]	Atmospheric	15
2	220	100	15[b]
3	280	0.5-1.5	10[c]

a. The heating chamber was preheated to 180 ºC
b. Including the ramp time (appx. 4 mins) from 180 to 220 ºC
c. Including the ramp time (appx. 6 mins) from 220 to 280 ºC

3.3.5. Sample Characterisations

The optical images of the printed samples were obtained using a microscope (Eclipse LV100ND, Nikon UK Ltd) with reflected illumination. A white light interferometer (ContourGT, Bruker) was used to provide the numerical characterisation of the surface structures of the thin films. The numerical results of the thin film surface were analysed by the Vision software. Due to the slope limitation of the white light interference to the samples, the surface profile of thick films with dome shaped top surfaces were observed with a focus variation microscope (Alicona Infinite Focus G5, Alicona Imaging GmbH). This scans the samples and moves in the vertical direction to generate a stack of 2D images, therefore generating a full 3D profile. The vertical resolution is ranging from 10 to 2300 nm depending on the objectives (153). As the samples were transparent, physical replica were prepared by using AccuTrans AB casting silicone. The surface profile was analysed using the MountainsMap software.

The molecular characterisation of the BPA-PC from the post processing was carried out with a gel permeation chromatography (GPC). The GPC machine used was an Agilent 1260 Infinity II Multi-Detector GPC/SEC System (Agilent, USA) which was configured with a Rayleigh light scattering (LS) detector to measure the absolute molecular weight without relevance to other standards.

The two columns used were PLgel 10 μm MIXED-B (Agilent, USA). The tetrahydrofuran (THF, HPLC grade, Fisher Scientific) stabilized with 250 ppm butylated hydroxytoluene (BHT) was used to dissolve the as-printed, post-processed and reference BPA-PC samples with a concentration of 3 mg/mL, and as an eluent at a flow rate of 1 mL/min at 35 ºC. The results were analysed by the ASTRA software (Wyatt Technology Corporation).

The polymer molecule structures were studied by a Bruker DPX300 nuclear magnetic resonance spectrometer (NMR) operating at 300 MHz. The as-printed, post-processed and reference BPA-PC samples were dissolved in Chloroform-d ($CDCl_3$, 99.8 atom % D, Sigma Aldrich) at a concentration of between 2 to 5 mg/mL. ^{1}H-NMR and ^{13}C-NMR spectra were obtained at 20 Hz spin rate with a 5 mm diameter quadruple nucleus probe. The ^{1}H-NMR spectra were normalized with the solvent standard chemical shift at 7.26 ppm (i.e. ^{1}H-NMR solvent residual resonance of $CDCl_3$) and the ^{13}C-NMR spectra were normalized with the solvent standard peak at 77.02 ppm (i.e. ^{13}C-NMR solvent residual resonance of $CDCl_3$) (154). No additional baseline correction was applied. The spectra were analysed by the MestreNova software (Mestrelab Research S.L., USA). The data was processed without any phase correction.

The glass transition temperatures of the BPA-PC samples were investigated by using a differential scanning calorimetry (DSC8000, PerkinElmer). For the as-printed samples, the program was set to a thermal cycle of (-50)-200-(-50) ºC at 10 ºC to obtain the heat flux profiles. For the post-processed and reference samples, the program was set to a thermal cycle of 0-360-0 ºC at 20 ºC/min. Nitrogen was used as the purge gas in a rate of 20 mL/min for all the samples and the data was analysed by the Pyris software. For each measurement, approximately 5 mg of the sample was added to the DSC pan which was crimped with an aluminium lid.

The thermal gravimetric analysis (TGA) of the BPA-PC samples was investigated using a TGA4000 (PerkinElmer) to study the thermal stability. Nitrogen was used as the purge gas at 20 mL/min. The temperature swept from 30 to 800 ºC and the sample size was between 15 to 20 milligrams. The data were collected and analysed by using the Pyris software.

4. Results: Reactive Inkjet Printing of Hot-melt Inks

This chapter has a focus on the investigation of hot-melt inks regarding their printability. Physical properties of reactive molten inks are characterised, and the performance of jetting is reported.

4.1. Introduction and Research Rationale

The melt polymerisation of BPA-PC has been widely studied and a process window has been established (130)(155). However, it has not been reported whether the monomers and process parameters for melt polymerisation are suitable for a reactive inkjet printing. Recently it has been reported by Kamps (152) that using an activated carbonate, such as bis-methyl salicyl carbonate (BMSC), could lower the reaction temperature and residence time compared to the traditional melt polymerisation using DPC as carbonate source. The enhanced reactivity of BMSC would potentially avoid the high volatility and thermal issues of DPC. The reason for choosing BMSC over DPC is that the literature has reported the undetectable Fries rearrangement product by using ester-substituted diphenyl carbonate compound (156,157). Normally by solely using DPC as a reactant for melt polymerisation, Fries rearrangement product is formed at high temperature which will give rise to the undesired and uncontrolled polymer branching. The branching is particularly detrimental to the mechanical properties of the polycarbonate. If the polycarbonate can incorporate an ester-substituted moiety, the impact of branching can be minimized. Additionally, it was also reported that the less reaction time using BMSC could decrease the polymer degradation (158,159). Therefore, BPA and BMSC were used as the monomers to study the reactive inkjet printing. Both jetting materials are wax-like, which exhibit sharp melting temperature in the thermal cycle measured by DSC. Therefore, the concept of reactive inkjet printing of BPA-PC by jetting hot-melt monomers can be investigated with several objectives:

- To characterise the viscosity and surface tension of BMSC and BPA and assess the droplet formation along with the deposition performance;
- To investigate and optimize the process windows for the polymerisation of BMSC and BPA to build polycarbonate parts by post-processing.

4.1.1. Reactive Inks Formulation

The result for the solubility test is shown in Figure 4-1. For toluene, the white reactive solid mixture precipitated after over-night settling regardless of the weight concentration. It indicates a low solubility of reactive mixture in toluene. For 10 and 20 wt% dioxane inks, the solutions were clear which suggested the full dissolution of reactive mixture. White solid precipitates were in the 30 and 40 wt% dioxane inks after settling, which suggests an oversaturation of the reactive mixture in dioxane. The similar white precipitates were also observed in the 40 wt% DMF ink.

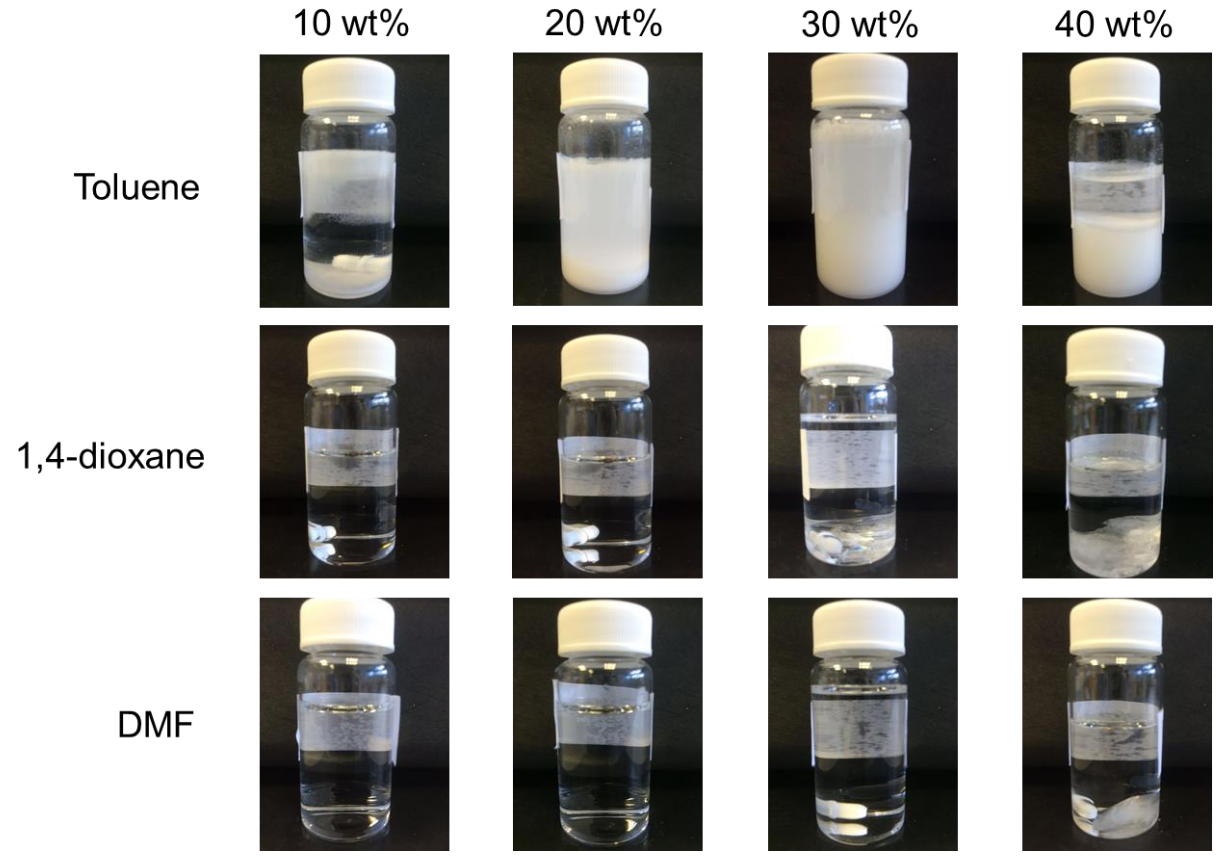


Figure 4-1: Solubility test for 3 different solvents (Toluene, Dioxane and DMF) used for reactive ink formulation

To ensure the particles were fully dissolved. it was decided to further heat and to magnetically agitate all the solutions with white precipitates at 50 ºC for 30 minutes on the hot plate. After 24 hours settling, there were still white precipitates in the toluene inks, dioxane inks with 30 and 40 wt%, and DMF inks with 40 wt%. For inkjet printing, the precipitates may block the nozzle in the print cartridge. Therefore, toluene is not a good solvent for the reactive mixture to achieve high loading as the other two solvents. From the solubility test result, it can be concluded that either dioxane or DMF are potential candidates for preparing the reactive inks

To narrow the range and find out the maximum solubility of the reactive mixture in dioxane and DMF solvent, further experiments were carried out using the same methodology as the previous solubility test. For dioxane inks, 20 to 30 wt% solutions were prepared at an increment of 1 wt%. It was found that precipitates existed in the solution when the weight concentration was greater than 25 wt%. For DMF inks, 30 to 40 wt% solutions were prepared at an increment of 1 wt%. It was observed that stable and clear solution could be obtained if the solid loading was equal to 35 wt% or lower. Therefore, it was decided to further carry out the printability assessment for 25 wt% dioxane inks (DOX25) and 35 wt% DMF inks (DMF35).

4.1.2. Composition and Stability of Reactive Inks

With the principles of maximizing the reactive mixture loading in the solvents, two reactive inks were formulated using dioxane and DMF, respectively. The compositions of the two inks are shown in Table 4-1.

Table 4-1: The two compositions of the reactive inks containing dioxane and DMF as solvents

Ink name	BMSC & BPA	Solvent	Catalyst
DOX25	25 wt% (ratio of BMSC to BPA =1.02)	Dioxane 75 wt%	TMAH (1×10^{-4} mol per mol of BPA)
DMF35	35 wt% (ratio of BMSC to BPA =1.02)	DMF 65 wt%	TMAH (1×10^{-4} mol per mol of BPA)

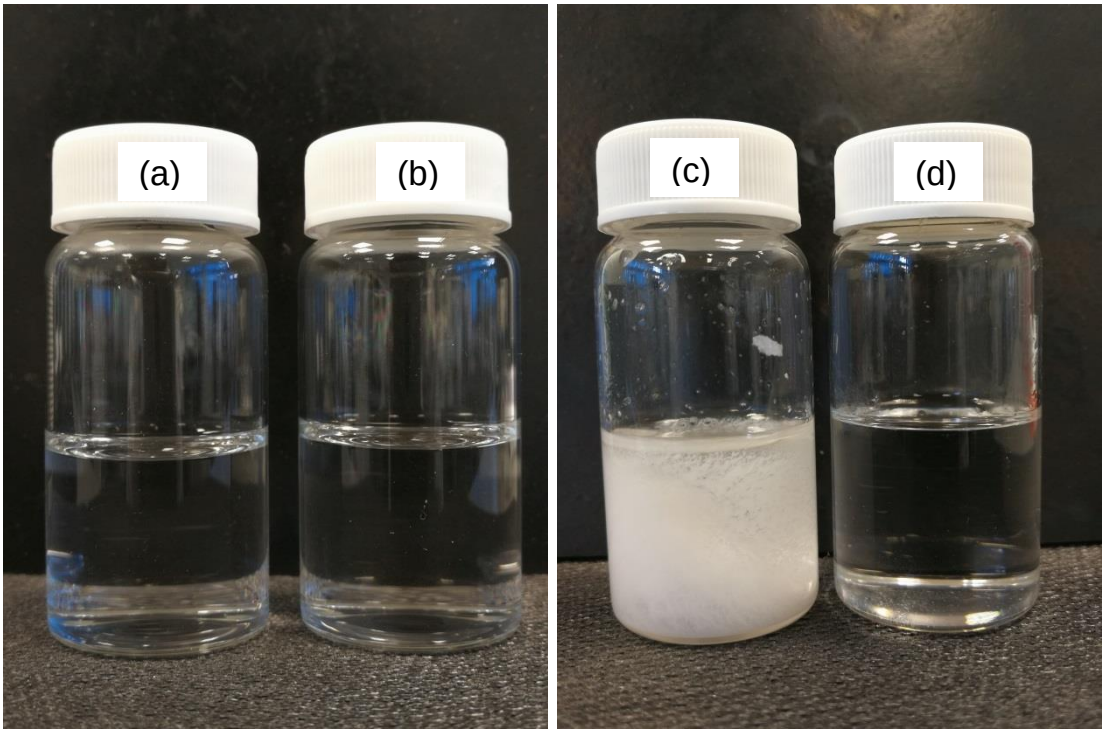


Figure 4-2: The stability of reactive inks over 90 days period: (a) fresh DMF35 as formulated; (b) fresh DOX25 as formulated; (c) DMF35 after storage for 90 days; (d) DOX25 after storage for 90 days

After formulation of the reactive inks, they were both free of visible large particles and transparent as shown in Figure 4-2(a) and (b). They were stored in sealed vials at room temperature. The homogeneity and precipitation were visually assessed after a 90-day period to understand their long-term stability. It was noted that DMF35 had milky white appearance after 90 days, also with precipitates on the inner wall of vials as seen in Figure 4-2(c). This was probably due to the oversaturation of the reactive mixture dissolved in the

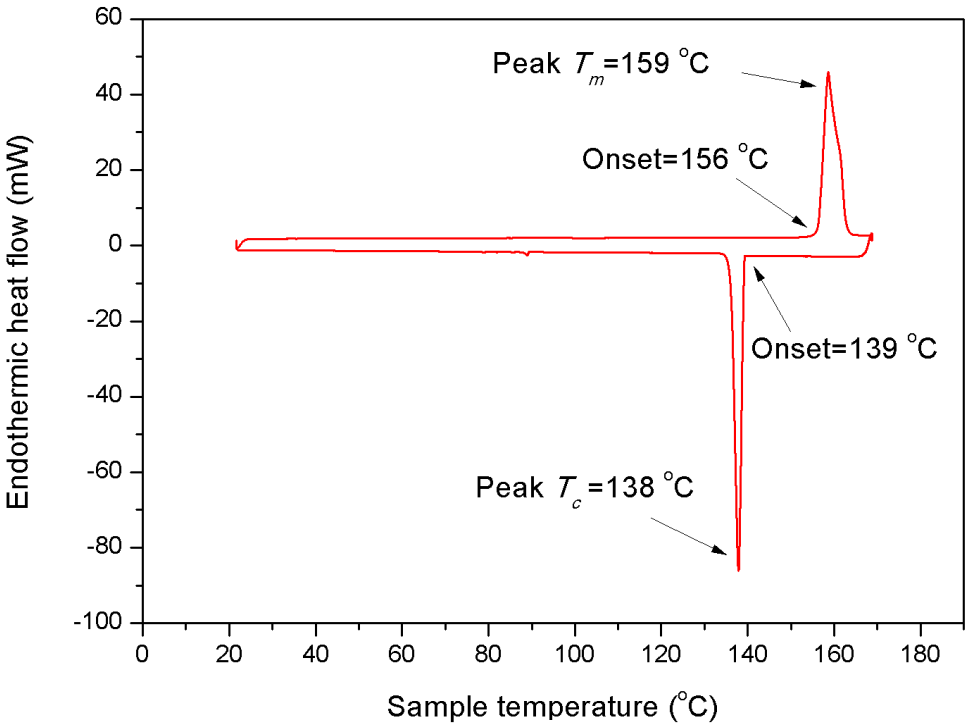
DMF solvent. DOX25 was still transparent after 90 days storage, and no precipitations or visible particles were observed (see Figure 4-2(d)), which indicated the dioxane solvent is more stable for polymerisation at room temperature. Therefore, all the reactive inks were freshly prepared and checked before printing.

4.2. Printability Assessment of Hot-melt Inks

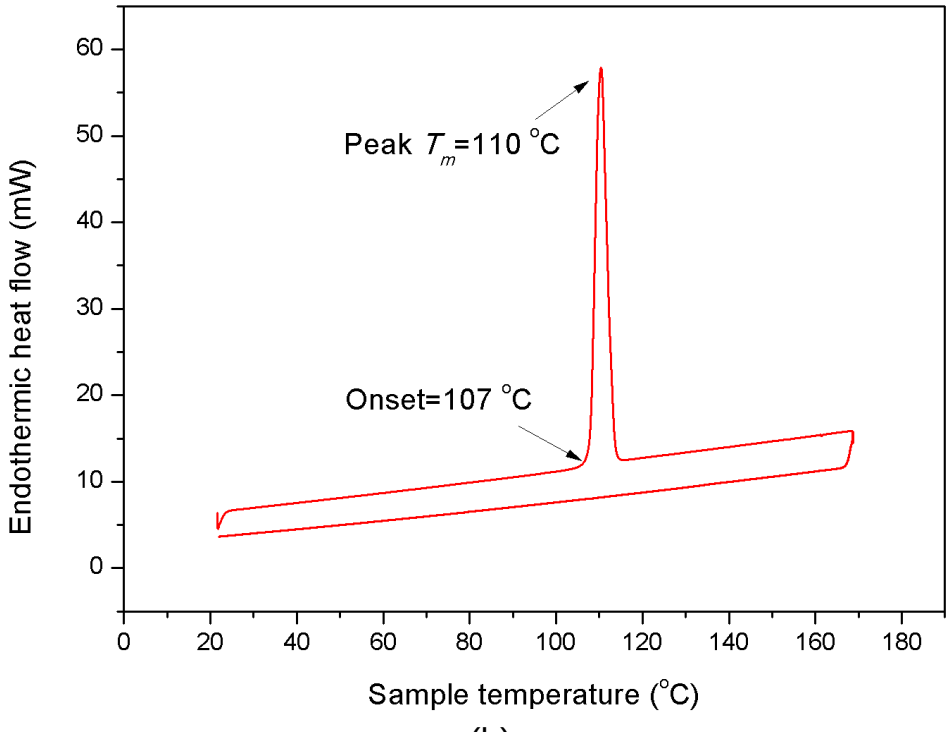
The critical factors for the printing assembly is the melting behaviour of the monomers, which was determined by DSC, the rheometer and the surface tension configuration. The physical characteristics above were surveyed and the detailed information on each characterisation is presented in the following sections.

4.2.1. Melt Behaviour of BPA and BMSC

One thermal cycle comprising heating and cooling at 10 ºC/min from room temperature to 170 ºC was performed for both monomers following the standard endothermic test method (ASTM E794-06). The results were shown in Figure 4-3 (a). BPA started phase change from 156 ºC and its peak corresponding to the melt point T_m was identified as 159 ºC. In the cooling cycle, crystallisation occurred at 138 ºC; whereas BMSC as shown in Figure 4-3 (b) exhibited melting behaviour at 110 ºC without crystallisation being observed upon cooling at the rate of 10 ºC/min.



(a)



(b)

Figure 4-3: Thermal analysis results of BPA (a) and BMSC (b) by DSC

The main purpose of the DSC thermal analysis was to determine the exact melting point for BPA and BMSC. Considering the temperature operability in terms of the upper limit, Océ CrystalPoint^{TM} was identified as a potentially feasible piezoelectric printhead for its temperature tolerance up to 170 ºC. However, the rheological properties of BPA and BMSC were to be further investigated to determine the applicability of Océ CrystalPoint^{TM} printheads.

4.2.2. Viscosity of BPA and BMSC

Figure 4-4 showed the result of viscosity analysis of BPA. It was clear that the viscosity of BPA in melt state (160 ºC) was around 8.5 cP (1 mPa·s=1 cP) at shear rate of 1000 s^{-1}. A slight decrease of viscosity can be seen when temperature rose to 165 and 170 ºC (6.8 and 6.0 cP, respectively), which indicated the printable hot melt fluid with a piezoelectric head that had temperature tolerance up to 170 ºC from 160 ºC.

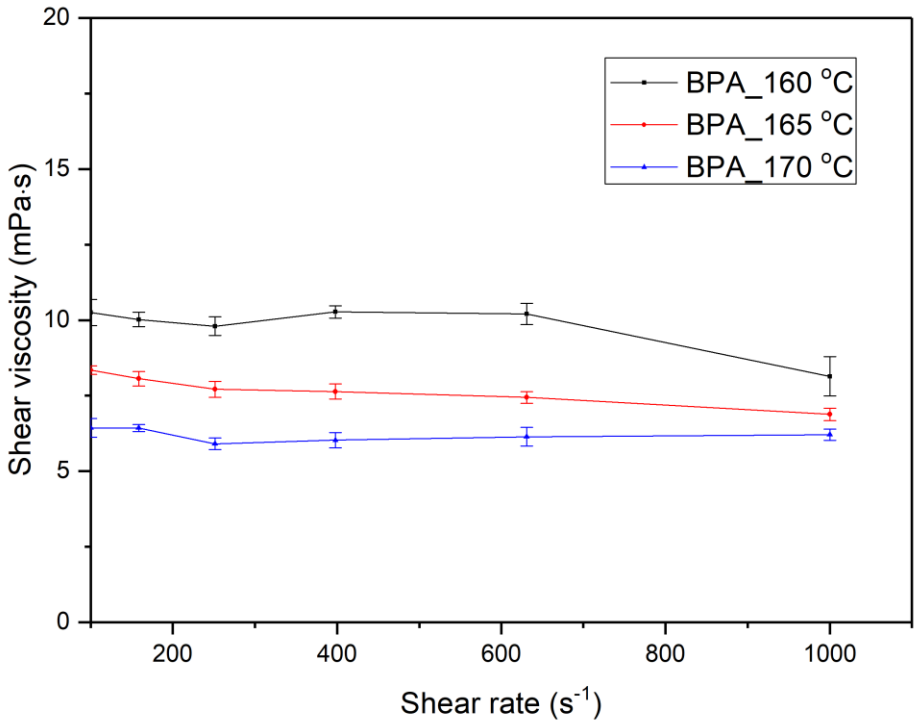


Figure 4-4: Viscosity for pure BPA monomer between 160 and 170 ºC (average ± standard deviation, n=5)

Figure 4-5 presents the viscosity measurement results for BMSC. At 120 ºC, the viscosity fell to below 20 cP when the shear rate increased to 350 s^{-1} and afterwards it became steady at 15.7 cP. It is within expectation that low molecular weight monomers usually have relatively low viscosity. For inkjet printing, 10 ºC beyond the melting point is a normal practice to avoid nozzle clogging due to solidification on the nozzle plate, although a reduction of viscosity as temperature increase was trivial to determine from the graph. Therefore, it was anticipated that 120 ºC would be a suitable jetting temperature for BMSC, provided that it was within the print head heating limit.

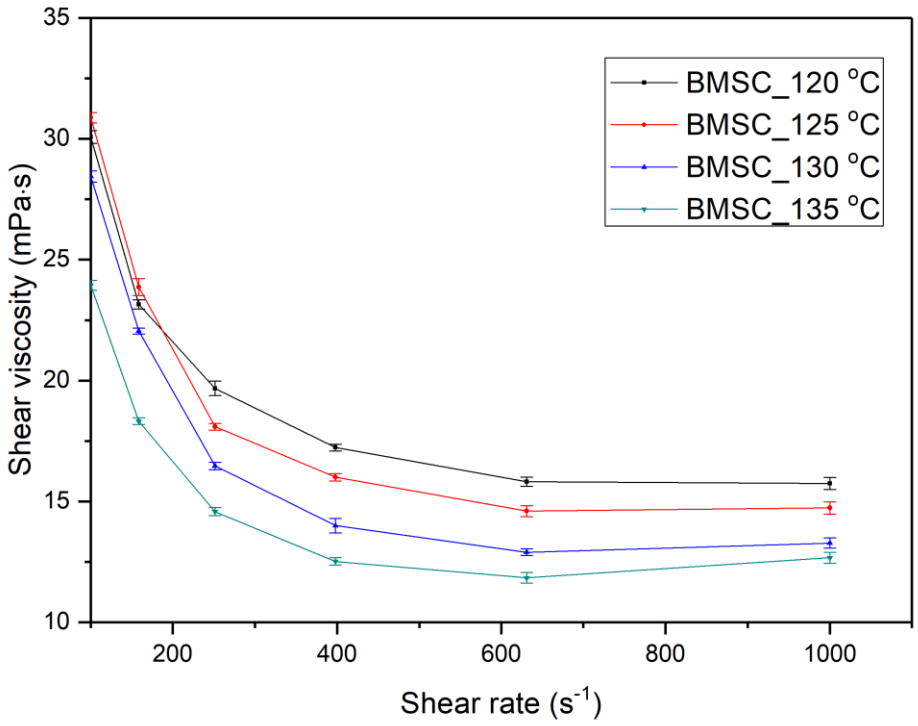


Figure 4-5: Viscosity for pure BMSC monomer between 120 and 135 ºC (average ± standard deviation, n=5)

4.2.3. Surface Tension of BPA and BMSC

Figure 4-6 showed the representative droplet shapes framed as a matter of time for BPA and BMSC, respectively. By using the Young-Laplace method, the shapes of pendant droplets had a good fit with the theoretical model with high consistency and minor deviations. The results showed that average

surface tension for BPA is 41.6 mN/m ± 1.83 and that for BMSC was 38.4 mN/m ± 0.60. The range of the surface tension results were consistent with the reported successful printing cases in the literature (59). Due to a lack of precise temperature measurement when the droplets are formed on the needle tip, however, this method only can only be considered an approximation. The effect of surface tension on droplet formation was expected to be tuned by jetting voltage and waveforms and further investigation would be carried out in the jetting phase of the research.

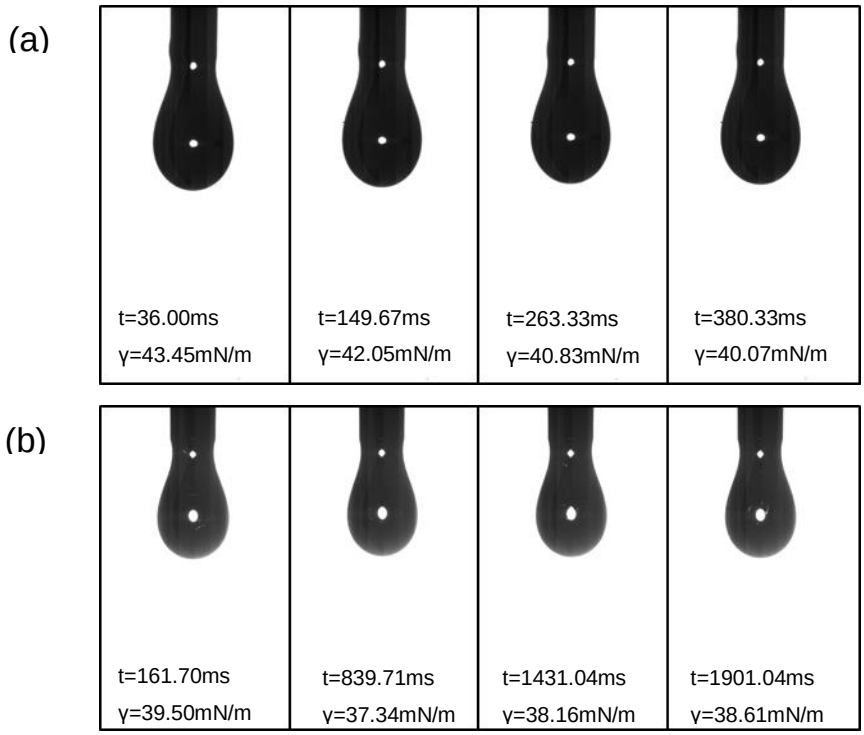


Figure 4-6: Pendant drops of (a) BPA and (b) BMSC captured by high speed camera (3000 fps, 1/50000 second, 1024×1024 pixels)

4.2.4. Printability Assessment for Molten BPA and BMSC

It was noted that BPA only became sufficiently molten beyond 160 ºC which was approaching the Curie temperature of the piezo-ceramics according to the Océ printhead manufacturer, where the performance and stability of the printhead between 160 and 170 ºC had not been studied. In Table 4-2, it was evident that as temperature varied, all printing indicators were within the suggested printable range ($1<Z<10$) as an empirical reference. It had been

reported that the maximum allowable frequency for quality inkjet printing had a linear relationship with the Z number (63). It was possibly useful when determining the jetting frequency and print speed for the droplet formation. However, the droplet formation behaviour was intrinsically very complex and generally influenced by the system's response to the pressure actuation. For stable drop formation and deposition, there are not only functions of fluid properties, but also the environment effect, printhead mechanical design and the compatibility of constituent materials with inks, thus affect droplet formation behaviour. Practically, each monomer should correspond to specific optimised printing conditions.

Table 4-2: Summary of physical properties of BPA and BMSC at various processing temperature beyond the melting point and theoretical printability assessment

Monomer	Process Temperature (ºC)	Viscosity at 1000 s^{-1} (cP)	Surface Tension (mN/m) [a]	Density (g/cm^3)	Nozzle diameter (µm)	*Z* number
BPA	160	9.5	41.6	1.15	40	4.60
	165	6.8	41.6			6.43
	170 [b]	6.0	41.6			7.29
BMSC	120 [c]	15.7	38.4	1.17	40	2.70
	125	14.7	38.4			2.88
	130	13.3	38.4			3.19

a. Assumed the temperature effect on surface is negligible

b. Suggested temperature upper limit of CrystalPoint™

c. An increase of 10 ºC beyond a nominal melting point is applicable as the nominal working temperature of CrystalPoint™ is 130 ºC.

4.3. Characterisation of Jetting Mixture

The idea of jetting the mixture of BPA and BMSC stemmed from the slow reaction dynamics of melt polymerisation. It was expected that within a short retention time of the hot-melt mixture in the ink channel, the hot-melt reactive

mixture of two monomers had limited polymerization so as to remain as a printable fluid (with low viscosity), then that the further polymerisation could be controlled after deposition on a substrate with higher temperature. If this concept was valid, the drop-on-drop mixing could be neglected with the main consideration being the change in rheological property after mixing two monomers. Further demonstration was assisted by the analysis of FT-IR spectrum of the corresponding polycarbonate obtained from bulk polymerisation.

4.3.1. Rheological Behaviour of Mixture

It has been reported that melt polymerisation starts immediately when two monomers melt and mix, even without catalyst (130). Here, there was a distinct change in the shear viscosity when the monomers were melted and mixed as shown in Figure 4-7.

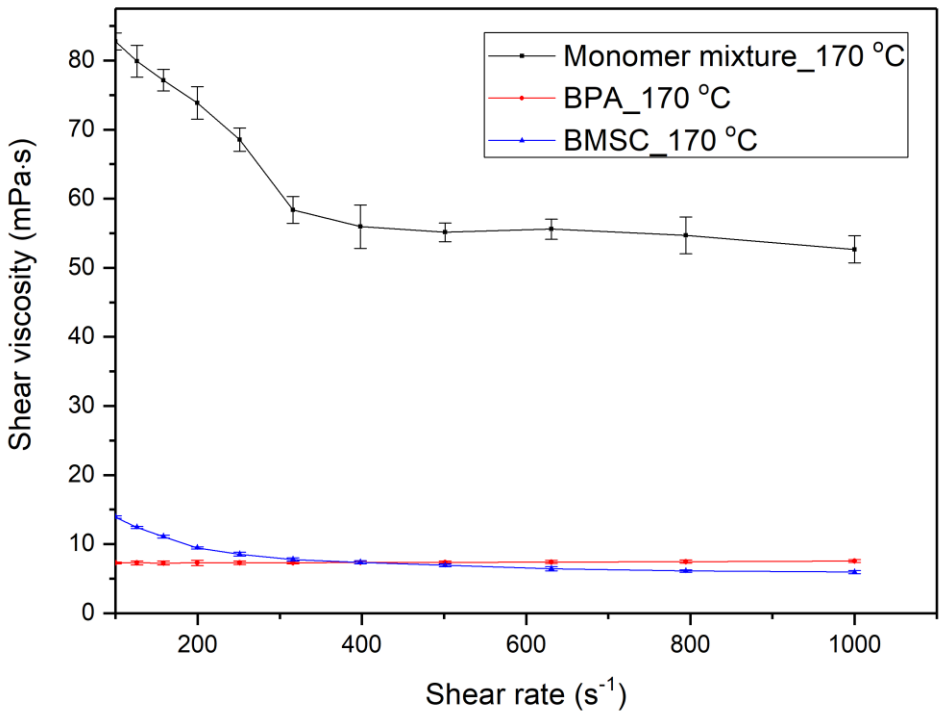


Figure 4-7: Comparison of shear viscosity for BPA, BMSC and their mixture upon melting (average ± standard deviation, n=5)

The mixture exhibited a viscosity up to 83 cP initially when the shear rate was 100 s^{-1}, and then gradually decreased to 53 cP at shear rate of 1000 s^{-1}. When compared to the viscosity of the pure monomers at the same temperature, the viscosity of the monomer mixture was dramatically higher which resulted from the production of BPA-PC oligomers which had molecular chain entanglement to increase the shear viscosity. The significant growth in the viscosity may lead to the failure of droplet ejection due to excess viscous dissipation of applied pressure stimulus. With the course of reaction time, the molecular weight of oligomers was expected to increase continuously. A possible consequence could be non-jettable materials in the channel block of the printhead due to constantly increased viscosity. Another observation during the melting of the mixture *in-situ* on the rheometer was the smell of methyl salicylate, indicating the formation of by-product that may also contributed to the viscosity change.

4.3.2. Bulk Polymerisation of BPA and BMSC

To study the relationship between degree of reaction and reaction time, bulk polymerisation in batch mode at 170 ºC was conducted. In a glass vial, 0.01 mol of BPA (~0.8423g) was mixed with 0.0102 mol of BMSC (~0.5708g) with aqueous 0.1 mol/L NaOH solution in a ratio of 1×10^{-3} mol/mol BPA. The polymerisation of the same composition without the catalyst was carried out as comparison. The final sample appearance was presented in Figure 4-8.

As seen in Figure 4-8, samples (a) and (d) were solely the mixture upon melting and heating that was terminated when the solid mixture becomes liquid. The catalyst had significant effects on accelerating the reaction as sample (d) turned turbid. Without catalyst, there was no evident difference on the reaction with duration of 1 hour and 2 hours, where a yellowish by-product was observed in the viscous mixture. By adding the catalyst, the effect was manifest in sample (d) to (f) that the reaction mixture was discoloured to golden yellowish over time. The coloured product was probably methyl

salicylate mixed with oxidisation product of monomers such as quinone. Further experiments were needed as future work to find out the composition of the product.

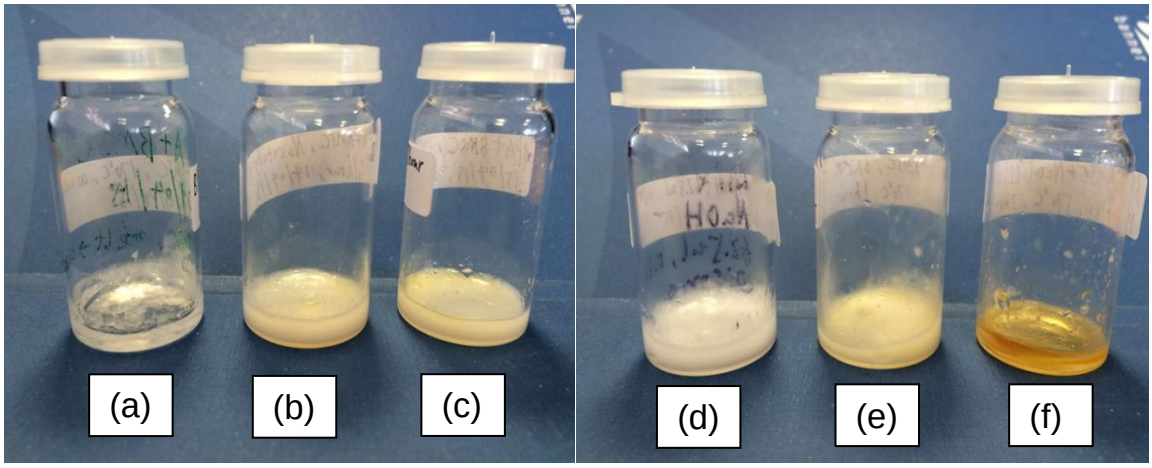


Figure 4-8: Bulk polymerisation for BPA (~0.8423g) and BMSC (~0.5708g) in a 170 ºC oil bath: 3 samples on the left are mixed without aqueous NaOH; 3 samples on the right are mixed with 62.5 µL 0.1 mol/L aqueous NaOH. (a) (d): reacted as melt for comparison; (b) (e): reacted for 1 hour; (c) (f): reacted for 2 hours

4.3.3. Interpretation of FT-IR Spectrum for Bulk Polymerisation

FT-IR in ATR mode was performed to trace the oligomerisation in the sample produced from bulk polymerisation. All the spectra were normalized against the peak at 1080 cm^{-1} which was a stationary C-C-C bending on the backbone structure of BPA throughout the chemical reaction (160). As presented in Figure 4-9, the FT-IR spectra for the polymerisation without catalyst showed a relatively broad peak between 2900-3400 cm^{-1}, which was attributed to O-H groups bonded on the benzene ring. The O-H groups were always in the 1,4-disubstituted aromatic ring position so no chemical structure change could be traced. There was aromatic C-H stretching overlapped with the O-H band at 2950 cm^{-1}. A C-O stretch was identified at 1220 cm^{-1} indicating the peak production of oligomer with a phenyl-carbonate endgroup at 1 hour and subsequently decreased as it was shifting to the equilibrium after 2 hours, which was the same as reported in the literature (129). However, C-O

stretching was in the 'finger print' region of the spectrum and so it was relatively uncertain to ascertain its dynamic change. Although it was not possible to uniquely assign a carbonyl group to PC, there was a peak region from 1720 to 1800 cm^{-1} that indicated the oligomerisation as shown in the sub-diagram. As the C=O stretching at 1720 cm^{-1} in the simple carbonate ester (BMSC) would be shifted to 1770 cm^{-1} in the BPA-PC oligomer or long-chain polymer, the formation of BPA-PC oligomers could be deducted from the increase in the intensity at 1770 cm^{-1} and decrease at 1720 cm^{-1} (161).

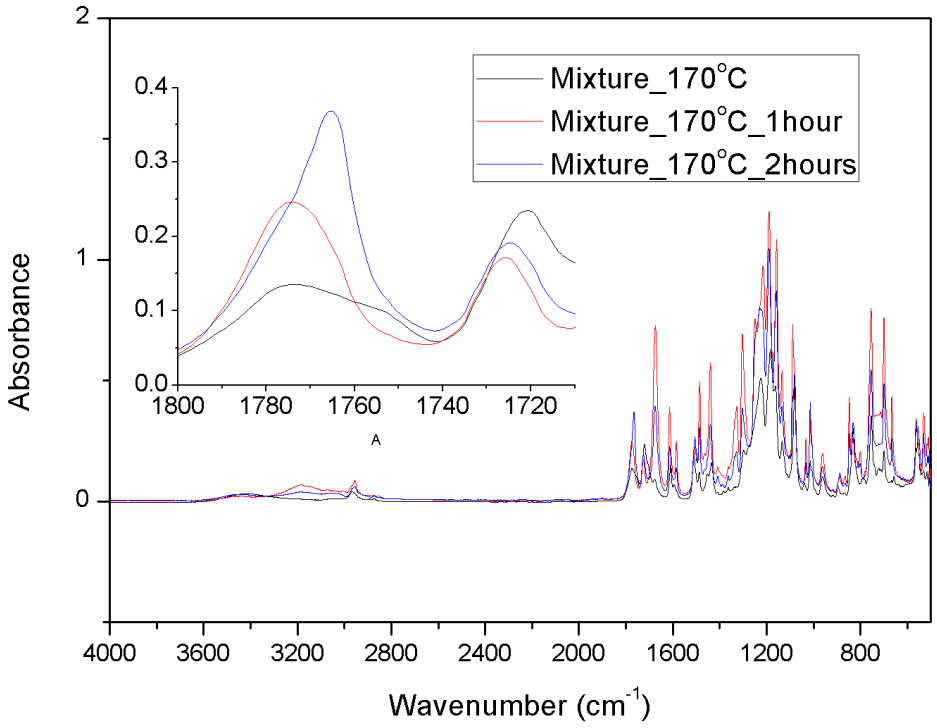


Figure 4-9: FT-IR spectrum for bulk polymerisation of BPA and BMSC without catalyst

The polymerisation with 1×10^{-3} mol NaOH / mol of BPA was also performed. The result was shown in Figure 4-10. Although the characteristic peaks identified in Figure 4-10 could be still distinguished, the major difference after adding basic catalyst from the spectrum was that effect of reaction time becomes minor. The milder shift in the absorption intensity, which can be seen from the larger scaled sub-diagram, indicated a more limited polymerisation in a batch mode. A possible explanation would be that the trapped methyl

salicylate in the reaction mixture would suppress the forward equilibrium. The results have provided evidence that jetting the mixture with a single piezoelectric printhead might be impractical in considerations of polymerisation to have viscous mixture before drop ejection. Using FT-IR spectroscopic analysis it was difficult to quantify the degree of oligomerisation and further study on the melt polymerisation would be recommended by other means of analytical measurement, such as HPLC or NMR.

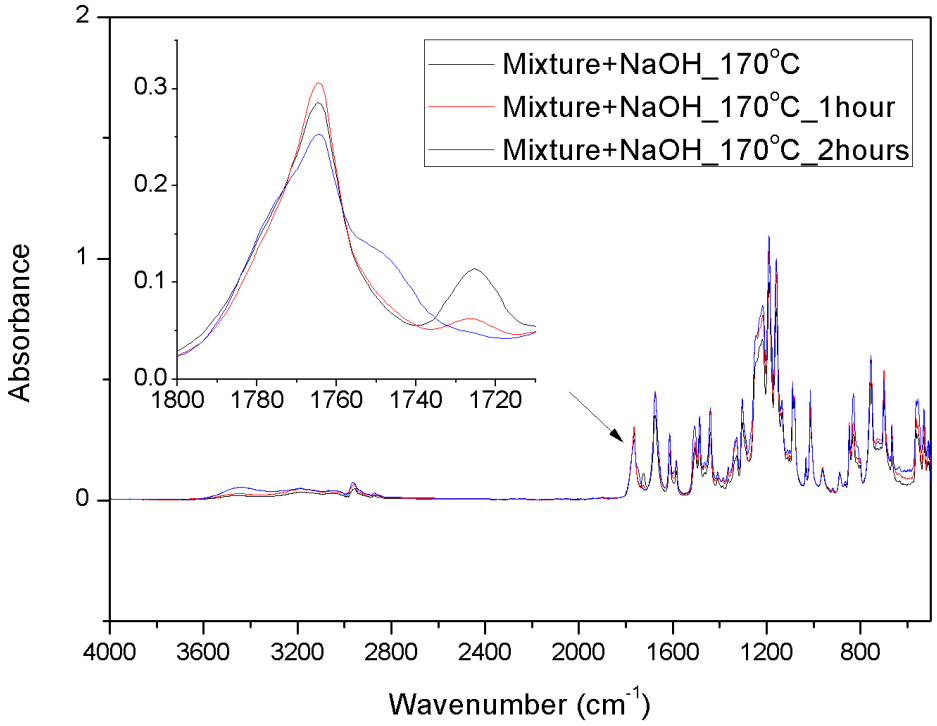
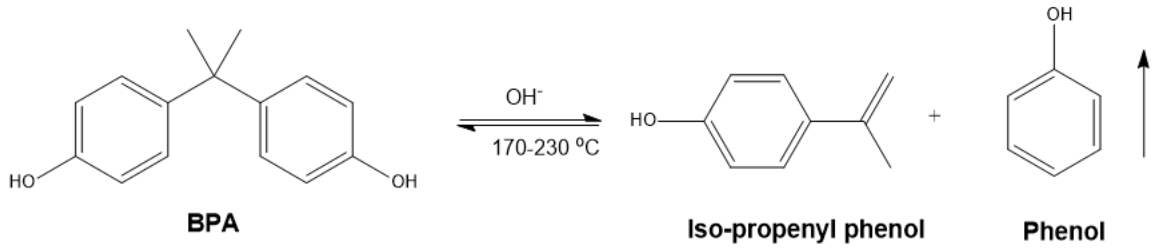


Figure 4-10: FT-IR spectra for bulk polymerisation of BPA and BMSC with catalyst

4.4. Thermal Stability of Hot-melt Inks

Although the melt polymerisation of BPA-PC avoids the use of phosgene and chlorinated solvents when compared to interfacial polymerisation, it has been reported that side reactions such as branching, cross-linking and other types due to an elevated temperature of 150-300 ºC and long residence time will lead to discoloured and degraded products (162). The thermal instability of BPA in the presence of an alkali catalyst has also been found along with side

reactions (155). Low thermal stability was also found in other studies (163), and an example for alkaline cleavage of BPA is illustrated in Scheme 4-1. On the other hand, there is a dearth of information regarding the thermal stability of BMSC and its potential side reactions associated with an alkali catalyst. Therefore, the thermal instability of BPA and BMSC beyond their melting point needs to be explored considering their residence in the ink reservoir, where the degradation and discolouration of the product might take place causing a change of viscosity profile.



Scheme 4-1: Alkaline cleavage of BPA at elevated temperature at 170-230 ºC

4.4.1. Thermal Stability Study of Monomers

The step-growth polymerisation for BPA-PC first requires the base catalyst (i.e. NaOH) to react with the hydroxyl group on BPA to form diphenolate ion (164). The diphenolate ion will promote the transesterification. Consideration is also given, however, that the thermal stability of the diphenolate ion plays a role when residing in the ink reservoir. To investigate the effect of the residence time of the BPA at elevated temperature and the interaction of base with BPA on the thermal stability, 3 residence durations were chosen as 0 (cooled immediately as melt), 2 and 4 hours.

The results for the thermal stability of BPA were observed in Figure 4-11. The pure molten BPA with or without nitrogen protection in the vial did not change colour within 2 hours, indicating the relatively stable state of molten BPA. From Experiment (c), there was a strong discolouration of BPA when mixed with NaOH, which was intensified with the relatively long residence time. The

discolouration was alleviated in an air-free environment which can be seen from Experiment (d), indicating the discolouration in (c) was possibly due to degradation. Similar results were found in other work (123). A rearrangement of the Kolbe-Schmitt type (163) may take place in the presence of alkali species at high temperatures leading to discoloured and degraded products. Moreover, the rearrangement products from BPA are known to form branched and cross-linked PC chains which degrade the mechanical and optical properties of linear BPA-PC. From the results, it can be concluded that the alkali catalyst may degrade BPA at elevated temperature with a long residence time, where a series of reactions may take place. Therefore NaOH was not to be mixed with BPA to form a nucleophilic reactive mixture in the printhead ink reservoir, due to strong thermal effects in the molten state.

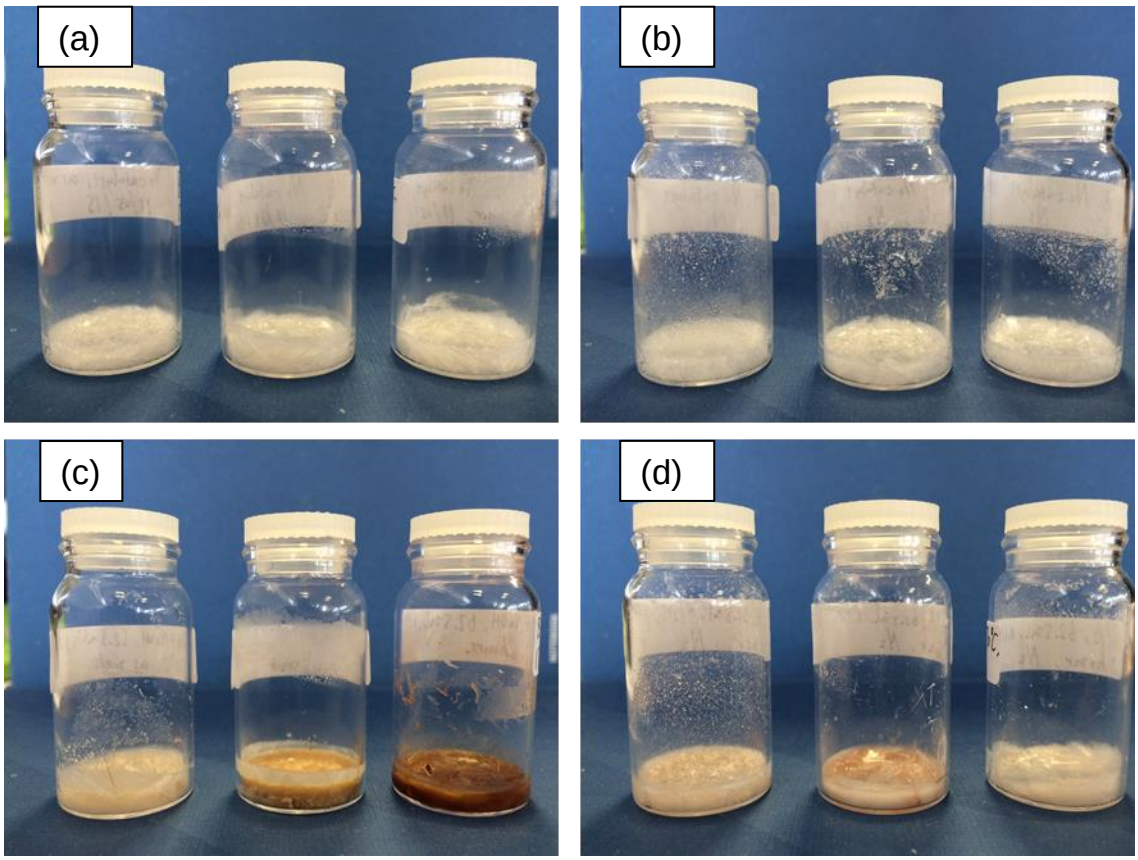


Figure 4-11: Results of thermal stability of BPA: (a) pure BPA; (b) pure BPA with nitrogen purge; (c) BPA with NaOH; (d) BPA with NaOH and nitrogen purge. From left to right in each set of experiment, the residence time is 0 hour (as melt), 2 hours and 4 hours, respectively. Temperature is kept at 170 ºC

The same experiments were conducted with BMSC and the results were shown in Figure 4-12, although adding an alkaline catalyst would not increase the electrophilicity of the carbon atom on the carbonyl group due to the nature of transesterification (164). It can be seen that there was no discolouration of the melt BMSC regarding the presence of nitrogen and NaOH. It had been reported that ortho-position substituents on the diaryl carbonate (i.e. $-COOCH_3$) would accelerate the hydrolysis of the carbonate ester group in the alkaline condition (165). The hydrolyzed products might not be sufficiently stable for inkjet printing and it might also affect the linear polymerisation for BPA-PC. Further experiments were to be carried out to detect alteration of rheological properties after the mild hydrolysis of BMSC with the moisture.

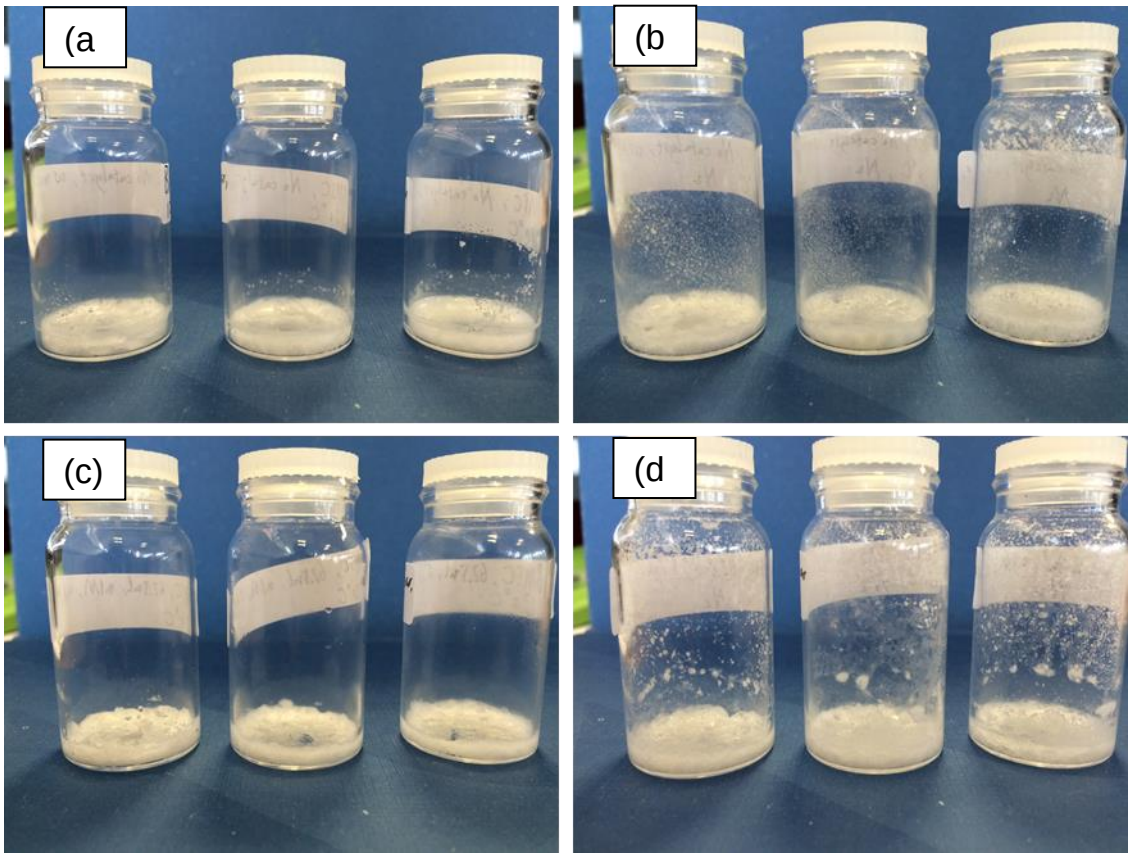


Figure 4-12: Results of thermal stability of BMSC: (a) pure BMSC; (b) pure BMSC with nitrogen purge; (c) BMSC with NaOH; (d) BMSC with NaOH and nitrogen purge. From left to right in each set of experiment, the residence time is 0 hour (as melt), 2 hours and 4 hours, respectively. Temperature is kept at 120 ºC.

4.5. Droplet Formation of Hot-melt BMSC

From the previous study of BPA and BMSC in terms of printability and thermal stability, it was concluded that, for the droplet formation of BMSC, Océ CrystalPoint Printhead's were suitable due to BMSC's relatively lower melting temperature and lower thermal effect. Research had shown that the melt polymerisation starts immediately when two monomers melt and mix evenly without a catalyst (130). Therefore, the droplet formation of pure hot-melt BMSC was carried out.

4.5.1. Droplet Formation Stability Observation

The droplet formation process was viewed with the stroboscopic camera with the ADA function in the software, which allowed the droplets to be viewed as a pseudo-sequence. The jetting frequency was set at 1 kHz to obtain a clear sequence, due to the limitation of the LED light exposure rate. A jetting experiment was carried out across different nozzles and the evolution of the droplet formation is as shown in Figure 4-13. The droplet formed a long filament before it ruptured from the nozzle plate at 70 μs. The filament behind the front head of the drop was about 350 μm long and had no tendency to recoil towards the head. From the elapsed time of 90 μs onwards, a transient droplet was observed attached to the tail and a continuous necking effect was seen. This indicated that the transient satellite was less likely to catch up with the primary drop due to the lower velocity and the secondary satellite might form before it impacted on the substrate. It could be seen that the default waveform needed to be optimized to achieve a better droplet formation where the transient satellites with enough velocity were able to consolidate with the main drop.

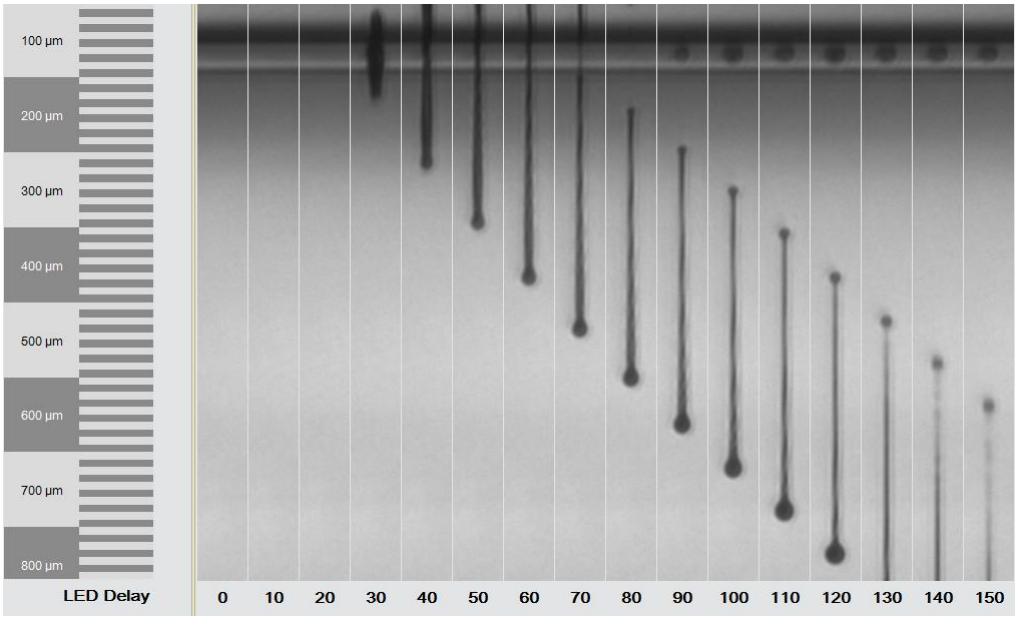


Figure 4-13: Jet experiment with BMSC at 1 kHz droplet ejection rate using single nozzle

4.5.2. Waveform Optimisation for Jetting Hot-melt BMSC

From the previous experiments of droplet formation for jetting hot-melt BMSC, it was evident that the default waveform used to actuate the jetting process could be optimised to achieve appropriate parameters. One of the most important criteria is the ligament behind the main droplet and break-up into small satellites. Moreover, the droplet volume is also an important factor considering the stoichiometric ratio control for BMSC with BPA. The velocity profile of the droplets with the jetting voltage was also investigated.

From the preliminary studies of the droplet ejection from 256 nozzles, only droplets from a few nozzles were found to experience misalignment from the vertical direction possibly due to the solidification and contamination on the nozzles. Therefore, several nozzles were selected to be focused on optimizing the different segments of the waveform. By holding the reference voltage, rise and fall time fixed at the default value, only varying the pulse width of a representative single nozzle was able to find the optimum value. With reference to Figure 4-14, a stroboscopic delay of 100 µs was chosen to ensure the entire droplet ligament had been detached from the nozzle and the

droplets formation with a pulse width from 3 to 20 μs was seen. When the pulse width was 3 μs or lower, separate droplets were observed in the sequence where ligaments did not exist behind the droplets. It could be explained by the fact that droplets were formed with small volumes due to insufficient time of pulse propagation in the ink channel. The small volumes also caused the deviation of droplet trajectory from vertical directions resulting from air flow in the environment. From 4 to 17 μs, a droplet velocity approximate to a parabola was observed. A maximum velocity exists at 9 μs pulse width and it was defined as ‘optimum’ according to the work by Bogy and Talke (65), where the droplet experienced less time of flight and less deviation. They quantitatively surveyed the correlation between drop velocity and pulse width, and similar results were found. The theoretical explanation behind this is that expansions and contractions of the channel will enhance or hamper the propagation of an acoustic pulse, which indicates the optimum enhancement of the droplet velocity due to acoustic resonance.

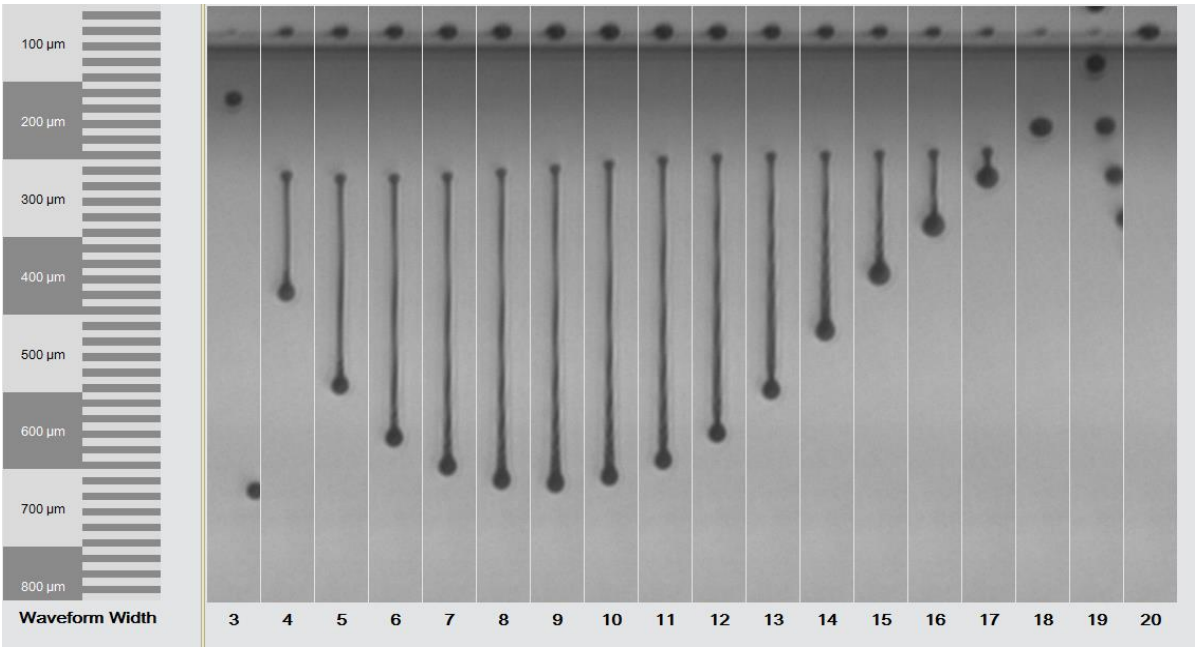
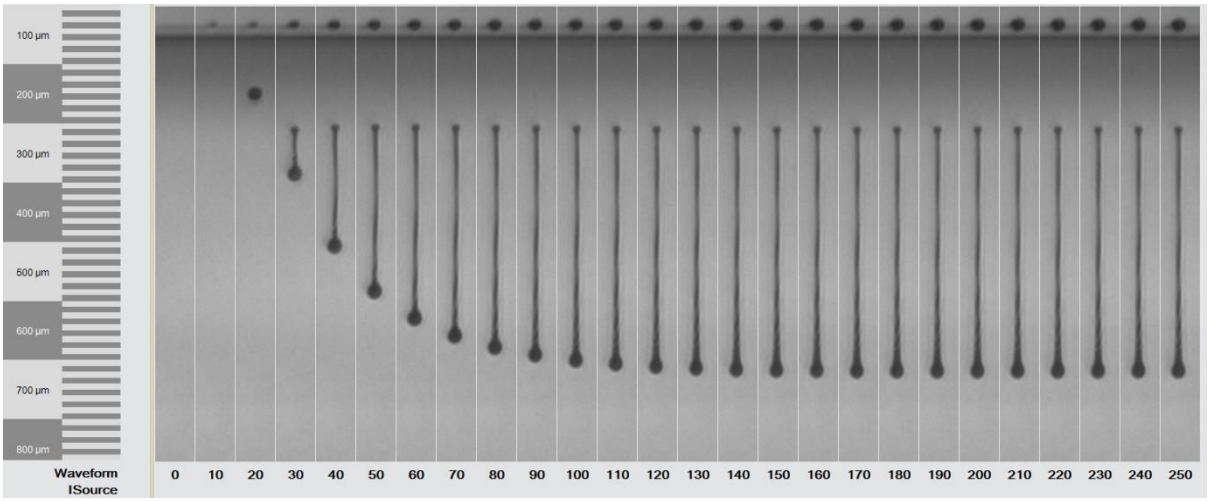
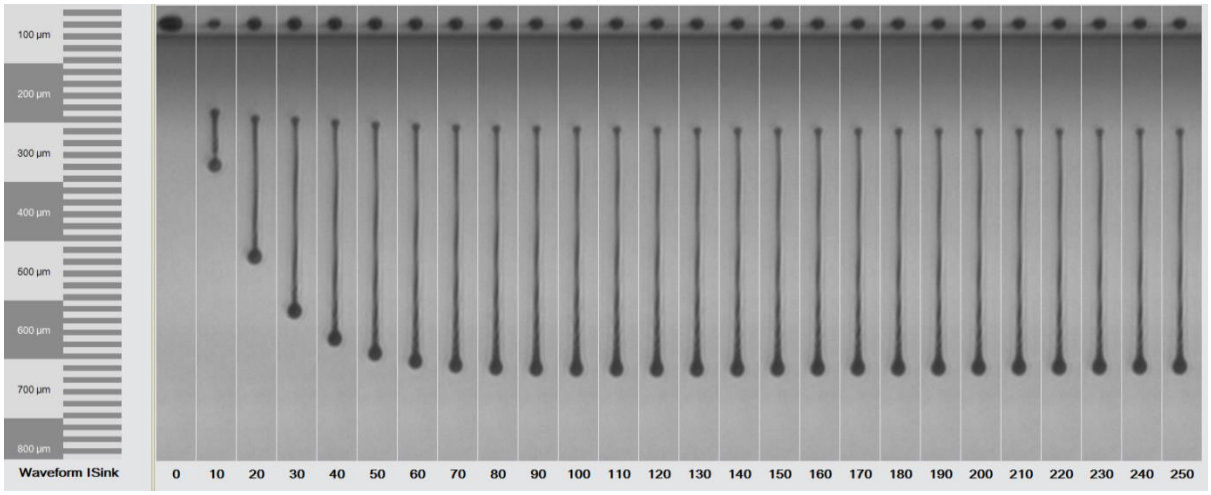


Figure 4-14: The effect of pulse width on the velocity of the droplets (unit of pulse width: μs)

The effect or rising and falling slopes (source current and sink current, i.e. Isource and Isink) were examined using the same strategy by varying them respectively at the fixed optimum pulse width as previously found. The whole range (0-250 dac units) of slopes was investigated and the increment of slopes is set at 10 dac units. From Figure 4-15 (a), the droplet velocity kept increasing with ascending rising slope until it reached a plateau from 130 dac units onwards. It satisfied the analysis which was undertaken by Bogy and Talke (65), that the rising slopes indicated the duration of introducing positive pressure disturbance to the ink channel to cause the initial expansion. In this case, the overall pulse width was the sum of rising time (t_R), dwell time (t_W) and fall time (t_F). The higher rising slope, i.e. less rise time, would have less effect on the optimal pulse width as it ramped up almost instantaneously. It was seen from 130 dac units onwards, the velocity of droplet remained insensitive to the rising slope and almost the same compared to the 'optimum' velocity found in Figure 4-14. The similar trend was also found in the falling slopes optimisation, from Figure 4-15 (b), that the velocity of the droplets remained steady when manipulating the slope greater than 80 dac units. It indicated less interference and that the most efficient droplet formation was expected when the slope was tuned at the travel times of the acoustic wave inside the ink channel.



(a)



(b)

Figure 4-15: Effect of the rising and falling slope (a and b, respectively) on the droplet formation of hot-melt BMSC (unit of ISource and ISink: µs)

4.5.3. Droplet Volume and Velocity Modulation

The previous waveform optimisation suggested a suitable range of overall pulse width including the rise and fall time to achieve a stable droplet formation. It was also important to know the droplet volume and velocity at fixed voltage amplitude in order to create stable and satellite-free droplets. It was also investigated by the drop camera for viewing the droplet evolution.

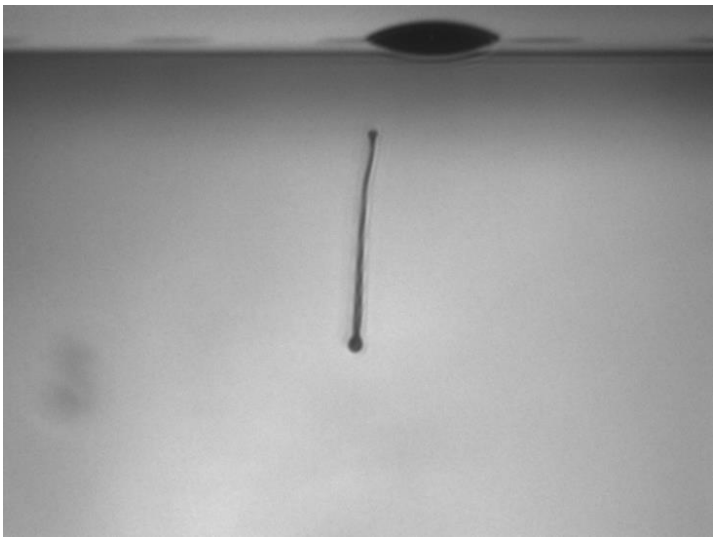


Figure 4-16: Trajectory error of droplet in flight at low voltage amplitude below 40 dac units

A preliminary experiment to modulate the droplet ejection by varying the voltage amplitude at fixed pulse width showed that low amplitude below 40 dac units (approx. 7.5V) would lead to droplet trajectory deviation in flight and create meniscus residue adjacent to the nozzle due to insufficient actuation. An example was shown in Figure 4-16. With time the ink would flow near to the nozzle and even block the neighbouring nozzles. It was also observed during the experiment that the nozzle instability occurred at this low range of voltage amplitude, without a successful droplet ejected out from the nozzle. This was due to the insufficient kinetic energy to overcome the viscous energy in the channel and surface energy outside the nozzle. Therefore the low voltage amplitude was not favourable to the droplet formation process and eliminated from the focus in this study.

The droplet velocity and volume were measured at different voltage amplitude using the droplet analysis function. Figure 4-17 showed the droplet volume and velocity against the voltage amplitude. It was evident that drop volumes increased almost linearly with the jetting voltage amplitude from 7.5 pL at 40 dac units (appx.7.5V) to 18 pL at 150 dac units (appx. 28.2 V). The drop volume at the voltage amplitude greater than 150 dac units were omitted here for the reason that the head of the droplet is missing from the droplet analysis picture due to a long ligament behind the head of the droplet. The error margin in the measurement resulted from the magnification of the picture. The limitation in the resolution may suggest the measurement of the volume as indication within the error range. Likewise, the droplet velocity also had a linear trend with voltage variation, ranging from 1 m/s to 9.5 m/s seen from Figure 4-17. The same results were also found by Gan *et al.* (166) that the droplet volume increased about 50-60% when enhancing the amplitude from 30 to 40V. A slight non-linearity below 90 dac units was observed, possibly due to the partial retainment of the drops on the nozzle plate and consequently lower kinetic energy of the drops. As suggested by the manufacturer, a nominal velocity of 6 to 9 m/s was able to give a roughly

optimum droplet velocity although it was also dependent on ink types, which corresponded to the voltage of 100-140 dac units for BMSC.

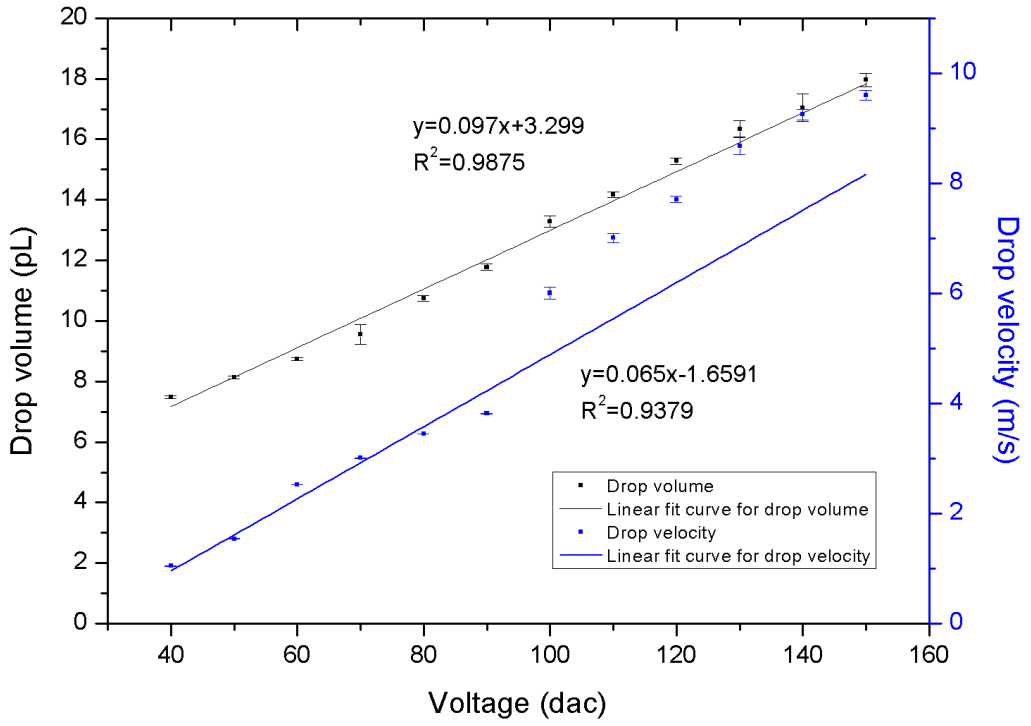


Figure 4-17: The BMSC drop volume and velocity variation with the reference jetting voltage amplitude (average ± standard deviation, n=5)

By increasing the voltage amplitude, the stronger actuation led to greater deformation of the piezoceramics. It consequently resulted in the amplification of the acoustic wave which was able to eject a droplet with greater volume. The enhanced acoustic wave provided higher kinetic energy for droplets which were measured by droplet velocity. However, a droplet with greater volume would more easily form satellite droplets and the long tail would experience more interference from the air flow. It was seen from Figure 4-18 that the length of the tail behind the head of the droplet was greater with the higher voltage amplitude. It was also noted that the droplets ejected at 70 to 90 dac units formed a satellite droplet which did not break up from the primary drop. They finally recombined with the primary droplets to form a single droplet.

Although the droplets formed above 100 dac units had acceptable velocity range as previously studied, they formed a significantly long tail and necking was observed which possibly suggested the break-up of the satellite from the main droplets. The droplet deposition was to be studied to further investigate the effect of the long ligament.

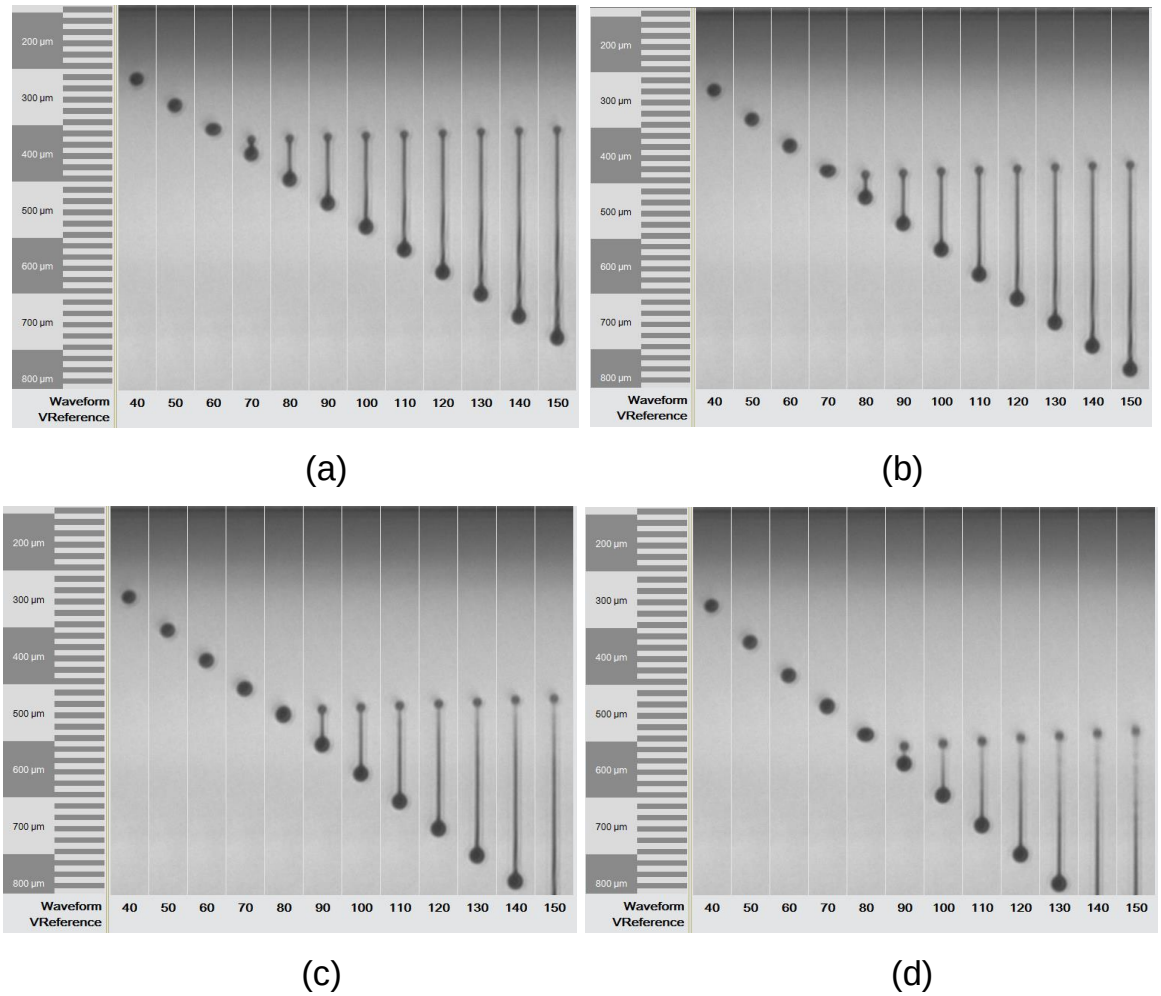


Figure 4-18: Droplet evolution of hot-melt BMSC at different voltage amplitude with a strobe delay at (a) 110 µs; (b) 120 µs; (c) 130 µs; (d) 140 µs

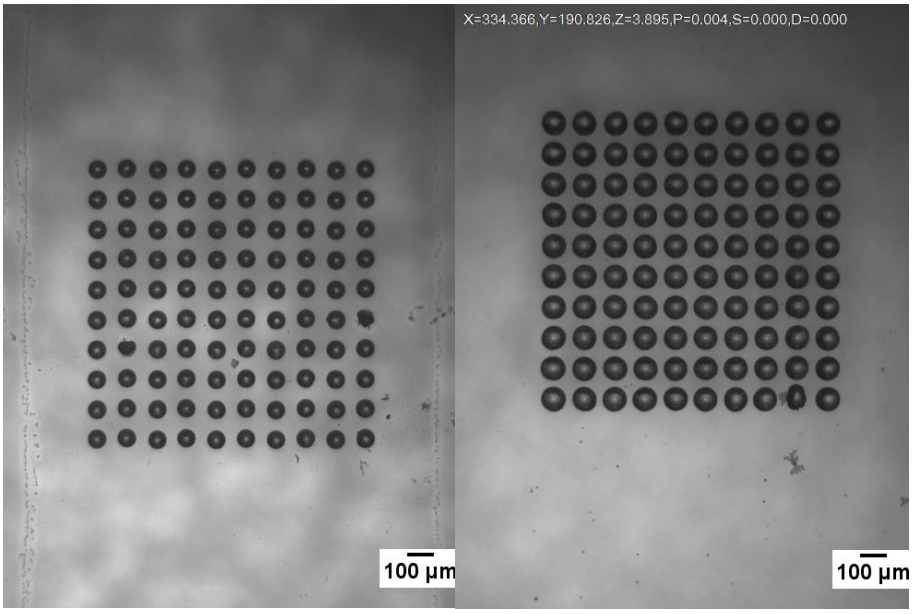
4.6. Ink Deposition of Hot-melt BMSC

From the previous study of droplet formation process of hot-melt BMSC, the long ligament of the droplets was observed at moderate voltage amplitudes. Although it had been reported (70) that by introducing a second trapezium

pulse after the first one, a part of residual acoustic oscillations could be significantly damped and the satellites could be suppressed, the waveform design embedded in the electronic drive of the Océ printheads limited creating a bipolar waveform. Therefore, the hot-melt BMSC were printed on a pre-cleaned glass slide to investigate the effect of a long ligament on the deposition of the ink.

4.6.1. Single Droplet Deposition of Hot-melt BMSC

A single droplet pattern (1×1 mm and 254 dpi) was printed on a pre-cleaned glass slide with the voltage amplitude between 100 and 150 dac units to investigate the deposition performance and the droplet size on the substrate. The printing distance was set at 1 mm from the nozzle plate to the surface of the substrate and the temperature of the substrate was maintained at 25 ºC.



(a) (b)

Figure 4-19: Droplet size on glass slide varied with voltage amplitude: (a) 120; (b) 150 dac units

From the printing results, there was no secondary droplet next to the main droplet, suggesting that the long ligament in flight emerged with the main droplet on impact and the angle of the ligament did not deviate in the printing

distance of 1 mm. Two examples of a single droplet deposited on the glass were shown in Figure 4-19. The droplet on the substrate was analysed using ImageJ to calculate the average droplet size and aspect ratio which were summarized in Table 4-3 showing the droplet size variation with the voltage amplitude. It was seen that the droplet deposited on the glass slide increased in size from 68.69 to 79.42 μm with voltage amplitude increasing from 100 to 150 dac units (approx. 18.8 to 28.2 V). The results were consistent with the previous results of droplet volume measurement, where the greater volume spread out on the substrate with a larger size at the same contact angle. The aspect ratio indicated that the roundness of single droplet was approaching unity due to the uniform surface of the substrate.

Table 4-3: BMSC droplet size variation on the glass with the voltage amplitude of waveform (average ± standard deviation, n=5)

Voltage (dac unit)	100	110	120	130	140	150
Droplet size (μm)	68.69±3.57	69.12±3.89	70.64±2.96	73.41±2.12	75.84±2.56	79.42±1.29
Aspect ratio	1.02±0.01	1.04±0.02	1.03±0.03	1.02±0.01	1.02±0.02	1.02±0.01

4.6.2. Film Printing of Hot-melt BMSC

The hot-melt BMSC was printed as 1 × 1 mm films on the glass slide and polyimide film substrates. Both substrates were sprayed and rinsed with deionized water and dried with the heat blower. The substrate temperature was set at 25 ºC. The waveform amplitude was set at 120 dac units (approx.22.6 V) and the droplet velocity was fixed at 7.71 m/s as previously measured. It was found in the early experiments that with a droplet spacing of

40 µm, a continuous film could be printed on both substrates. On the glass slides, the edge of the film was found to recede towards the centre and to finally become the single liquid agglomerate with a round shape within about 5 min. The results were shown in Figure 4-20. It indicated the relatively low surface energy of the glass surface compared to the hot-melt BMSC and poor adhesion of the hot-melt BMSC on the glass slide. It was noticed that the film did not solidify immediately on contact with the substrate and during the receding of the contact angle, the volume of the liquid in the unit area increased so it further lowered the solidification rate. The low solidification rate was suspected to be due to moisture in the ambient environment, as the droplet ligament in flight was likely to absorb moisture. Since the contact line between hot-melt BMSC and the glass slide was not able to pin, further printing was carried out on a polyimide substrate.

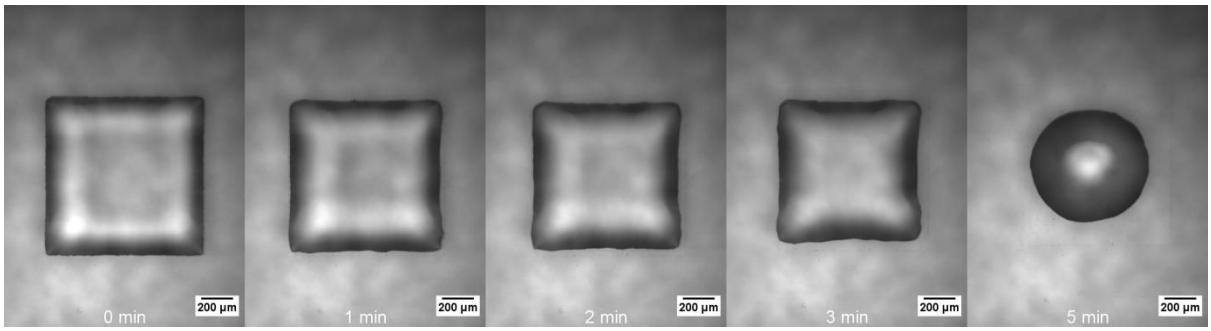
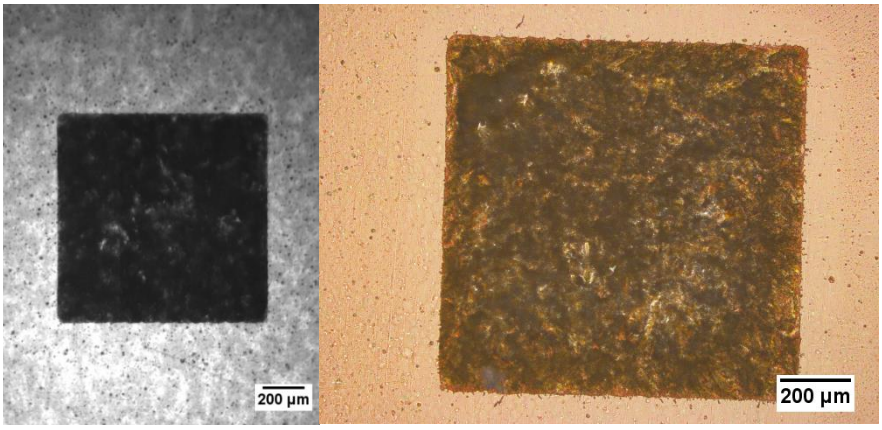


Figure 4-20: Optical images of hot-melt BMSC films (1 × 1 mm) printed on glass slide at 25 ºC showing receding of the film within 5 mins (0 to 5 min from left to right)

The hot-melt BMSC solidified upon impact and no movement of the film edges was observed as shown in Figure 4-21 (a). From the results in Figure 4-21 (b), there was no waviness across the film which indicates that each swath printed had merged before it solidified. The hot-melt BPA was expected to be printed on the layer of BMSC prior to polymerisation.



(a) (b)

Figure 4-21: Optical images of hot-melt BMSC films (1 × 1 mm) printed on polyimide (Kapton) substrate at 25 ºC (a) camera view; (b) microscopic view

The surface profiling results are presented in Figure 4-22. There was a portion of the film on the edge spalling off the substrate during handling which suggested poor adhesion between the BMSC and Kapton substrate. The spatial height variation indicated that further development to improve surface homogeneity is needed. The average thickness of the film was estimated to be approximately 15 µm from profiles in both X and Y directions.

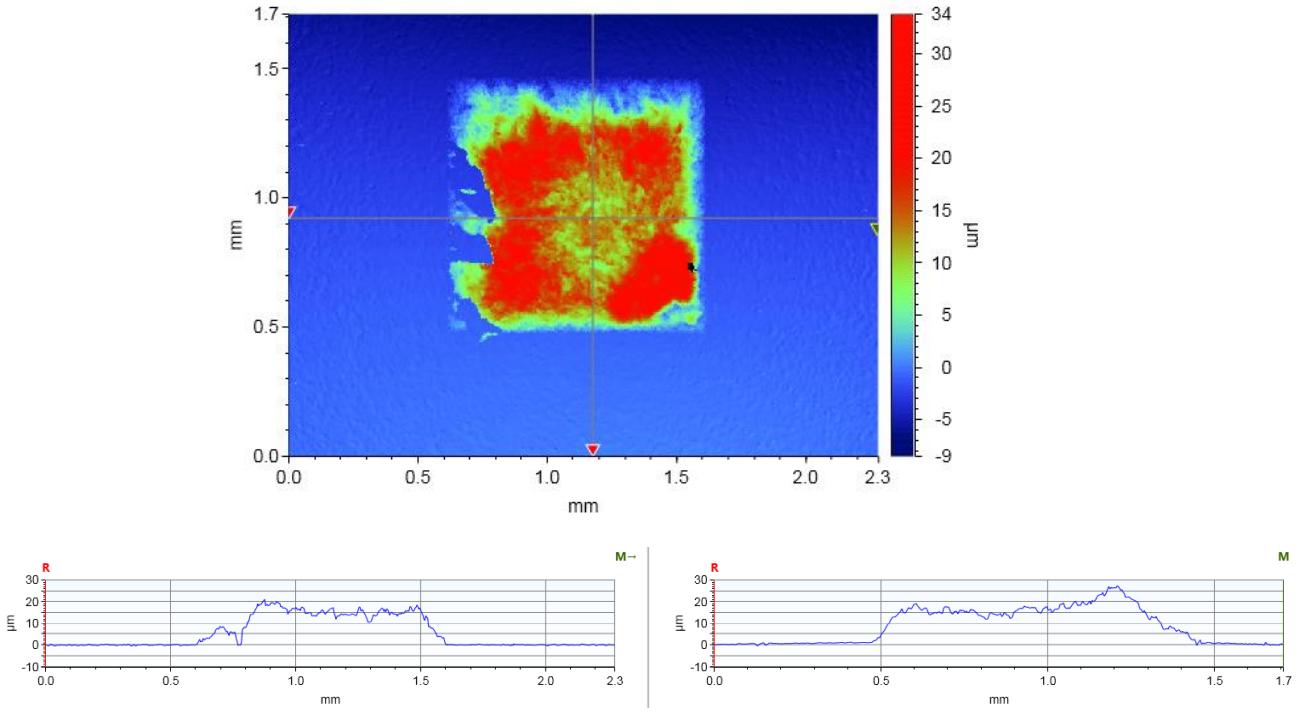


Figure 4-22: Results of white light surface of printed hot-melt BMSC film (1 × 1 mm) on polyimide (Kapton) substrate (X and Y axis profiles)

4.7. Droplet Formation of Hot-melt BPA

To achieve the two-component reactive inkjet printing, the droplet formation of hot-melt BPA was assessed using an Océ CrystalPoint printhead on a Pixdro LP50 printing system.

4.7.1. Droplet Formation Optimisation with Waveform

The initial experiments of jetting BPA revealed its printability at 170 ºC with the same waveform optimized for hot-melt BMSC. During the jetting process, however, satellites were observed to break up from the liquid column as shown in Figure 4-23. It was due to the weak damping effect of acoustic oscillation for the low viscosity molten BPA (6.9 cP at 170 ºC). Wetting on the nozzle plate was also observed at both low frequency (1 kHz) and high frequency (5 kHz).

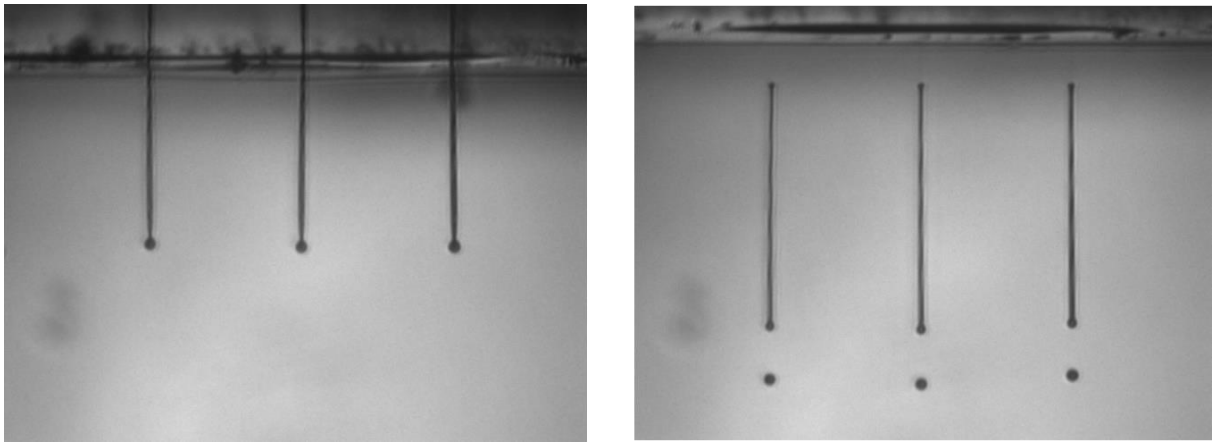
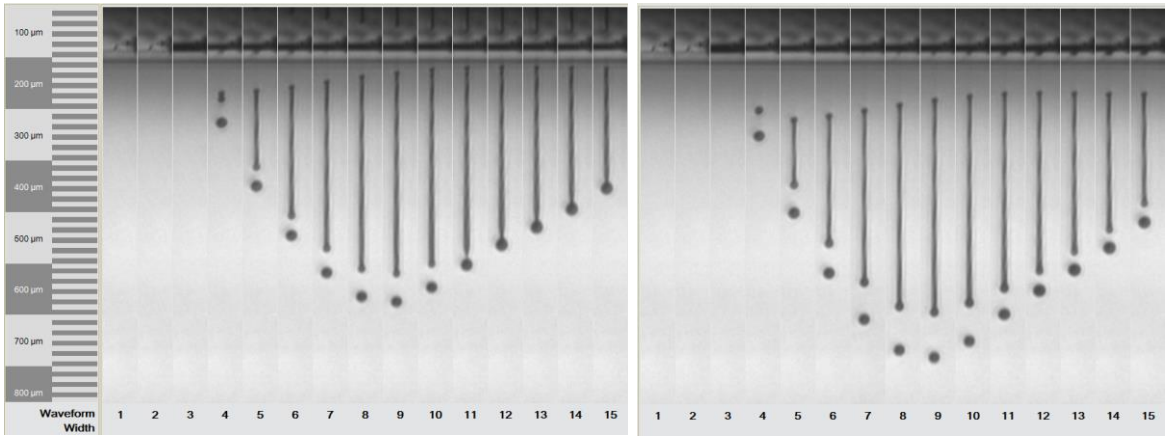


Figure 4-23: Satellite effect of hot-melt BPA and its wetting area development on the nozzle plate

To stabilize the droplet formation, the waveform for BPA needed to be specifically tuned. A nozzle which had shown consistent jetting performance during initial jetting experiments was selected to optimize the waveform using ADA tools. In Figure 4-24, the optimum droplet formation was found at the pulse width of 9 µs to achieve the maximum jetting efficiency. It remained the same with the optimum pulse width for jetting hot-melt BMSC. According to

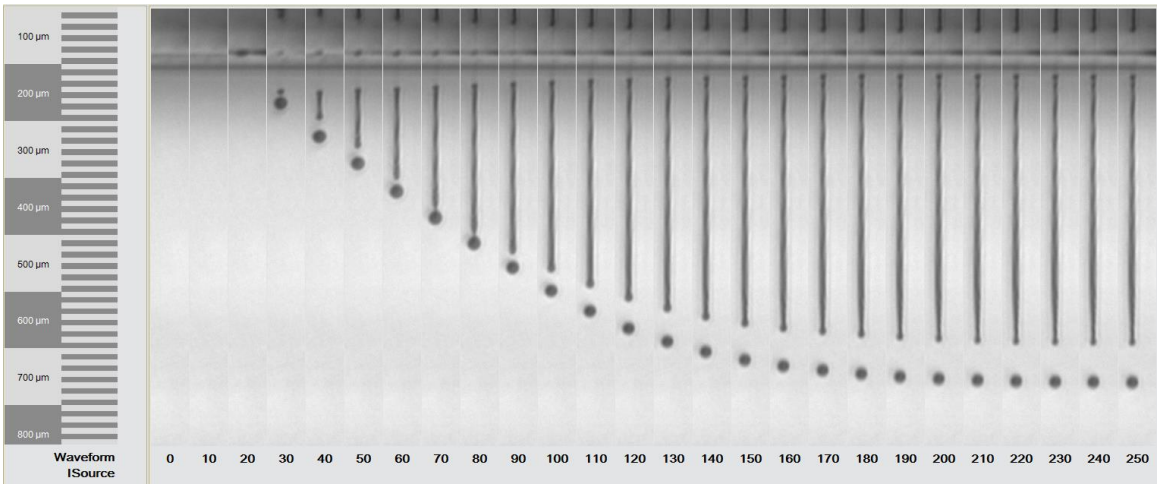
Bogy *et al.* (65), the optimum pulse width equals to *L*/*c*, where *L* is the length of the ink channel and *c* is the acoustic speed in the fluid. Since BMSC and BPA have very similar density (1.17 and 1.15 g/cm^3) and low molecular weight, the acoustic speed can be reasonably assumed similar. Therefore, in this case, the optimum pulse width for BPA and BMSC had a good agreement. The satellite of end-pinching mode was observed in all pulse widths, where the leading satellite travelled faster than the liquid thread behind so that the distance between was growing with the evolution of the droplet formation.



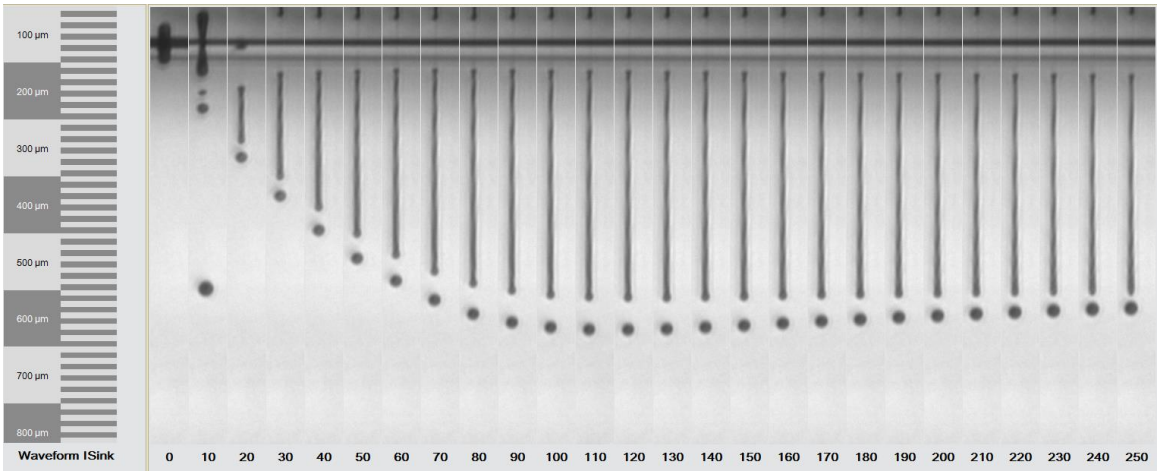
(a) (b)

Figure 4-24: The effect of pulse width on droplet velocity of hot-melt BPA (unit of pulse width: µs), the strobe LED delay is 70 (a) and 80 µs (b) from left to right, respectively

With the total pulse width of 9 µs, the rising and falling slope of the waveform were varied to investigate their effect on BPA jetting. The results were displayed in Figure 4-25. The droplet velocity was sensitive to the increase of the rising slope until 210 dac units. Afterwards, the velocity remained constant until the maximum slope was reached. Therefore, the rising slope at 230 dac units was considered the optimum where the disturbance had a minor effect on droplet velocity. A slightly different scenario was found in the falling slope tuning, where the maximum velocity of the droplet was found in the moderate fall time at 120 dac units where the velocity sharply increased with the falling slope. From 120 to 250 dac units the droplet velocity declined smoothly and approached a plateau.



(a)

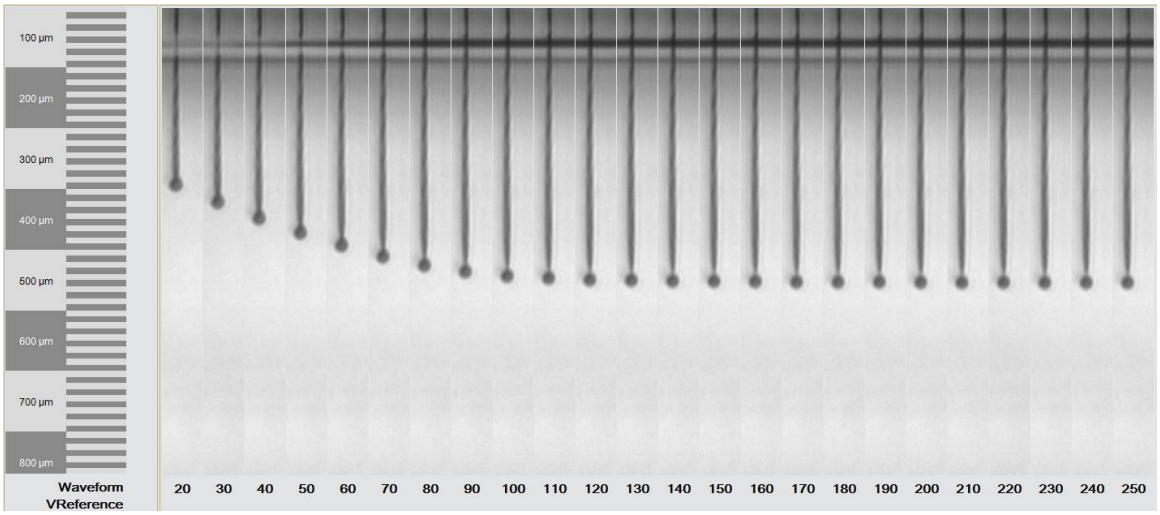


(b)

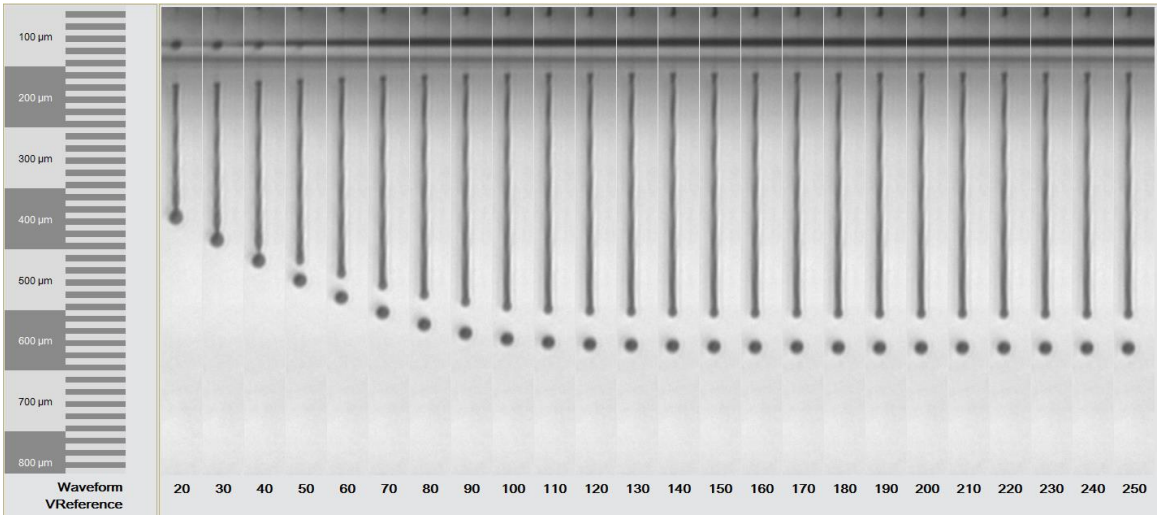
Figure 4-25: Effect of the rising and falling slope (a and b, respectively) on the droplet formation of hot-melt BPA (unit of ISource and ISink: µs)

4.7.2. Droplet Volume and Velocity Modulation

The droplet velocity and volume at various voltage amplitudes were measured to find the stoichiometric ratio between the BPA and BMSC droplets. The pulse width, rise and fall slopes were fixed at the optimum value as previously studied (9 µs, 230 dac and 120 dac).



(a)



(b)

Figure 4-26: The droplet evolution of hot-melt BPA at different voltage amplitude with a strobe delay at (a) 60 µs; (b) 70 µs;

As Figure 4-26 demonstrates, it was seen from the droplet evolution that the droplet velocity became almost constant when the voltage amplitude was greater than 120 dac units. The same trend also applied to the end-pinching satellites. This phenomenon was inconsistent with the results found in the BMSC droplet size modulation, which was possibly due to the inactivation of piezo-ceramics beyond its Curie temperature at approximately 140 ºC in the Océ printhead. It was believed that at 170 ºC the polarisation properties of the piezo-ceramics had been seriously compromised. Therefore, the deformation of the piezo-ceramics was limited at the elevated temperature above the Curie

temperature and the displacement of the piezo-ceramics became insignificant when a higher voltage was introduced, resulting in the fixed droplet volume above a critical point.

The droplet volume and velocity were measured by the image analysis function in the ADA tool and plotted against the voltage amplitude in Figure 4-27. Due to the end-pinching of the liquid thread, the measurement of the velocity was focused on the satellites as it would impact on the substrate first. The droplet volume was measured before the break-up of satellites where it incurred an error due to the long liquid column. However, there was some deviation due to a limitation in the pixels of processed images; it could be revealed the droplets were growing in velocity and volume sharply at the lower range of jetting voltage and constant above 120 dac units (approx. 22.6 V). The maximum velocity achieved was 11 m/s with a volume of 21.5 pL.

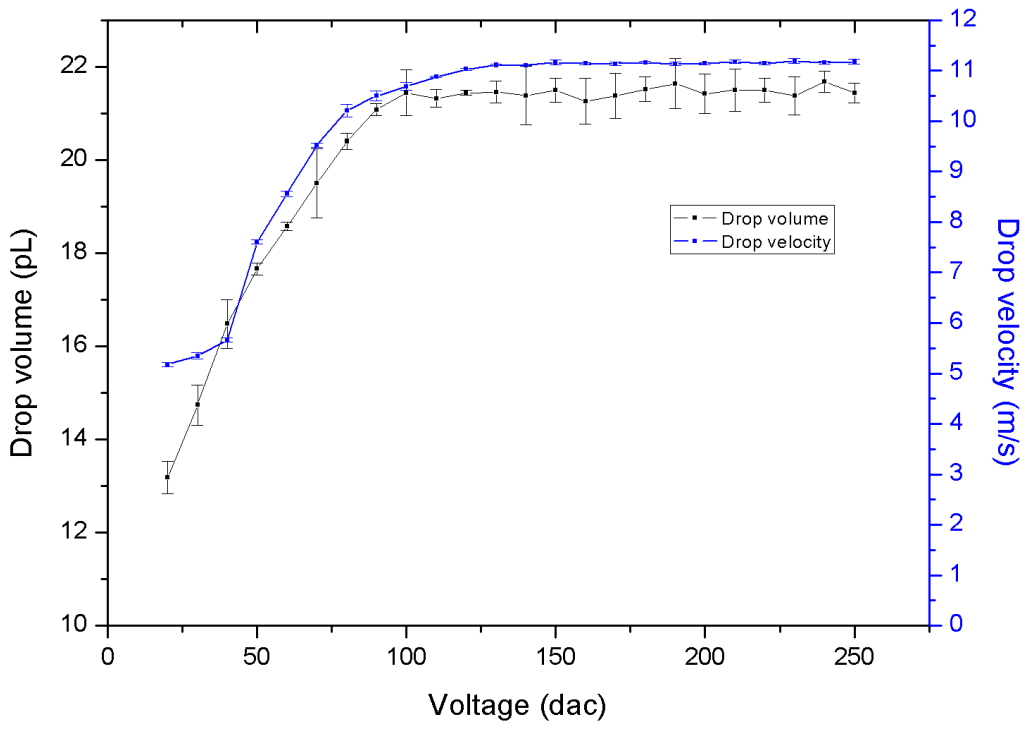


Figure 4-27: The BPA drop volume and velocity variation with the reference jetting voltage amplitude (average ± standard deviation, n=5)

4.8. Ink Deposition of Hot-melt BPA

The previous study showed that BPA formed poor droplet formation using Océ actuation control, where the end-pinched satellites were not caught up with by the long liquid thread. With the limitation of single trapezium waveform input, the satellites were not able to be eliminated without a complex waveform. The ink deposition of hot-melt BPA was reported in this section to investigate the deposition behaviour onto the cold surface and to narrow the deposition parameters to achieve a stable printed pattern.

4.8.1. Single Droplet Deposition of Hot-melt BPA

From the droplet formation study in the previous sector, the satellites pinched off after the head of the liquid thread travelled approximately 400 to 450 μm. A bead with 100 μm droplet spacing was printed to evaluate the effect of the end-pinched satellites on deposition at two different printing distances off the nozzle plate, 300 and 500 μm. The voltage amplitude was fixed at 120 dac unit (approx. 22.6 V). Figure 4-28 showed the single droplet deposition on the glass slide at room temperature. With a printing distance of 500 μm, there were secondary droplets in the vicinity of the main drops, which indicated the trajectory of pinched-off satellites may be influenced by the air flow. As a comparison, no secondary droplets were observed when the printing distance was 300 μm due to the drop impinging before the end-pinching.

The size of the hot-melt BPA droplets was measured by ImageJ to determine the droplet spacing needed for printing continuous patterns. At various voltage amplitudes from 20 to 120 dac units (3.8 to 22.6 V), 1 × 1 mm dot arrays with a droplet spacing were printed on the glass slide. Table 4-4 was the summary of the droplet size measured. This agreed with the droplet volume estimation, the maximum diameter of the droplets was achieved at 51.43 ±1.65 μm.

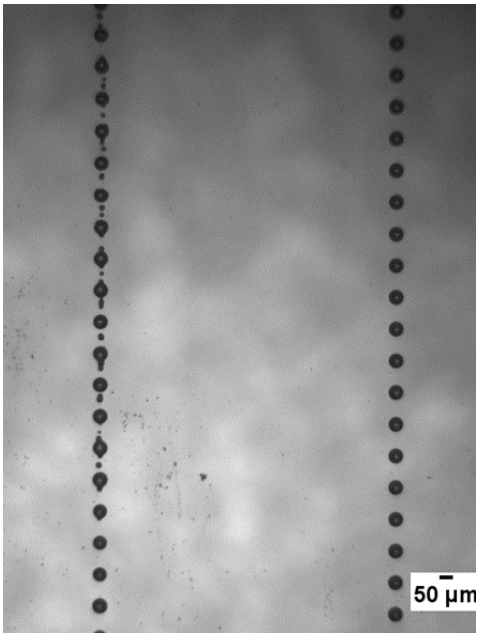


Figure 4-28: Printed droplets with a printing distance of 500 (left) and 300 µm (right)

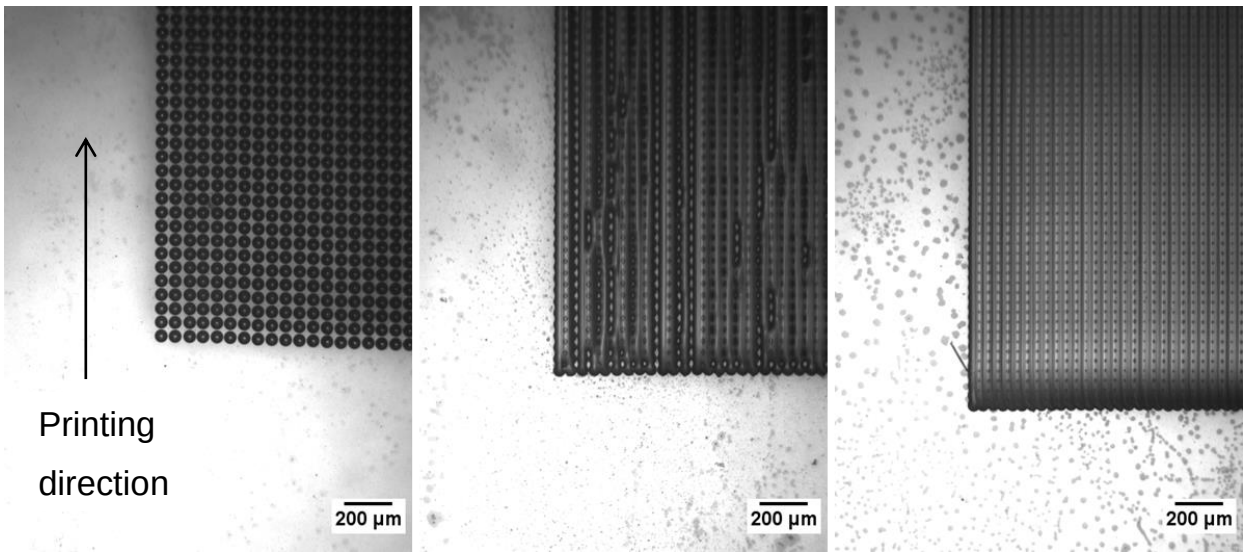
Table 4-4: BPA droplet size variation on the glass slide with the voltage amplitude of waveform (average ± standard deviation, n=5)

Voltage (dac unit)	20	40	60	80	100	120
Droplet size (µm)	45.98±0.95	49.35±2.43	50.36±1.81	50.62±1.32	51.39±2.56	51.43±1.65
Aspect ratio	1.02±0.02	1.04±0.05	1.05±0.04	1.02±0.02	1.02±0.01	1.02±0.03

4.8.2. Film Printing of Hot-melt BPA

Hot-melt BPA was printed on a glass slide with a dot resolution of 500, 600 and 700 dpi (50.8, 42.3, 36.3 µm spacing, respectively) to investigate the droplet spacing effect on the film formation. The printed pattern was a 5 × 5

mm square film for each droplet spacing value. The waveform voltage amplitude was set at 120 dac units. The optical images of the film were presented in Figure 4-29. With the droplet spacing of 50.8 μm which was approximately equal to the diameter of the droplets, no overlap between droplets was observed in Figure 2-24 (a). To form a continuous film, the droplet spacing should be smaller than the diameter of the droplets. The droplet spacing was reduced to ~42.3 μm where about 20 % of the droplet area overlap with each other as Figure 2-24 (b) showed. Droplets printed in the direction of printhead movement merged next to each other to form a continuous bead. It was also noted that a periodic bulge in each vertical swath led to the discontinuity of the line next to each other, which was due to the arrest of the contact line prior to the liquid merging (167). The bulges became less significant when the droplet spacing was further reduced to ~36.3 μm. Due to a higher volume of the liquid deposited in the unit area with reduced droplet spacing, the solidification rate of the hot-melt ink was lowered therefore the droplets have sufficient time to merge with each other before the contact lines became stationary.



(a) (b) (c)

Figure 4-29: Hot-melt BPA printed on glass slide with droplet spacing: (a) 50.8 μm (500 dpi); (b) 42.3 μm (600 dpi); (c) 36.3 μm (700 dpi)

Further printing of hot-melt BPA was unlikely to be carried out, however, due to the failure of the printhead internal heating element after exposure to overheating. The excessive temperature at 170 ºC led to the malfunction of the heating element and piezo-ceramics, and the ink continuously leaked from the channel block which was not able to be sealed with the sealant paste. It was supposed that the internal sealing material was dissolved by the hot-melt BPA ink and recovery to the nominal service performance was impossible.

4.9. Summary

In this chapter, the inkjet printing using hot-melt BMSC and BPA have been studied. The objective from this was to achieve stable droplet formation and deposition for both hot-melt inks so that the proper printing assembly for *in-situ* polymerisation of BPA-PC with necessary environmental control and reactive conditions could be designed.

It was found that BMSC gave droplet formation in the molten state at 130ºC, with a long liquid thread behind leading droplets using an Océ CrystalPoint printhead. The necking of the liquid thread was observed but it recoiled towards the head eventually. With the optimized waveform for hot-melt BMSC, the maximum jetting efficiency was found at a pulse width of 9 µs. The rising slope greater than 130 dac units and falling slope higher than 80 dac units were found to introduce a minimum disturbance to the droplet formation. The droplet volume and velocity were generally proportional to the increase of the voltage amplitude applied. The ink deposition of BMSC was carried out to determine the droplet size on the substrate and subsequent to determine the droplet spacing needed to form a continuous film by jetting. The droplet sizes varied between 68.69 to 79.42 µm with the waveform voltage amplitude from 18.8 to 28.2 V. With a droplet spacing of 40 µm, the continuous films could be formed on both glass and polyimide (Kapton) substrates. Considering the pinning of droplets, Kapton substrates achieved better printing quality when compared to glass slides. The surface profiling results revealed the

inhomogeneous surface which needed further development. The average thickness of the film was estimated to be 15 µm. The results demonstrated the potential to build 3D patterns using BMSC hot-melt ink.

The jetting of BPA was studied subsequently to investigate its printability as a hot-melt ink at 170 ºC. Due to a high melting temperature of BPA, the second Océ printhead was modified to break through the nominal temperature limit. During the waveform optimisation, it was found that a pulse width of 9 µs could be also applied to BPA to achieve the maximum jetting efficiency. It was also noted, however, that manipulating the voltage amplitude greater than 120 dac units (approx. 22.6 V) caused the minor change to the droplet velocity and volume. This was possibly due to the inactivation of piezoelectricity of the actuation element exposed to overheating. End-pinched satellites were found in the droplet formation which did not cause the secondary droplet deposition near the primary, when minimizing the printing distance between the nozzle plate and substrate down to 300 µm. The maximum droplet size that could be achieved was 51.43±1.65 µm on the glass slide. The best film formation was found when the droplet spacing was 36.3 µm, although the bulge on each single swathe was present. Due to the failure of the heating element of the printhead, further experiments to print hot-melt BPA cannot be carried out. Although the printability of hot-melt BPA had been demonstrated, the temperature specification of the printhead remained as the primary obstacle.

5. Results: Reactive Inkjet Printing of Solvent-based Inks

This chapter reports the development of solvent inks by dissolving BPA and BMSC in an organic solvent to prepare printable inks. The jetting method was established, and printing performance was reported.

5.1. Introduction and Research Rationale

Since there was a temperature limit in melting BPA using an Océ printhead, the 2-component reactive inkjet printing in the principle of hot-melt inks was not able to be further studied, although both BMSC and BPA have demonstrated considerable printability and potential applications in building 3D BPA-PC structures. The main obstacle when manipulating an Océ printhead was the temperature tolerance of the piezo-ceramics due to the Curie temperature, and incompatibility of the internal structure with the chemical aggressiveness of BPA. With the current printing assembly on the Pixdro LP50 printer, the hot-melt reactive inkjet printing of BPA using the Océ printhead could not proceed without development and probable modification of the printhead assembly. Therefore, alternative methods were considered to prepare the reactive inks using an organic solvent, e.g. N, N-dimethylformamide (DMF, bp = 153 ºC) and dioxane (1, 4-dioxane, bp = 101 ºC), to carry out reactive inkjet printing to build BPA-PC parts.

For the hot-melt inkjet printing, the thermal effect of NaOH with BPA remains as an issue because its produces undesirable products due to the long residence in the ink reservoir. Although polymerisation will continue without the presence of the catalyst, the reaction rate can be significantly improved when introducing the catalyst into the reactive mixture (164). The catalyst is considered to be dissolved and mixed with both monomers in the solvent to form a reactive mixture which will be then transferred onto the target substrate. Then with the necessary environmental control of high temperature and vacuum, the polymerisation can be initiated in the post-processing stage.

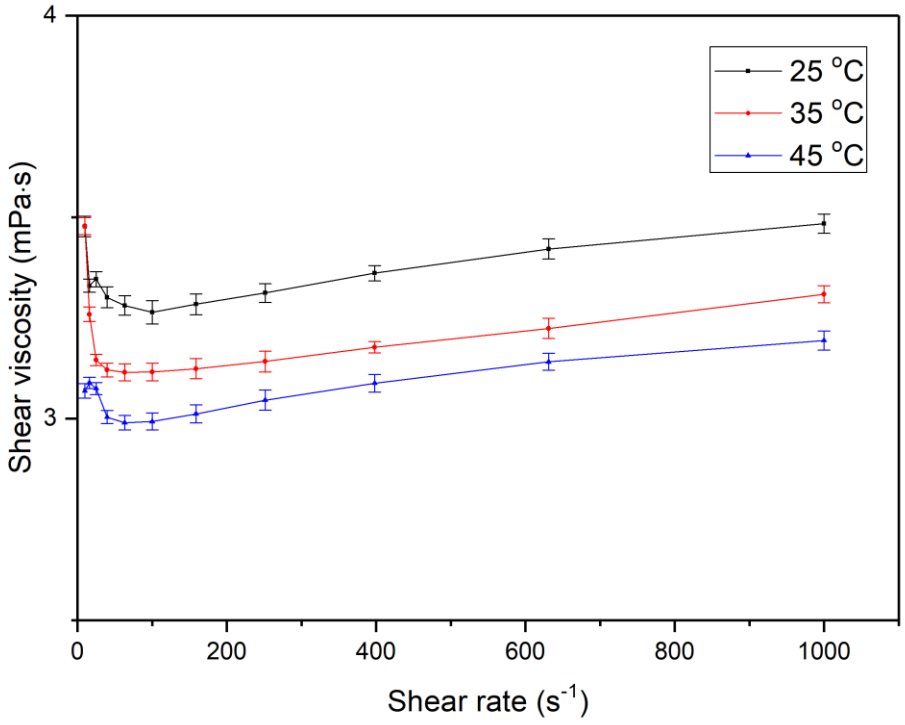
5.2. Printability Assessment for Reactive Inks

The printability assessment for reactive inks was required to check whether the inks were suitable for printing. The shear viscosity and surface tension for DOX25 and DMF35 were measured.

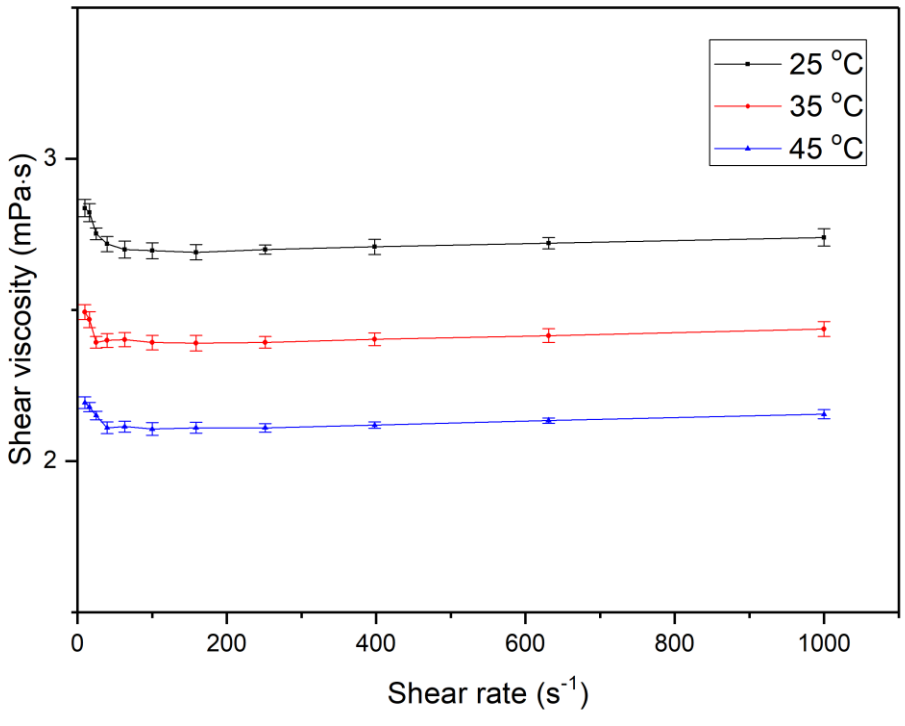
5.2.1. Viscosity of Reactive Inks

The result of the shear viscosity for DOX25 is shown in Figure 5-1 (a). It can be observed that the viscosity at 25 ºC and 1000 s^{-1} was 3.5 cP. With the increase of temperature, the viscosity was decreased accordingly with the same trends as 25 ºC. The viscosity range was between 3.1 and 3.3 cP at 35 ºC, and at 45 ºC it was between 3.0 to 3.2 cP. At each temperature, there was a constant increase of viscosity with the increment of shear rate, which was possibly due to the evaporation of dioxane.

The result of the shear viscosity for DMF35 is shown in Figure 5-1 (b). The viscosity also showed a temperature-dependent profile where it decreased with temperature elevation. The viscosities were approximately 2.7, 2.4 and 2.1 cP at 25, 35 and 45 ºC, respectively. As DMF has a higher boiling point (153 ºC) and a lower vapor pressure (4.9 mbar at 20 ºC) when compared to dioxane (bp = 101 ºC, vp = 41 mbar at 20 ºC), its evaporation rate was lower accordingly. Therefore, DMF35 had a more constant viscosity profile across the range of shear rate.



(a)



(b)

Figure 5-1: The viscosity of the 2 reactive inks from 25 to 45 ºC with a shear rate range between 10 and 1000s^{-1}: (a) DOX25; (b) DMF35 (average ± standard deviation, n=5)

5.2.2. Surface Tension of Reactive Inks

The results of surface tension of two reactive inks are shown in Figure 5-2. The surface tensions measurements were repeated 10 times for each ink at each temperature. DMF35 had a surface tension of 35.7 mN/m at 25 ºC and it decreased with the increase of the temperature, down to 30.4 mN/m at 45 ºC. A similar trend was observed for the viscosity of DOX25 in the same scope of temperature, where the surface tension ranged from 25.2 to 21.1 mN/m.

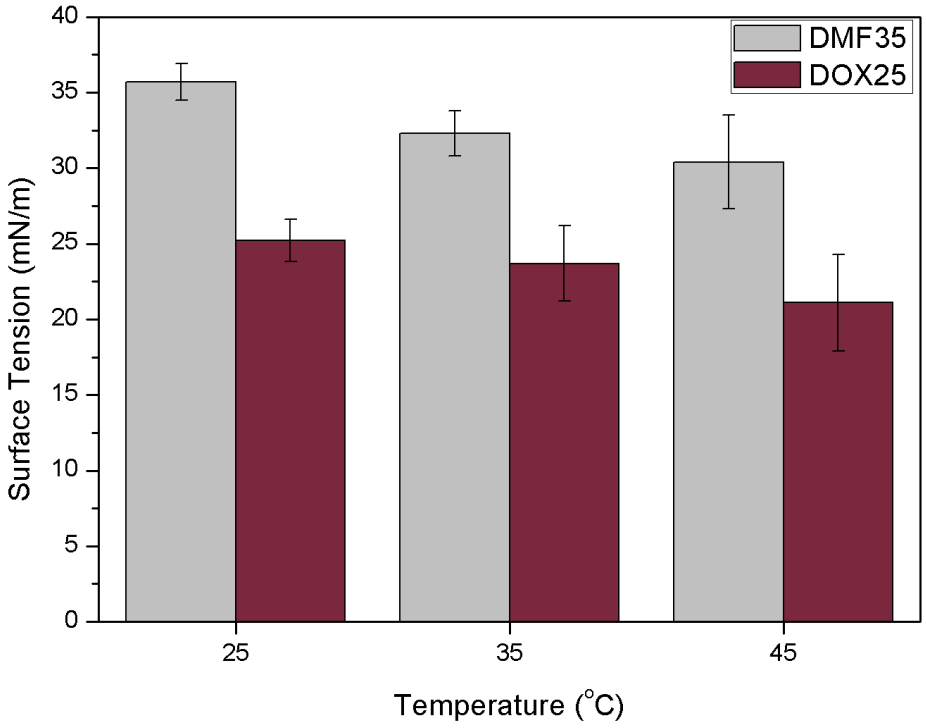


Figure 5-2: Surface tension measurement by pendent drop method for DMF35 and the DOX25 from 25 to 45 ºC (average ± standard deviation, n=10)

5.2.3. Overall Consideration for the Printability of Reactive Inks

From the characterisation for physical properties of the two reactive inks (Figure 5-1 and Figure 5-2), it can be concluded that the shear viscosity of both inks were in the printable range (<20 cP) from 25 to 45 ºC and that the surface tension was also acceptable in this temperature range. As a general

guidance for assessing the overall printability, the printability indicator Z for each ink at different temperatures were calculated and shown in Table 5-1.

Table 5-1: Summary of physical properties of DOX25 and DMF35 at various processing temperature for reactive inkjet printing and theoretical printability assessment

Reactive inks	Temperature (ºC)	Shear viscosity (cP) (at 1000 s^{-1})	Surface tension (mN/m)	Density (g/cm^3)	Nozzle diameter (μm)	Z
DOX25	25	3.5	25.2	1.06	20	6.60
	35	3.3	23.7			6.79
	45	3.2	21.1			6.61
DMF35	25	2.7	35.7	1.12		10.47
	35	2.4	32.3			11.21
	45	2.1	30.4			12.43

The inks were loaded into the Dimatix cartridge which had a nozzle diameter of 20 μm on the nozzle plate. The printing indicator Z was calculated for the inks at 25, 35 and 45 ºC, respectively. Table 5-1 presents the results of the overall consideration for theoretical printability of the two reactive inks. For DOX25, the Z numbers were all varying between 6.60 and 6.79 in the temperature range from 25 to 45 ºC. As suggested by the previous studies (47)(168), the Z number is considered to indicate the printability of inks where the droplets can be stably generated if $1<Z<10$. For DMF35, the Z numbers were slightly greater than 10 and it was decided to further observe the actual droplet formation to evaluate the printability at different temperatures.

5.3. Droplet Formation of Reactive Inks

Followed by the theoretical printability assessment, the droplet formation process for DOX25 and DMF35 were examined respectively. This section will

discuss the actuation waveform used for the reactive inkjet printing and the effects of temperature for the droplet formation process.

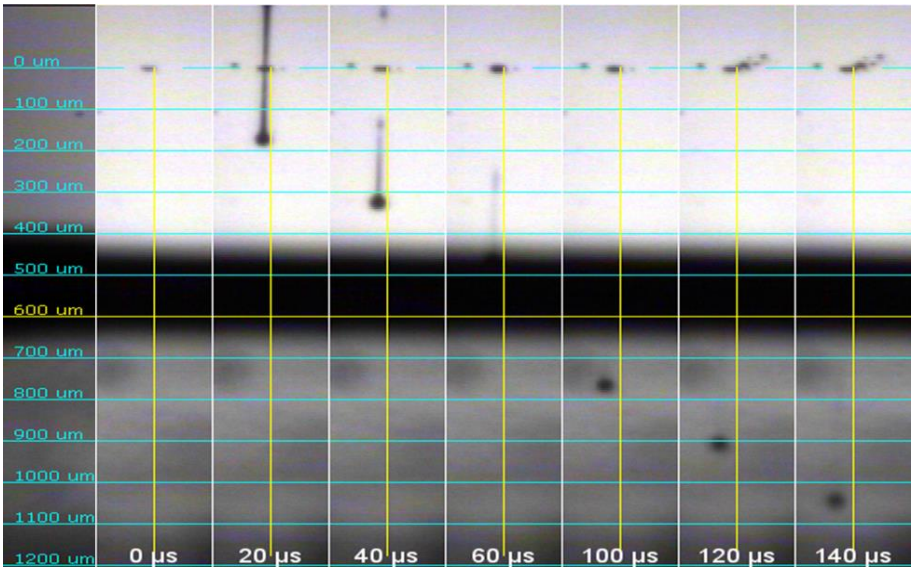
5.3.1. Effect of Temperature on Droplet Formation

The effect of ink temperature on the droplet formation was investigated to compare the printability of both reactive inks. The aim of the experiment was to observe whether the temperature has an impact on the solvent evaporation on the nozzle plate to potentially block the nozzles, and to investigate the droplet formation stability at different temperatures for different solvent systems. To correspond to the temperatures during the printability assessment, the temperature in the cartridge was set to 25, 35 and 45 ºC, respectively. The droplet formation was studied by the Dimatix drop watcher camera. Figure 5-3 and Figure 5-4 have shown the droplet formation process at varied temperatures for DOX25 and DMF35, respectively.

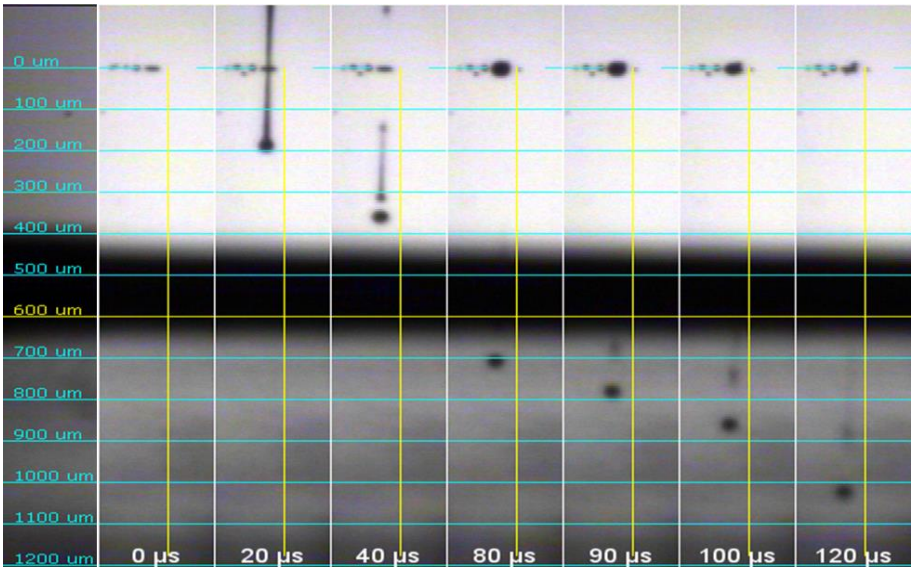
There were two different droplet formation evolutions for DOX25: the single droplet before impinging on the substrate (Figure 5-3(a)) and the satellite effect without recombination (Figure 5-3(b) and (c)). At 25 ºC, a long tail was behind the leading droplet after the droplet column was detached from the nozzle. Then after 800 μm travel distance, the tail was retracted to the leading drop which formed a single droplet to impinge on the substrate. There was a satellite droplet for the droplet formation at 35 ºC and it did not recombine with the primary droplet. A similar phenomenon has been explained by van der Meulen (169) that the tail was not able to coalesce into the leading drop if its velocity was lower than leading drop velocity. Driven by the capillary force in this case, the tail would form a spherical cap at the end which would not catch up with the leading droplet. With the increase of temperature, the surface tension and viscosity of the liquid changed, hence the droplet formation evolution was different. There was a more extreme case of satellite effect at 45 ºC as seen in Figure 5-3(c), where the satellite was not able to merge with the leading droplet but also lost its straight trajectory. It was also noticed that

the droplet velocity was decreased compared to the droplets formed at lower temperatures. It was possibly due to the more intensive solvent evaporation on the nozzle meniscus to result in a partial clogging of the nozzle. Fathi *et al*.(170) also observed the similar jet instability where it was pointed out that the nozzle blockage would decrease the kinetics of droplets. This could change the velocity of the droplet by the effect of air motion and heat convection to eventually induce the jet trajectory error. From this study, it can be concluded that the acceptable and stable droplet formation was achieved at 25 ºC for DOX25 rather than at higher temperatures, because the satellite droplets formed at higher temperatures would possibly cause the nozzle instability and depreciate the printing quality.

(a)



(b)



(c)

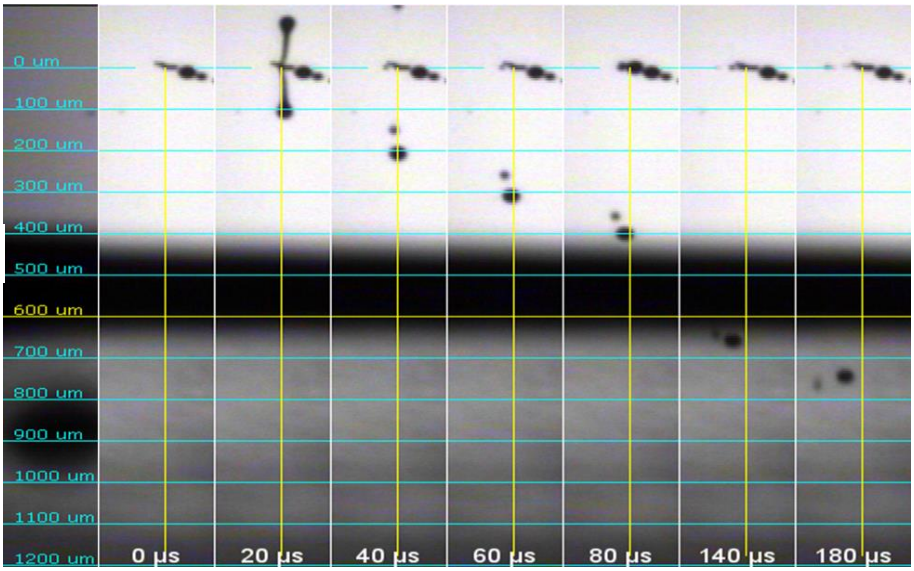
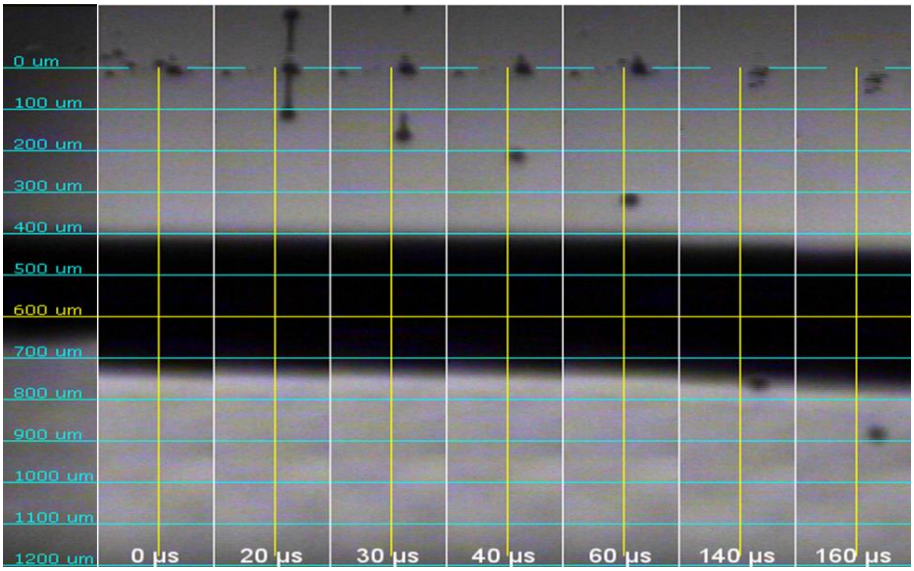


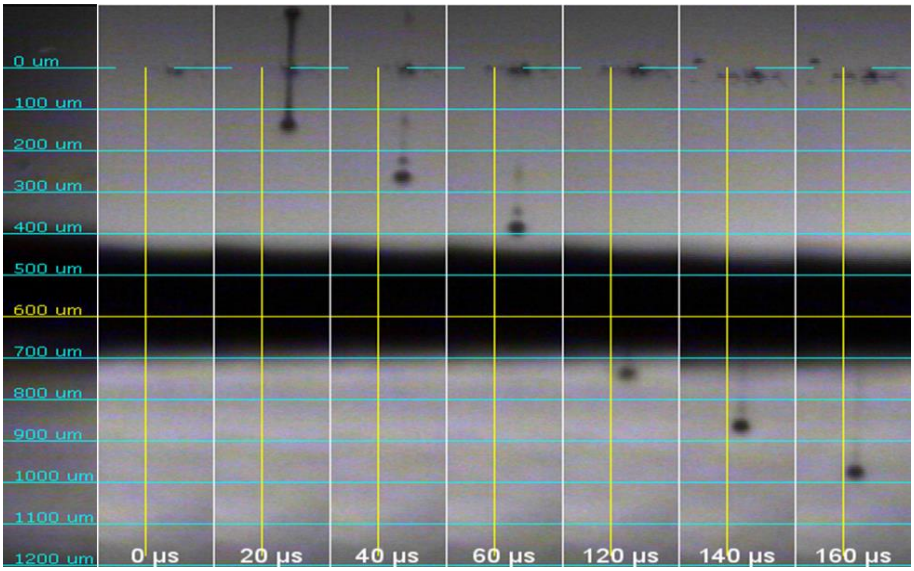
Figure 5-3: The droplet formation evolutions of DOX25 at different temperatures: (a) 25 ºC; (b) 35 ºC and (c) 45 ºC, viewed by the stroboscopic camera on the Dimatix printer

For DMF35, there was an increase of droplet velocity with the increase of cartridge temperature as seen in Figure 5-4. At a cartridge temperature of 25 ºC, the short tail was quickly retracted to the leading droplet at the stroboscopic delay of 40 µs and travelled at an average velocity of 5.6 m/s to impinge on the substrate as a single droplet. With the increase of cartridge temperature to 35 ºC, the liquid was ruptured from the nozzle between the elapsed time of 20 and 40 µs, which was followed by a recoiling filament detached from the falling droplet at an elapsed time of 40 µs as seen in Figure 5-4(b). The filament had a larger velocity and finally the tip of the filament caught up and merged with the primary droplet. The droplet was subject to elongation afterwards to a stand-off distance (i.e. the distance between the nozzle tip and the substrate). The average velocity of the droplet was larger at approximately 6.3 m/s compared to the droplet formation at 25 ºC. It was reported by a similar work (171) that due to the decrease of the ink viscosity at higher temperature, less driving pressure applied to the liquid was viscously dissipated and more energy was transformed to the kinetic energy of the ejected liquid. It subsequently resulted in a larger travelling velocity of the droplet. With a further increase of the cartridge temperature to 45 ºC, the evolution of the droplet formation remained almost the same as that at 35 ºC, except the final droplet had a slightly larger velocity of 6.5 m/s as seen in Figure 5-4(c). Analogously, a single droplet impinging onto the substrate was preferred therefore the cartridge temperature for DMF35 was set to 25 ºC.

(a)



(b)



(c)

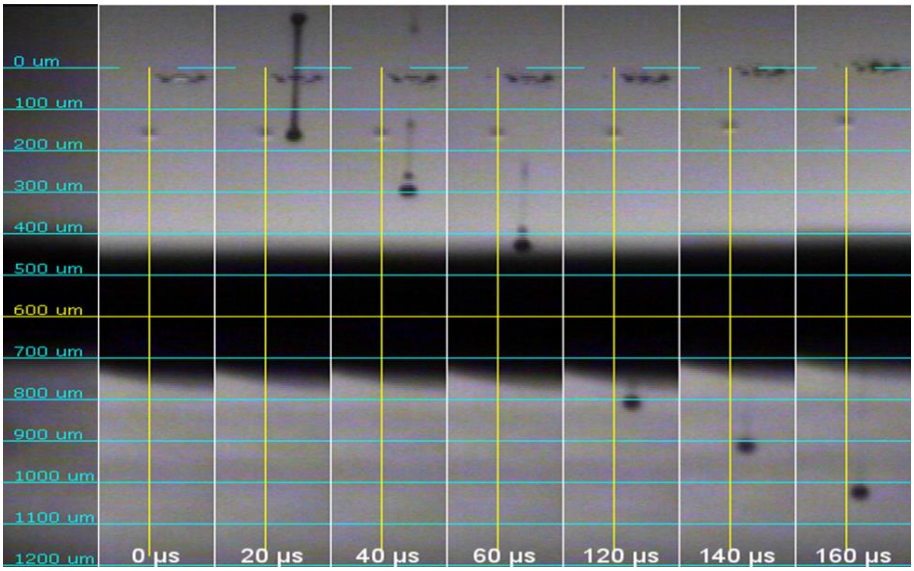


Figure 5-4: The droplet formation evolutions of DMF35 at different temperatures: (a) 25 ºC; (b) 35 ºC and (c) 45 ºC, viewed by the stroboscopic camera on the Dimatix printer

Overall, the droplet formation behaviour for DOX25 and DMF35 are summarized in Table 5-2. The average velocity of the leading droplet was calculated based on the travel time over a stand-off distance of 1000 μm. From the results, the appropriate droplet formations for the both reactive inks were suggested at 25 ºC without formation of satellite droplets.

Table 5-2: Summarisation of droplet formation behaviour at varied cartridge temperatures and the corresponding droplet velocity

Reactive ink	Cartridge Temperature (ºC)	Droplet Behaviour on Impact (at 1000 μm stand-off distance)	Average Velocity of Leading Droplets (m/s)
DOX25	25	A single droplet (no tail)	7.5
	35	A leading droplet and a satellite with a tail (not rejoin with the leading droplet)	8.6
	45	A leading droplet and a satellite without a tail (satellite has side-trajectory error)	4.2
DMF35	25	A single droplet (no tail)	5.6
	35	A single droplet with an elongated tail	6.3
	45	A single droplet with an elongated tail	6.5

5.4. Droplet Deposition Study for Reactive Inks

Following the establishment of stable droplet formation, the study of droplet deposition onto a substrate and the interaction between the droplet and the substrate was investigated. A single dot array of each reactive ink was printed with different substrate temperatures to investigate the deposition process. Then a square-shape thin film was printed with different substrate temperatures and droplet spacing to evaluate the morphological quality of the film. Both optical microscopy and surface profiling results are presented.

5.4.1. Single Droplet Deposition

To investigate the influence of substrate temperature on droplet morphology, 5 × 5 mm single droplet arrays with a droplet spacing 100 μm were printed using DOX25 and DMF35. Before printing the droplet with the Dimatix printer, the inks were pipetted onto the heated microscope glass slide to determine the temperature range for quick solvent evaporation within 1 second. Then the inks were deposited with the printer on the microscope glass slide with different temperatures. The droplets were observed with an optical microscope and analysed using ImageJ software.

Figure 5-5 and Figure 5-6 show the optical images for single droplet arrays printed on the microscope glass at different temperatures. For both reactive inks, the continuous dot surface morphology was obtained without fractals. For DOX25, the droplets showed a similar shape and coverage on the substrate at the substrate temperature of 50 to 70 ºC. It could also be seen that the diameters of the droplets were almost invariant with respect to the change in the substrate temperature (Figure 5-7), which indicated that the rate of solvent evaporation within this temperature range had limited effects on the droplet size and quality. There was also no ring-like droplet observed due to the ‘coffee-ring effect’. However, the more detailed surface morphology of the droplet was analysed in Figure 5-9.

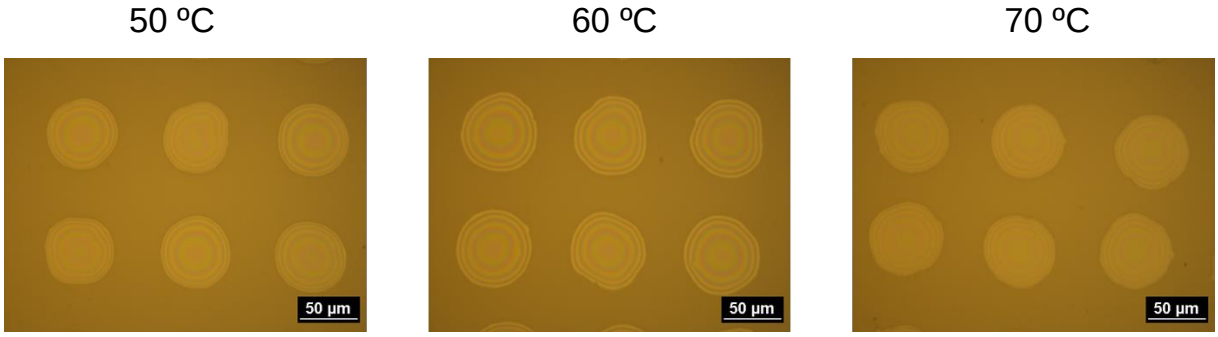


Figure 5-5: The optical microscope images of the single droplet deposition of DOX25 on the microscope glass slide at different substrate temperatures

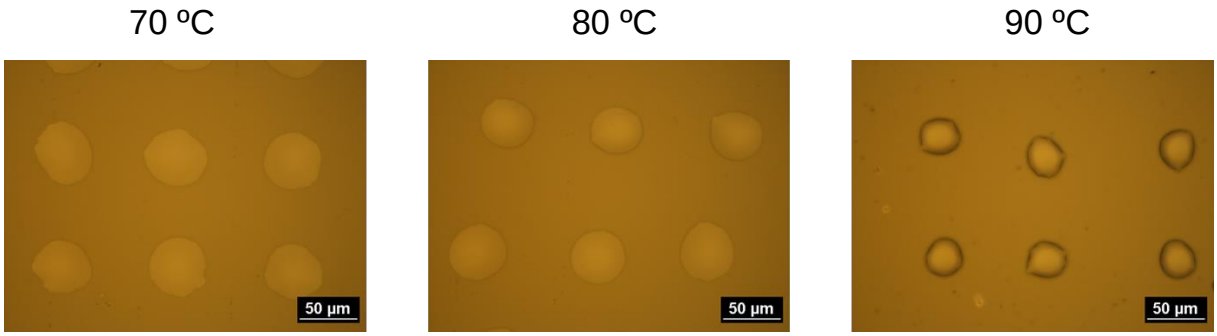


Figure 5-6: The optical microscope images of the single droplet deposition of DMF35 on the microscope glass slide at different substrate temperatures

For DMF35, the droplets showed more irregular shapes compared to DOX25, among different substrate temperatures from 70 to 90 ºC. There was also a trend showing the decrease of droplet size with the increase of the substrate temperature, from 51.2 to 32.7 µm. This effect could be explained by the higher substrate temperature resulting in a higher rate of solvent evaporation, where the droplet would experience less time spreading on the substrate to have smaller droplet size (172). On the other hand, the temperature of nozzle plate would also be elevated due to the small stand-off distance. It was noticed as in Figure 5-8 that the cartridge temperature would have a significant increase to due to the heat convection from the substrate. The increase was likely affected by the printing duration and printing frequency. This phenomenon would accelerate the solvent evaporation on the meniscus of the nozzle plate and in flight to have a reduced droplet size before impinging on the substrate. Although a high rate of solvent evaporation was preferred to incur an instant solidification of droplets on the substrate, it would also increase the risk in blocking the nozzles and thus had lower jetting stability. Therefore, there needs to be a trade-off between the solidification speed and jetting stability.

Table 5-3: The droplet diameters of two reactive inks deposited onto the microscope glass slide with different substrate temperatures

DOX25			
Substrate temperatures	50 ºC	60 ºC	70 ºC
Droplet diameter (µm) (Mean ± standard deviation, n=6)	63.0 ± 1.2	61.7 ± 0.9	64.8 ± 1.7
DMF35			
Substrate temperatures	70 ºC	80 ºC	90 ºC
Droplet diameter (µm) (Mean ± standard deviation, n=6)	51.2 ± 2.2	46.6 ± 1.8	32.7 ± 1.5

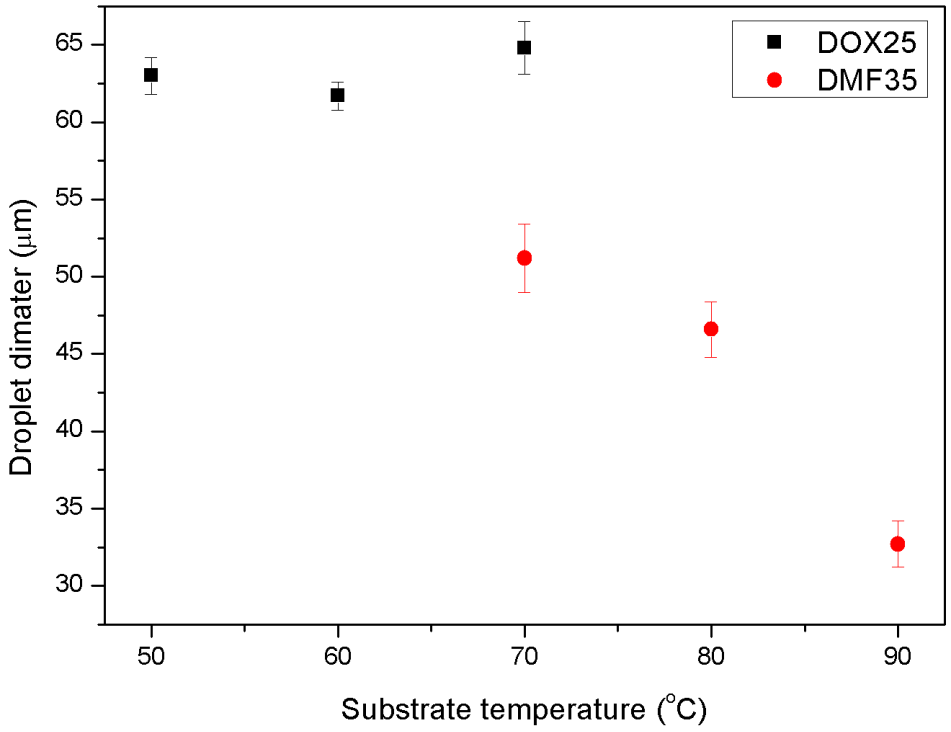


Figure 5-7: The effect of different substrate temperatures on the droplet diameter of DOX25 and DMF35 (average ± standard deviation, n=6)

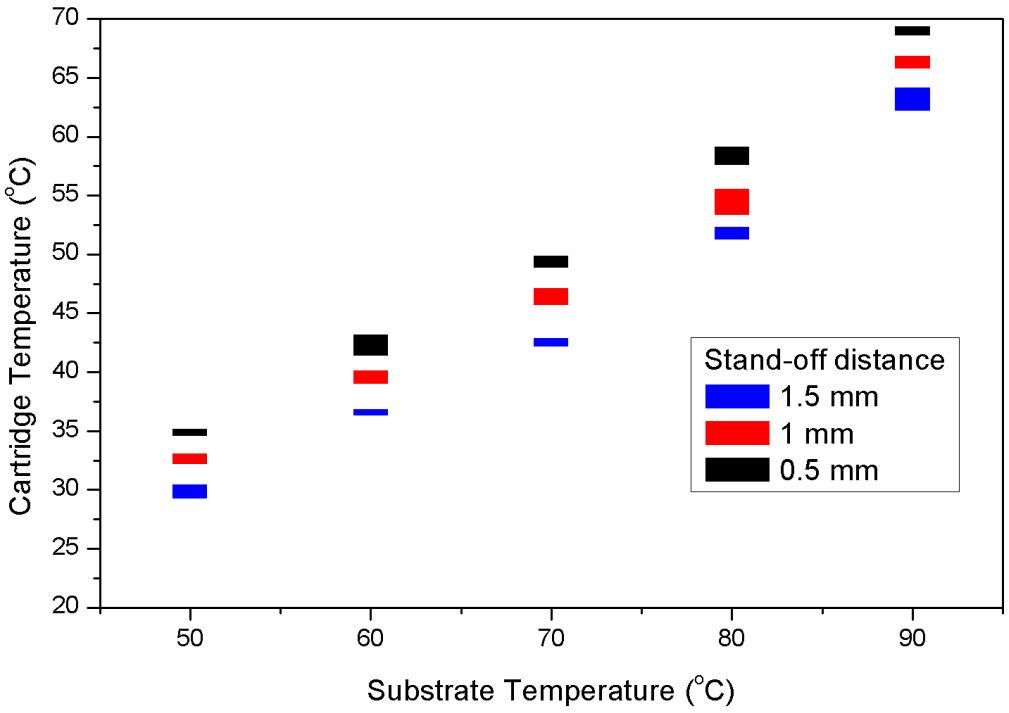


Figure 5-8: The effect of the substrate temperatures on the cartridge temperatures at different stand-off distances.

The morphology of the single droplets was observed by using a white light interferometer and two examples of the surface profiling results are presented in Figure 5-9. The droplets were heated on the printing plate at an elevated substrate temperature to ensure the solvent evaporated. The results in Figure 5-9(a) confirmed the previous optical results for DOX25 in that there was no 'coffee ring effect' for the droplets, indicating the evaporation rate of the dioxane solvent was much faster than the particle movement to the contact line at the edge of the droplet. Instead of forming a ring-like structure on the substrate, the droplet tended to form a dome structure which could contribute to the uniform layer printing. In the contrast, the droplets printed by DMF35 showed higher thickness of the outer-ring compared to the central position, which was known as 'coffee ring effect'. This suggests that there is a relatively slower evaporation of the DMF solvent when compared to the dioxane.

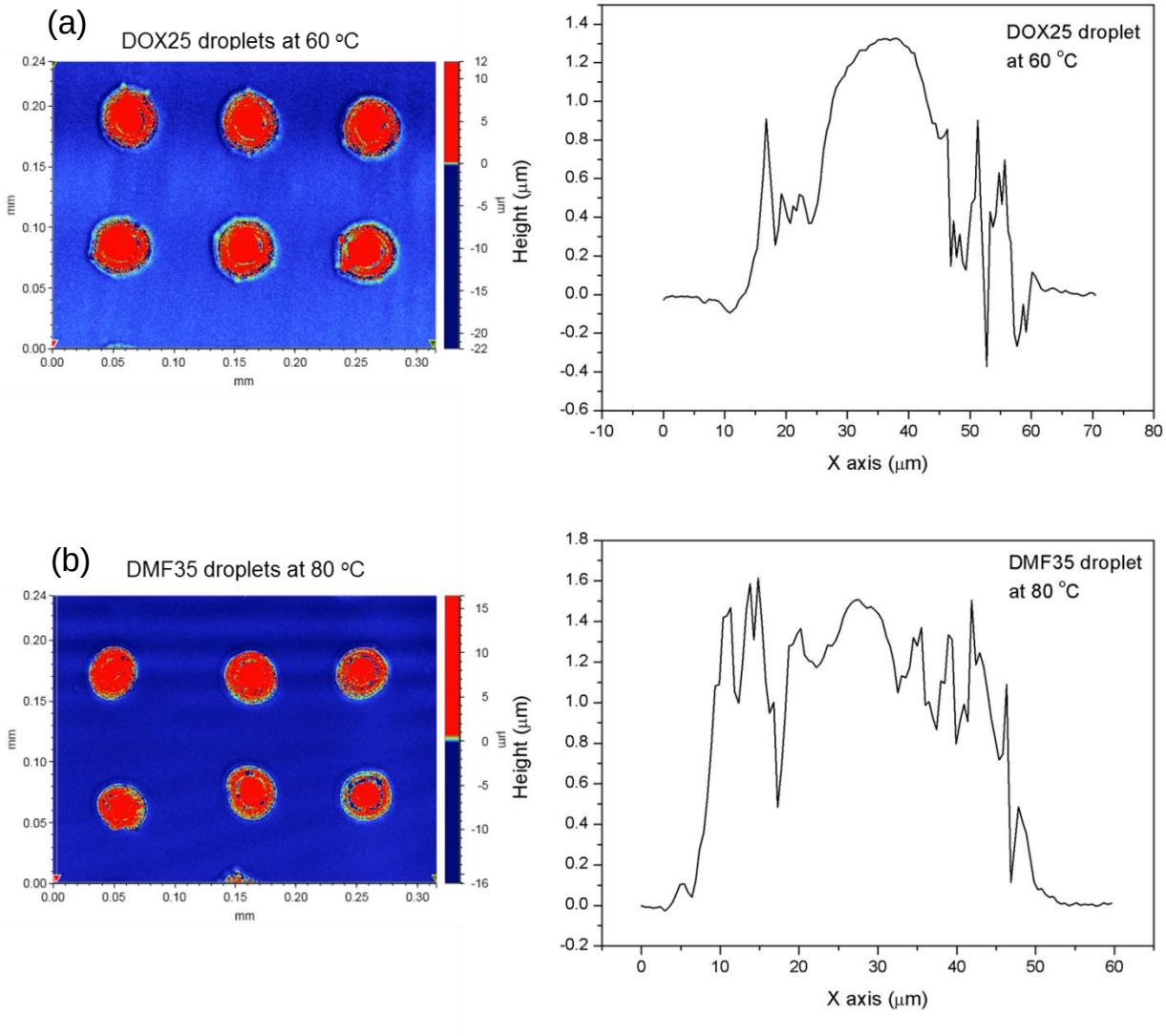


Figure 5-9: The surface profiling results of (a) DOX25 droplet at a substrate temperature of 60 ºC and (b) DMF35 droplet at a surface temperature of 80 ºC

Table 5-4 summarized the central height of the droplets for the two reactive inks at different substrate temperatures. For DOX25, there was no significant variation of the droplet height at different substrate temperatures. Given that each droplet had the same volume ejected from the nozzle, the similar droplet diameter in a unit region on the substrate would give rise to a similar height of the droplet. For the DMF inks, the height of the solidified droplet increased at the higher substrate temperature, possibly due to a receding contact angle of the droplet.

Table 5-4: The average central height of the solidified droplet on microscope glass slides at different substrate temperatures

DOX25			
Substrate temperatures	50 ºC	60 ºC	70 ºC
Average central height of the droplet (μm) (Mean ± standard deviation, n=6)	1.5 ± 0.1	1.4 ± 0.1	1.7 ± 0.3
DMF35			
Substrate temperatures	70 ºC	80 ºC	90 ºC
Average central height of the droplet (μm) (Mean ± standard deviation, n=6)	0.9 ± 0.2	1.6 ± 0.1	2.1 ± 0.2

5.4.2. Thin Film Printing

In order to form a continuous thin film on the substrate, the droplets must be partially overlapped onto each other, where the droplet spacing is one of the main contributors to the film formation. In addition, the substrate temperature also plays a key role in the interaction between the droplet and the substrate to affect the film formation process and quality. DOX25 and DMF35 were printed respectively at different substrate temperatures (50, 60 and 70 ºC for DOX25; 70, 80 and 90 ºC for DMF35) with a selected range of droplet spacing (20, 30 and 40 μm for DOX25; 15, 25 and 35 μm for the DMF35) on the microscope glass slide to investigate the films formation and their surface morphology. The size of the thin films was 5 × 5 mm for the microscope observation.

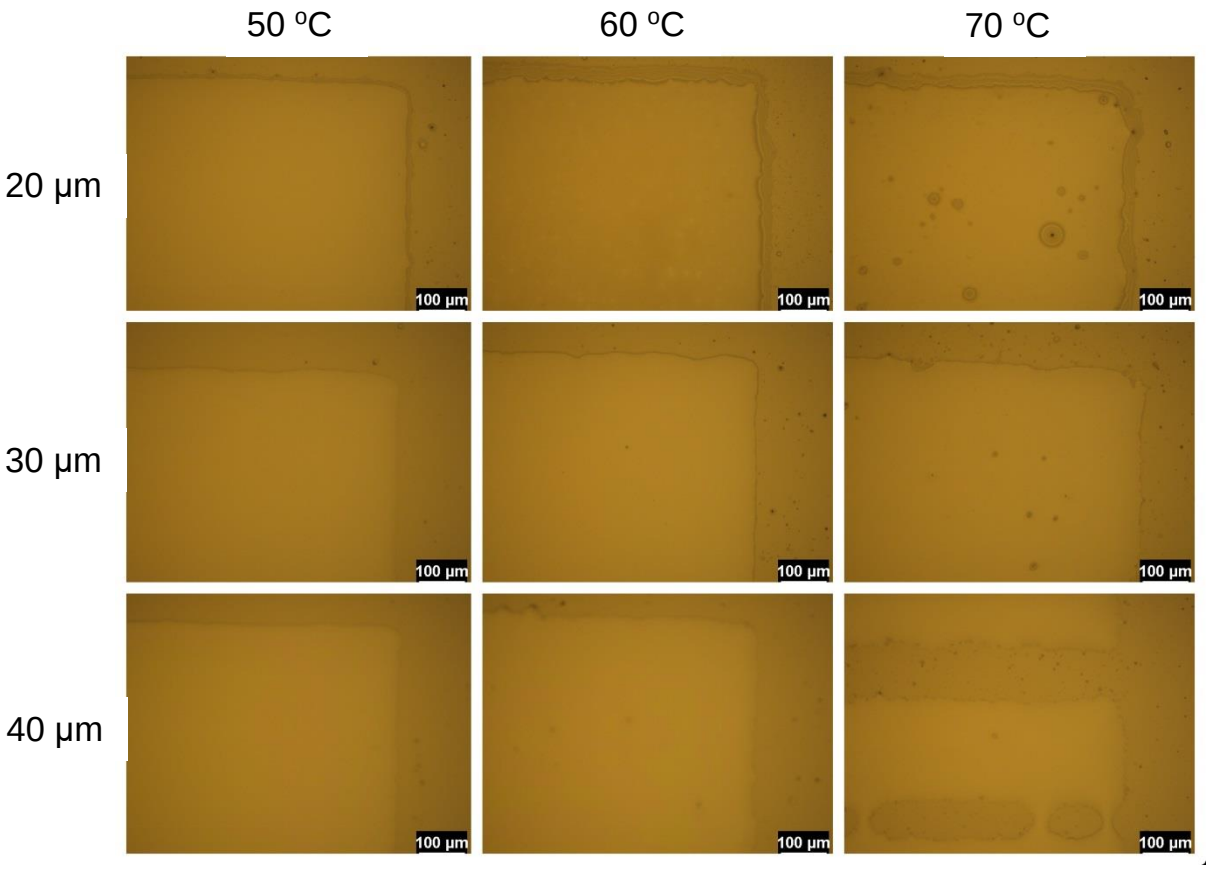


Figure 5-10: The optical images for the thin films of DOX25 with different droplet spacing at different substrate temperatures

Figure 5-10 shows the optical images for the thin films of DOX25 with 20, 30 and 40 µm droplet spacing printed on the microscope glass slide at 50, 60 and 70 ºC respectively. There was clear evidence showing that continuous films were obtained when the droplet spacing was fixed at 20 µm and no waviness on the surface was observed. The printing was conducted line by line horizontally and no significant solid boundaries were seen between the lines, which indicated that the line of reactive mixtures did not completely solidify before merging with the next one. However, crater-like pores were on the film surface which disrupted the film continuity when the substrate temperature was elevated to 70 ºC. This was due to the jet instability resulting from the nozzles being heated by the hot substrate. The jet instability would lead to either the droplet size reduced in flight or the droplet missing in the desired location where the crater-like pores would be formed (145)(173). A similar film

formation was obtained when the droplet spacing was 30 μm, where the jet instability led to the pores on the surface. When the droplet spacing was increased to 40 μm, the continuity of the films was maintained at a surface temperature at 50 ºC and some pinholes existed on the surface at 60 ºC. At a substrate temperature of 70 ºC, the adjacent droplets were not able to merge with each other and this resulted in the separate lines instead of continues films. This would be a combined effect of the jet instability and the larger droplet spacing (174).

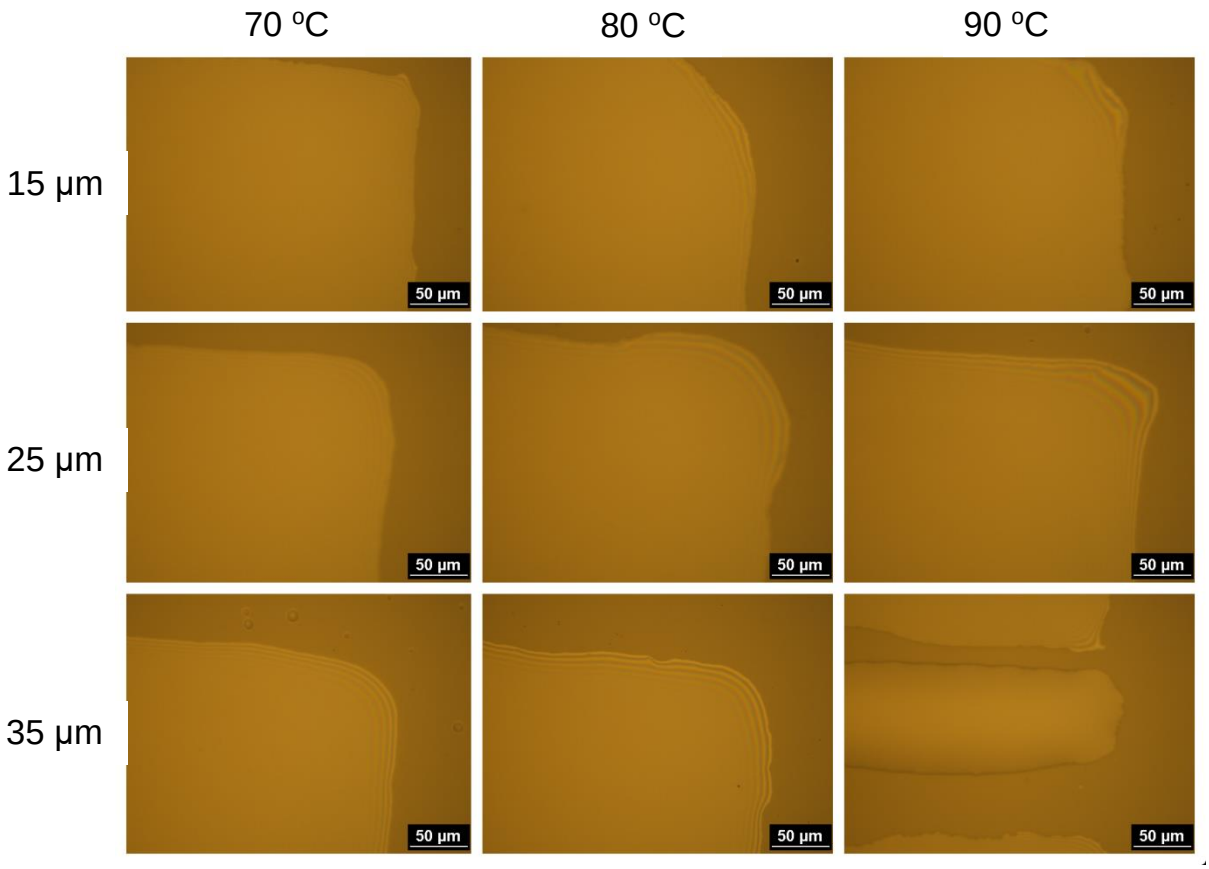


Figure 5-11: The optical images for the thin films of DMF35 with different droplet spacing at different substrate temperatures

DMF35 was printed to form films with the droplet spacing of 15, 25 and 35 μm at 70 to 90 ºC. As shown in Figure 5-11, the continuous films were formed with the droplet spacing of 15 μm regardless of the substrate temperatures, which

suggested that the substrate heating from 70 to 90 ºC had a negligible influence on the jet stability. When the droplet spacing was set to 25 μm the nozzles were not consistently stable at 80 or 90 ºC, as occasionally some voids appeared on the films. Moreover, it was also noticed that the continuity of the films disappeared, and separate lines formed, when the droplet spacing was increased to 35 μm and the substrate temperature was set to 90 ºC.

The surface profiles of the thin films were also characterised by the white light interferometer to investigate the morphology in detail and Figure 5-12 shows two examples of the results. Figure 5-12 (a) displayed the surface morphology of a 1-layer thin film of DOX25 with a droplet spacing of 30 μm at substrate temperature of 60 ºC. Note that the edges of the film did not represent the actual results due to the limitation of measuring sample slopes. The average thickness of the film was measured to be about 1.2 μm. The surface showed the morphology where the boundaries between the printed threads existed, as that the surface height varied more intensively in Y axis (X axis was the printing direction). This was caused by the evaporation of the solvent and the solidification of the reactive mixture before the next thread was printed.

In contrast, the 1-layer thin film printed by DMF35 showed a different profile in Figure 5-12 (b). The thickness was much higher than that of the single layer film printed by DOX25, due to a higher loading of the reactive mixture. No significant boundaries between the printed threads were observed which suggests a relatively low evaporation of the solvent and a well-mixed fluid before solidification. However, the distribution of the reactive mixture was found to be inhomogeneous. A similar phenomenon was also reported by other work (175) where the heat flux from the substrate to the edge of the drop led to a locally enhanced solvent evaporation and the central solutes would tend to move towards the edge to replace the lost fluid. In this case, because of the slow evaporation of the DMF solvent, it is likely that the film remained fluid to allow the solutes to transfer to the edge. Also, it was noted that the

fluid tended to transfer from the top and bottom edge of the film to the centre due to the bulk flow driven by the surface tension (176).

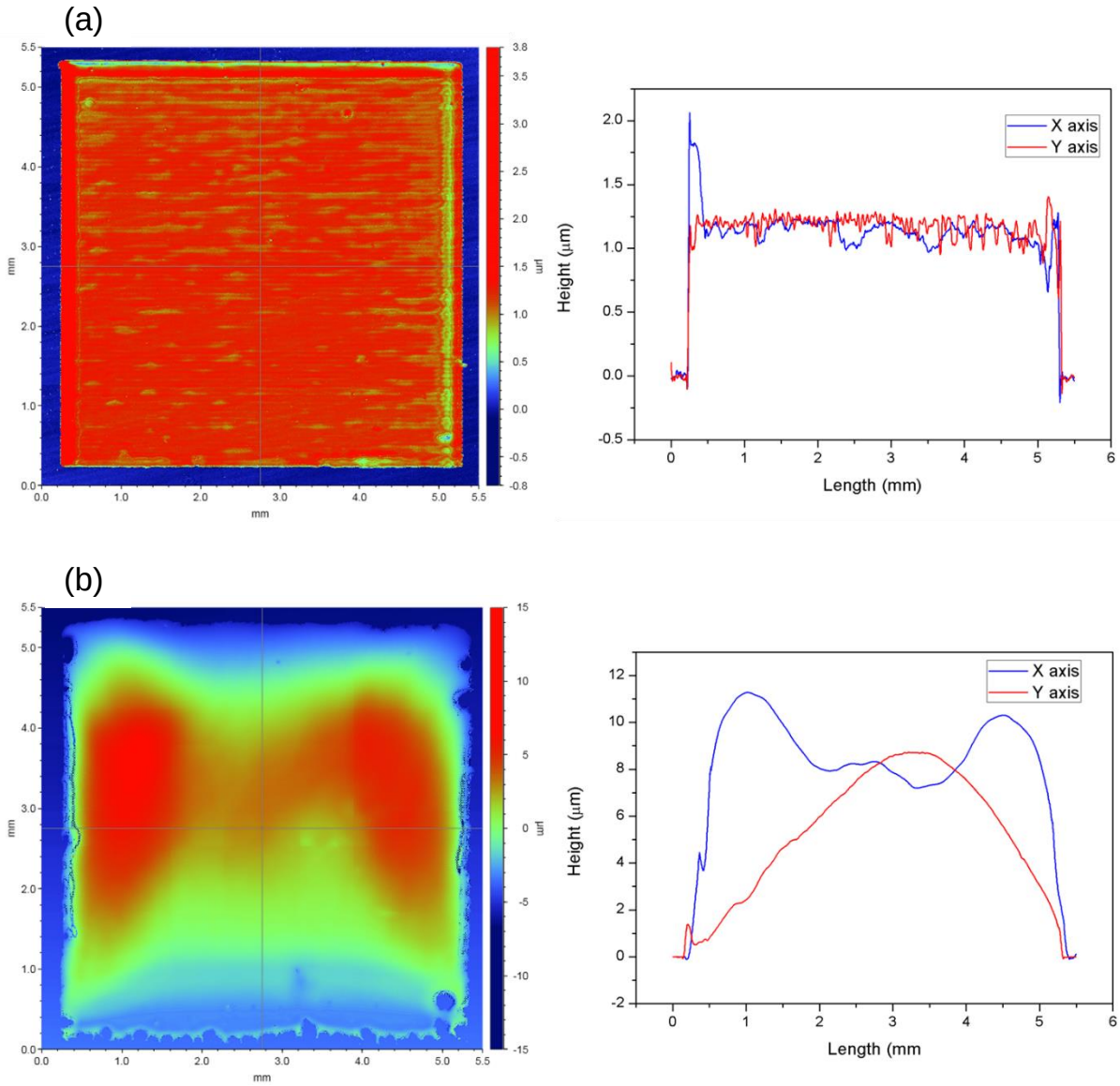
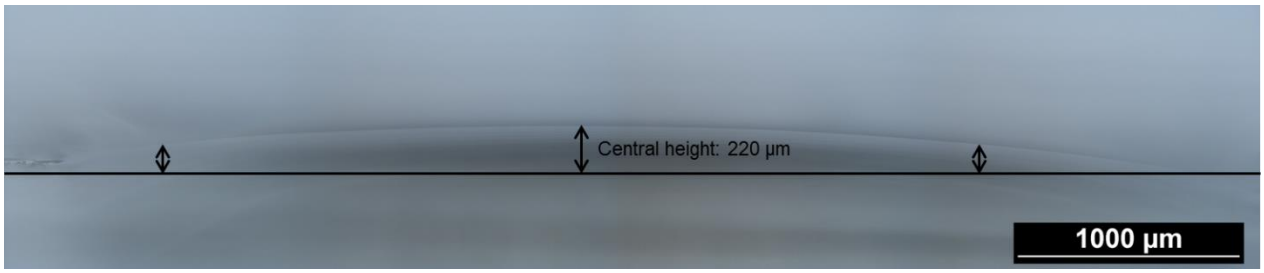


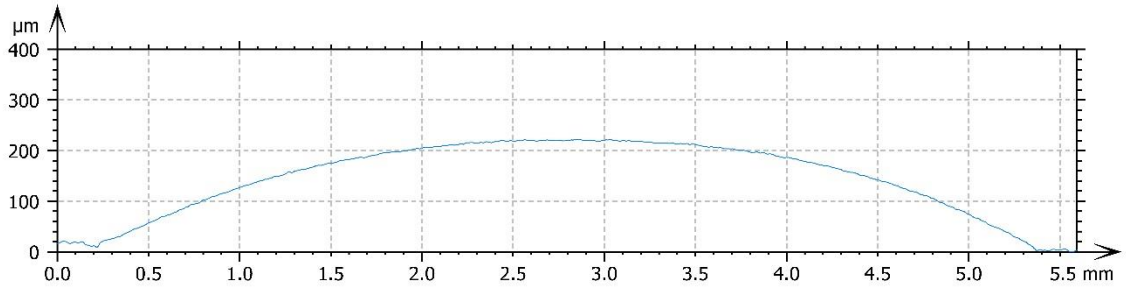
Figure 5-12: The surface profiles of the thin films as printed by white light inteferometer: (a) 1 layer film of DOX25 with a droplet spacing of 30 µm at 60 ºC substrate temperature; (b) 1 layer film of DMF35 with a droplet spacing of 15 µm at 80 ºC substrate temperature. (The X and Y profiles in the right-hand side figure pertain to the lines of crosshair in the left side figures)

5.4.3. Thick Film Printing

Following by the single layer printing, multi overprints of the reactive mixtures were also deposited on the microscope glass slide in order to build thicker samples. The boundary of the top of the overprints was found not to be flat and a surface curvature was observed as shown in Figure 5-13. This ‘dome’ shape was due to the capillary pressure difference between both sides of the interface of the reactive mixture and air. The surface tension acted as a balancing force to compensate the pressure difference therefore the interface remained curved. A poke test with a needle tip also evidentially indicated a non-solidified nature of the as-printed reactive mixture, where the printed layer would intermix with the layers printed previously to form a dome. This dome structure was undesirable when a 3D structure with high feature resolution was required, and it indicated a further exploration of printing and post-processing strategies which will be discussed in the next chapter.



(a)



(b)

Figure 5-13: The optical images of multi overprints of reactive mixtures (5 × 5 mm) in side view: (a) a film of 80 successive layers of DOX25 with a droplet spacing of 30 µm on the glass surface of 60 ºC; (b) The surface profile of the 80 layer thick film of DOX25, taken by Alicona G5 Infinite

The deposited reactive mixture, or the deposited low molecular weight PC oligomer, was then characterised by DSC to evaluate its thermal property and to understand the as-printed structure. A thermal cycle of (-50)-200-(-50) ºC at 10 ºC/min in a nitrogen environment was used to obtain the glass transition temperature T_g and the heat flux profile of the reactive mixture during heating and cooling stage (the lower and upper temperature limits were chosen to cover the glass transition range of linear BPA-PC). Approximately 5 mg of the as-printed reactive mixture was taken for each run of DSC.

Figure 5-14 shows the DSC result for the as-printed reactive mixture of DOX25. In the heating run, an endothermic shift was firstly observed where the specific heat was increased by 0.374 J/(g ºC). Using 'half Cp' method the T_g of the reactive mixture was calculated to be 17 ºC. It validated the result (in Section 5.4.3) that the soft gel-like reactive mixture leading to a 'dome' shape printed structure due to a low glass transition temperature. Then a broad endothermic peak in the heating run was observed from 139 ºC which was due to the melting of the reactive mixture and the initiation of polymerisation. It was assumed that the molecular mobility of the reactive mixture became sufficient for the melt polymerisation from this onset temperature. Polymerisation was further confirmed by the weight loss of the sample after the DSC measurement, which was due to the evaporation of the by-product from the melt polymerisation, i.e. methyl salicylate. In the cooling run, the peak for the melt polymerisation was not seen as the polymer would have formed.

Figure 5-15 shows a typical thermogram of the as-printed reactive mixtures of DMF35. The T_g (i.e. 4 ºC) was also found to be relatively lower than the normal room temperature which could explain the soft gel-like 'dome' structure printed as shown in Figure 5-13. Similarly, the rate of melt polymerisation significantly increased from 140 ºC.

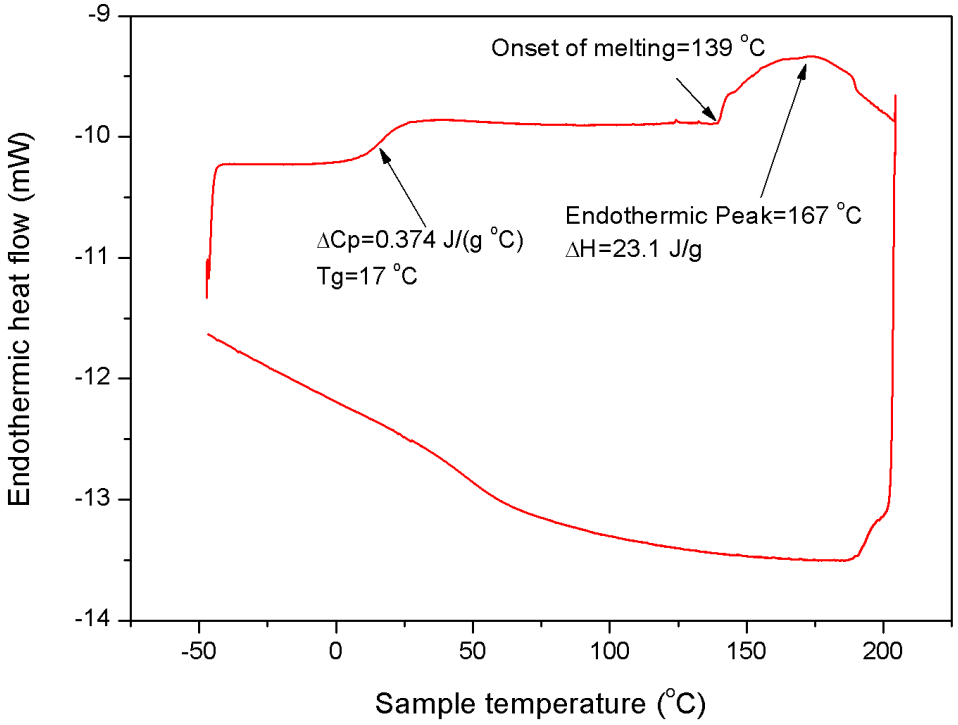


Figure 5-14: The DSC thermogram of the as-printed reactive mixture in DOX25.

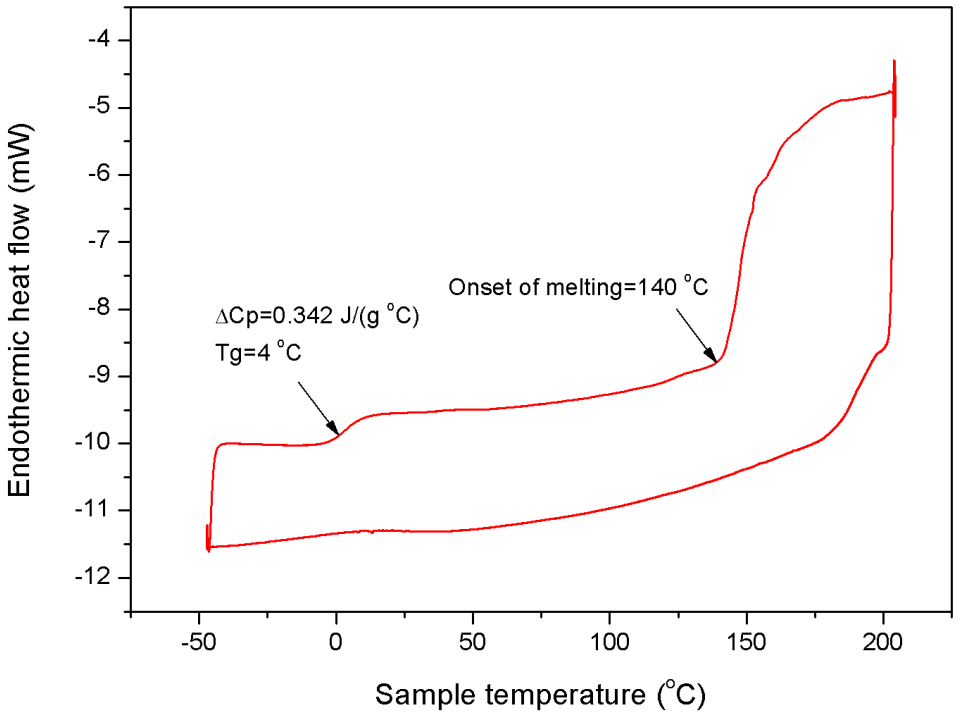


Figure 5-15: The DSC thermogram of the as-printed reactive mixture in DMF35

5.5. Summary

In this chapter, a reactive inkjet printing method for producing BPA-PC part by using solvent-based reactive inks was fundamentally investigated. The objective of this study was to formulate reactive inks with a printable composition using the reactive mixture (BPA, BMSC and the catalyst) for the melt polymerisation so that the reactive mixture could be directly deposited onto the substrate.

Two different compositions of the reactive inks were formulated with the 1, 4-dioxane and the DMF solvent, respectively (see Table 4-1 for the detailed ink formulations). The loading of the reactive mixture in the solvent was maximized to have less passes during printing whilst the printability was maintained. The viscosity and surface tension of DOX25 (with 25 wt% reactive mixture) and DMF35 (with 35 wt% reactive mixture) at 25, 35 and 45 ºC were found to be within the printable range. With a specific single waveform, the droplets were formed from a Dimatix material printer cartridge. To minimize the nozzle clogging due to solvent evaporation on the nozzle plate and to avoid the formation of satellite droplets, a cartridge temperature of 25 ºC for the both reactive inks was chosen for the continued printing experiments.

In the droplet deposition experiment, the both reactive inks were deposited on the microscope glass slide as single droplet arrays with different substrate temperatures according to the requirement for the solvent evaporation rate. It was found that the solvent evaporation rate was subject to the substrate temperature and the printing stand-off distance. To ensure the nozzle stability and continuity of the printed films, different droplet spacing and substrate temperatures were chosen to evaluate the quality of the printed films. Typically for DOX25 a continuous film could be formed with 30 μm droplet spacing on a surface of 60 ºC while for DMF35 a 15 μm droplet spacing could lead to a continuous film on a substrate temperature of 80 ºC.

The morphology of the printed single films was examined by the white light interferometer (See Figure 5-12). It showed a homogeneous film surface printed by DOX25. By contrast, DMF35 reactive mixture was found not evenly distributed on the printed film due to local heat flux and solute transfer. The multi overprints of the reactive mixture were attempted and the ‘dome’ structure was printed. The layer printed intermixed with the previously printed uncured layer to form the ‘dome’ structure. The DSC analysis of the as-printed reactive mixture showed the ‘dome’ structures were due to the relatively low glass transition temperature (17 ºC for the reactive mixture in DOX25, 4 ºC for the reactive mixture in DMF35). The further investigation on producing the PC with the desired molecular weight is discussed in the next chapter.

6. Results: Post Processing and Characterisations for BPA-PC

This chapter will focus on the post processing of the as-printed reactive mixture and a range of service property characterisations for the cured PC component including GPC, NMR, DSC, and TGA. The method of 3D reactive inkjet printing BPA-PC is also introduced to demonstrate the material capability for AM.

6.1. Introduction and Research Rationale

The reactive mixture was printed successfully as in a solvent-based ink formulation to demonstrate its printability. However, it showed a ‘dome’ shaped top surface of the multi overprints of the reactive mixture, due to the low glass transition temperatures of the PC oligomer. To have the final PC product, the as-printed reactive mixture must be post processed to enhance the molecular weight and to achieve the desired service properties.

The bulk process of melt polymerisation for the PC has been reported widely in the literature (177–179). None of these processes, however, were suitable for processing the micro-scale reactive mixture for PC since the geometry of the printed samples must be retained during the curing process. Therefore, a post-processing system, without destroying the geometry of the printed pattern, must be employed to accommodate the reaction environment for the melt polymerisation. In this research a vacuum oven was used to polymerise the as-printed samples. Analysis of the service quality of the final PC component produced by this post-processing method, including the chemical, thermal and mechanical properties, was also required. Finally, it was necessary to demonstrate the 3D printing capability of the PC material by an appropriate post-processing strategy which could potentially broaden the material library for AM.

6.2. Post Processing for As-Printed Reactive Mixture

In general, there are two strategies for the curing of the reactive mixture: polymerisation as a whole (i.e. to polymerise samples after all the layers are printed), or polymerisation layer by layer (i.e. to polymerise each layer before the next layer is printed). As it would be slower to produce a sufficient mass and volume of PC component by the second post-processing strategy, the first strategy was investigated here to produce the samples for the service property characterisations.

6.2.1. Post Processing for the Thin Films

There was a need to investigate the quality and stability of the thin films after post processing in the vacuum oven. For the both reactive inks, the 1 to 5 layers of 5×5 mm thin films were printed with the previously determined jetting parameters. The profiles of the thin films printed by the both reactive inks were shown in Figure 6-1 and Figure 6-3, respectively as the comparison between the as-printed and post-processed samples.

In Figure 6-1, it can be seen that the as-printed thin films by DOX25 have relatively flat surface profiles with sharp edge features. There were pinholes on the films observed after polymerisation, which was caused by the escape of the volatile by-product, i.e. methyl salicylate. With the increase of the number of layers printed, the effect of the pinholes became less significant which reasonably implied that the diffusion of the methyl salicylate during polymerisation was a mechanism for its escape. The edge of the 3, 4 and 5 layers thin films was observed to slightly recede inwards, which was likely due to a surface tension effect during the molten state (180).

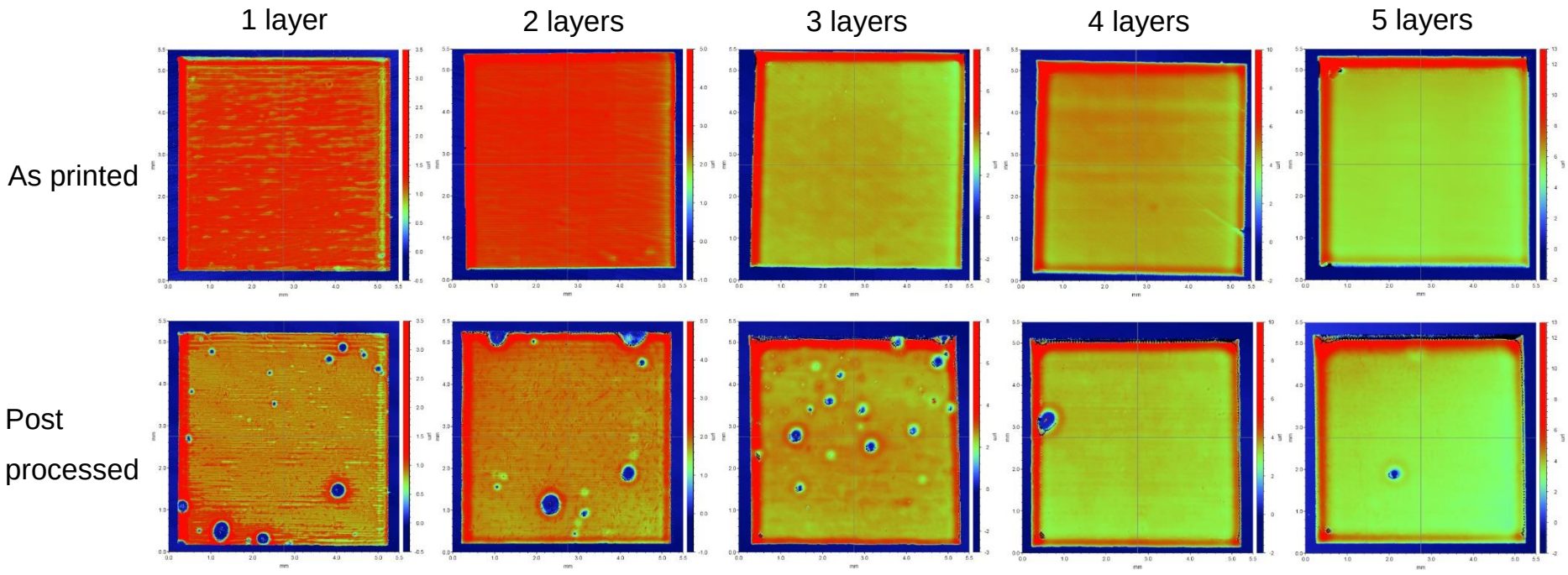


Figure 6-1: The comparison of 1 to 5 layers thin film surface profiles between the as-printed and post-processed samples produced by DOX25

The results in Figure 6-1 also show a decrease in the thickness of the post-processed thin films compared with those as-printed samples by DOX25. The change in the layer thickness was plot in Figure 6-2, and this thickness was reduced by 25.0%, 28.6%, 27.7%, 25.0% and 32.1% for the 1 to 5 layers thin films respectively. This reduction was expected because of the escape of methyl salicylate and the volatilisation of the monomer residue in the reactive mixture. This would be further validated by the TGA study in this chapter. A consequence of the thickness reduction would be the potential shrinkage of the structures. The shrinkage issues could be potentially addressed by controlling the reaction dynamics thus controlling the released rate of methyl salicylate. However, this may lead to the incomplete polymerisation. Further investigations could focus on the post-processing methods to rinse the by-product residue in the reaction system.

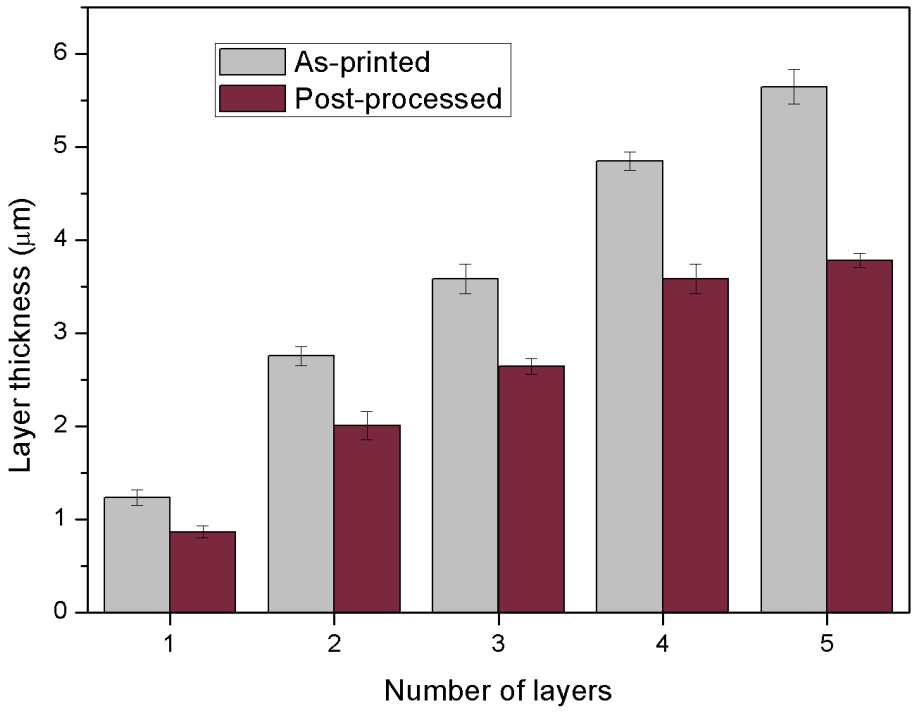


Figure 6-2: The comparison of the thickness of the thin films from 1 to 5 layers between the as-printed and the post-processed samples produced by the dioxane inks (average ± standard deviation, n=3)

Compared to the thin films printed by DOX25, those which were printed by the DMF35 showed non-flat surface profiles regardless of as-printed or post-processed samples, as seen in Figure 6-3. Typically, with 1 or 2 thin film-layers, the effect of depinning (i.e. receding of the film edge) was significant and leading to the non-homogenous and non-flat surface distribution. This indicated a weak interaction between the ink and the substrate, which was attributed to a low adhesive force between the deposited droplets and the substrate surface before the solvent evaporation could complete (181). With further printing of up to 5 layers, more stable films were produced as the depinning effect was mitigated; however, dome shaped surface profiles were created due to the low glass transition temperature as discussed in Section 5.4.3. It was reported that the movement of the contact line between the ink and surface was a resultant of pinning, ink-air interfacial tension and the gravitational force (80,119).

It was also noted in Figure 6-3 that the surface profile of the post-processed films differed from the as-printed DMF35 films. It was difficult though to quantify this difference by a single parameter of the whole layer thickness due to the dome shaped structures. A typical surface profile analysis of the 5 layers film was plotted in Figure 6-4 as a comparison between the as-printed and the post-process specimen. The edges receded approximately by 0.3 mm after post processing which was caused by surface tension during the melting stage of the reactive mixture. The top of the dome sunk from 73 to 54 μm, possibly resulting from the escape of the methyl salicylate. The entire surface also showed a much higher thickness when compared to those produced by DMF35, due to the higher loading of the reactive mixture.

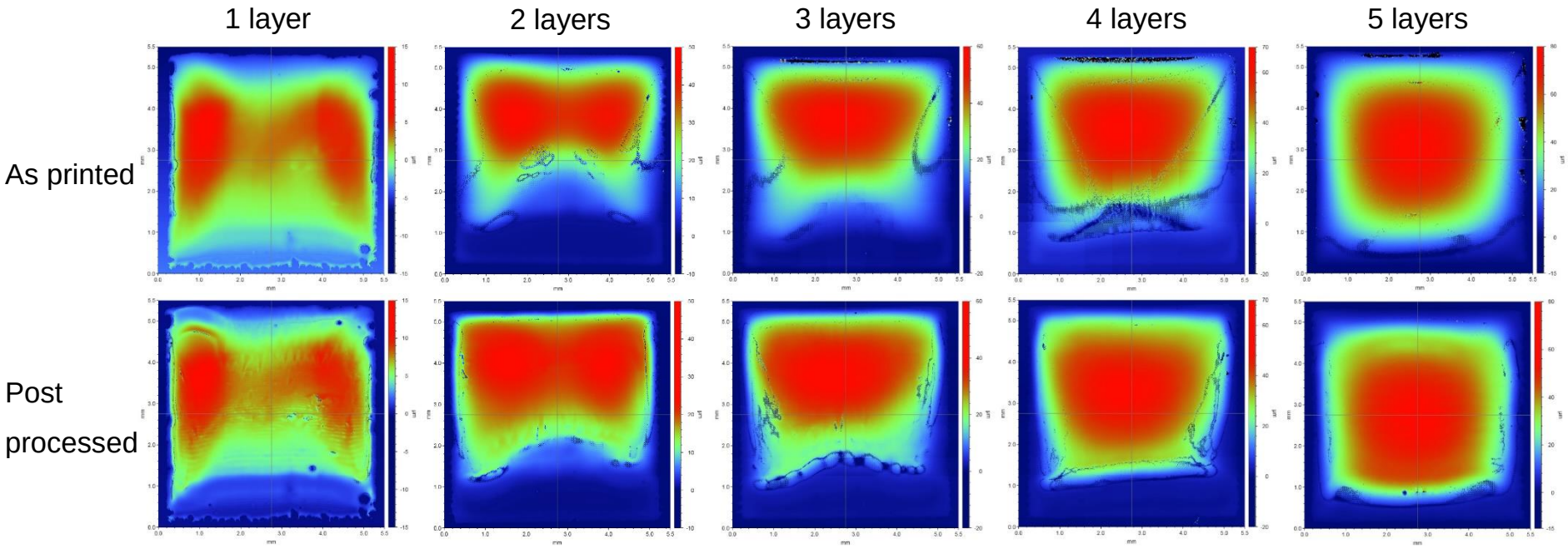


Figure 6-3: The comparison of 1 to 5 layers thin film surface profiles between the as-printed and post-processed samples produced by DMF35

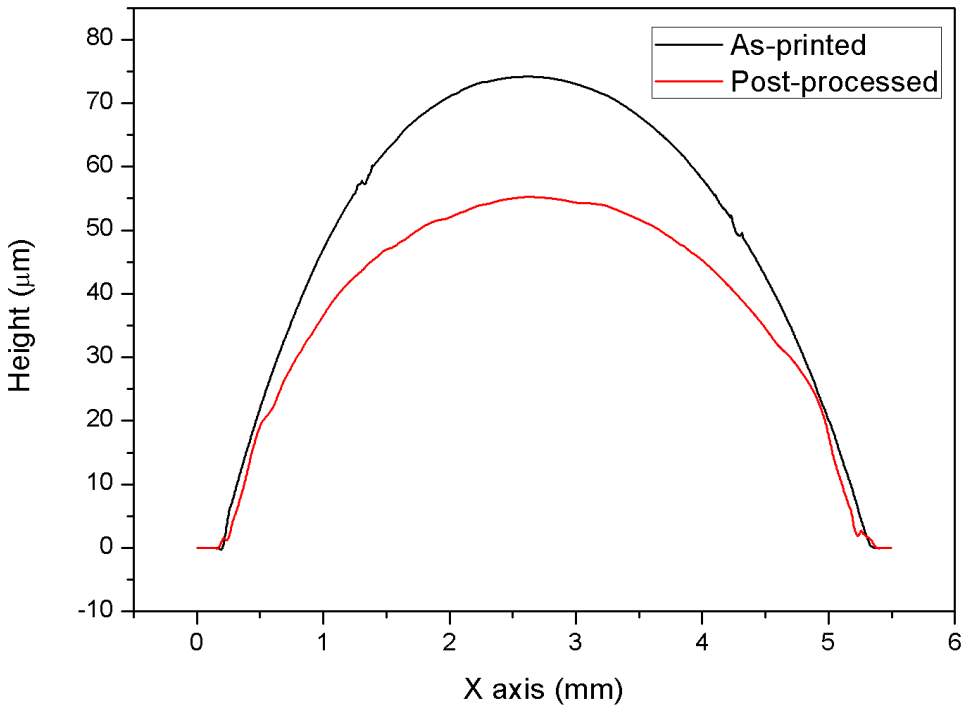


Figure 6-4: Surface profile analysis of 5 layers films produced by DMF35 as the comparison between the as-printed and the post-processed films

6.2.2. TGA Study for Melt Polymerisation

To further investigate the reduction of the film thickness after polymerisation, a TGA experiment was carried out to imitate the polymerisation environment and to study the polymerisation process. Approximately 5 mg of the as-printed 5 layers thin film sample was detached from the substrate and heated in the nitrogen atmosphere. A multi-stage isothermal profile was used to create the reaction conditions for the melt polymerisation, i.e. firstly the temperature was rapidly elevated to 180 ºC and then kept isothermal for approximately further 15 minutes; in the 2nd stage the temperature was raised to 220 ºC at about 10 ºC/min and then kept constant (15 minutes for the entire 2nd stage); then it was heated to 280 ºC at the same rate and then kept isothermal (10 minutes for the 3rd stage) to complete the polymerisation. By this method, the reduction of the film thickness as seen in the previous section was anticipated to be correlated to the weight loss of the reactive mixture.

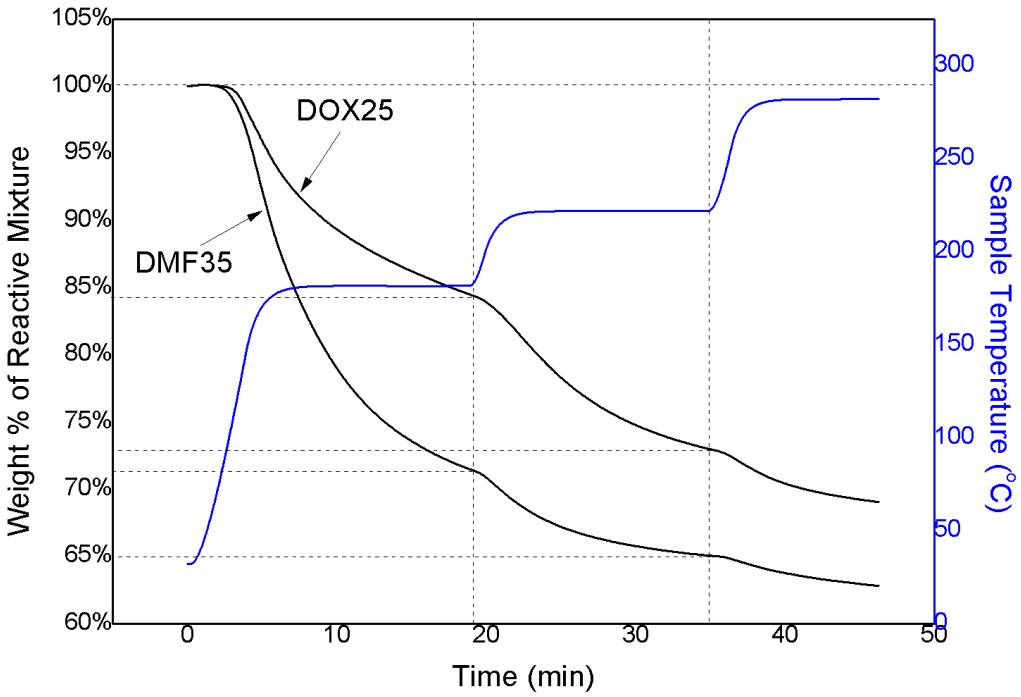


Figure 6-5: A multi-stage isothermal TGA curve for the melt polymerisation process of the as-printed thin film samples

Figure 6-5 shows the multi-stage isothermal TGA results for the as-printed thin film samples. There was about 15.7% weight loss for DOX25 printed samples during the 1st heating and isothermal stage, which corresponded to a combination of moisture loss and by-product volatiles (i.e. methyl salicylate and other volatiles) from the melt polymerisation. During the 2nd stage, the weight loss accounted for 11.3% indicating a continuous escape of methyl salicylate. The completion of the melt polymerisation at the final isothermal stage 280 ºC was associated with a weight loss of about 4.0% which was due to the increased viscosity of the PC polymer with the continuous increasing molecular weight. The total weight loss during the melt polymerisation for the dioxane inks sample was about 31.0% which was close to the 32.1% thickness reduction of the films aforementioned. Given that the thin films had a flat top surface and pinned contact lines with the substrate, the reduction of the thickness could be attributed to the weight loss during the polymerisation.

For DMF35 printed samples, the weight losses during the 3 isothermal stages also followed a reduced profile, which were 28.8%, 6.2% and 2.7% respectively, subject to the significant increase of polymer viscosity thus suppressed the escape of the methyl salicylate.

6.3. Chemical Characterisations

In order to evaluate the effectiveness of the post-processing method, the molecular weight enhancement of the PC component formed after polymerisation was characterised by GPC and the monomer incorporation to the PC polymer was characterised by NMR. This section reports the chemical characterisation results from the GPC and NMR experiments.

6.3.1. Study of BPA-PC Molecular Weight Growth

The post-processing treatment for the as-printed samples was to provide a suitable reaction environment for the melt polymerisation; therefore, the molecular weight could be built up and the mechanical properties could be improved. The GPC results are presented as number-average (M_n), weight-average (M_w) molecular weight and polydispersity ($Đ$) in Table 6-1.

Similarly, the degree of polymerisation (DP) was estimated by the equations following assuming the end-cap effect is negligible, and the results were presented in Table 6-2:

$$DP_w = \frac{M_w}{\bar{m}} \tag{6-1}$$

$$DP_n = \frac{M_n}{\bar{m}} \tag{6-2}$$

where DP_w and DP_n represent the weight-average and the number-average degree of polymerisation, and $\bar{m}$ is the molecular weight of the repeating unit

of the PC ($C_{16}H_{14}O_3$) which is 254 g/mol. The molecular weight of cast samples was measured to demonstrate the printing temperature effect on the initial oligomerisation of the reactive mixture. For DOX25, the DP_w of the ink formulation before printing was about 2.2 which indicated a low degree of oligomerisation, and the as-printed sample did not show a significant increase of DP_w which suggested the printing temperature (60 ºC) did not evidently favour the oligomerisation. In addition, the DP_w for DMF35 showed a limited increase from 4.3 to 10.2 when depositing the reactive mixture onto the 80 ºC substrate, which implied a limited facilitation of the substrate temperature to the oligomerisation with the DMF solvent system due to the fast evaporation rate of the solvent.

However, as a polycondensation reaction, *Đ* below 2 is generally considered low yield of the products. It was likely to be the low amount of catalyst used in the reaction system thus the conversion of monomers was low. In addition, it was possible that the fractionation of the GPC results led to the underestimated molecular weight and distribution. Future studies are recommended to explore the phenomenon and improve the yield of polymers.

Table 6-1: Molecular weight and polydispersity index (PDI) of different reactive inks compared to the reference PC materials produced from the bulk polymerisation

	Cast [a] (M_w/M_n/$Đ$)	**As-printed (M_w/M_n/$Đ$)**	**Polymerised (M_w/M_n/$Đ$)**
DOX25	550/500/1.10	650/550/1.18	53200/27800/1.91
DMF35	1100/950/1.16	2600/1900/1.37	29700/17400/1.71
Low PC [b]	N/A	N/A	20700/14400/1.44
High PC	N/A	N/A	30700/20800/1.48

a. The cast samples indicated the properties of the original reactive mixtures in the solvent, which were produced by pipetting the reactive inks droplets onto a 10 × 10 × 0.1 mm stainless steel recessed plate and then evaporating the solvent without heating for 2 days.

b. Reference PC was the polymer synthesized by SABIC Innovative Plastics lp B.V. and was graded as the Low M_w PC (relatively low molecular weight) and the High M_w PC (relatively high molecular weight).

Table 6-2: Degree of polymerisation for the reactive samples and reference PC materials

	Cast DP_w/DP_n	**As-printed** DP_w/DP_n	**Polymerised** DP_w/DP_n
DOX25	2.2/2.0	2.6/2.2	209.5/109.5
DMF35	4.3/3.7	10.2/7.5	116.9/68.5
Low M_w PC	N/A	N/A	81.5/56.7
High M_wPC	N/A	N/A	120.9/81.9

For the both reactive inks they exhibited a significant enhancement of the molecular weight after the polymerisation stage. When compared to the reference commercial PC materials which were synthesized by the bulk polymerisation, the polymerised DMF35 samples had a comparable molecular weight to the 'High PC' grade, and DOX25 samples had a much greater molecular weight to the 'High PC' grade. It is proposed by previous chemistry focused work that melt polymerisation followed a transesterification mechanism (164)(182). Therefore, the difference between the molecular weights using the two different solvents during the reaction could possibly be explained by this mechanism. As DMF is a polar aprotic solvent, it may attack the intermediates which contain a positive-charge, so the reaction rate is slowed; while the dioxane is a non-polar solvent which will not hinder the polymerization.

6.3.2. NMR Spectroscopic Analysis for BPA-PC

The ^{1}H-NMR spectra for the samples from DOX25 and DMF35 are presented in Figure 6-6 and Figure 6-7, respectively. There was minor alteration of the chemical shifts between the cast and the as-printed samples, which is in a good agreement with the GPC results where the substrate temperature did not contribute significantly to the oligomerisation. The successful polymerisation of BPA-PC was confirmed by the observation of the resonance intensity increase at 1.70 ppm which was assigned to the protons on the methyl group at the repeating unit of BPA-PC. In addition, the existence of a resonance at 3.95

ppm was attributed to the protons of the methyl group on methyl salicylate, suggesting polymerisation occurred even before the post-processing stage. The significant attenuation of the resonance at 3.95 ppm in the polymerised samples indicated the removal of methyl salicylate by the elevated temperature and the vacuum environment. Also the ^{13}C-NMR spectra as shown in Appendix A also proved the synthesis of BPA-PC from the post-processing stage, which showed the appearance of the carbonate group resonance signal at 148.96 ppm, and the resonances at 120.34 and 127.94 ppm assigned to the unsubstituted aromatic carbons (183).

In addition, the appearance of the peak at 3.73 ppm (i.e. the protons in $–CH_2$ on 1, 4-Dioxane, as seen in Figure 6-6) in the cast and as-printed samples implied that a least a portion of the solvent did not effectively evaporate off by the sole heating from the substrate. The solvent might be trapped in the deposited reactive mixture due to a limited mass transfer rate, and it was removed by the post processing as the solvent peak disappeared in the polymerised samples. Similarly, the evaporation of DMF was not complete (i.e. the proton resonance of –CH at 8.04 ppm, and the proton resonances of *trans*- and *cis*- methyl groups at 2.98 and 2.91 ppm, as seen in Figure 6-7) until polymerised in the elevated temperature and vacuum environment.

Table 6-3: ^{1}H-NMR data for the cast, as-printed and post-process BPA-PC, $CDCl_3$, 300 MHz

ID	Assigned H	δ H (ppm)
a	CH_3 (3H)	1.70
b	CH (1H)	7.28
c	CH (1H)	7.18
d	CH_3 (3H)	3.95
e	CH_2 (2H)	3.73
f	CH_3 (3H)	2.98
g	CH_3 (3H)	2.91
h	CH (1H)	10.78

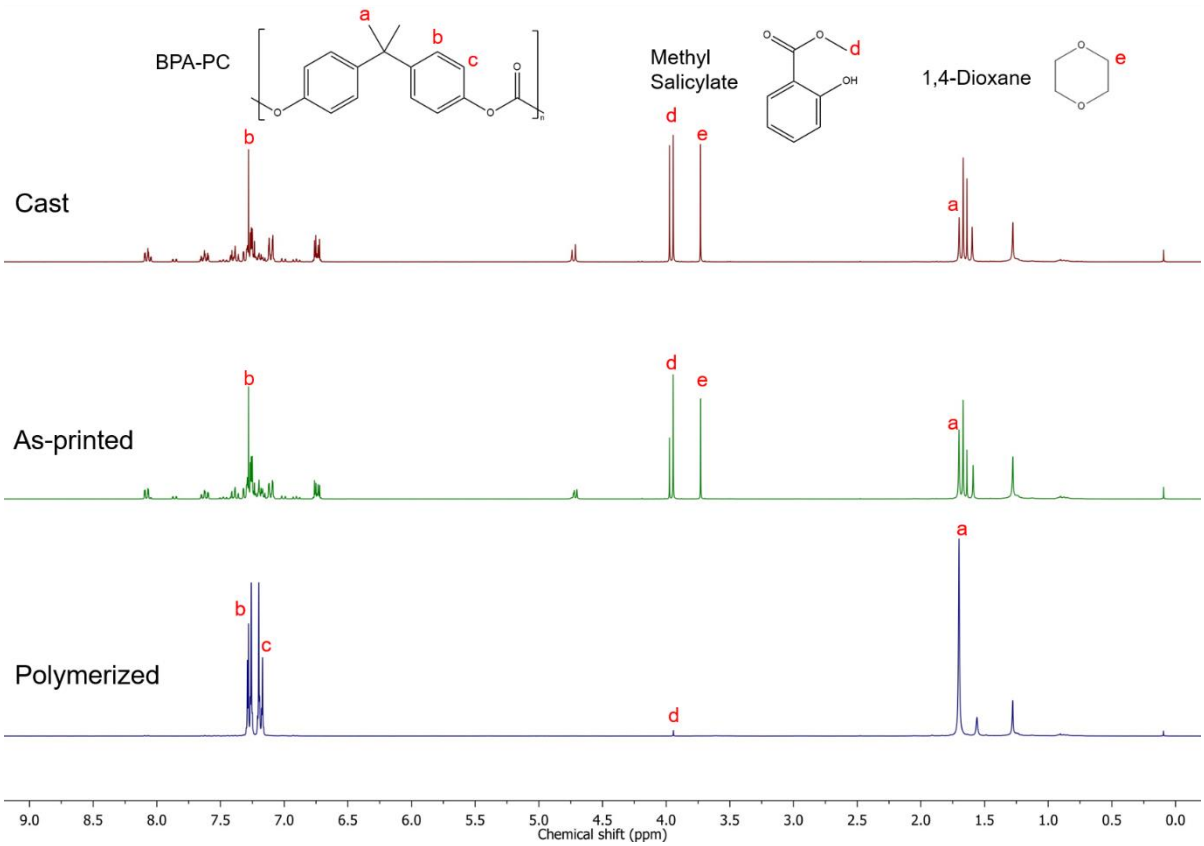


Figure 6-6: The ^{1}H-NMR spectra for the samples from DOX25, $CDCl_3$, 40 ºC

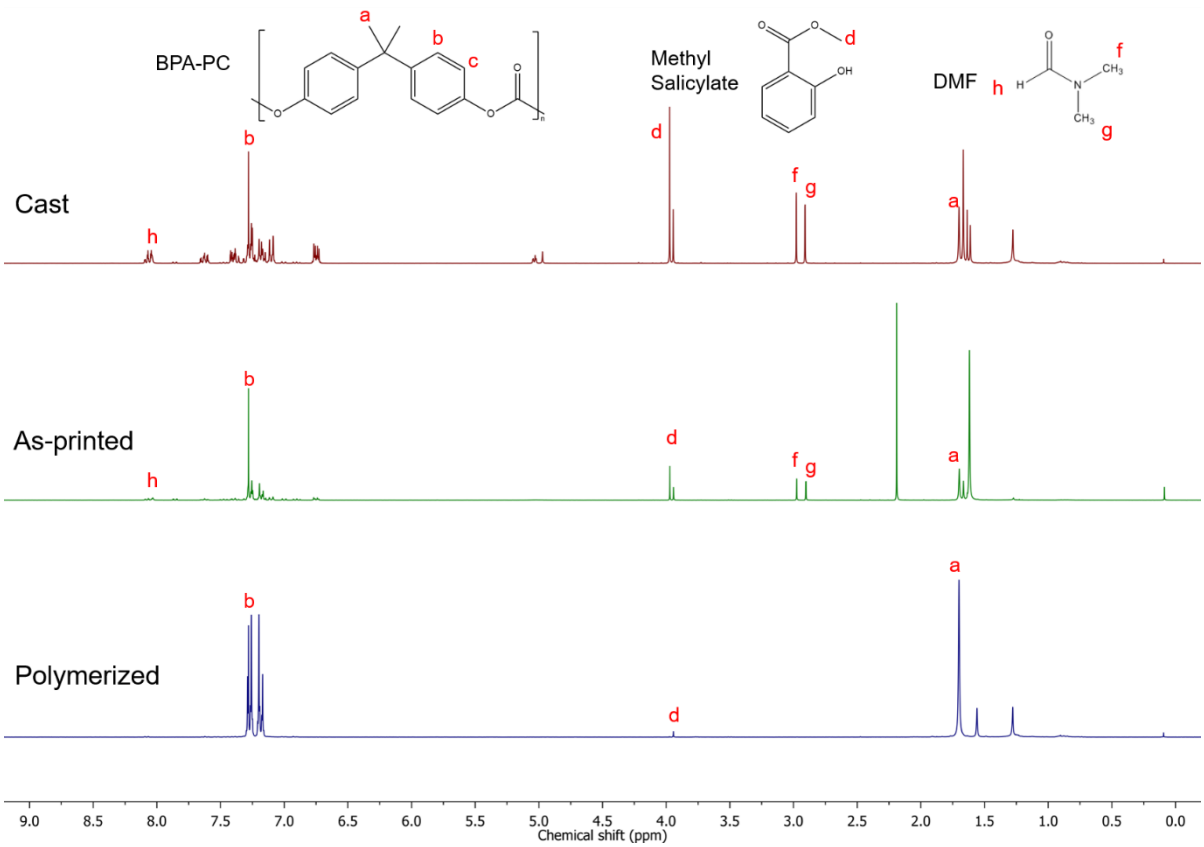


Figure 6-7: The ^{1}H-NMR spectra for the samples from the DMF35, $CDCl_3$, 40 ºC, 300 MHz

6.4. Thermal Characterisations

The BPA-PC features in a material with a high temperature tolerance because of its relatively high glass transition temperature (T_g above 140 ºC). Therefore the T_g of the polymerised PC samples after the vacuum oven treatment was measured by DSC to evaluate its thermal properties, as well as the reference PC samples for comparison. In addition to T_g measurement, the thermal degradation of the BPA-PC at different heating rate was studied by TGA to assess its thermal stability compared to the traditional BPA-PC synthesized from the bulk process of melt polymerisation.

6.4.1. DSC Study for BPA-PC

The response of PC to application of heat was assessed by DSC to evaluate its service temperature range. A thermal cycle of 0-360-0 ºC at 20 ºC/min in the nitrogen environment was used to obtain the T_g from the DSC thermogram by 'half Cp' method. At the highest temperature (360 ºC) an isothermal scan for 5 minutes was also introduced to erase the possible thermal history and to ensure the entire sample in the DSC pan was thermally equilibrated. Approximately 5 milligrams of the polymerised PC from the vacuum oven treatment or the reference PC sample was taken for each measurement of DSC. The DSC thermograms of different samples were shown in Figure 6-8 and the T_g were summarized in Table 6-4.

As shown in Figure 6-8, the thermograms of the both PC samples from the inkjet printing were similar to those from the reference PC from bulk polymerisation. In the heating stage, the DOX25-PC and DMF35-PC exhibited a single thermal shift; in the cooling stage the both samples showed a reverse thermal shift in the same temperature range. In addition, melting peaks were not observed in the full thermal cycles. All those facts indicated the amorphous state of the PC from the post-processing treatment.

The T_g values were summarized in Table 6-4. Although the M_w of DOX25-PC was higher than the reference high M_w PC as previously shown in the GPC results, the measured T_g by this method was not accordingly higher which might indicate that the T_g measurement was affected by the microstructure of the samples (i.e. reactive printed PC film samples v.s. the granular reference PC samples) (184) . It was still evident that the T_g of polymerised PC samples from RIP was close to the reference PC samples, suggesting a similar service temperature range at which the polymerised PC could be handled.

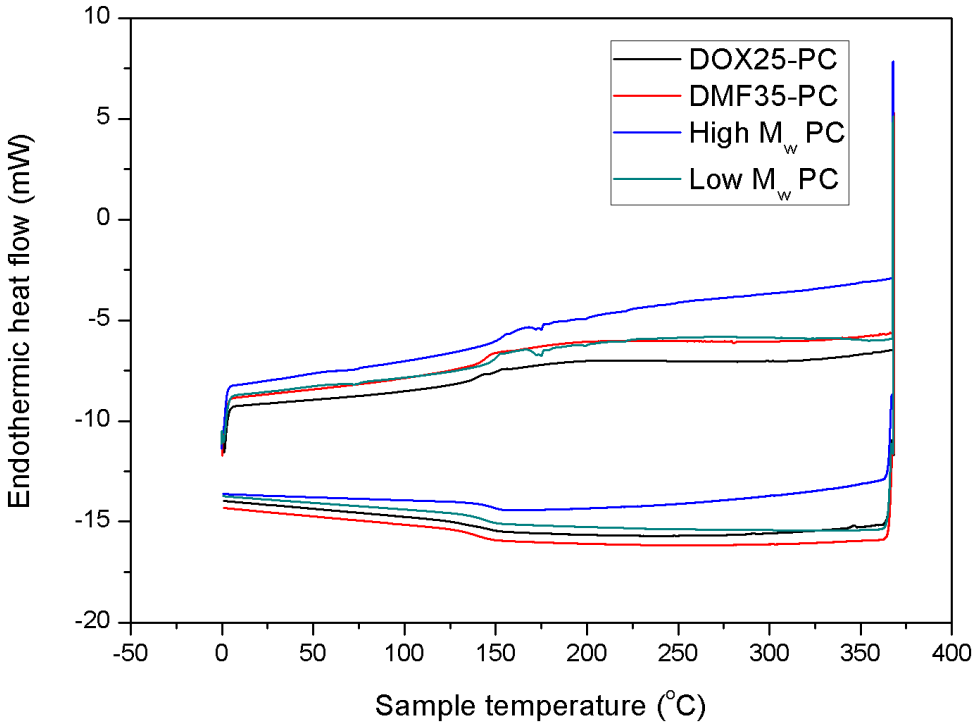


Figure 6-8: The DSC thermogram of the polymerised PC samples as a comparison among the DOX25-PC, DMF35-PC, reference high M_w PC and low M_w PC

Table 6-4: The T_g values of the PC samples from the DSC thermogram

	DOX25-PC	DMF35-PC	High M_w PC	Low M_w PC
T_g (ºC)	144	141	151	149

6.4.2. Thermal Stability Analysis of BPA-PC by TGA

The thermal stability of BPA-PC was studied by TGA to understand its degradation characteristics at the high temperature. TGA was carried out at various heating rates from 10 to 40 ºC/min in a nitrogen flow of 20 mL/min. The temperature swept from 30 to 800 ºC and the sample size was between 15 to 20 milligrams. The samples included the DOX25-PC, DMF35-PC and the two grades of reference PC samples.

The results of TG and DTG curves of the PC made from the two reactive inks were given in Figure 6-9 and Figure 6-10. TG and DTG curves for the reference PC samples have been included in Appendix B. All the corresponding data of sample mass were summarized in Table 6-5. The TG curves of all samples showed a one-step thermal degradation process and one peak rate was observed from the DTG curves. Among the PC samples made from the two reactive inks at 40 ºC/min heating rate, T_0, $T_{5\%}$ and T_{max} of DMF35-PC were slightly higher than those of DOX25-PC by 5 to 11 ºC. The similar difference of the degradation temperatures was also observed at the heating rate of 20 ºC/min and 10 ºC/min. It indicated the different thermal degradation properties of PC by using the two different solvents for the reactive printing. However, the difference was probably also subject to the higher heat transfer across the samples as the porous surface of DMF35-PC samples were observed due to the more aggressive escape of methyl salicylate. The two grades of the reference PC samples showed similar thermal degradation characteristics compared to other commercial PC samples (185)(186) and significant higher T_0, T_{max} and Y_c than those of reactive printed PC samples, as shown in Table 4-5. It suggested the further improvement for the thermal stability of PC made from the reactive inkjet printing and the proposed post-processing method, and it also required a detailed study of the char and volatile products from the TGA.

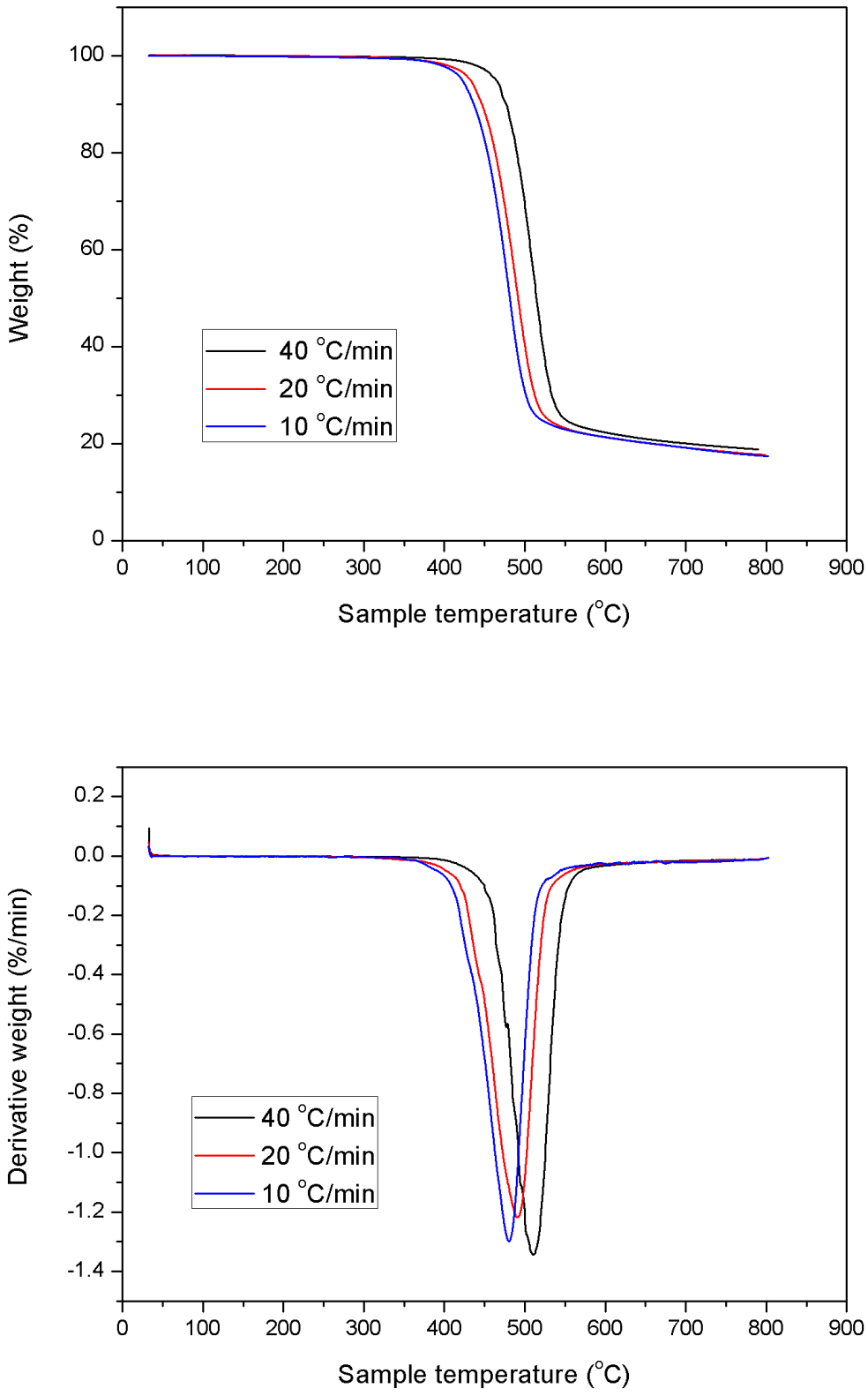


Figure 6-9: The TG and DTG curves of DOX25 at different heating rates in a nitrogen environment

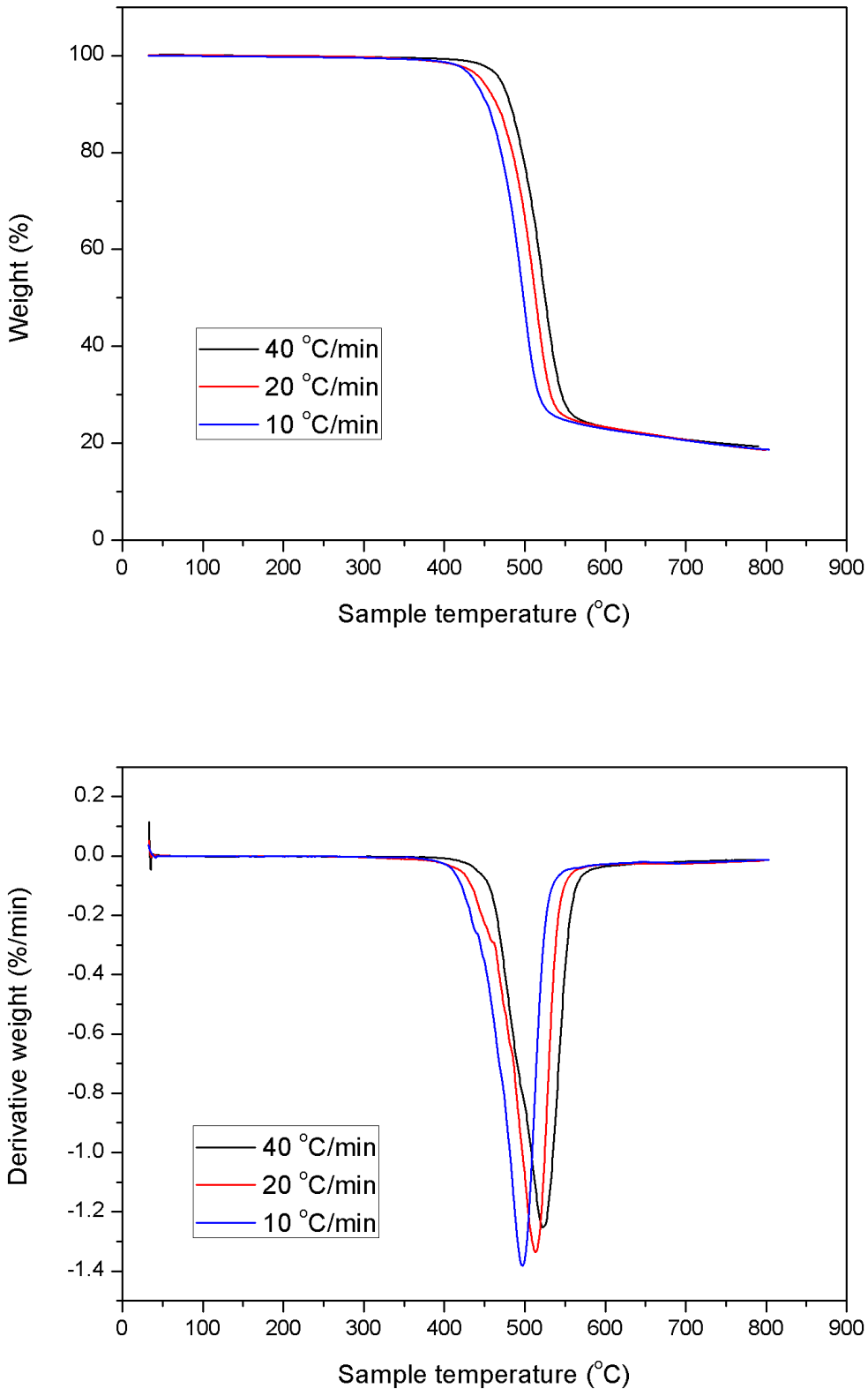


Figure 6-10: The TG and DTG curves of DMF35-PC at different heating rates in a nitrogen environment

Table 6-5: The thermal data obtained from the TG and DTA curves

Sample	Heating rate (ºC/min)	T_0 [a] (ºC)	$T_{5\%}$ [b] (ºC)	T_{max} [c] (ºC)	Peak rate (%/min)	Y_c [d](%)
DOX25-PC	40	416	464	511	1.35	18.8
	20	373	432	490	1.22	17.7
	10	371	422	481	1.30	17.4
DMF35-PC	40	424	469	522	1.25	19.4
	20	377	446	513	1.34	18.6
	10	383	436	497	1.38	18.6
High M_w PC	40	489	521	554	1.93	24.3
	20	469	505	539	1.49	24.9
	10	445	489	525	1.55	24.3
Low M_w PC	40	470	522	559	1.46	24.8
	20	456	497	539	1.60	25.1
	10	443	484	523	1.70	23.6

a. T_0 is the onset of degradation, and recorded as the temperature at which the sample had 1 wt% loss

b. $T_{5\%}$ is the temperature at which the sample had 5 wt% loss

c. T_{max} is the temperature at which the sample had the maximum rate of weight loss

d. Y_c is the yield of char residue

6.5. 3D Reactive Inkjet Printing of BPA-PC

The previous post-processing strategy of ‘polymerisation as a whole’ showed a dome-shaped top surface of the multi-layer printed BPA-PC structure, which was impossible to repeat the successive layers with the flat top surface. An example of the thick film post-processed by this mean was shown in Figure 6-11. With the purpose of demonstrating the capability of building a 3D structure of BPA-PC with high resolution features using the reactive inkjet printing technique, the second post-processing strategy, ‘polymerisation layer by layer’ (i.e. to polymerise each layer before the next layer is printed) was explored to determine the topographic feature profile of the 3D structure.

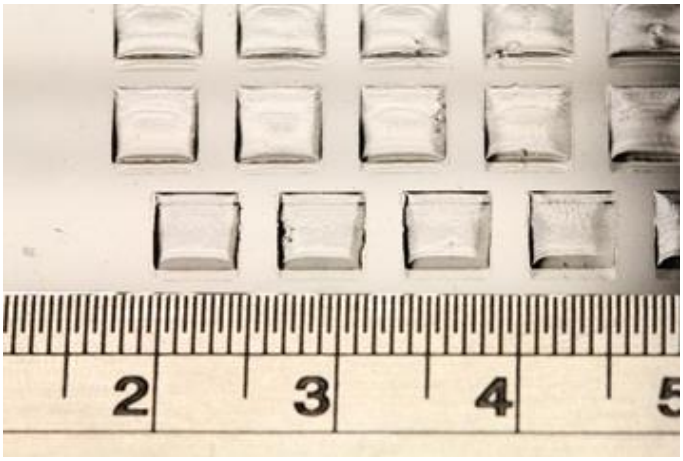
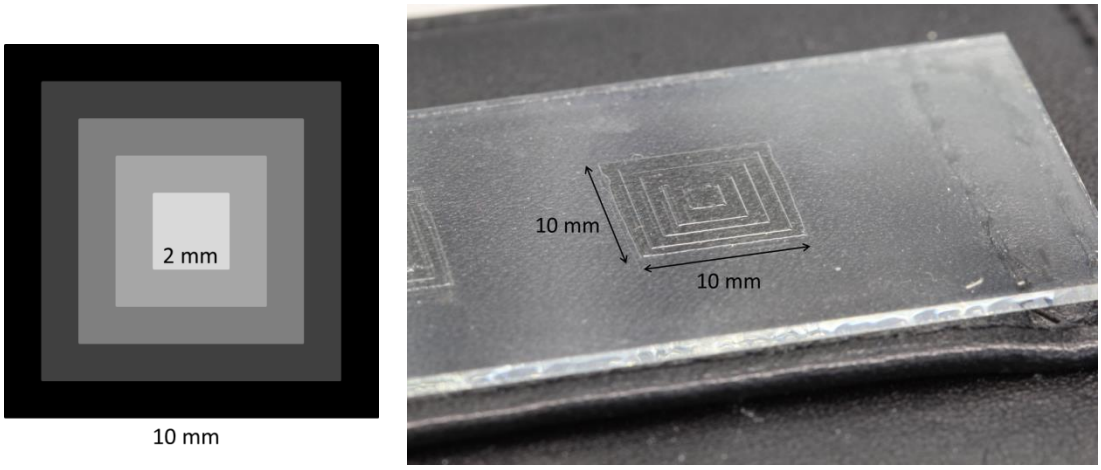


Figure 6-11: An example of the 40 layers thick PC film printed DOX25 and post-processed by the 'polymerisation as a whole' approach

6.5.1. The Design of the 3D Printing Pattern

To illustrate the capability of 3D printing, a 5-step ziggurat structure was designed, where the bottom layer had a dimension of 10 × 10 mm with a uniform decrement to the top layer of 2 × 2 mm as shown in Figure 6-12(a). There was either 1 or successive 5 layers printed in each step to determine the effect of the step height on the profile. The structure was post processed using the polymerisation method described in Table 6-1 before the consequent step was printed onto it. It showed previously that the thin film printed by DOX25 had a flat surface whereas the one printed by DMF35 was not flat possibly due to the low rate of evaporation and the effect of the heat flux on the solute transfer. It was also noted that the white film around the nozzle plate would detach, causing damage to the cartridge, if DMF35 were kept in the cartridge for several hours. This implies the incompatibility of the DMF solvent with the Dimatix jetting unit. Therefore only DOX25 was attempted to ensure the flatness of the steps and the reliability of the jetting, to demonstrate the 3D printing capability. Figure 6-12(b) shows a printed ziggurat structure with 5 layers per step.



(a) (b)

Figure 6-12: The designed ziggurat structure to demonstrate the 3D printing capability: (a) the ziggurat bitmap design for the Dimatix printing pattern; (b) the printed ziggurat structure (5 layers per step, 25 layers in total)

6.5.2. The Surface Profile Analysis of the 3D Printed Structure

The surface profile analysis results for the ziggurat structures were shown in Figure 6-13. The boundaries and heights of each step were clearly distinguished as each step could be built on the previous step which was fully cured after post processing in the vacuum oven. The results could be used to determine the step height and the surface uniformity therefore to evaluate the topographic feature of the structure printed by the method. For example, the ziggurat which had 1 layer printed for each step had a flatter feature in the X direction (printing direction) while the Y direction showed a waviness as shown in Figure 6-13(a). The cause for this different variation in X and Y directions was that no sufficient reactive mixture in a one single layer would be able to spread over to have the uniform distribution. It was also noted that the bottom step had voids which was due to the repeated heat treatment for 5 times and that it caused depinning during the molten state. The voids formation was also likely to be facilitated by the escape of methyl salicylate from the thin layer. As for the ziggurat that had 5 layers per step as shown in Figure 6-13(b), the surface showed more flat and uniform topography across X and Y directions for each step. No significant de-pinning phenomenon was

seen on the surface, but the edge of the bottom step receded due to the surface tension effect.

The surface profile of the ziggurat showed an increased step height from the bottom to the top step. For example, the step height increased from approximately 0.8 µm at the bottom step to 1.4 µm at the top step for the ziggurat structure with 1 layer per step; while the ziggurat with 5 layers per step had a step height in the range of 5 and 7 µm. The main cause of this was likely to be the more exposure of the bottom steps to the polymerisation environment compared to the top steps, leading to the volume reduction due to the escape of methyl salicylate. In general, the step height was able to be varied by the number of layers printed.

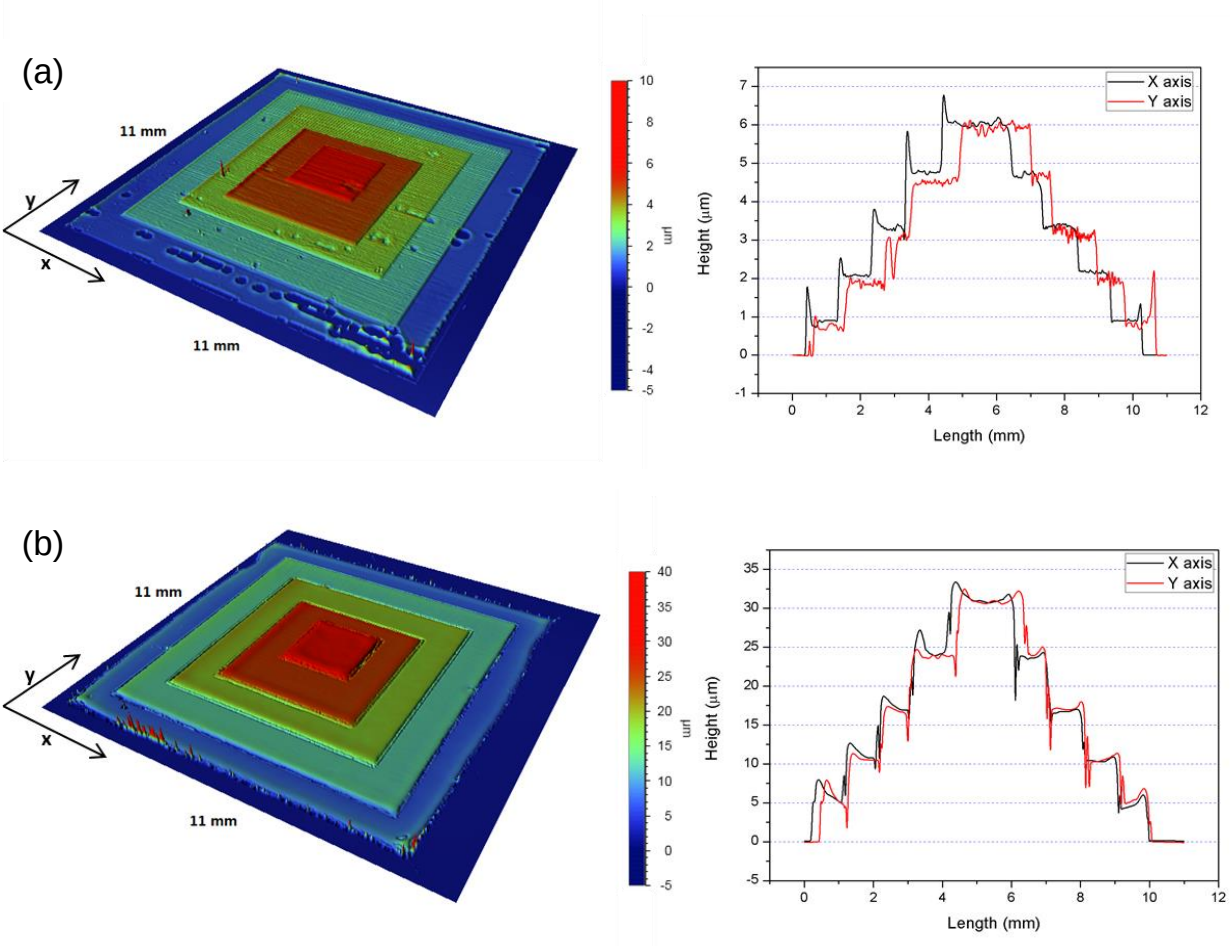


Figure 6-13: The surface profile analysis for the 3D ziggurat structure using Bruker Contour GT by the 'polymerisation layer by layer' approach: (a) 1 layer per step; (b) 5 layers per step

6.6. Summary

This chapter reported two post-processing methods to polymerise the reactive mixture which was deposited on the substrate by the inkjet printhead. The 1st post processing strategy of 'polymerisation as a whole' was investigated using a vacuum oven to create the high temperature (up to 280 ºC) and the vacuum (0.5-1.5 mbar) environment. The polymerised thin films produced by DOX25 had relatively flat surface morphology while the one produced by DMF35 had non-flat surface feature. But printing with either ink would produce a dome shaped top surface of the thick films due to layers merging before polymerised as a whole. It was also found the film would be subject to the volume and mass reduction after polymerisation due to the generation and escape of the by-product, methyl salicylate.

The samples post-processed by the 'polymerisation as a whole' approach were characterised in terms of their chemical composition and thermal properties compared with the commercial reference samples. The molecular weight of the polymerised BPA-PC samples was found to be comparable to the commercial PC and the NMR spectroscopic analysis confirmed the structure of the BPA-PC. The DSC study showed that the glass transition temperature was close to that of commercial materials. The TGA study suggested a need for the further development of the thermal stability.

Finally, the 2nd post-processing strategy, 'polymerisation layer by layer', was explored to show the 3D printing capability for reactive inkjet printing of BPA-PC by printing a stepped ziggurat structure. It was found by the surface analysis that the uniform distribution of the layer surface could be achieved by printing multiple layers for each step. In addition, those results revealed that the step height was able to be controlled by the number of layers printed and it was also subject to the polymerisation process.

7. Conclusion and Future Work

7.1. Conclusion

This thesis has investigated two different Reaction Inkjet Printing methods to fabricate BPA-PC parts. With the experimental results and analysis, the key findings of the research are concluded as following:

Reactive Inkjet Printing Study of Hot-melt Inks

- The direct jetting of the mixture of BMSC and BPA was found not to be possible with a piezoelectric inkjet printing assembly as the viscosity of the molten mixture was much greater (up to 53 cP) when compared to the pure molten monomers, due to the formation of the BPA-PC oligomer leading to the polymer chain entanglement.

- The printability of BMSC as molten liquid was demonstrated with an Océ Crystalpoint^{TM} print head at 120 ºC which was slightly higher than its melting temperature to keep it sufficiently liquefied. The waveform for actuating the inkjet was optimized to achieve a stable and satellite-free droplet formation. The droplet speed and volume were found to be linearly controlled by the jetting voltage. The printed thin-films were found to have an average thickness of 15 μm with *Ra* of 3.9 μm.

- The printability of BPA as molten liquid was also demonstrated with an Océ Crystalpoint^{TM} print head at 170 ºC. The droplets were found to have end-pinched effect which was not eliminated by the optimisation of the waveform, possibly due to the compromised performance of the piezo-ceramics beyond its Curie temperature. The continuous films were expected to be printed with a droplet spacing less than 36.3 μm (700 dpi) but further experimentation was suspended due to the failure of the print head resulting from overheating.

Reactive Inkjet Printing Study of Solvent-based Inks

- Two solvent-based reactive inks (DOX25, DMF35) were formulated using the reactive mixture (BPA, BMSC and TMAH) and two different solvents (dioxane, DMF). The loadings of the reactive mixture were maximized by the investigation of the solubility, which were within the printable range (i.e. $1<Z<10$).

- The droplet formation of the solvent-based reactive inks was observed by the printer's drop watcher camera at 25, 35 and 45 ºC, respectively. It was found that the temperature had an effect on the droplet formation to have different scenarios. Generally, the tail of the droplet was able to merge with the leading droplet at 25 ºC and no satellites were found. However, a long tail was observed when the temperature raised up to 35 and 45 ºC for the both inks and satellite droplets were found for DOX25. It was concluded that stable droplet formation was achieved at 25 ºC for the both inks.

- The spreading diameters of DOX25 droplets were found to be similar between a substrate temperature of 50 and 70 ºC due to the limited change of solvent evaporation rate within this temperature range. The spreading diameters of DMF35 droplets were greatly affected by the substrate temperature between 70 and 90 ºC possibly because the droplet experienced less time for spreading at higher temperature to have a smaller size.

- The 1-layer thin film printed by DOX25 at a substrate temperature of 70 ºC were found to have a flat surface morphology with boundaries between the printed threads due to solvent evaporation and reactive mixture precipitation. The 1-layer thin film printed by DMF35 at a substrate temperature of 80 ºC was found to be in-homogeneous in terms of the reactive mixture distribution which was possibly caused by

the different solvent evaporation rate due to heat flux. The continuity of the films could be reduced if the substrate temperature was further increased, which was due to the nozzle instability to have unpredictable droplet formation failure. The different droplet spacing was also investigated to print continuous and stable films.

- The direct overprints of multilayer thick films were attempted, and the dome shaped structure was observed. The DSC investigation confirmed that the dome shaped resulted from the low glass transition temperature of the as-printed reactive mixture.

Post Processing and Characterisations for BPA-PC

- Post-processing using a vacuum oven was investigated to polymerise the as-printed samples to the final BPA-PC components. Using a 'polymerisation as a whole' strategy (i.e. to polymerise samples after all the layers are printed), the surface morphology of thin film samples (1-5 layers) were characterised. The thin films printed by the both reactive solvent-based inks showed a reduction of film thickness after post processing, which were also correlated to the weight loss characterised by the TGA study. Some cavities were seen on the film surface due to the escape of methyl salicylate and the effect of surface tension. The thin films printed by DOX25 showed a flat-top surface whilst the thin films printed by DMF35 showed a non-flat top surface.

- The GPC characterisations of the post-processed samples showed a larger molecular weight (DOX25-PC) or a comparable molecular weight (DMF35-PC) when compared to the commercial reference BPA-PC samples. The ^{1}H-NMR and ^{13}C-NMR spectra confirmed the formation of the BPA-PC with the post-processing method. The DSC study showed the similar glass transition temperatures of the post-processed BPA-PC

product with the commercial ones. The TGA results showed the thermal degradation temperature of the post-processed BPA-PC was lower than the commercial samples.

- Using a ‘polymerisation layer by layer’ (i.e. to polymerise each layer before the next layer is printed) post-processing strategy, a 3D stepped ziggurat structure using DOX25 was printed with either 1 or 5 layers per step. The surface profile analysis showed the layer flatness and a clear stepped feature of the structure, which demonstrated the capability of the 3D printing BPA-PC by RIP.

7.2. Future Work

Due to the time constraint for the research, some parts of the project could not proceed further. However, this research has established a solid foundation for the future work developed upon the 3D printing of BPA-PC by RIP. A few potential considerations are recommended as following:

- A printhead assembly which has a higher temperature limit is required to further investigate the promising hot-melt inkjet printing of BPA. The aim is to obtain stable droplet formation and to print the pattern with high repeatability. After the printability of BMSC and BPA are fully demonstrated, a dual-head system is expected to be customized to enable the alternative deposition of molten BMSC and BPA and its *in-situ* polymerisation. Due to the hot-melt nature of the materials, support materials with high temperature tolerance are also to be explored to expand the design freedom.

- For this research, a heating system up to 280 ºC and a vacuum system for the *in-situ* polymerisation were not mounted within the printing

chamber due to the lack of an efficient cooling system, which resulted in a separate vacuum oven for the polymerisation. The integration of the printing system and the post-processing unit is desired in order to allow in-process production of the BPA-PC and scale-up of the process in the future. With a proper design and installation of the cooling system, a heating unit such as a radiation heater to illuminate the printed samples on demand could be placed next to the printing area. A vacuum system can be also equipped in the post-processing unit to apply the pressure when necessary.

- The characterisation and modulation of the mechanical properties of BPA-PC printed by the solvent-based inks are of great interest. The mechanical properties can be evaluated using the method such as a tensile test. The modulation of the mechanical properties can be correlated to the process parameters of the post processing, which require a detailed study of the reaction kinetics. This will help the production of the mechanical gradient components.

- Currently the BPA-PC attracts intensive demands for optical media, automotive lenses and roofing elements due to its excellent transparency. The optical performance of the inkjet printed BPA-PC is to be characterised and evaluated to consider the potential optical applications. A full optical measurement and study of BPA-PC is suggested to evaluate its optical properties including the colour, yellowness, gloss, haze and refractive index which can be correlated to the chemical formulation of the precursors, the thermal conditions for polymerisation and the morphology of the polymer.

- Pure polymer products built by AM normally result in the lack of mechanical strength and functionality. The production of the BPA-PC composite by RIP is desired to solve those problems. The further

variation of the reactive ink formulation should be investigated to illustrate the capability of printing the fibre reinforced BPA-PC composite by RIP, and the further mechanical characterisations of the BPA-PC composite are required to demonstrate the improvement of the mechanical strength and functionality.

- Melt polymerisation requires relatively long thermal residence time of up to 40 minutes to achieve the desired molecular weight, which lowers the printing efficiency and limits the structural design freedom. Alternative curing method to polymerise the BPA-PC can be investigated such as incorporating the photo-sensitive functional groups to the BPA monomer and carbonate source monomer to produce cross-linked UV curable BPA-PC. This UV curing characteristic will help the fast build-up of the 3D structure and realize additional design complexity to fabricate parts.

8. Reference

1. Horn TJ, Harrysson OLA. Overview of current additive manufacturing technologies and selected applications. Sci Prog. Science Reviews 2000 Ltd; 2012 Sep 1;95(3):255–82.
2. Ho HCH, Cheung WL, Gibson I. Morphology and Properties of Selective Laser Sintered Bisphenol A Polycarbonate. Ind Eng Chem Res. 2003 Apr;42(9):1850–62.
3. Senvol. PC materials results for material extrusion [Internet]. 2017 [cited 2018 Jan 17]. Available from: http://senvol.com/5_material-results/
4. ASTM F2792. Standard Terminology for Additive Manufacturing Technologies. ASTM; 2012. p. 3.
5. Gebhardt A. Understanding Additive Manufacturing: Rapid Prototyping, Rapid Tooling, Rapid Manufacturing. Hanser Publications; 2012. 164 p.
6. Gibson I, Rosen D, Stucker B. Additive Manufacturing Technologies: 3D Printing, Rapid Prototyping, and Direct Digital Manufacturing. 2nd ed. New York: Springer US; 2015. 498 p.
7. Calvert P, Crockett R. Chemical Solid Free-Form Fabrication: Making Shapes without Molds. Chem Mater. American Chemical Society; 1997 Mar;9(3):650–63.
8. Chua CK, Leong KF. 3D Printing and Additive Manufacturing: Principles and Applications. 4th ed. World Scientific Publishing Company Pte Limited; 2014. 518 p.
9. Jacobs P. Stereolithography 1993: epoxy resins, improved accuracy, and investment casting. In: Guenther AH, Higgs LD, editors. Coupling Technology to National Need. International Society for Optics and Photonics; 1994. p. 41–52.
10. Sachs E, Cima M, Cornie J. Three-Dimensional Printing: Rapid Tooling and Prototypes Directly from a CAD Model. CIRP Ann - Manuf Technol. 1990;39:201–4.
11. Crump S. Apparatus and method for creating three-dimensional objects.

U.S.5,121,329, 1992.

12. Feygin M. Apparatus and method for forming an integral object from laminations. U.S. 4,752,352, 1988.
13. Feygin M. Apparatus and method for forming an integral object from laminations. EP 0,272,305, 1994.
14. Feygin M. Apparatus and method for forming an integral object from laminations. U.S.5,354,414, 1994.
15. Pomerantz I, Cohen-Sabban J, Bieber A, Kamir J, Katz M, Nagler M. Three dimensional modelling apparatus. Israel; U.S. 4,961,154, 1990.
16. Wohlers T. History of Additive Manufacturing. In: Wohlers Report 2014. Colorado, USA: Wohlers Associates, Inc; 2014.
17. Prinz FB, Atwood CL, Aubin RF, Beaman JJ, Brown RL, Fussell PS, et al. Rapid prototyping in Europe and Japan-JTEC/WTEC Panel Report. Vol. 1. Baltimore: Rapid Prototyping Association of the Society of Manufacturing Engineers; 1997.
18. Kruth J-P, Leu MC, Nakagawa T. Progress in Additive Manufacturing and Rapid Prototyping. CIRP Ann - Manuf Technol. 1998 Jan;47(2):525–40.
19. Hornick J, Roland D. Many 3D Printing Patents Are Expiring Soon: Here's A Round Up & Overview of Them - 3D Printing Industry [Internet]. 3D Printing Industry. 2013 [cited 2015 Mar 5]. Available from: http://3dprintingindustry.com/2013/12/29/many-3d-printing-patents-expiring-soon-heres-round-overview/
20. Burns M. Automated fabrication: improving productivity in manufacturing. NJ, USA: Prentice-Hall, Inc.; 1993. 369 p.
21. Kruth JP. Material Incress Manufacturing by Rapid Prototyping Techniques. CIRP Ann - Manuf Technol. 1991 Jan;40(2):603–14.
22. Pham D., Gault R. A comparison of rapid prototyping technologies. Int J Mach Tools Manuf. 1998 Oct;38(10–11):1257–87.
23. Noorani R. Rapid Prototyping: Principles and Applications. John Wiley; 2006. 377 p.

24. Cooper K. Rapid Prototyping Technology: Selection and Application. CRC Press; 2001. 248 p.
25. Wohlers T. Wohlers Report 2009. Colorado, USA: Wohlers Associates, Inc; 2009.
26. Baumers M, Tuck C, Hague R. Realised levels of geometric complexity in additive manufacturing. Int J Prod Dev. 2011 Jan 1;13(3):222–44.
27. Baumers M, Tuck C, Wildman R, Ashcroft I, Rosamond E, Hague R. Transparency built-in: energy consumption and cost estimation for additive manufacturing. J Ind Ecol. 2013 Jun 7;17(3):418–31.
28. Wong K V., Hernandez A. A Review of Additive Manufacturing. ISRN Mech Eng. 2012;2012:1–10.
29. Dimitrov D, Schreve K, De Beer N. Advances in Three Dimensional Printing - state of the art and future perspectives. J New Gener Sci. 2006;4(1):21–49.
30. Vaezi M, Seitz H, Yang S. A review on 3D micro-additive manufacturing technologies. Int J Adv Manuf Technol. 2012 Nov 25;67(5–8):1721–54.
31. Chua J. Are 3D-Printed Fabrics the Future of Sustainable Textiles? [Internet]. Wearable technology. 2010 [cited 2015 Mar 10]. Available from: http://www.ecouterre.com/are-3d-printed-fabrics-the-future-of-sustainable-textiles/
32. Wohlers T. Making Products By Using Additive Manufacturing. Manufacturing Engineering. 2011 Apr;
33. Wohlers T. Wohlers Report 2013: Additive Manufacturing and 3D Printing State of the Industry: Annual Worldwide Progress Report. Colorado, USA: Wohlers Associates, Inc; 2013.
34. Singh S. Beginning Google SketchUp for 3D Printing. Berkeley, CA: Apress; 2010.
35. Michael S. 3-D Printing a Goo Goo: Conceive and Build Your Own Tasty Designs with Sticky Food or Clay. Technology & Learning. 2008;
36. Rayleigh, Lord. On the Instability of Jets. Proc London Math Soc. 1878;10:4–13.

37. Rune E. Measuring instrument of the recording type. U.S. 2,566,443, 1951.
38. Sweet RG. High Frequency Recording with Electrostatically Deflected Ink Jets. Rev Sci Instrum. AIP Publishing; 1965 Dec 29;36(2):131.
39. Sweet RG. Fluid droplet recorder. U.S. 3,596,275, 1971.
40. Buehner WL, Hill JD, Williams TH, Woods JW. Application of Ink Jet Technology to a Word Processing Output Printer. IBM J Res Dev. IBM; 1977 Jan 1;21(1):2–9.
41. Zoltan S, Heights S. Pulsed droplet ejecting system. U.S. 3,693,212, 1972.
42. Le HP. Progress and Trends in Ink-jet Printing Technology. J Imaging Sci Technol. 1998;42(1):49–62.
43. Masters W. Computer automated manufacturing process and system. U.S. 4,665,492, 1987.
44. de Gans B-J, Duineveld PC, Schubert US. Inkjet Printing of Polymers: State of the Art and Future Developments. Adv Mater. 2004 Feb 3;16(3):203–13.
45. Wijshoff H. The dynamics of the piezo inkjet printhead operation. Phys Rep. 2010 Jun;491(4–5):77–177.
46. Yamada T, Matsuda Y, Yoshino M, Sakata M. Micro-dot ink jet recorder. U.S. 4,746,928, 1988.
47. Derby B. Inkjet Printing of Functional and Structural Materials: Fluid Property Requirements, Feature Stability, and Resolution. Annu Rev Mater Res. 2010 Jun;40(1):395–414.
48. Raje PV, Murmu NC. A Review on Electrohydrodynamic-inkjet Printing Technology. Int J Emerg Technol Adv Eng. 2014;4(5).
49. Shin K-Y, Hong J-Y, Jang J. Flexible and transparent graphene films as acoustic actuator electrodes using inkjet printing. Chem Commun (Camb). Royal Society of Chemistry; 2011 Aug 14;47(30):8527–9.
50. Hon KKB, Li L, Hutchings IM. Direct writing technology—Advances and developments. CIRP Ann - Manuf Technol. 2008 Jan;57(2):601–20.

51. Bugdayci N, Bogy DB, Talke FE. Axisymmetric Motion of Radially Polarized Piezoelectric Cylinders Used in Ink Jet Printing. IBM J Res Dev. IBM; 1983 Mar 1;27(2):171–80.
52. Fathi S. Fundamental investigation on inkjet printing of reactive nylon materials. University of Loughborough; 2011.
53. Haskal EI, Bolink HJ, Büchel M, Duineveld PC, Jacobs B, de Kok MM, et al. Passive-matrix polymer light-emitting displays. J Soc Inf Disp. 2003;11(1):155.
54. Gao F, Sonin AA. Precise Deposition of Molten Microdrops: The Physics of Digital Microfabrication. Proc R Soc A Math Phys Eng Sci. 1994 Mar 8;444(1922):533–54.
55. Chovancova-Lovell V, Pekarovicova A, Fleming PD. Novel Phase Change Inks for Printing Three-Dimensional Structures. J Imaging Sci Technol. 2006;50(6):550.
56. Carrilho E, Martinez AW, Whitesides GM. Understanding wax printing: a simple micropatterning process for paper-based microfluidics. Anal Chem. American Chemical Society; 2009 Aug 15;81(16):7091–5.
57. Smith PJ, Morrin A. Reactive inkjet printing. J Mater Chem. 2012;22(22):10965.
58. Derby B, Reis N. Inkjet Printing of Highly Loaded Particulate Suspensions. MRS Bull. 2003;28(11):815–8.
59. Dong H, Carr WW, Morris JF. An experimental study of drop-on-demand drop formation. Phys Fluids. AIP Publishing; 2006 Jul 6;18(7):072102.
60. Attinger D, Zhao Z, Poulikakos D. An Experimental Study of Molten Microdroplet Surface Deposition and Solidification: Transient Behavior and Wetting Angle Dynamics. J Heat Transfer. 2000;122(3):544.
61. Martin GD, Hoath SD, Hutchings IM. Inkjet printing - the physics of manipulating liquid jets and drops. J Phys Conf Ser. 2008 Mar 1;105(1):012001.
62. Reis N, Derby B. Ink Jet Deposition of Ceramic Suspensions: Modeling and Experiments of Droplet Formation. In: MRS Proceedings.

Cambridge University Press; 2011. p. 65.

63. Jang D, Kim D, Moon J. Influence of fluid physical properties on ink-jet printability. Langmuir. American Chemical Society; 2009 Mar 3;25(5):2629–35.

64. Khalate AA, Bombois X, Scorletti G, Babuska R, Koekebakker S, de Zeeuw W. A Waveform Design Method for a Piezo Inkjet Printhead Based on Robust Feedforward Control. J Microelectromechanical Syst. 2012 Dec;21(6):1365–74.

65. Bogy DB, Talke FE. Experimental and Theoretical Study of Wave Propagation Phenomena in Drop-on-Demand Ink Jet Devices. IBM J Res Dev. IBM; 1984 May 1;28(3):314–21.

66. MicroFab. MicroFab Technote 99-03:Drive Waveform Effects on Ink-Jet Device Performance [Internet]. MicroFab Technologies, Inc. 1999 [cited 2015 Nov 5]. Available from: http://www.microfab.com/images/pdfs/technote99-03.pdf

67. Kwon K-S, Kim W. A waveform design method for high-speed inkjet printing based on self-sensing measurement. Sensors Actuators A Phys. 2007 Oct;140(1):75–83.

68. Fathi S, Dickens P. Nozzle Wetting and Instabilities During Droplet Formation of Molten Nylon Materials in an Inkjet Printhead. J Manuf Sci Eng. American Society of Mechanical Engineers; 2012 Aug 1;134(4):041008.

69. Fathi S, Dickens P. Jet array driven flow on the nozzle plate of an inkjet printhead in deposition of molten nylon materials. J Mater Process Technol. 2013 Mar;213(3):383–91.

70. Shin P, Sung J, Lee MH. Control of droplet formation for low viscosity fluid by double waveforms applied to a piezoelectric inkjet nozzle. Microelectron Reliab. 2011 Apr;51(4):797–804.

71. Savart F. Mémoire sur la constitution des veines liquides lancées par des orifices circulaires en mince paroi. Ann Chim Phys. 1833;(53):337–86.

72. Henderson D, Segur H, Smolka LB, Wadati M. The motion of a falling liquid filament. Phys Fluids. AIP Publishing; 2000 Mar 1;12(3):550.
73. Yarin AL. Drop Impact Dynamics: Splashing, Spreading, Receding, Bouncing…. Annu Rev Fluid Mech. 2006 Jan;38(1):159–92.
74. Šikalo Š, Ganić EN. Phenomena of droplet–surface interactions. Exp Therm Fluid Sci. 2006 Nov;31(2):97–110.
75. Chandra S, Avedisian CT. On the Collision of a Droplet with a Solid Surface. Proc R Soc A Math Phys Eng Sci. The Royal Society; 1991 Jan 8;432(1884):13–41.
76. Pasandideh-Fard M, Qiao YM, Chandra S, Mostaghimi J. Capillary effects during droplet impact on a solid surface. Phys Fluids. 1996 Mar;8(3):650–9.
77. Rein M. Phenomena of liquid drop impact on solid and liquid surfaces. Fluid Dyn Res. IOP Publishing; 1993 Aug;12(2):61–93.
78. Rodriguez F, Mesler R. Some Drops Don't Splash. J Colloid Interface Sci. 1985;106(2):347.
79. Chen C-T, Hung T-Y. Morphology and deposit of picoliter droplet tracks generated by inkjet printing. J Micromechanics Microengineering. 2016 Nov 1;26(11):115005.
80. Stringer J, Derby B. Formation and stability of lines produced by inkjet printing. Langmuir. American Chemical Society; 2010 Jun 15;26(12):10365–72.
81. Deegan RD, Bakajin O, Dupont TF, Huber G, Nagel SR, Witten TA. Capillary flow as the cause of ring stains from dried liquid drops. Nature. 1997 Oct 23;389(6653):827–9.
82. Deegan RD, Bakajin O, Dupont TF, Huber G, Nagel SR, Witten TA. Contact line deposits in an evaporating drop. Phys Rev E. American Physical Society; 2000 Jul 1;62(1):756–65.
83. Hu H, Larson RG. Marangoni Effect Reverses Coffee-Ring Depositions. J Phys Chem B. 2006 Apr;110(14):7090–4.
84. Still T, Yunker PJ, Yodh AG. Surfactant-Induced Marangoni Eddies Alter

the Coffee-Rings of Evaporating Colloidal Drops. Langmuir. 2012 Mar 20;28(11):4984–8.

85. Nguyen VX, Stebe KJ. Patterning of Small Particles by a Surfactant-Enhanced Marangoni-Bénard Instability. Phys Rev Lett. 2002 Apr 3;88(16):164501.
86. Kajiya T, Kobayashi W, Okuzono T, Doi M. Controlling the Drying and Film Formation Processes of Polymer Solution Droplets with Addition of Small Amount of Surfactants. J Phys Chem B. 2009 Nov 26;113(47):15460–6.
87. Kim D, Jeong S, Park BK, Moon J. Direct writing of silver conductive patterns: Improvement of film morphology and conductance by controlling solvent compositions. Appl Phys Lett. 2006 Dec 25;89(26):264101.
88. McManus D, Vranic S, Withers F, Sanchez-Romaguera V, Macucci M, Yang H, et al. Water-based and biocompatible 2D crystal inks for all-inkjet-printed heterostructures. Nat Nanotechnol. 2017 Jan 30;12(4):343–50.
89. Burns SE, Cain P, Mills J, Wang J, Sirringhaus H. Inkjet Printing of Polymer Thin-Film Transistor Circuits. MRS Bull. 2003;28(11):829–34.
90. Perelaer J, Smith PJ, van den Bosch E, van Grootel SSC, Ketelaars PHJM, Schubert US. The Spreading of Inkjet-Printed Droplets with Varying Polymer Molar Mass on a Dry Solid Substrate. Macromol Chem Phys. WILEY-VCH Verlag; 2009 Mar 25;210(6):495–502.
91. Mustonen T, Kordás K, Saukko S, Tóth G, Penttilä JS, Helistö P, et al. Inkjet printing of transparent and conductive patterns of single-walled carbon nanotubes and PEDOT-PSS composites. Phys status solidi. 2007 Nov;244(11):4336–40.
92. Kordás K, Mustonen T, Tóth G, Jantunen H, Lajunen M, Soldano C, et al. Inkjet Printing of Electrically Conductive Patterns of Carbon Nanotubes. Small. 2006 Aug;2(8–9):1021–5.
93. Carey T, Cacovich S, Divitini G, Ren J, Mansouri A, Kim JM, et al. Fully

inkjet-printed two-dimensional material field-effect heterojunctions for wearable and textile electronics. Nat Commun. 2017 Dec 31;8(1):1202.

94. Tekin E, Wijlaars H, Holder E, Egbe DAM, Schubert US. Film thickness dependency of the emission colors of PPE–PPVs in inkjet printed libraries. J Mater Chem. 2006;16(44):4294–8.
95. Eom SH, Senthilarasu S, Uthirakumar P, Yoon SC, Lim J, Lee C, et al. Polymer solar cells based on inkjet-printed PEDOT:PSS layer. Org Electron. 2009 May;10(3):536–42.
96. Yun YH, Kim JD, Lee BK, Cho YW, Lee HY. Polymer inkjet printing: Construction of three-dimensional structures at micro-scale by repeated lamination. Macromol Res. 2009;17(3):197–202.
97. van den Berg AMJ, Smith PJ, Perelaer J, Schrof W, Koltzenburg S, Schubert US, et al. Inkjet printing of polyurethane colloidal suspensions. Soft Matter. The Royal Society of Chemistry; 2007;3(2):238–43.
98. Hart LR, Li S, Sturgess C, Wildman R, Jones JR, Hayes W. 3D Printing of Biocompatible Supramolecular Polymers and their Composites. ACS Appl Mater Interfaces. 2016 Feb 10;8(5):3115–22.
99. Hart LR, Li S, Sturgess C, Wildman R, Jones JR, Hayes W. 3D Printing of Biocompatible Supramolecular Polymers and their Composites. ACS Appl Mater Interfaces. 2016 Feb;8(5):3115–22.
100. Pekarovicova A, Bhide H, Fleming PD, Pekarovic J. Phase-Change Inks. J Coatings Technol. 2003 Jan;75(1):65–72.
101. Hancock A, Lin L. Challenges of UV curable ink-jet printing inks – a formulator’s perspective. Pigment Resin Technol. 2004 Oct;33(5):280–6.
102. Crivello J V., Reichmanis E. Photopolymer Materials and Processes for Advanced Technologies. Chem Mater. 2014 Jan 14;26(1):533–48.
103. Bourell D, Kruth JP, Leu M, Levy G, Rosen D, Beese AM, et al. Materials for additive manufacturing. CIRP Ann. 2017;66(2):659–81.
104. Löffelmann U, Wang N, Mager D, Smith PJ, Korvink JG. Solvent-free inkjet printing process for the fabrication of conductive, transparent, and flexible ionic liquid-polymer gel structures. J Polym Sci Part B Polym

Phys. 2012 Jan 1;50(1):38–46.

105. Maejima K, Tomikawa S, Suzuki K, Citterio D. Inkjet printing: an integrated and green chemical approach to microfluidic paper-based analytical devices. RSC Adv. 2013;3(24):9258.
106. Begines B, Hook AL, Alexander MR, Tuck CJ, Wildman RD. Development, printability and post-curing studies of formulations of materials resistant to microbial attachment for use in inkjet based 3D printing. Rapid Prototyp J. Emerald Group Publishing Limited; 2016 Aug 15;22(5):835–41.
107. Pilkenton M, Lewman J, Chartoff R. Effect of oxygen on the crosslinking and mechanical properties of a thermoset formed by free-radical photocuring. J Appl Polym Sci. 2011 Feb 15;119(4):2359–70.
108. Sangermano M, Sordo F, Chiolerio A, Yagci Y. One-pot photoinduced synthesis of conductive polythiophene-epoxy network films. Polymer (Guildf). 2013 Apr;54(8):2077–80.
109. Sangermano M, Razza N, Crivello JV. Cationic UV-Curing: Technology and Applications. Macromol Mater Eng. 2014 Jul;299(7):775–93.
110. Smith PJ, Morrin A. Reactive Inkjet Printing: A Chemical Synthesis Tool. The Royal Society of Chemistry; 2018. 270 p. (Smart Materials Series).
111. Lemmo A V., Fisher JT, Geysen HM, Rose DJ. Characterization of an Inkjet Chemical Microdispenser for Combinatorial Library Synthesis. Anal Chem. American Chemical Society; 1997 Feb;69(4):543–51.
112. Limem S, McCallum D, Wallace GG, in het Panhuis M, Calvert P. Inkjet printing of self-assembling polyelectrolyte hydrogels. Soft Matter. The Royal Society of Chemistry; 2011 Apr 5;7(8):3818.
113. Zhang R, Liberski A, Khan F, Diaz-Mochon JJ, Bradley M. Inkjet fabrication of hydrogel microarrays using in situ nanolitre-scale polymerisation. Chem Commun (Camb). The Royal Society of Chemistry; 2008 Mar 21;(11):1317–9.
114. Stempien Z, Rybicki E, Rybicki T, Kozanecki M. Reactive inkjet printing of PEDOT electroconductive layers on textile surfaces. Synth Met.

Elsevier B.V.; 2016;217:276–87.
115. Kröber P, Delaney JT, Perelaer J, Schubert US. Reactive inkjet printing of polyurethanes. J Mater Chem. 2009;19(29):5234.
116. Khodabakhshi K, Gilbert M, Dickens P, Hague R. Optimizing conditions for anionic polymerization of caprolactam for inkjetting. Adv Polym Technol. 2010 Dec 16;29(4):226–36.
117. Fathi S, Dickens P. Droplet characterisation of molten caprolactam for additive manufacturing applications. Proc Inst Mech Eng Part B J Eng Manuf. 2012 Mar 7;226(6):1052–60.
118. Fathi S, Dickens P, Khodabakhshi K, Gilbert M. Microcrystal Particles Behaviour in Inkjet Printing of Reactive Nylon Materials. J Manuf Sci Eng. 2013 Jan 22;135(1):011009.
119. Sturgess C, Tuck C, Ashcroft IA, Wildman RD. 3D Reactive Inkjet Printing of Polydimethylsiloxane. J Mater Chem C. The Royal Society of Chemistry; 2017;
120. Fenn DR, Olson KG, Rock RM, Hague RJM, Tuck CJ, Ma L, et al. Methods for reactive three-dimensional printing by inkjet printing. Google Patents; WO 2016085976 A1, 2016.
121. Brunelle D, Korn M. Advances in Polycarbonates. In: ACS Symposium Series 898. Washington, DC: American Chemical Society; 2005. p. 281.
122. Bendler J. Handbook of polycarbonate science and technology. New York: CRC Press; 1999. 376 p.
123. Schnell H. Chemistry and physics of polycarbonates, Polymer Review 9. New York: Interscience Publishers; 1964. 225 p.
124. Schnell H. Linear Aromatic Polyesters of Carbonic Acid. Ind Eng Chem. American Chemical Society; 1959 Feb;51(2):157–60.
125. Brunelle D. Polycarbonates. In: Encyclopedia of Polymer Science and Technology. Hoboken, NJ, USA: John Wiley & Sons, Inc.; 2002. p. 12344.
126. Kim WB, Joshi UA, Lee JS. Making Polycarbonates without Employing Phosgene: An Overview on Catalytic Chemistry of Intermediate and

Precursor Syntheses for Polycarbonate. Ind Eng Chem Res. 2004 Apr;43(9):1897–914.

127. Vouyiouka SN, Karakatsani EK, Papaspyrides CD. Solid state polymerization. Prog Polym Sci. 2005 Jan;30(1):10–37.
128. Ye Y, Machado B, Choi KY, Kim JH, Woo BG. Modeling of Solid-State Polymerization of Bisphenol A Polycarbonate. Ind Eng Chem Res. American Chemical Society; 2005 Apr;44(8):2494–505.
129. Hersh SN, Choi KY. Melt transesterification of diphenyl carbonate with bisphenol a in a batch reactor. J Appl Polym Sci. 1990;41(56):1033–46.
130. Kim Y, Choi KY. Multistage melt polymerization of bisphenol-A and diphenyl carbonate to polycarbonate. J Appl Polym Sci. 1993 Aug 5;49(5):747–64.
131. Woo B-G, Choi KY, Song KH, Lee SH. Melt polymerization of bisphenol-A and diphenyl carbonate in a semibatch reactor. J Appl Polym Sci. 2001 May 23;80(8):1253–66.
132. Nelson JC, Xue S, Barlow JW, Beaman JJ, Marcus HL, Bourell DL. Model of the selective laser sintering of bisphenol-A polycarbonate. Ind Eng Chem Res. American Chemical Society; 1993 Oct;32(10):2305–17.
133. Nelson JC, Vail NK, Sun MM, Barlow JW, Marcus HL, Beaman JJ, et al. Post-processing of selective laser sintered polycarbonate parts. In: Proceedings of the SFF Symposium Austin, Texas. Austin, Texas; 1991.
134. Novakova-Marcincinova L. Applications of Rapid Prototyping Fused Deposition Modeling Materials. In: Annals of DAAAM for 2012 & Proceeding of the 23rd International DAAAM Symposium. Vienna, Austria; 2012. p. 57–60.
135. Smith WC, Dean RW. Structural characteristics of fused deposition modeling polycarbonate material. Polym Test. 2013 Dec;32(8):1306–12.
136. Novakova-Marcincinova L, Kuric I. Basic and Advanced Materials for Fused Deposition Modeling Rapid Prototyping Technology. Manuf Ind Eng. 2012;11(1):24–7.
137. Horne R. Reprap development and further adventures in DIY 3D printing:

Indestructamendel - Polycarbonate 3D Printing with Prusa Mendel [Internet]. Reprap. 2011 [cited 2015 Jun 4]. Available from: http://richrap.blogspot.co.uk/2011/09/indestructamendel-polycarbonate-3d.html

138. Hall AJ, Hodge P. Recent research on the synthesis and applications of cyclic oligomers. React Funct Polym. 1999 Jul;41(1–3):133–9.
139. van Rijswijk K, Bersee HEN. Reactive processing of textile fiber-reinforced thermoplastic composites – An overview. Compos Part A Appl Sci Manuf. 2007 Mar;38(3):666–81.
140. Palit SR. Thermodynamic Interpretation of the Eötvös Constant. Nature. 1956;177(4521):1180–1180.
141. PiXDRO B.V. Ducumentation PiXDRO Inkjet Printing Systems. PiXDRO B.V.; 2011.
142. Genuchten E. Printing beyond paper. DSPE: Mikroniek. 2011;51(1):5–10.
143. Silvi N, Giammattei M, McCloskey PJ, Nisoli A, Day J, Ramesh N, et al. Method for making an aromatic polycarbonate. WO 2003106149 A1, 2003.
144. Torrisi F, Hasan T, Wu W, Sun Z, Lombardo A, Kulmala TS, et al. Inkjet-printed graphene electronics. ACS Nano. American Chemical Society; 2012 Apr 24;6(4):2992–3006.
145. He Y, Wildman RD, Tuck CJ, Christie SDR, Edmondson S. An Investigation of the Behavior of Solvent based Polycaprolactone ink for Material Jetting. Sci Rep. Nature Publishing Group; 2016 Jan 12;6:20852.
146. Gregory DA, Zhang Y, Smith PJ, Zhao X, Ebbens SJ. Reactive Inkjet Printing of Biocompatible Enzyme Powered Silk Micro-Rockets. Small. 2016 Jun;
147. He Y, Kilsby S, Tuck C, Wildman R, Christie S, Edmonson S. Processing Biodegradable Polycaprolactone through 3D Printing. In: 24th Annual International Solid Freeform Fabrication Symposium. Texas; 2013. p. 200–14.

148. Jansen B, Kamps JH, Kung E, McCloskey PJ, Smigelski Jr PM. Method of Preparing Polycarbonate. US 7498400 B2, 2009.
149. Fujifilm. Dimatix Materials Printer DMP-2850 Data Sheet. Fujifilm Support Documentation. Fujifilm; 2016. p. 1–2.
150. Gunasekera DHAT, Kuek S, Hasanaj D, He Y, Tuck C, Croft AK, et al. Three dimensional ink-jet printing of biomaterials using ionic liquids and co-solvents. Faraday Discuss. The Royal Society of Chemistry; 2016;190(0):509–23.
151. Hocker T, Gu H, Kamps JH, Noorrdegraaf D. System and method for reactive inkjet printing of polycarbonate. WO 2016179491 A1, 2016.
152. Kamps JH, Hoeks T, Kung E, Lens JP, McCloskey PJ, Noordover BAJ, et al. Activated carbonates: enabling the synthesis of differentiated polycarbonate resins via melt transcarbonation. Polym Chem. The Royal Society of Chemistry; 2016;7(33):5294–303.
153. Alicona. InfiniteFocus Technical Specifications [Internet]. 2018 [cited 2018 Jan 12]. Available from: http://www.alicona.com/products/infinitefocus/
154. Fulmer GR, Miller AJM, Sherden NH, Gottlieb HE, Nudelman A, Stoltz BM, et al. NMR chemical shifts of trace impurities: Common laboratory solvents, organics, and gases in deuterated solvents relevant to the organometallic chemist. Organometallics. 2010 May 10;29(9):2176–9.
155. Hsu J-P, Wong J-J. Melt Transesterification of Polycarbonate Catalyzed by DMAP. Ind Eng Chem Res. 2006 Apr;45(8):2672–6.
156. McCloskey PJ, Day J, Smigelski PM, Maxam JL, Osaheni JA. Extrusion method for making polycarbonate. US 6420512, 2002.
157. McCloskey PJ, Lens JP, Cella JA, Kamps JH, Longley KL, Ramesh N, et al. Method of polycarbonate preparation. US 6870025 B2, 2005.
158. Colonna M, Acquasanta F, Gioia C, Celli A. Effect of telechelic ionic groups on the dispersion of organically modified clays in bisphenol A polycarbonate nanocomposites by in-situ polymerization using activated carbonates. Express Polym Lett. 2017;11(5):396–405.

159. Brunelle DJ. (Ortho-alkoxycarbonyaryl)-carbonate transesterification. US 4323668, 1982.
160. Kraus RG, Emmons ED, Thompson JS, Covington AM. Infrared absorption spectroscopy of polycarbonate at high pressure. J Polym Sci Part B Polym Phys. 2008 Apr 1;46(7):734–42.
161. Lobo H, Bonilla J. Handbook of Plastics Analysis, Volume 68 of Plastic Engineering. CRC Press; 2003. 656 p.
162. Akola J, Jones RO. Branching Reactions in Polycarbonate: A Density Functional Study. Macromolecules. American Chemical Society; 2003 Feb;36(4):1355–60.
163. Schnell H, Krimm H. Formation and Cleavage of Dihydroxydiarylmethane Derivatives. Angew Chemie Int Ed English. 1963 Jul;2(7):373–9.
164. Hsu J-P, Wong J-J. Kinetic modeling of melt transesterification of diphenyl carbonate and bisphenol-A. Polymer (Guildf). 2003 Sep;44(19):5851–7.
165. Cooper GD, Johnson HT, Williams B. Substituent Effects in Hydrolysis of Diaryl Carbonates. J Org Chem. American Chemical Society; 1965 Nov;30(11):3989–91.
166. Gan HY, Shan X, Eriksson T, Lok BK, Lam YC. Reduction of droplet volume by controlling actuating waveforms in inkjet printing for micro-pattern formation. J Micromechanics Microengineering. IOP Publishing; 2009 May 1;19(5):055010.
167. Schiaffino S, Sonin AA. Formation and stability of liquid and molten beads on a solid surface. J Fluid Mech. 1997;343(01).
168. Reis N, Ainsley C, Derby B. Ink-jet delivery of particle suspensions by piezoelectric droplet ejectors. J Appl Phys. AIP Publishing; 2005 Apr 14;97(9):094903.
169. Van der Meulen M-J. Meniscus motion and drop formation in inkjet printing. University of Twente; 2014.
170. Fathi S, Dickens P, Hague R. Instability behaviours of a jet array in inkjet

printing of molten caprolactam. Rapid Prototyp J. 2013;19:189–98.

171. Vadillo DC, Tuladhar TR, Mulji AC, Jung S, Hoath SD, Mackley MR. Evaluation of the inkjet fluid's performance using the "Cambridge Trimaster" filament stretch and break-up device. J Rheol (N Y N Y). The Society of Rheology; 2010 Mar;54(2):261–82.
172. Zhang F, Tuck C, Hague R, He Y, Saleh E, Li Y, et al. Inkjet printing of polyimide insulators for the 3D printing of dielectric materials for microelectronic applications. J Appl Polym Sci. 2016 May 10;133(18):n/a-n/a.
173. Perelaer J, Smith PJ, Wijnen MMP, van den Bosch E, Eckardt R, Ketelaars PHJM, et al. Droplet Tailoring Using Evaporative Inkjet Printing. Macromol Chem Phys. WILEY-VCH Verlag; 2009 Mar 5;210(5):387–93.
174. Teichler A, Eckardt R, Friebe C, Perelaer J, Schubert U. Film formation properties of inkjet printed poly(phenylene-ethynylene)-poly(phenylene-vinylene)s. Thin Solid Films. 2011;519(11):3695–702.
175. Soltman D, Subramanian V. Inkjet-printed line morphologies and temperature control of the coffee ring effect. Langmuir. American Chemical Society; 2008 Mar 4;24(5):2224–31.
176. Kajiya T, Doi M. Dynamics of Drying Process of Polymer Solution Droplets: Analysis of Polymer Transport and Control of Film Profiles. J Soc Rheol Japan. The Society of Rheology, Japan; 2011 May 10;39(1_2):17–28.
177. Kim Y, Choi KY, Chamberlin TA. Kinetics of melt transesterification of diphenyl carbonate and bisphenol A to polycarbonate with lithium hydroxide monohydrate catalyst. Ind Eng Chem Res. American Chemical Society; 1992 Sep;31(9):2118–27.
178. Ignatov VN, Tartari V, Carraro C, Pippa R, Nadali G, Berti C, et al. New Catalysts for Bisphenol A Polycarbonate Melt Polymerisation, 2. Polymer Synthesis and Characterisation. Macromol Chem Phys. 2001 Jun 1;202(9):1946–9.

179. Qin J, Xie X, Cao X, Qu J. Modeling the continuous melt transesterification of bisphenol-A and diphenyl carbonate in a continuous stirred tank reactor. Chem Eng Sci. 2006 Sep;61(18):6154–64.
180. Thompson AB, Tipton CR, Juel A, Hazel AL, Dowling M. Sequential deposition of overlapping droplets to form a liquid line. J Fluid Mech. Cambridge University Press; 2014 Dec 21;761:261–81.
181. Lee SH, Cho YJ. Characterization of silver inkjet overlap-printing through cohesion and adhesion. J Electr Eng Technol. 2012;7(1):91–6.
182. Nishihara R. The Novel Process for Diphenyl Carbonate and Polycarbonate Production. Catal Surv from Asia. 2010 Jun 15;14(3–4):140–5.
183. Goyal M, Nagahata R, Sugiyama J, Michihiko Asai, Ueda M, Takeuchi K. Direct synthesis of aromatic polycarbonate from polymerization of bisphenol A with CO using a Pd–Cu catalyst system. Polymer (Guildf). 1999 May;40(11):3237–41.
184. Thorat SD, Phillips PJ, Semenov V, Gakh A. Physical properties of aliphatic polycarbonates made from CO2 and epoxides. J Appl Polym Sci. Wiley Subscription Services, Inc., A Wiley Company; 2003 Aug 1;89(5):1163–76.
185. Jang BN, Wilkie CA. A TGA/FTIR and mass spectral study on the thermal degradation of bisphenol A polycarbonate. Polym Degrad Stab. Elsevier; 2004 Dec 1;86(3):419–30.
186. Liu S, Ye H, Zhou Y, He J, Jiang Z, Zhao J, et al. Study on flame-retardant mechanism of polycarbonate containing sulfonate-silsesquioxane-fluoro retardants by TGA and FTIR. Polym Degrad Stab. Elsevier; 2006 Aug 1;91(8):1808–14.

9. Appendix A: 13C-NMR Spectra for the RIP samples

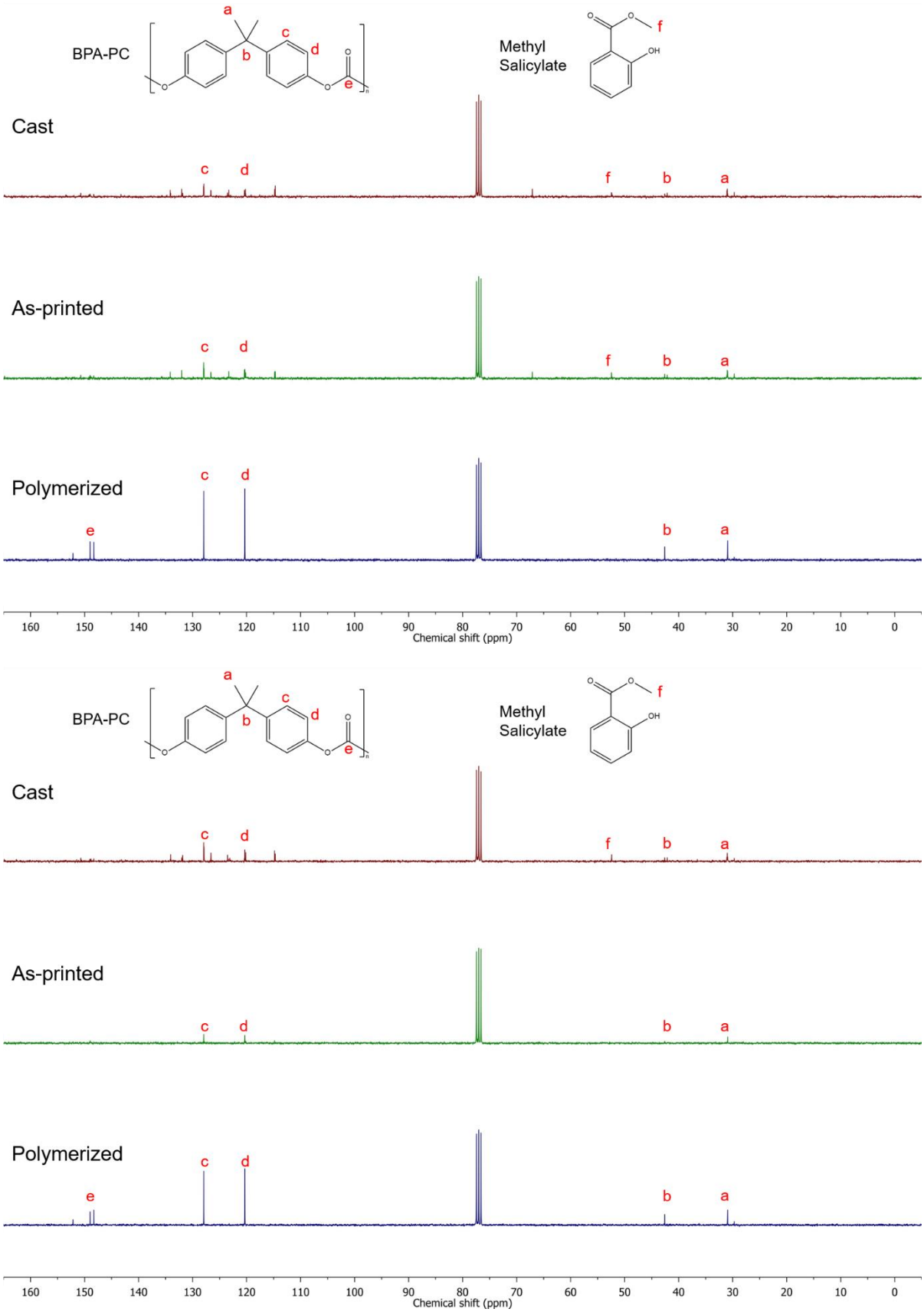


Figure 9-1: The ^{13}C-NMR spectra for the samples from DOX25 and DMF35, $CDCl_3$, 40 ºC

Table 9-1: ^{13}C-NMR data for the cast, as-printed and post-process BPA-PC, $CDCl_3$, 300 MHz

ID	Assigned C	δ C (ppm)
a	CH_3	30.95
b	C	42.67
c	CH	127.94
d	CH	120.34
e	C	148.96
f	CH_3	52.42

10. Appendix B: TG and DTA for Reference BPA-PC

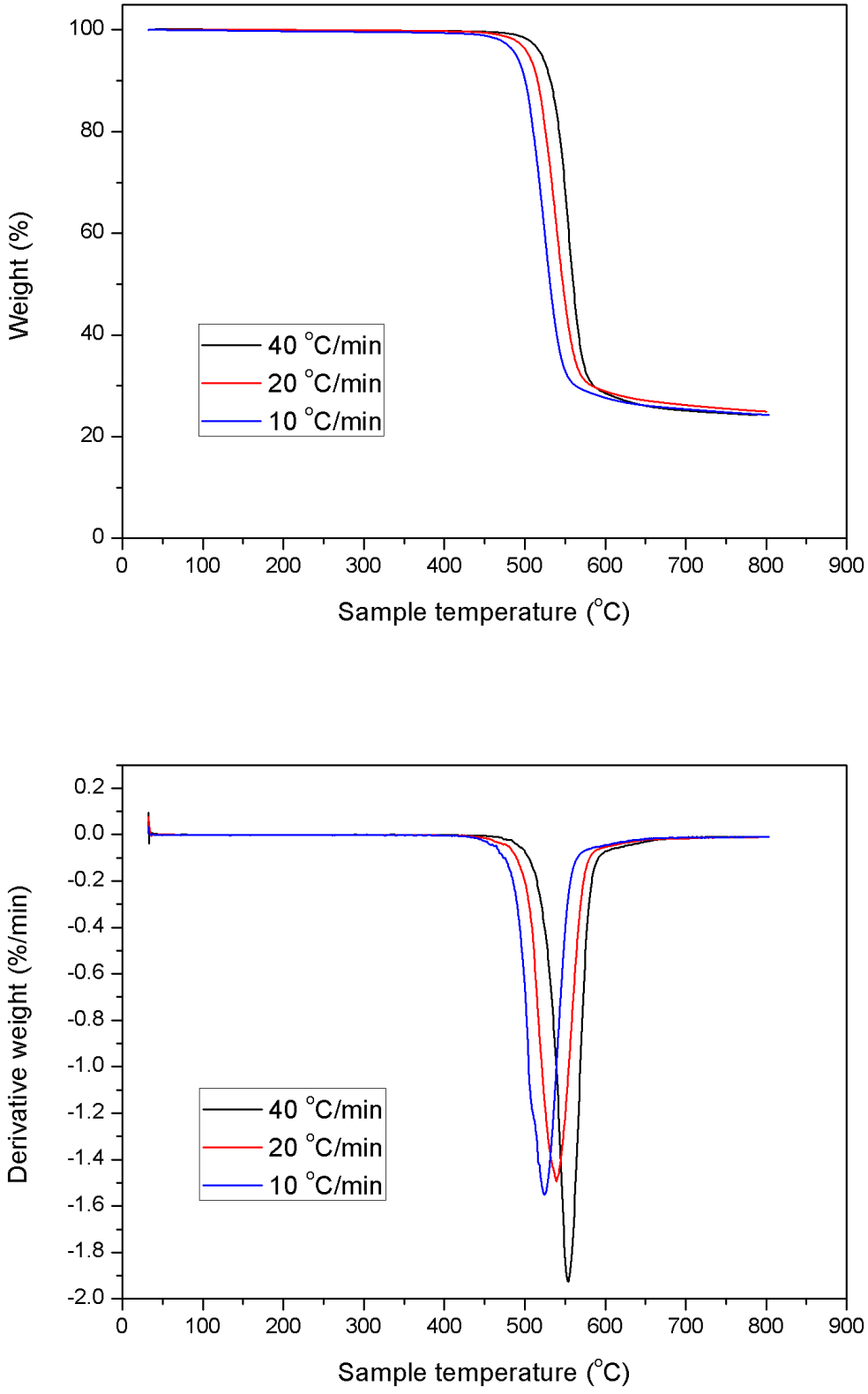


Figure 10-1: The TG and DTG curves of the reference high M_w PC samples

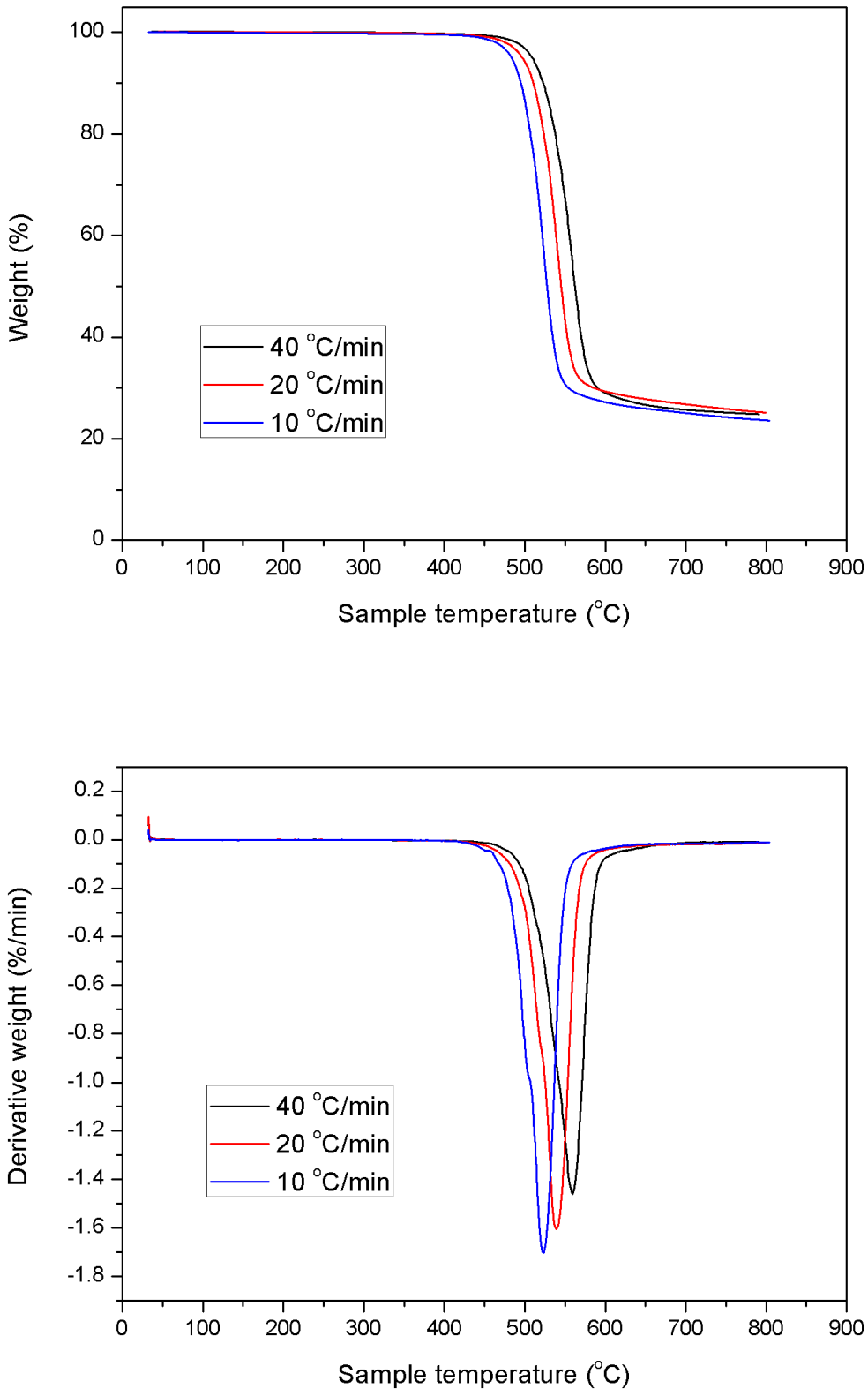


Figure 10-2: The TG and DTG curves of the reference low M_w PC samples